Wideband mobile propagation channels: Modelling measurements and characterisation for microcellular environments

Unar, Manzoor Hussain

Award date:
2006

Awarding institution:
University of Bath

Wideband Mobile Propagation Channels: Modelling, Measurements and Characterisation for Microcellular Environments

Submitted by

Manzoor Hussain Unar

for the degree of

Doctor of Philosophy in Electronic and Electrical Engineering

The University of Bath, UK

February 2006

Copyright

Author's signature 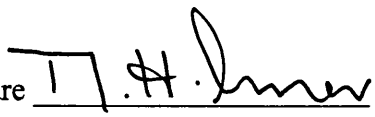 Date 15-02-06

ProQuest LLC
789 East Eisenhower Parkway
P.O. Box 1346
Ann Arbor, MI 48106-1346

Table of Contents

List of Figures

List of Tables

List of Abbreviations

1G	First generation
2D	Two dimensional
3D	Three dimensional
2G	Second generation
2.5D	Two-and-one-half dimensional
3G	Third generation
ADC	Analogue to digital converter
AV-DS	Average delay spread
AWGN	Additive white Gaussain noise
AMPS	Advanced mobile phone service
AOA	Angle-of-arrival
AOD	Angle-of-departure
APDP	Average power delay profiles
BER	Bit error rate
BRAN	Fixed broadband radio access network
BT	Time-bandwidth
cdf	Cumulative distribution function
CDMA	Code division multiple access
COA	Centre-of-area
CIR	Channel impulse response
CW	Continuous wave
D-AMPS	Digital advanced mobile phone service
DAC	Digital to analogue converter
DE	Diffracting edge
DEM	Digital elevation model
DOA	Direction-of-arrival
DS	Delay-spread
DSB-AM	Double sideband amplitude modulation
DSP	Digital signal processing
DT	Data type
DTM	Digital terrain model
DXF	Drawing exchange format
EM	Electromagnetic
ERO	European radio communications office
ETSI	European telecommunications standards institute
ETACS	European total access cellular system
FCC	Federal communication commission
FDTD	Finite-difference time-domain
FWN	Fixed wireless network
FPLMTS	Future public land mobile telephone systems
FCF	Frequency correlation function
GO	Geometrical optics
GR	Ground reflection
GRIMM	Geometrical ray implementation for mobile propagation modelling

GSM	Global system for mobile
GTD	Geometrical theory of diffraction
HCMTS	High capacity mobile telephone system
HIPERACCESS	High performance radio access
HIPERLAN	High performance LAN, Local area network
IEEE	Institute of Electrical and Electronic Engineers
ISI	Inter-symbol-interference
ISM	Industrial Scientific and Medical
IMT	International mobile telecommunication
ITU	International telecommunication union
JTACS	Japanese total access cellular system
LAN	Local area network
LF	Low frequency
LoS	Line of sight
LMDS	Local multipoint distribution service
MCRC	Mobile cellular radio communication
MIMO	Multiple input multiple output
MoM	Method of moments
MRT-1	Micro-ray-tracer-1
NADC	North American digital cellular
NLoS	Non-line of sight
NMT	Nordic mobile telephony
N_E	Facet edge number
N_P	Facet number
NTT	Nippon telephone and telegraph
ODSV	Ordinance Survey
OS	Operating system
PL	Optical path length,
PEM	Parabolic equation method
PDC	Pacific digital cellular
PCN	Personal communication network
PCS	Personal communication services
PC	Personal computer
PDA	Personal digital assistant
pdf	Probability density function
PDP	Power delay profile
PHY	Physical layer
PMR	Private mobile radio
PO	Physical optics
POD	Point-of-diffraction
POGR	Point-of-ground-reflection
POR	Point-of-reflection
RG	Ray-segment
RF	Radio frequency
RFP	Reflecting polygon
ROM	Read only memory
RP	Received power
RMS-DS	Root mean square delay spread
PRBS	Pseudo random binary sequence
QoS	Quality-of-service

RO	Ray optics
SAW	Surface acoustic wave
SBR	Shooting-and-bouncing ray
SHF	Supreme high frequency
TL	Transmission loss
TIN	Triangular irregular network
UNV	Unit-normal-vector
UHF	Ultra high frequency
UMTS	Universal mobile telecommunication systems
UK	United Kingdom
UTD	Uniform theory of diffraction
US	Uncorrelated scattering
USA	United States of America
USDC	US digital cellular
USGS	United States Geological Survey
UTRA	UMTS terrestrial radio access
VHF	Very high frequency
VIP	Very important point
VLSI	Very large scale integrated
VPE	Vector parabolic equation
VPL	Vertical plane launch
VRPM	Valid-ray-path-matrix
WARC	World administration radio conference
WCDMA	Wideband CDMA, Code division multiple access
WISE	Wireless System Engineering
WLAN	Wireless LAN, Local area network
WMAN	Wireless metropolitan area networks
WPAN	Wireless personal area network
WPABX	Wireless private automatic branch exchanges
WPAN	Wireless personal area network
WSS	Wide-sense stationary
WSSUS	Wide-sense stationary and uncorrelated scattering
WWLAN	Wide area WLAN, Wireless local area network

List of Publications

1. Unar M.H. and Glover I.A., "Measurements and Modelling of the Wideband Mobile Radio Channel in Residential Suburban Environments," *The Convergence of Telecommunications, Networking and Broadcasting, PGNet Conference, Liverpool, UK*, 2006.

2. Unar M.H., Glover I.A., and Cannon P.S., "3-D Ray-Tracing Propagation Model for the Microcellular Environment in the UHF Band," *PREP 2005 Conference, Lancaster University, UK.*, 2005.

3. Unar M.H., Glover I.A., and Vaccaro G., "Propagation Modelling for the Microcellular Environment in the UHF Band," *UK National URSI Symposium, University of Bath, UK*, 2004.

4. Unar M.H., Glover I.A., Heaton J., Williams C., and Cannon P.S., "Wide-Band Mobile Radio Channel Characterisation in UHF Band for Residential Suburban Areas," *12th International Conference on Antennas and Propagation, (ICAP -2003), University of Exeter, UK*, 2003.

Acknowledgments

I would like to express my sincere thanks to my academic supervisor, Dr Ian A Glover. His guidance, supervision, expertise and patience has made my research experience meaningful and fulfilling.

I want to thank QinetiQ (formerly Defence Evaluation Research Agency, (DERA), UK) for sponsoring my Doctoral Research Program. Special thanks to Professor Paul S Cannon and Dr C Williams for arranging the sponsorship. I would like to thank Dr J Heaton for his support in many aspects of this research activity.

I would like to thank my part-time employer, Bath University Computing Services (BUCS), and especially my work supervisor Mrs. Heather Kellaway who has provided me flexible job and enable me to complete my Ph. D studies without financial problems.

I would thanks to Dr Nandini Sengupta, Dr J Sharma, Mr Andy Matthews, Mr Richard Carruthers, Mr Patrick Van Barneveld and Ms Emma Bryant of the University of Bath for their encouragements.

I would like to also thank Professor Ishak bin Ismail of the University Technology, Malaysia and Dr A R Memon (former Vice Chancellor), Mehran University of Engineering and Technology, Pakistan for their encouragements in motivating me to pursue the Ph. D studies in the area of radio communications.

I am grateful for the constant support, encouragements and critique from my wife Nasim Fatima and children. Their presence enables me to complete my academic journey with courage and confidence.

These acknowledgements would be incomplete without thanks to those who made long term commitments to my success. I give many special thanks to my father Muhammad Usman, relatives and family friends for their continuous, unconditional love and support, and encouragements and patience in completing Ph. D studies.

Abstract

The work reported in this thesis is concerned with measurement, modelling and characterisation of wideband mobile radio channels in suburban microcellular environments.

As the demand for the radio communication systems and services increases, new cellular systems are needed to accommodate more users within limited spectral resources. Concurrently, the recent proliferation, activity and interest of UMTS and PCN systems and services have triggered increased demand for high data rate microcellular mobile radio communications systems.

Multipath is the major cause of signal degradation by the radio channel. Due to multipath propagation the radio channel becomes dispersive and time-variant. In order to determine optimum methods of mitigating the impairment caused by multipath propagation, the radio channels must be properly characterised. This is a pre-requisite to reliable planning, design and implementation of future high-performance, high data-rate, wideband, microcellular systems.

A new three-dimensional, wideband, ray-tracing propagation prediction model has been developed. The model takes into account direct (line-of-sight) paths, ground reflected paths, paths due to reflection from terrain cover (primarily buildings) and paths due to diffraction around and over buildings.

In order to characterise the channel the amplitude, phase, polarisation, angle-of-departure, angle-of-arrival and optical path length of each ray-path is tracked. Measurements have been made in a suburban, residential, area of Malvern, UK at 2.38 GHz and channel statistics including number of paths, received power, transmission loss, delay spread have been obtained.

Comparisons between the simulated and measured results confirm the utility of the model.

Chapter 1: Introduction

Mobile cellular and wireless personal communication networks (PCNs) are the fastest growing fields in modern radio communications engineering. As we begin the 21st century, more than 100 million people, about 10% of the world's population, pay a monthly subscription for a mobile telephone service, and this figure will approach 50% by the end of the first decade of this century [1], [2]. Exponential growth worldwide has demonstrated conclusively that mobile cellular and PCN systems are viable future high-speed transmission technologies.

The widespread use of current radio systems, along with the concurrent evolution of universal mobile telecommunication system (UMTS) systems, has increased demand for more sophisticated radio systems to accommodate increased numbers of users within the constraint of limited available frequency spectrum. Future UMTS systems are aimed at supporting new applications and services at high data rates interactively in a wide range of environments (Figure 1.1).

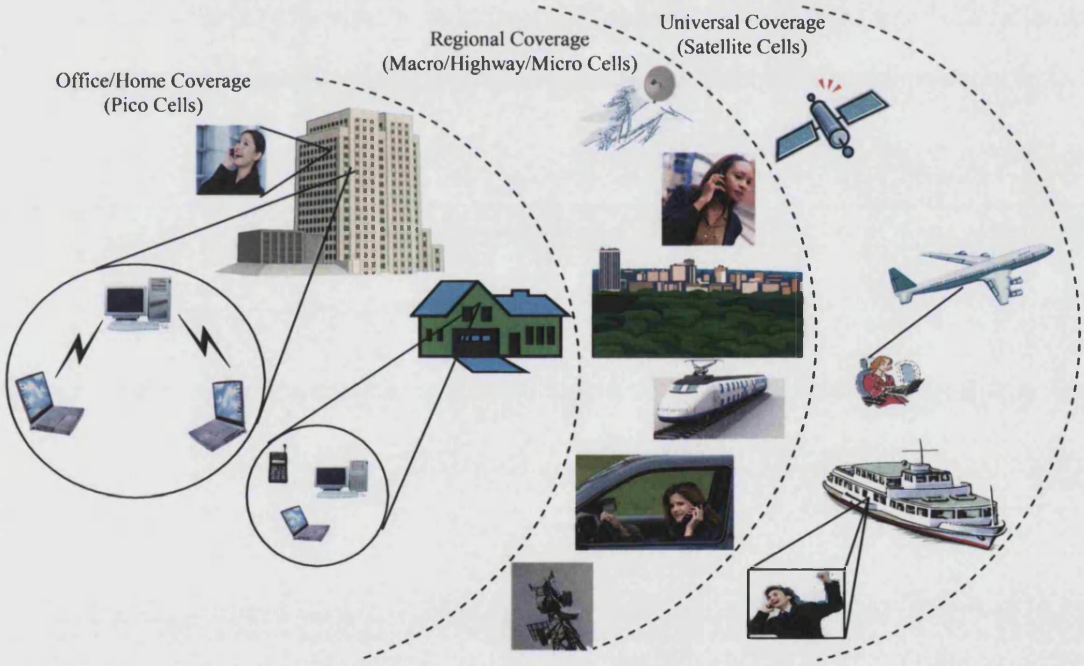

Figure 1.1: *An illustration of UMTS environments.*

The aim of this chapter is to present a brief review of the evolution, state-of-the-art and future trends in relation to radio communication systems, and to describe the motivation, aims, contribution and structure of this thesis.

1.1 Evolution of mobile radio communication systems

1.1.1 Historical background

The era of radio communications began when Guilielmo Marconi, in 1897, first demonstrated the transmission and reception of Morse code between the United Kingdom (UK) and the United States of America (USA) [3]. Six years later, in 1901, Marconi succeeded in establishing a radio communication service, between ships sailing in the English Channel. This first radio communication service was operated at frequencies less than 100 kHz [4]. In the early 20th century, the popularity of radio systems grew and radio communication services were extended to public security services such as police forces and fire brigades. In 1906, the first world administration radio conference (WARC) was held, and recommendations regarding the assignment of radio frequency bands or spectrum were introduced and issued. Early radio communication systems used the low frequency (LF) portion of the radio spectrum. As the demand for new and different radio communication services increased, more spectrum at higher frequencies was required. New services in the very high frequency (VHF), 30 – 300 MHz, ultra high frequency (UHF), 300 – 3000 MHz, and supreme high frequency (SHF), 3000 – 30000 MHz bands have emerged. Since then new radio communications methods, techniques, standards, systems and services, have been enthusiastically adopted, developed and deployed throughout the world in various frequency bands.

In 1934, the Federal Communication Commission (FCC) [5] was formed and mobile radio systems were introduced for public safety in the USA. In 1946, the first commercial USA public mobile radio telephone system was commissioned. The system used a single, high-powered base-station on a large tower to provide coverage of over 50 km. Only a limited number of subscribers could be accommodated, however, due to congestion of the limited frequency spectrum allocated. Figure 1.2(a) shows an illustration of such a single base-station mobile radio communication system.

From World War 2 to the mid 1960s continuous efforts were made to increase frequency spectrum efficiency in order to increase the number of subscribers and reduce congestion.

In 1968, the concept of cellular radio was proposed by AT&T Bell laboratories in the USA. The idea of cellular radio was to divide a large coverage zone (geographical area) into smaller coverage areas, each of which reused part of the allocated frequency spectrum to increase spectral efficiency and capacity [4], [6].

In late 1970s, the era of mobile cellular radio communication (MCRC) systems was born and a number of commercial MCRC systems were developed and deployed throughout the world, e.g. advanced mobile phone service (AMPS) in USA, European total access cellular system (ETACS) in Europe, Japanese total access cellular system (JTACS), pacific digital cellular (PDC), Nippon telephone and telegraph (NTT) and high capacity mobile telephone system (HCMTS), in Japan, Nordic mobile telephony (NMT) in Scandinavia., etc. These MCRC systems [4], [7], [8] operated in an interference limited environment and rely on frequency re-use. They require many base stations to provide coverage to a large geographical area, with low levels of transmitted

power. These systems used analogue technology and are known as first generation or 1G systems. The main advantages were the accommodation of more subscribers, reduced spectrum congestion and higher traffic capacity. They operated in 450 MHz to 960 MHz bands and were designed for large geographical (macro-cellular) environments. The transmission rates of these systems were around 2.4 kbps [1]. Figure 1.2(b) shows an illustration of a mobile cellular radio communication system.

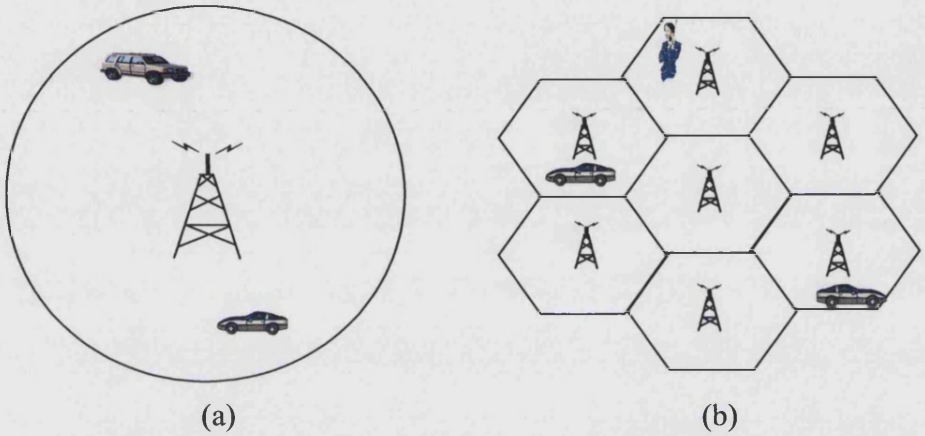

(a) (b)

Figure 1.2: *Illustration of mobile radio communication systems*, (a) *Classical system*, (b) *Cellular system*.

1.2 State-of-the-art and future trends of radio communication systems

1.2.1 2G systems

MCRC systems developed and deployed during the 1970s to 1980s were based on analogue technology and generally known as the *first generation* (1G) systems. In the early 1990s, due to advances in digital signal processing and RF technology, there has been enormous activity to develop digital MCRC systems to facilitate high-speed data communications services in addition to voice calls. In late 1991, the US digital cellular (USDC), North American digital cellular (NADC) or digital advanced mobile phone service (D-AMPS) system was launched in the USA. Subsequently, the pan European digital cellular standard, global system for mobile (GSM) was deployed in 900 MHz band [1]. The GSM standard has gained worldwide acceptance as the first universal digital cellular system with modern network features, and became the main digital MCRC system around the world. The USDC and GSM systems are generally known as *second generation* (2G) systems. 2G systems use digital modulation to enable signals to tolerate a higher level of interference while maintaining the same quality-of-service (QoS). They also allow digital speech compression techniques to be used in order to increase the number of channels in a given bandwidth, thus increasing capacity over the 1G systems [4]. (Almost all 2G systems offer at least a three times increase in spectrum efficiency, and offers at least a three times increase in overall system capacity compared to 1G analogue systems.) 2G systems generally operate in 890 MHz - 960 MHz frequency bands. The transmission rates of these systems are up to 14.4 kbps [2].

1.2.2 2.5 systems

Since the mid 1990s, 2G digital MCRC systems have been widely deployed. These systems were designed before the widespread use of the Internet. All the 2G systems were originally developed to support single user data rates (~ 14.4 kbps) which were too slow for rapid email and Internet browsing applications. In an effort to retrofit the 2G standards for compatibility with increased data rates that were required to support modern Internet applications, new standards have been developed that can be overlaid upon existing 2G systems. These new standards represent 2.5G technology and allow existing 2G equipment to be modified and supplemented with new base station add-ons and subscriber unit software upgrades to support higher data rate transmissions for web browsing, e-mail traffic, mobile commerce (*m-commerce*), and location-based mobile services [2]. A wide range of 2.5G standards have been developed and significant improvements in Internet access speed over 2G systems have been achieved, supporting new Internet-ready mobile handsets. Most of today's MCRC systems are based on the enhanced version of GSM, generally known as GSM$^+$. The GSM$^+$ offers data rates up to 384 kbps [1], [9], [10].

In addition to 2.5G systems, specialised fixed and mobile radio communication systems were also introduced with additional services, such as: 1) radio paging [1], [11], 2) private mobile radio (PMR) [4], 3) cordless telephone [12], and 4) personal communication networks (PCNs), or personal communication services (PCS) [13]. These systems are incompatible to each other and perform subtly different tasks, with no one system being ideal. They must all, however, compete with each other for limited frequency spectrum. The coverage area, cost, complexity, performance and applications of these systems vary as they are specifically designed for different users having different needs. The types of services offered by each of these systems are, therefore, very different [2]. In order to establish compatibility and to integrate various fixed and mobile systems and services MacNamee [14], proposed that future mobile radio communication systems should seek to integrate all mobile radio communication systems and services under a single specification. This concept has stimulated the need and demand for a new generation of radio communication systems.

1.2.3 3G systems

The rapid growth for MCRC and PCN systems has created concurrent demand for a new generation of radio systems. In 1995, a worldwide standard, 'the Future Land Mobile Telephone Systems' (FPLMTS), later renamed 'International Mobile Telecommunication 2000' (IMT-2000), was formulated by the International Telecommunication Union (ITU) for global mobile radio communications [15]. One year later, in 1996, the European Telecommunications Standards Institute (ETSI) initiated similar activities in Europe for global mobile radio communications and proposed the 'Universal Mobile Telecommunication Systems (UMTS) [1], [16] - [19] for 3G MCRC systems.

In 1998, UMTS was submitted by ETSI to ITU's IMT-2000 body for consideration as a world-wide single universal standard. At that time, UMTS was known as UMTS Terrestrial Radio Access (UTRA), and was designed to provide

a high capacity upgrade path for GSM and its extended versions such as GSM^{+} [1], [2].

At present IMT-2000/UMTS or simply UMTS is a 3G universal, multi-function, globally compatible digital mobile radio system that will integrate a range of radio communication systems and services such as paging, cordless, MCRC and PCN systems, as well as low Earth orbit (LEO) satellites, into single universal radio communication system. UMTS is also called wideband CDMA (WCDMA) [2], [20], [21]. It is necessary to emphasise here that the LEO satellite communication systems were developed in the 1990s but, although successful technologically, failed commercially at the turn of the 21st century. Due to the large area, represented by the entire Earth's surface, illuminated by satellites, space borne cellular systems are unlikely to approach the capabilities provided by land mobile cellular systems [2].

The major objectives and advantages of UMTS will include simultaneous multifunctional interactive radio access in ways that have never been possible before. For example, compatibility and integration between the radio communication systems, involvement of a range of frequencies, higher data rates, multi-operational environments (indoor, indoor-to-outdoor, outdoor, dense-urban, urban, suburban, rural), mobility (fixed, nomadic and mobile), availability (anytime, anywhere, anyplace). All these at high performance and quality-of-service (QoS) [22].

The success of UMTS depends on the integration of different MCRC and PCN systems. UMTS operates at 1.7 GHz to 2.7 GHz at bit rates up to 2 Mbps [23], [24] and offer simultaneous voice, video and data (multi-media) services including Internet access, voice-activated Internet calls, television, fax, videoconferencing, online distant-learning, etc. with multi-user capabilities, at user speeds up to 500 km/h [1].

1.2.4 Personal communication networks (PCNs)

In the late 1980s, due to advances in very large scale integrated (VLSI) electronics, high speed personal computers (PCs) were developed and the concept of the wired local area networks (LANs) was introduced [25]. Since the early 1990s, due to phenomenal growth of Internet services, widespread demand for broadband Internet access through individual PCs and LANs has increased exponentially throughout the world. With the advances in, and popularity of, portable (terminal) devices, in 1995, the personal communication services (PCS) concept was originated in the UK. PCS resides in the 1.8 GHz to 2 GHz band. The terms PCS is often used interchangeably with PCN (personal communications network) [13], [26]. The term PCS, however, refers to the services offered by a PCN. PCN systems are designed and developed in competition with MCRC systems, as a high capacity communications technology allowing any user to access radio services using portable devices, domestic electronic appliances, PCs and/or wireless LANs (WLANs). PCN systems can either be fixed, mobile, or both. PCNs originally referred to a radio communication network that incorporated more network features and personalised services than existing MCRC systems.

PCN systems can be categorised as: 1) fixed wireless or wireless local loop (WLL) networks, 2) wide area WLANs (WWLANs), 3) wireless LANs (WLANs), 4) wireless personal area networks (WPANs). These systems are briefly described in the next section.

1.2.4.1 Fixed wireless networks (FWNs)

Recent rapid growth and demand for high-speed data communications networks have stimulated the development of fixed wireless networks (FWNs). Applications include emergency-services, airports, hospitals, corporate-businesses, educational-institutes, industries, individual domestic users throughout the world and point-to-point and point-to-multipoint topologies are employed. FWN systems aim to provide services such as high data rate Internet access and voice activated telephony from portable and fixed devices.

Wireless local loop (WLL) is the industrial name of the FWN [27]. The FWN systems uses radio links rather than wires, cable or fiber-optic connections.

FWNs may operate in a variety of environments providing universal long-range coverage; regional macro-cells coverage, micro-cells coverage, pico-cell coverage and short-range coverage (see Figure 1.3). If the coverage area extends to city level then these systems are also referred to as wireless metropolitan area networks (WMANs) [28] - [30].

FWN systems operate at microwave or millimetre radio frequencies in the 28 GHz band and higher, which is greater than ten times the carrier frequency of 3G terrestrial MCRC systems.

In 1998, the USA government proposed a fixed wireless local multipoint distribution service (LMDS) in the 27 GHz to 31 GHz band which aimed to provide broadband radio access between main and local wireless private automatic branch exchanges (WPABXs) and between local WPABXs and end users [2]. The IEEE 802.16 standards committee developed interoperability standards for LMDS [2]. In Europe, a similar standard, HIPERACCESS, was developed by the European telecommunications standards institute (ETSI) standardisation committee for a fixed broadband radio access network (BRAN) [25], [31, [32]. The main objective of BRAN systems is to develop a family of broadband WLAN type networks that allow user interoperability, covering both short range (e.g. WLAN) and long range (e.g. WWLANs).

Long range BRAN systems operate in the 40.5 GHz to 43.5 GHz band. Short range BRANs operate in the 17 GHz band supporting data rates up to 155 Mbps with a range of 150 metres [2].

Taking together FWN, LMDS and BRANs systems will use microwave links. They may use high-gain (directional) antennas and employ spatial filtering to reject multipath signals allowing transmission of very wide bandwidth signals (on the order of 10s or 100s of Mbps) without distortion. FWN systems at very high microwave frequencies are only viable where LOS conditions predominate.

FWN systems aim to provide a wide range of services, e.g. telephone, television, radio, fax, data communication and wideband Internet [3]. They are likely to be deployed in near future and, eventually, integrated with future UMTS systems.

1.2.4.2 Wireless local area networks (WLANs)

In early 1980s new standards and technologies were proposed to replace wired computer communication networks such as local area networks (LANs) with wireless equivalents [25], [32]. Despite the unrestricted spectrum allocation and intense industry interest, the WLAN movement did not gain momentum until the late 1990s, when the use of high-speed data communications grew and the popularity of the Internet combined with wide scale acceptance of PCs, laptops and portable-devices.

Wireless products based on the WLAN concept emerged at the beginning of 1990s [4], [33]. Several different WLANs products offering differing bit rates ranging from 100s of bps to more than 10 Mbps are now available. Accurate definitions of the needs and objectives of WLANs are, therefore, difficult. Important characteristics for a typical WLAN can be identified, however, as [4], [34]: 1) coverage, 2) power consumptions, 3) bit rate, 4) protocol and 5) safety related aspects. WLANs are based on various architectural topologies e.g. bus, ring and/or star. If a WLAN is interconnected with other WLANs then the resulting network may become a wide area WLAN (WWLAN). The transmission medium may be infrared (IR) or radio. Three radio bands are allocated for WLANs.

Three radio bands are commonly used for WLANs. These are 1) 4.9 to 6.0 GHz band [35], [36], 2) industrial, scientific and medical (ISM) band: 900 MHz, 2.4 GHz and 5.8 GHz [37], 3) 18 to 19 GHz band [4].

The major objective of the WLANs is to allow low power and high bit rate radio communication links between low mobility users over a limited coverage area [33]. They are suitable for short-range or pico-cell wireless networking that could facilitate private or personal radio communication services in the indoor environments. Indoor wireless networking products are rapidly emerging and promise to become a major part of the radio communications infrastructure in the near future. Figure 1.3 shows an example of fixed wireless networks and typical configurations of WWLANs and WLANs.

1.2.4.2.1 Standardisation of WLANs

The IEEE 802.11 standard in the USA and the HIPERLAN standard in Europe were initiated concurrently for WLAN technologies.

1.2.4.2.1.1 The IEEE 802.11 standards

IEEE 802.11 was formed in 1987 for fixed WLANs by the Institute of Electrical and Electronic Engineers (IEEE) in the USA [38]. The Industrial Scientific and Medical (ISM) bands were proposed for WLANs. The main objective of IEEE 802.11 standard is to replace wired LANs with WLANs. IEEE 802.11 was

finalised in 1997 with the specifications for the physical (PHY) layer. The original specification provided data rates up to 2 Mbps. Many extensions to, and variation in, IEEE 802.11 now exist, however. For example, IEEE 802.11a operates at 5.2 GHz with data rates up to 54 Mbps. In 1999, the high rate IEEE 802.11b standard was specified to operate in the 2.4 GHz ISM band with a data rate up to 11 Mbps while IEEE 802.11g is specified to operate in the 2.4 GHz band and will support roaming capabilities and dual-band users for public WLAN networks, while supporting backward compatibility with 802.11b. Further extensions in IEEE 802.11 standard are expected for wireless wide area networks (WWLANs).

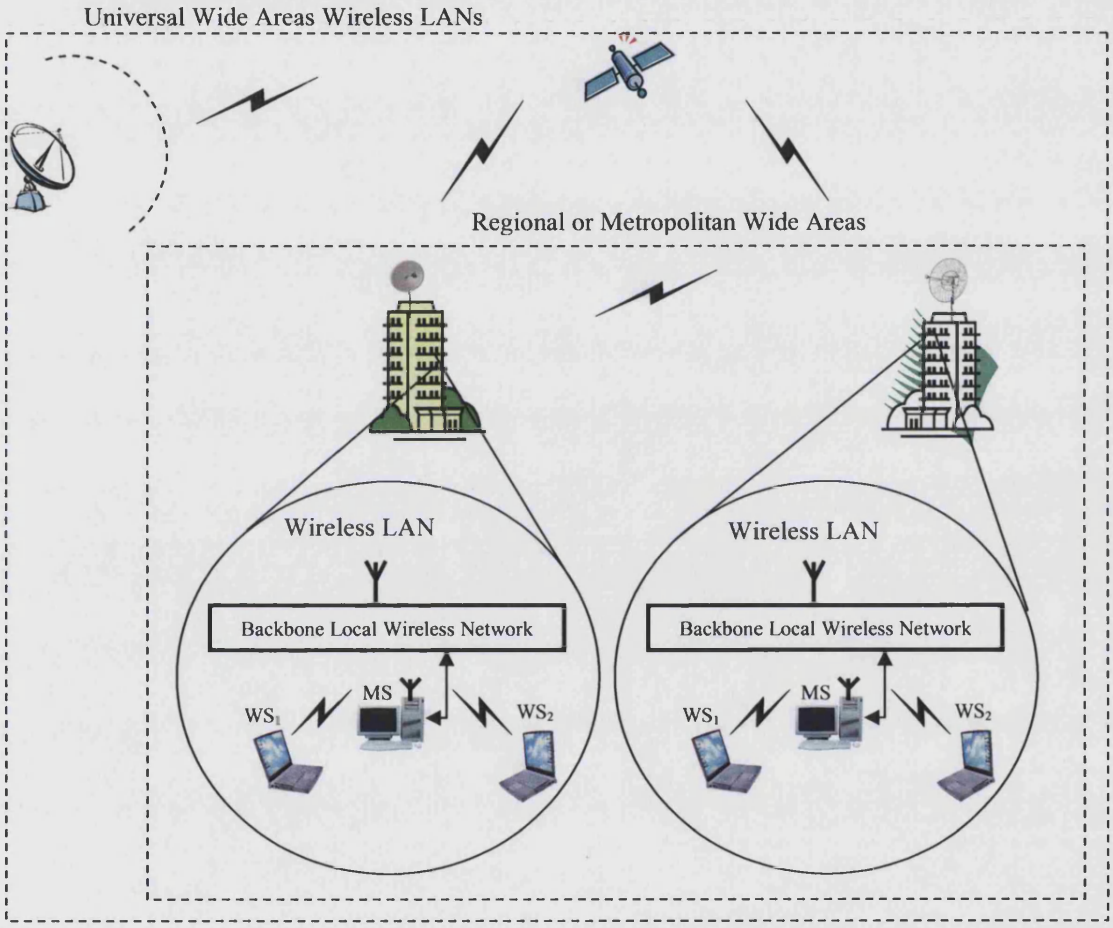

Figure 1.3: *An example of fixed wireless networks showing typical configuration of WWLANs and WLANs.*

Detailed discussions on WLAN standardisation are available in the literature e.g. [1], [2], [4], [35] - [37], [39].

1.2.4.2.1.2 High performance radio LAN standards

In 1995 ETSI established a standard for a high performance radio LAN (HIPERLAN) to provide capabilities similar to the IEEE 802.11. The HIPERLAN standard was designed to provide individual WLANs for high-speed data communications in the 5.2 GHz and 17.1 GHz bands. HIPERLAN was

designed to operate for individual fixed and mobile communication (vehicle speed up to 35 km/h) and offers bit rates up to 20 Mbps at 50 m range [1].

In 1997, the high-performance-LAN-2 (HIPERLAN-2) standard was proposed by the ETSI broadband radio access networks (BRANs) project [3], [4], [40]. It operates in the 5 GHz band and offers data rates up to 54 Mbps to a variety of devices (e.g. laptops, personal digital assistants - PDAs, electronic diaries, pocket PCs, smart mobile phones) in a variety of environments (e.g. hotspots: airports, hospitals) and for a variety of application (e.g. emergency and rescue services). HIPERLAN-2 can also be used as an alternative access technology for 3G cellular networks under a UMTS core. The most recent application is in the home environment to create a wireless networks for domestic electronic appliances. HIPERLAN-2 is intended to provide almost all radio communication services with different (and appropriate) QoS for different networks. It will allow a mix of services, e.g. voice, video, data and multimedia.

1.2.4.2.1.3 Wireless personal area networks (WPANs)

There has been significant recent demand to replace cumbersome cables that connect electronic devices (e.g. headphone-cables, printers, keyboards and mice) to PCs with cheap, low-power, short-range wireless connections, Figure 1.4. Wireless connectivity provides convenience and flexibility, and allows equipment to be moved easily nominally anywhere within a particular room. The resulting network of devices is known as a wireless personal area network (WPAN) [2], [4]. WPANs connect devices in close vicinity to each other (typically separated by < 10 m). The interoperability of WPANs can be extended to one or more groups of interconnected devices, (e.g. PCs or WLANs) when required.

1.2.4.2.1.3.1 Bluetooth

Bluetooth is an open standard for WPANs. It provides an ad-hoc approach to enable wireless connectivity between various devices within 10 m range. It aims to unify the wireless connectivity between domestic electronic appliances within the personal workplace (or living-space) of an individual [2]. The Bluetooth standard enables interoperability between many different electronic devices made by different manufacturers [1]. Bluetooth operates in the ISM band at 2.4 GHz with a raw data rate up to 1 Mbps and is emerging as a universal short-range radio link [1].

The IEEE 802.15 standard was created to establish a Bluetooth-like standard for WPANs [2]. With the rapid proliferation of wearable communications and computing devices, WPANs may provide a connectivity technology for an entirely new era of monitoring of, and data retrieval from, the immediate space around us [1], [2], [4].

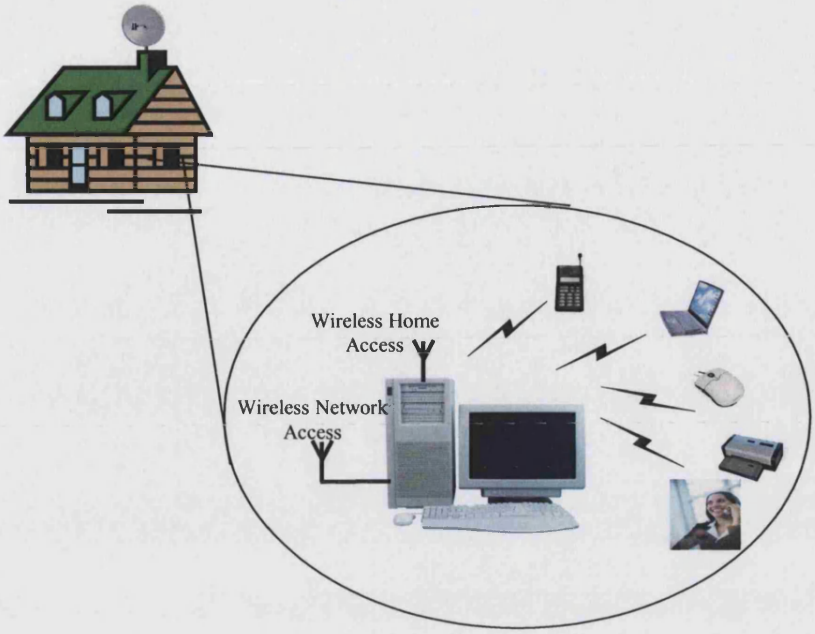

Figure 1.4: *A typical example of WPANs.*

1.2.5 4G systems

Various organisations are currently conducting research on the future development of 3G (UMTS) which will result in a *fourth-generation* (4G) MCRC/PCN system [1], [15], [41], [42]. The reality of 4G will rely on the successful implementation and success of 3G systems which, in turn, will depend on the matching, compatibility or integration between a variety of radio system services, and on the cost-effective provision of these services.

4G systems will not be a replacement for UMTS but an enhancement to it. They will provide higher data rates and higher capacity. To achieve high data rates (e.g. 100 Mbps to 1 Gbps). 4G systems will use a larger bandwidth and new radio system technologies that are suited to high-rate transmission. They will accommodate adaptive cell configurations such as conventional fixed cells and modern smart or intelligent moving cells. These systems will cover different geographical areas with high level of flexibility and mobility.

No specifications or standardisation currently exist for 4G systems. The European radio communications office (ERO), however, has been working towards the frequency spectrum needs of 4G services [1]. To realise the required performance innovative concepts are needed that may not be found by evolutionary enhancements to the existing systems [41]. It is not yet possible to clearly specify the precise aim of 4G mobile and PCN systems but it seems likely that 4G mobile radio communication systems will be dominated by heterogeneous, high-data-rate, fixed and mobile, broadband services with varying degrees of mobility and with a low degree of environment dependency. They will allow interoperability between individual PCs, laptops, pocket PCs, WPANs, WLANs, FWNs and MCRC systems and will provide high-mobility

(high-speed) with high data rates. They will operate at bit rates up to 100 Mbps for high-mobility applications and up to 1Gbps for fixed PCN applications [23].

1.2.6 MIMO systems

Multiple input multiple output (MIMO) systems have received considerable recent attention. They will utilise multiple transmitting and multiple receiving antennas and, in richly scattering environments, can increase channel capacity without the expansion of bandwidth. They achieve this by applying space diversity at transmitting and receiving antennas. The transmit antennas, for example, can each transport a different information stream. If each sub-channel is independent of the others, then the total capacity of the systems increases linearly, as the lesser number of antennas at transmitter and receiver increases.

1.2.7 Capacity improvement techniques and classifications of cell size

The capacity of any radio system depends upon the channelisation of the radio frequency spectrum. 1G MCRC systems were deployed to provide services to a large geographical area with limited radio frequency spectrum using frequency reuse inherent in the cellular concept. 1G and 2G cellular systems are, now, generally known as macro-cellular systems. The rapid growth in the number of users have created congestions in these macro-cell systems [43], [44] and, in order to reduce this congestion and facilitate more users, current and future MCRC and PCN systems such as 3G UMTS and 4G, are evolving towards the use of micro- and pico-cells.

Macro-cell provides coverage to cells with a radius from about 1 km to many tens of kilometres [4] and are used in urban, suburban, rural and mountainous environments.

Micro-cells provide additional capacity in the areas where macro-cells are unable to satisfy user demand. They may be designed as a cluster of cells to provide contiguous coverage over an area or as isolated cells at so-called hot-spot locations [45]. They provide more intensive frequency reuse, lower power terminals and higher data rates. A micro-cell provides coverage to cells with radius up to about 500 m [4]. Micro-cell antennas are deployed below rooftop level [46], [47]. Recently, microcellular systems have become popular and gained interest in dense-urban, urban, suburban, residential-suburban and large indoor environments [47], [48]. Microcellular systems are also suitable for fixed PCN systems. Moreover, they are also a promising candidate to support indoor-to-outdoor or outdoor-to-indoor communication in campus, factory, multi-story-business and hot-spot environments.

Picocells are the smallest cell, providing coverage within a radius up to about 50 m [4]. Pico-cells are proposed for indoor or in-building environments. They are designed to support broadband services at very high data rates. The boundary of a pico-cell is highly dependent on the structure and location of (scattering) objects present in the cell. Radio wave propagation between floors within a single building must be taken into consideration when in-building cellular systems are deployed.

Very short-range cells are suitable to home environments for in house applications [25], such as WPANs.

1.3 Motivations

The radio propagation environment clearly places fundamental limitations on the performance of any mobile radio communication system. These systems suffer from a variety of channel impairments such as multipath interference, which causes inter-symbol-interference (ISI) and frequency-selective-fading (FSF). In order to determine optimum methods of mitigating the impairment caused by multipath propagation, it is essential that the radio propagation channels be properly characterised and modelled.

Recently, deterministic site-specific ray-tracing techniques have emerged as an alternative to time consuming and expensive field trial measurements (empirical modelling). Recent advances in affordable computational power and memory, and the availability of high resolution geographic databases, have made deterministic, site-specific, 3D ray-tracing propagation prediction a practical alternative to empirical or semi-empirical models and extensive (and expensive) field trials.

As increased demand and expectations for reliable, accurate, high performance and high data rate microcellular communications increase, the importance of propagation measurements, modelling and characterisation of the wideband mobile channel in the microcellular environment continues to grow. This was the primary motivating factor behind the research work reported in this thesis.

1.4 Aims and objectives

1. To characterise the dispersive, time-variant, multipath mobile radio channel in a microcellular environment experimentally
2. To analyse multipath channel parameters in terms of received power, average delay spread, RMS delay spread, coherence bandwidth, etc. These channel parameters have become widely accepted as the most appropriate statistical descriptors with which to compare the severity of multipath propagation in different channels
3. To develop a new 3D wideband ray-tracing propagation prediction tool
4. To use the result of 3 to predict the propagation characteristics in a microcellular residential suburban environment
5. To validate the proposed 3D ray-tracing model with the results of 1

1.5 Contribution

In this thesis a new 3D, wideband, ray-tracing propagation prediction tool (3D Micro-ray-tracer-1', MRT-1) has been developed.

The functionality of 3D MRT-1 utilises novel algorithms to implement fast, efficient and accelerated ray-tracing. The following outlines the contributions

made in terms of new ray-tracing approaches and algorithms. To best of our knowledge these approaches are new and not reported elsewhere in the literature.

Modelling of environment
In any site-specific ray-tracing model, modelling of the environments is a crucial task. In order to model the physical environments, a new 3D object-oriented vector format is developed and implemented.

Computational complexity and speed
In order to reduce computational complexity and memory requirements, a visibility matrix is proposed and implemented. The visibility matrix takes account of all possible reflected and diffracted ray-paths in the environment and runs once for each modelled environment.

Diffraction and 0-face of diffracting edge
In order to find the transmitter image and location of diffracted ray-paths, a transmitter rotation algorithm is developed and implemented. A new method of identifying the 0-face (in the UTD problem) is proposed and implemented.

Distributed partitioning and segmentation technique
In order to further reduce computational complexity and processing time, and avoid memory deadlocks, a distributed partitioning and segmentation technique is developed and implemented.

Filtered paths
A filtering algorithm is proposed and implemented to exclude invalid or obscured reflected or diffracted ray-paths.

Equivalent Sources
In order to find the field strength resulting from each valid reflected or diffracted ray-path an equivalent-sources algorithm is proposed and implemented.

In addition to the development of 3D MRT-1 new measurements have been made simulating a microcellular system in a suburban residential environment. These measurements add to the existing measurement databases.

1.6 Structure and outline of the thesis

Chapter 2 presents some fundamental concepts related to radio channel characterisation that are widely used as benchmarks and which are commonly used to compare and/or validate measurements, models and simulations. Chapter 3 presents a comprehensive literature review of existing work relevant to propagation prediction modelling methods and approaches. Chapter 4 is concerned with the development and implementation of a new algorithmically efficient 3D wideband ray-tracing propagation prediction tool 3D MRT-1. Chapter 5 describes a wideband, microcellular, channel measurement campaign at 2.38 GHz for a residential suburban environment. Chapter 6 presents channel simulation results using 3D MRT-1 and compares the equivalent results from the measurement campaign. Finally, Chapter 7 presents conclusions and suggestions for further work.

Chapter 2: Fundamentals of mobile radio channel characterisation

2 Introduction

The mobile radio propagation channel places fundamental limitations on the performance of any radio communication system. Unlike wired channels, mobile radio channels vary randomly and do not offer easy, deterministic, analysis. A proper knowledge of the mobile radio channel is essential, however, in understanding the planning, design and analysis of MCRC systems.

As described in Chapter 1, there is growing interest in propagation prediction models for future high data-rate microcellular mobile communication systems. The characterisation of mobile radio channels can be approached in a number of different ways. Certain fundamental concepts, however, are both common and central to nearly all of these approaches. Furthermore these concepts are widely used as benchmarks with which different channels and different measurement and simulation techniques can be validated or compared.

In order to simplify comprehension, the fundamental technical concepts, which are relevant to the objectives of this thesis, are recapitulated in this chapter.

This chapter begins (Section 2.1) with the classification of physical environments. Section 2.2 reviews important concepts relevant to the design of any mobile radio communication system and describes channel characterisation methods. Section 2.3 briefly describes channel sounding techniques. Section 2.4 and Section 2.5 describe modelling of the channel impulse response (CIR) and power delay profile (PDP). Section 2.6 describes the wideband channel parameters (i.e. multipath delay dispersion parameters). These parameters define the time-variant mobile radio channel and are essential for system design. Finally, Section 2.7 presents fading statistics.

2.1 Classifications of physical environments

Propagation environments exhibit large variations depending on their topological properties [49]. The propagation of radio waves in any area is strongly influenced by the nature of the environment, in particular the size and density of buildings and, sometimes, the presence of vegetation. In propagation studies for mobile radio channels, a qualitative description of the environment is often employed using terms such as dense urban, urban, suburban, residential, commercial, rural or hilly [47]. Dense urban or urban refers to environments containing high-rise buildings, office blocks and other commercial buildings. Suburban refers to environments containing residential or commercial buildings, gardens, parks and trees. Rural refers to open farmland with widely separated buildings, woodland and forest; and hilly refers to mountainous areas. These qualitative descriptions are open to different interpretations by different authors. An area described as urban in one city, for example, might be termed suburban in

another. (This problem often occurs in the context of USA and European cities [50].) This leads to doubts as to whether propagation prediction models based on measurements or simulations made in one city are generally applicable elsewhere.

There is an obvious need to describe the environment quantitatively to avoid ambiguity arising from cultural differences and subjective judgement [47].

2.2 Important concepts

The characterisation of mobile radio communications channels can be approached in a number of different ways. Certain fundamental concepts, however, are both common and central to nearly all of these approaches. Furthermore these concepts are widely used as benchmarks with which different channels and different measurement and simulation techniques can be validated or compared. A subset of the concepts thought to be most relevant to the research work reported in this thesis is therefore reviewed here.

2.2.1 Mobile radio propagation channels

The mobile radio propagation channel is a physical, time-varying, medium that supports electromagnetic waves propagating between transmitting and receiving antennas. In other words it consists of everything that influences propagation between the antenna pair [2], [51]. The channel places fundamental limitations on the performance of any radio communication system. Unlike wired channels that are (largely) static and predictable, radio channels have, at least partially, random characteristics and do not offer easy analysis and are generally predictable only in a probabilistic sense. Furthermore, mobile radio channels can be more severe in terms of their degrading effects than fixed radio channels (e.g. terrestrial radio relay, PCN or WLAN channels).

The mobile radio channel is time-variant (i.e. it suffers time variation of amplitude and phase and delay). This is due, primarily, to movement of the mobile terminal through the spatially varying field caused by multipath propagation.

2.2.1.1 Characterisation of multipath phenomena

It is important to know the characteristics of the time-varying, dispersive, mobile channel if improved design and quality-of-service of cellular radio systems are to be realised [52]. Multipath propagation is a well know phenomena described extensively in the literature, e.g. [2], [47], [48], [53] – [68]. This section briefly reviews the characteristics of the multipath propagation channel.

A multipath channel contains several different propagation paths by which energy travels from the transmitter to the receiver. If we begin with the case of a (physically) stationary transmitter (and a physically stationary environment) then the resulting spatial field is static and the signal observed by a stationary receiver will be constant (in term of carrier amplitude and phase). If we now turn the case

when the receiver is in motion then the spatial variation of the multipath field will be translated to temporal variation of the received signal [47], [64].

Multipath propagation is probably the single most destructive influence on any urban or suburban microcellular environment [47, [64] and it can severely degrade performance of a mobile radio systems [69], [70]. Multipath microcellular propagation can be divided into two broad categories: (i) non-line-of-sight (NLoS) propagation in which the mobile terminal is located well below the mean height of surrounding objects, and propagation due to (at least) several paths of comparable strength, (ii) line-of-sight (LoS) propagation in which a direct path from transmitter to receiver exists that typically dominates the other (scattered) paths. Figure 2.1 uses ray concepts to illustrate multipath propagation.

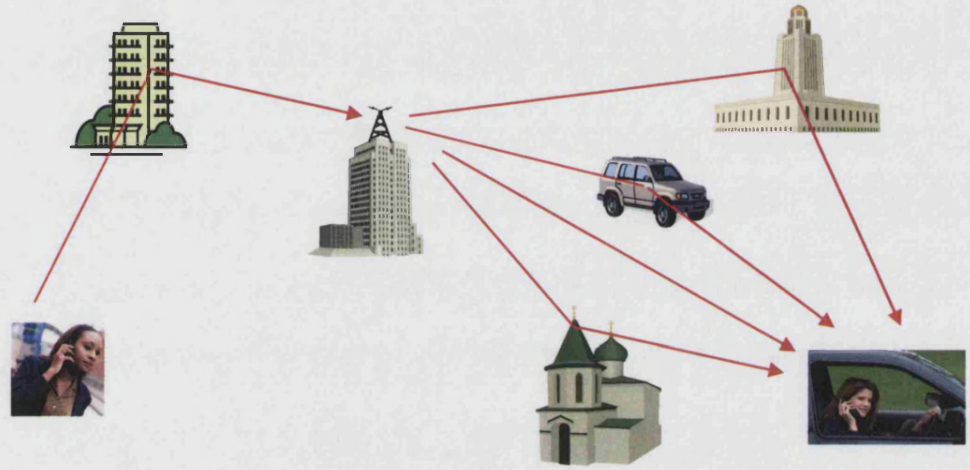

Figure 2.1: *Illustration of multipath propagation.*

Each ray-path may be determined by a combination of propagation mechanisms, namely reflection, transmission (i.e. refraction), diffraction and scattering and is therefore gives rise to a signal component with its own particular combination of amplitude, time delay, phase angle and direction-of-arrival (DoA). Scattering is sometimes taken to include all these mechanisms and sometimes is used to distinguish between interactions with objects that are large with respect to wavelength (reflections, refractions and diffractions) from those which are small with respect to wavelength (scattering). (A more precise distinction can be formulated by defining the fields in the absence of scatterers to be the incident field, the field in the presence of scatterers to be the scattered field and the latter minus the former the diffracted field.) Ray-paths combine both vectorially and phasorially at the receiver and give a resultant signal which is the superposition of signals due to each path alone. The resultant signal can be enhanced in amplitude (due to constructive interference) or reduced in amplitude (due to destructive interference) depending on the distribution of phases between paths. Substantial variation, therefore, can occur in the received signal amplitude. These signal fluctuations are known as fading. The mean signal strength (after fading has been removed by averaging) decreases, of course, due to spreading loss, as the distance between transmitter and receiver increases [2]. Generally, the

multipath effects are modelled in an empirical or statistical way although detailed deterministic models (such as ray-tracing) can be used [394] – [398].

2.2.1.2 Doppler shift

If transmitter, receiver, or significant scatterers are in motion there is an apparent shift in frequency between transmitted and received signals due to Doppler shift. This is related to the rate of change of path length. Doppler shift is directly proportional to the relative radial velocity of receiver with respect to transmitter (or transmitter image). The phenomenon of Doppler shift is well known and widely documented in the literature, e.g. [2], [47], [53], [54], [64], [67].

Consider the receiver (Rx) moving at a velocity v, along a path PQ, receiving a signal from the transmitter (Tx), Figure 2.2. The incremental distance R is given by $\Delta R = v\Delta t$, where Δt is the time required for the mobile Rx to travel from P to Q, and θ the spatial angle. The phase change is therefore:

$$\Delta\phi = \frac{2\pi\Delta R}{\lambda} = \frac{2\pi v\Delta t}{\lambda}\cos\theta \tag{2.1}$$

and

$$f_D = \frac{1}{2\pi}\frac{\Delta\phi}{\Delta t} = \frac{v}{\lambda}\cos\theta \tag{2.2}$$

where f_D is the Doppler shift (in Hz). It can be seen from Eq. (2.2) that f_D is a function of both the direction of motion with respect to the direction of arrival of the signal and the speed of the terminal. A signal coming from the transmitter approaching the receiver from behind will have a negative Doppler shift with a maximum magnitude f_m.

2.2.1.3 Fading effects

Fading is used to describe the fluctuations of the amplitudes, phases, or multipath delays of a radio signal over periods of time or distances of travel of a mobile terminal.

Prediction of a received signal is a two-stage process which involves estimating the mean or median signal level in a small area and describing the signal variability about that mean or median value. Quantifying the extent to which the signal fluctuates is a problem in which there are two contributing factors: large-scale variations (leading to slow fading) and small-scale variations (leading to fast fading.) Some authors have confused the terms fast and slow fading with the terms large-scale fading and small-scale fading. Taking a pedantic view it should be emphasised that fast and slow fading deals with the relationship between the time rate of change of channel characteristics (often due to mobile movement), and not with propagation path loss models [2].

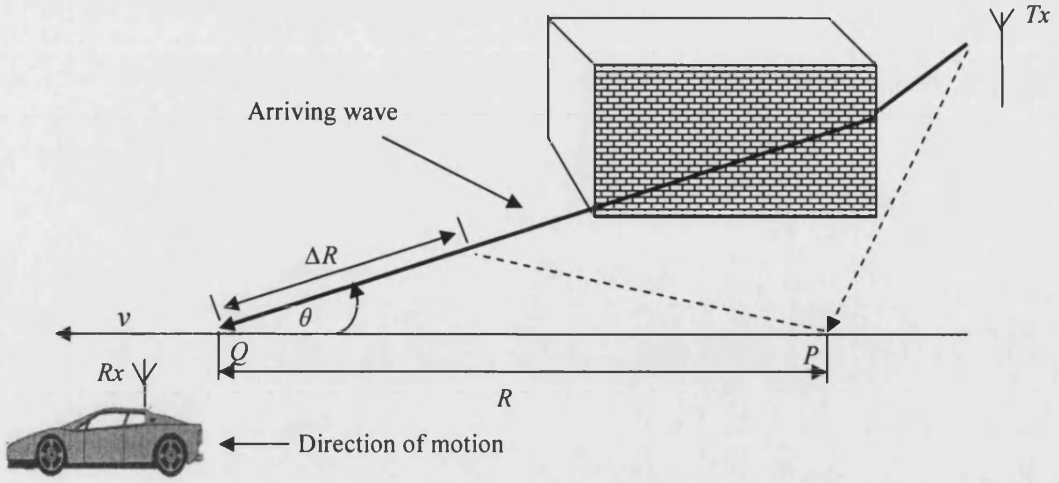

Figure 2.2: *Illustration of Doppler shift (Doppler shift due to diffracted ray-path).*

Large-scale fading

Large-scale variations in the local mean are caused by gross variations in the environment (or terrain profile) between the transmitter and receiver due to the movement of the mobile terminal and consequent changes in the local topography. Large-scale variation in mean signal level is also known as slow fading. The variations are caused by the terminal moving into the shadow of buildings (or obstacles) and are therefore often referred to as shadowing [47]. Measurements indicate that the large-scale fading closely fits a lognormal distribution with a standard deviation that depends on frequency and the environment (see Chapter 3). For this reason the term lognormal fading is also sometimes used [47].

Small-scale fading

Small scale fading is used to describe the rapid fluctuations of amplitudes over a short period of time or travel distance. When the mobile terminal moves over a short distance, the instantaneous received signal level may fluctuate rapidly because the received signal is a sum of many multipath components, each having different (and essentially random) phase. When the receiver is moved only a significant fraction of a wavelength, the received signal strength (or power) may vary by as much as three to four orders of magnitude (30 or 40 dB), Figure 2.3, [2], [47]. For this reason small-scale fading is also referred to as multipath fading or fast fading. Consideration of the central limit theorem for the sum of many independent random variables leads to the expectation that small-scale fading will be Rayleigh distributed if no one path is dominant, or Ricianly distributed if one path (e.g. a LoS path) dominates the others. A Rician distribution is especially common in micro- or pico-cell environments where a LoS path is likely.

Figure 2.3 illustrates the distinction between the large-scale variations of local mean and the small-scale variations due to multipath effects. Received signal power is represented by the solid line and mean signal power after filtering out

fast fading (and which therefore represents slow fading) is represented by the dashed line.

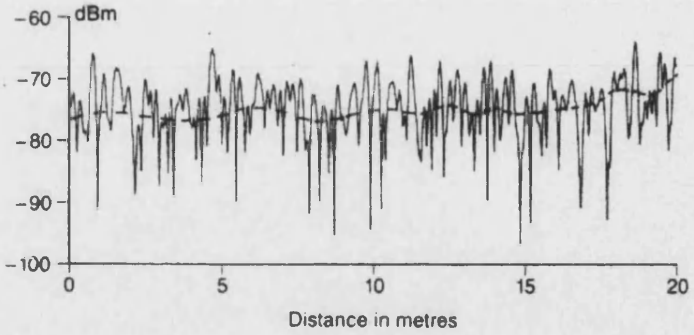

Figure 2.3: *Received signal as a function of distance in an urban environment, (After Parsons J. D. [47]).*

As the receiver moves away from the transmitter, over much greater distances than those associated with slow fading, the local mean received signal gradually decreases. It is this mean signal path loss that is predicted by narrowband, large-scale, propagation models [2], [47].

2.2.1.4 Classification of mobile radio channels

Mobile radio channels fall into two major categories. These are narrowband channels and wideband channels.

2.2.1.4.1 Narrowband and wideband channels

Signals and channels are often referred to as either narrowband or wideband. These terms, however, have more than one definition depending on context. Several definitions of narrowband and wideband are reported in the literature and universally agreed definitions are not available. One definition appropriate, for example, to amplifier design distinguishes narrowband from wideband signals simply using their normalised bandwidths. If the bandwidth, B, is more than about one percent of the carrier frequency, f_c, then the signal is considered wideband. If the bandwidth is less than about one percent of the carrier frequency the signal is considered to be narrowband [71]. A second definition in the context of services, distinguishes between broad- and narrow-band systems on the basis of bit rate; services with data rates greater than 2 Mbit/s being considered wideband (or broadband), all others being considered narrowband.

The above definitions are less appropriate in the context of mobile radio channel studies where time and frequency dispersion are the central issues. Time dispersion refers to the spreading of the signal in time as it propagates from transmitter to receiver along several paths (multipaths), each of different length and, therefore, different delay. Frequency dispersion refers to spreading in frequency due to the different relative motions, between the transmitter, receiver and scatterers and the consequent introduction of a spread of Doppler shifts.

The important distinguishing feature between narrowband and wideband signals in this context is the time-delay spread relative to symbol length. When the ratio

of delay spread to symbol length is small then the signal may be regarded as narrowband and all frequency components in the signal fade in sympathy. When the ratio of delay spread to symbol length is large then the signal must be regarded as wideband and fading becomes frequency selective [67]. The same distinction can be made in the frequency domain by comparing the bandwidth of the transmitted signal with the correlation (sometimes called coherence) bandwidth of the channel.

In a narrowband system, the received signal varies widely and rapidly in strength while in a wideband system the received signal suffers from inter-symbol-interference (ISI) due to the time spreading nature of the channel [51]. ISI occurs when some part of the energy of a symbol is spread into the next symbol.

2.2.1.4.2 Wideband channels

The wideband channel is more complex than the narrowband channel and has recently gained increased importance due to the high data rates required to support recently introduced broadband multimedia services. The wideband channel is both time- and space-dispersive, a single transmitted impulse becoming a sequence of impulses spread in time and space.

A wideband mobile radio propagation channel may be thought of as a system element, such as a linear filter, that transforms input signals to output signals. The transmission characteristics of the equivalent filter are time varying since the mobile radio channel behaviour is generally time-variant. This description demands that the channel be a function of two independent variables selected from time delay τ, time t, frequency f, and Doppler shift ν. The physical interpretation of the channel descriptions using different pairs of these variables and the relationships between the descriptions was developed by Bello, [72]. The set of transmission functions for general deterministic channels are widely known as Bello functions. (When the analysis of the channel behaviour is extended to random time-variant channels the system functions become random or stochastic processes [4]). Bello's functions are summarised below.

2.2.1.4.2.1 Bello functions

In [72], four complete linear systems descriptions for time-varying (multipath) channels are described. These are summarised below.

Time-variant impulse response, $h(\tau, t)$

This characterises the channel in the time/delay domain and is usually represented by a set of impulse responses $h(\tau)$ stacked side-by-side along a time axis, t. (The impulse response magnitude is usually adopted for the purposes of illustration so that $h(\tau)$ can be represented as a one-dimensional function.) It is the response of the channel at time t to a unit strength impulse transmitted at time $t-\tau$ (i.e. τ seconds in the past). It is defined in terms of channel input, $v_T(t)$, and output, $v_R(t)$ by:

$$v_R(t) = \int_{-\infty}^{\infty} h(\tau,t) v_T(t-\tau) d\tau \qquad (2.3)$$

where the subscripts R and T refer to received and transmitted signals respectively.

Bello calls $h(\tau, t)$ the input-delay-spread function since in the corresponding tapped delay line model of the channel it is the input signal that is delayed by the delay line, the tap weights $h(n \Delta\tau, t)$, $n = 0,1, 2, \ldots$ being applied to the delayed versions of the input.

Time-variant frequency response H(f, t)
This characterises the channel in the frequency/time domain and is usually represented by a set of frequency responses $H(f)$ stacked side-by-side along a time axis, t. (The amplitude response, i.e. frequency response magnitude, is usually adopted for the purposes of illustration so that $H(f)$ can be represented as a one-dimensional function.) $H(f, t)$ is defined in terms of the transmitted and received signals by:

$$V_R(f,t) = H(f,t) V_T(f) \qquad (2.4)$$

$H(f, t)$ represents the spectral response (voltage gain and phase shift) of the channel at time t for a transmitted sinusoid with frequency f. The differential quantity $|H(f, t)|^2\ df\ dt$ represents the power gain of the channel for power arriving at the receiver between time t and $t+dt$ in a frequency band between f and $f+df$. The time-variant frequency response is the delay domain Fourier transform of the time-varying impulse response. (Bello calls $H(f, t)$ the time-variant transfer function and denotes it by $T(f, t)$.)

Doppler-variant impulse response, d(τ, ν)
This is the channel gain (voltage gain and phase shift) experienced by signal components that suffers a delay between τ and $\tau+d\tau$ followed by a Doppler shift between ν and ν+dν. It is defined in terms of input and output signals by:

$$v_R(t) = \int_{-\infty}^{\infty} \int_{-\infty}^{\infty} d(\tau,\nu) v_T(t-\tau) e^{j2\pi\nu t} d\nu d\tau \qquad (2.5)$$

The Doppler-variant impulse response is the time domain Fourier transform of the time-varying impulse response. (Bello calls this the delay-Doppler-spread function.)

Doppler-variant frequency response D(f, ν)
$D(f, \nu)$ is the spectral response (amplitude gain and phase shift) of the channel at a frequency ν Hz above a (sinusoidal) spectral line transmitted at a frequency f Hz. It is defined in terms of input and output signals by:

$$V_R(f) = \int_{-\infty}^{\infty} D(f-\nu,\nu)V_T(f-\nu)d\nu \tag{2.6}$$

D(f, ν) is the time domain Fourier transform of the time-variant frequency response and the delay domain Fourier transform of the delay-Doppler function. (Bello calls *D(f, ν)* the output-Doppler-spread function and denotes it by *H(f, ν).)*

2.2.1.4.2.2 Relationships of Bello functions

The relationship between the Bello's system descriptions are summarised in Figure 2.4. Each function is connected via Fourier (F) and inverse Fourier (F^{-1}) transform with a pair of the other functions.

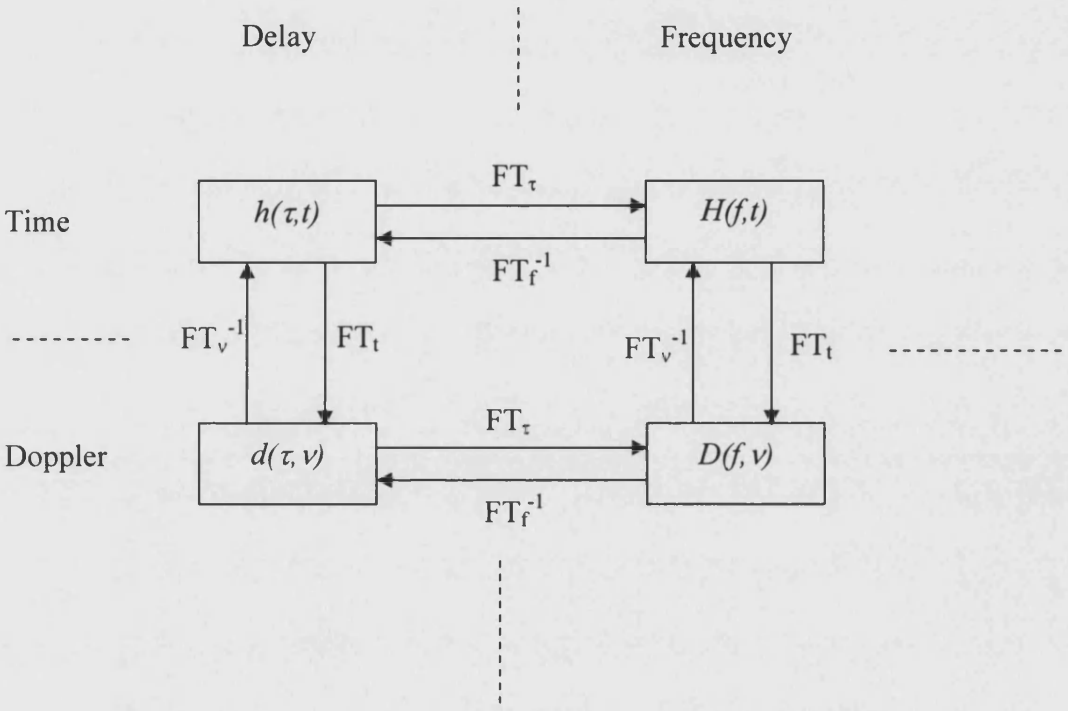

Figure 2.4: *Relationships between Bello system descriptions, (After Bello P. A. [72]).*

2.2.1.5 Wide-sense stationary and uncorrelated scattering (WSSUS)

If the (ensemble) mean or expected value of the (time-varying) impulse response is independent of time, i.e.:

$$E_\tau\{h(\tau,t)\} = E\{h(\tau)\} \tag{2.7}$$

and the correlation function between impulse responses at times t_1 and t_2, i.e.:

$$R_{hh}(\tau_1,t_1;\tau_2,t_2) = 0.5E\{h^*(\tau_1,t_1)h(\tau_2,t_2)\} \tag{2.8}$$

depends only on time difference, $\Delta t = t_1 - t_2$, i.e.:

$$R_{hh}(\tau_1,\tau_2,\Delta t_1) = 0.5E\{h^*(\tau_1,t)h(\tau_2,t-\Delta t)\} \tag{2.9}$$

then the channel is said to be wide-sense stationary (WSS). This means that the statistical properties of the channel (at least as summarised by its first order statistics) do not change with time. If the values of impulse response at different delays are uncorrelated, i.e.:

$$R_{hh}(\tau_1,t_1;\tau_2,t_2) = \begin{cases} 0.5E\{h^*(\tau,t_1)h(\tau,t_2)\}, & \text{for } \tau_1 = \tau_2 = \tau \\ 0, & \text{for } \tau_1 \neq \tau_2 \end{cases} \tag{2.10}$$

or, equivalently:

$$E\{h^*(\tau)h(\tau-\Delta\tau)\} = E\{h^*(\tau)h(\tau-\Delta\tau)\}\delta(\Delta\tau) \tag{2.11}$$

then the channel is said to display uncorrelated scattering (US). Physically this means that the scatterers have locations and scattering cross-sections which are statistically independent of each other, i.e. the existence of a component in the impulse response with a given strength and delay has no influence on the probability of components existing with other specified strengths and delays.

Over short time-scales the mobile radio channel is often assumed to be both wide-sense stationary in time and uncorrelated in its scattering. In this case:

$$\begin{aligned} R_{hh}(\tau_1,t_1;\tau_2,t_2) &= \begin{cases} R_{hh}(\tau,\Delta t), & \text{for } \tau_1 = \tau_2 = \tau \\ 0, & \text{for } \tau_1 \neq \tau_2 \end{cases} \\ &= \begin{cases} 0.5E\{h^*(\tau,t)h(\tau,t-\Delta t)\}, & \text{for } \tau_1 = \tau_2 = \tau \\ 0, & \text{for } \tau_1 \neq \tau_2 \end{cases} \end{aligned} \tag{2.12}$$

This idealised WSSUS channel has been thoroughly investigated in [71].

2.2.1.6 Frequency-selective fading

Frequency selectivity is a direct consequence of time dispersion arising due to multipath propagation. The effect of frequency selectivity on a radio communications system depends on the channel bandwidth of the system. Consider two frequency components within the message bandwidth. If these frequency components are close together then the different propagation paths within the multipath medium have approximately the same electrical length for both components and their amplitude and phase variations will be similar. As the frequency separation increases, however, the behaviour at one frequency tends to become uncorrelated with that at the other, because the phase shifts along the various multipath components are different at the two frequencies.

The extent of the decorrelation depends on the spread of time delays since the phase shifts arise from the excess path length. For larger delay spreads, the phases of the incoming components can vary over several radians even if the frequency separation is quite small.

Signals which occupy a bandwidth greater than the bandwidth over which spectral components are affected in a similar way will become distorted since the amplitudes and phases of the various spectral components in the received version of the signal are not the same as they were in the transmitted version. This phenomenon is known as '*frequency-selective fading*' (sometimes abbreviated to selective fading) [47], [53].

Systems that have narrow bandwidth with respect to a channel's frequency selectivity are said to be frequency non-selective channels and suffer from flat fading. The space-selective fading which exists as a result of multipath propagation is experienced as time-selective fading by mobile terminals travelling through the field [47].

2.3 Channel sounding

Channel sounding is the means by which the channel impulse response (CIR) of the time-variant mobile radio channel is measured. The measurement almost always results in a complex equivalent baseband representation and CIR is sometimes, therefore, taken to mean complex impulse response. A comprehensive review of channel sounding techniques is given in e.g. [52], [73], [74] and it is therefore only an overview that is presented here.

Mobile radio channels present two fundamental characteristics. On the one hand these channels are time varying, and on the other hand they are frequency selective. Channel sounding systems were developed to measure this variability and selectivity. A variety of channel sounding techniques have been proposed over many years in the context of conventional mobile radio systems [50], [75] – [80].

Significant channel sounding research has also been undertaken more recently using several new techniques appropriate to future radio systems, both narrow- and broadband, [52].

The choice of channel sounding technique depends upon the intended application. At its most elementary, a choice must be made between narrowband or wideband sounding, and whether time and/or frequency characterisation is required. The choice between narrowband and broadband measurements is fundamental since the former yields frequency dispersion information about the channel but no information about time dispersion. The latter yields time dispersion information but may also give frequency dispersion information providing the measurement rate is sufficiently high. If wideband sounding equipment is adequately characterised, and has sufficient dynamic range, it may also yield long-term fading statistics. In practice, however, these statistics are often found separately from narrowband measurements. The choice between time or frequency domain characterisation is usually secondary since the same information is typically present in both types of measurement.

Channel characteristics for mobile applications are usually determined by measuring directly, or inferring, either the time-varying power delay profile or the time-varying amplitude response. More complete descriptions, i.e. the time-

variant impulse response or the time-variant frequency response, are measured less often due to the inconvenience of maintaining a proper phase reference at the mobile channel sounder receiver.

Wideband sounding
The choice of channel sounder depends on the parameters to be measured and its intended applications.

Sounders must cope with a number of different constraints arising from:

(i) the environment
(ii) the expected maximum excess delay
(iii) the required measurement time resolution
(iv) the required measurement frequency resolution
(v) the flexibility requirements

Wideband channels can only be characterised by the transmission and reception of wideband signals. Wideband channel sounding techniques provide a practical means of measuring the time-dispersive characteristics of the mobile radio channel. Several types of wideband sounder are in widespread use. They can be classified as follows.

- Time domain
  - Impulse
  - Pulse compression (or correlation)
    - PRBS
      - Sliding correlator
      - Synchronised
    - Chirp
      - Continuous sweep
      - Stepped sweep
- Frequency domain
  - PRBS
  - Swept frequency (or slow chirp)
    - Continuous sweep
    - Stepped sweep

The principles, implementation methods, techniques, comparisons, advantages and limitations of above mentioned wideband channel sounders are extensively described in the literature e.g. [2], [50], [52], [55], [73] - [75], [78], [80] - [97].

Chirp Sounders
Chirp sounding makes use of a swept frequency continuous wave and like PRBS sounding takes advantage of pulse compression to avoid the peak power limitation of conventional pulse sounding. The advantages of using chirp sounders in preference to pulse sounders have long been recognised [73], [74].

Chirp sounders are popular in high-resolution radar and HF ionospheric studies. They have also been used, with some limitations, in studies of mobile radio channels [73] – [75], [82], [93].

Chirped pulse signals have many properties that make them an attractive choice for channel sounding. They are easily generated and the channel response can be processed in the time or frequency domain. A channel sounding experiment has been described that employs particularly simple hardware to generate and record chirp responses for off-line processing. Continuous transmission of chirped pulses using a duty cycle of 1.0 (i.e. without inter-pulse gaps) gives good autocorrelation properties, [82].

The time-bandwidth product (BT) of a chirp signal determines its processing gain, G_p, i.e.:

$$G_p = 10\log_{10}(BT) \quad \text{dB} \tag{2.13}$$

For BT > 100, 95% of the power spectrum is contained within a bandwidth $|f_1-f_2|$ where f_1 and f_2 are the chirp start and stop frequencies, a condition which is satisfied for practical sounding applications [73], [74].

Like pseudo random binary sequence (PRBS) signals a chirp signal can be compressed in the sounder receiver using either a matched filter [82] or a cross-correlator [86]. Matched filters in chirp sounders have been realised by both surface acoustic wave (SAW) delay lines and by digital signal processing (DSP) methods. The use of SAW delay lines, however, generally degrades the dynamic range of the measurement system. Digital matched filtering with a sampling rate of 125 MHz has been used in real-time sounder measurements and has achieved 30 dB of dynamic range [98] combined with Doppler shift measurements of several kilohertz [74], however, identifies the heterodyne detector as an optimum choice.

Improvements to the dynamic range and flexibility of SAW-based devices have been realised in recent years, but no advantage has been achieved over DSP based receivers which do not suffer from the non-ideal nature of practical analogue components.

The recent availability of high speed ADCs and DACs has enabled both the digital generation of chirp signals and their digital compression. RUSK mobile radio chirp channel sounders generate the baseband chirp signal digitally at the transmitter and correlate it with the reference signal at the receiver also digitally, [74].

Channel sounder limitations

A serious limitation in channel sounding is that measured responses depend on both the physical channel, and the antenna patterns used to couple transmitter and receiver to the channel. Unless spatial information about the angular distribution of power launched and received from transmit and receive antennas, respectively, is available it is not, in general, possible to determine the channel response that would have been obtained using another antenna. (Techniques have

been proposed and implemented that provide this spatial information (e.g. [88] though this generally makes the sounder rather complex. If measurements are made with antennas that closely mimic those expected to be used in the application for which the soundings are being required then the channel can be defined to include the antennas and this limitation becomes unimportant.

The choice of sounding technique depends on the parameters to be measured and the intended application. At its most fundamental, however, the task of any channel sounding system is to measure the radio channel's $h(t)$ (or at least $|h(t)|$) with specified maximum delay, minimum temporal resolution, and acceptable accuracy. The required delay resolution is determined by the intended bandwidth of the signals to be transmitted over the channel and the required temporal resolution (minimum time period between independently measured impulse responses) is determined by the expected maximum rate of change of the channel. (The channel's rate of change is related to the width of its Doppler spectra that determines, in turn, the maximum measurement interval.)

2.4 Channel impulse response (CIR)

The wideband mobile radio channel, within a certain bandwidth of interest, is determined completely in terms of its time-frequency characteristics or by its complex time-variant impulse response or its time-variant frequency response. (The channel's spatial characteristics have not been a concern until recently. With the advent of multiple input multiple output (MIMO) systems, however, 'double directional' sounding techniques have become important.) In the time domain, the channel is described by the time-variant complex impulse response. The input delay-spread function in the family of Bello functions, described earlier, is essentially the impulse response of the channel. Figure 2.5 shows a system model of time-varying complex channel impulse response, (CIR), $h(\tau, t)$.

In Figure 2.5, the impulse response, $h(\tau, t)$ is a function of both t and τ with the variable t representing the time variation due to the physical motion in space and the variable τ representing the channel multipath delay for a fixed value of t. If the channel is bandpass (as will certainly be the case for any radio application) it can be described by an equivalent complex baseband impulse response $h_b(t, \tau)$ with the input and output being complex envelope representations of the RF transmitted and the received signal.

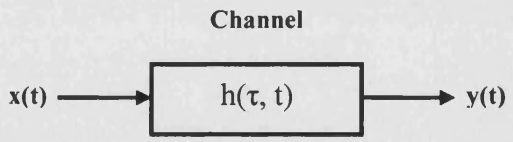

Figure 2.5: *System model of time-varying channel impulse response.*

The magnitude of a typical CIR is shown in Figure 2.6(a) [51]. If we partition the time delay axis as shown in Figure 2.6(b) into equal delay segments, usually called delay bins or excess time delay bins, then there will be, in general, a number of received signals in each bin corresponding to the different paths whose time of arrival are within the bin duration. These signals when

vectorically combined can be represented by delta function occurring in the centre of the bin, see Figure 2.6(c). As the smaller impulses are of less significance we may introduce a threshold T and discard all components whose weight is below T. This leads to the simplified discrete impulse response shown in Figure 2.6(d). If we denote the first time delay bin as τ_o, representing the first arriving component of a signal at the receiver, then the excess delay measures the delay of all components with respect to τ_0. By convention $\tau_o = 0$, $\tau_1 = \Delta\tau$ and $\tau_i = i\Delta\tau$, for i=0 to N-1, where $\Delta\tau$ is the width of the time delay bins and $N\Delta\tau$ is the maximum excess delay of the channel. The baseband time-variant complex CIR can then be expressed as [4], [51], [80], [99]:

$$h_b = \sum_{i=o}^{N(t)-1} \tilde{A}_i(t,\tau_i)\delta[\tau_o - \tau_i(t)]e^{j\phi_i(t,\tau_i)} \qquad (2.14)$$

where $\tilde{A}_i(t,\tau_i)$ is complex amplitude, $\delta[\tau_o - \tau_i(t)]$ is the delay and $e^{j\phi_i(t,\tau_i)}$ is the phase shift of the *ith* component at time t, respectively. This expression for the impulse response of the channel is due to the fact that the received signal is a series of attenuated, phase shifted and time delayed copies of the transmitted signal.

2.5 Power delay profile (PDP)

The equivalent baseband complex channel impulse response (CIR) determines the system behaviour of a channel completely. In practice, however, it is often the power delay profile (PDP) of a channel that is measured. The PDP is the square magnitude of time-variant complex baseband CIR. The time-varying PDP, p(τ, t), is related to the equivalent complex baseband impulse response by:

$$p(\tau,t) = |h_b(\tau,t)|^2 \qquad (2.15)$$

PDPs are generally represented as plots of received signal strength or power (in dB) as a function of excess delay with respect to some fixed reference. Examples of PDPs measured at conventional mobile frequencies in three different environments are shown in Figure 2.7.

2.6 Wideband (or multipath) channel parameters

Several parameters are employed to summarise the time dispersion characteristics of a channel and used as first order indications of channel quality. These, and some associated quantities are illustrated in Figure 2.8, extracted from Recommendation ITU-R P.1145 [53].

2.6.1 Excess delay

Excess delay is delay measured from the time of arrival of the line-of-sight (LoS) component. This often corresponds, at least approximately, to the first component (or 'leading edge') of the PDP. In Figure 2.8, the first component is t_{LoS}.

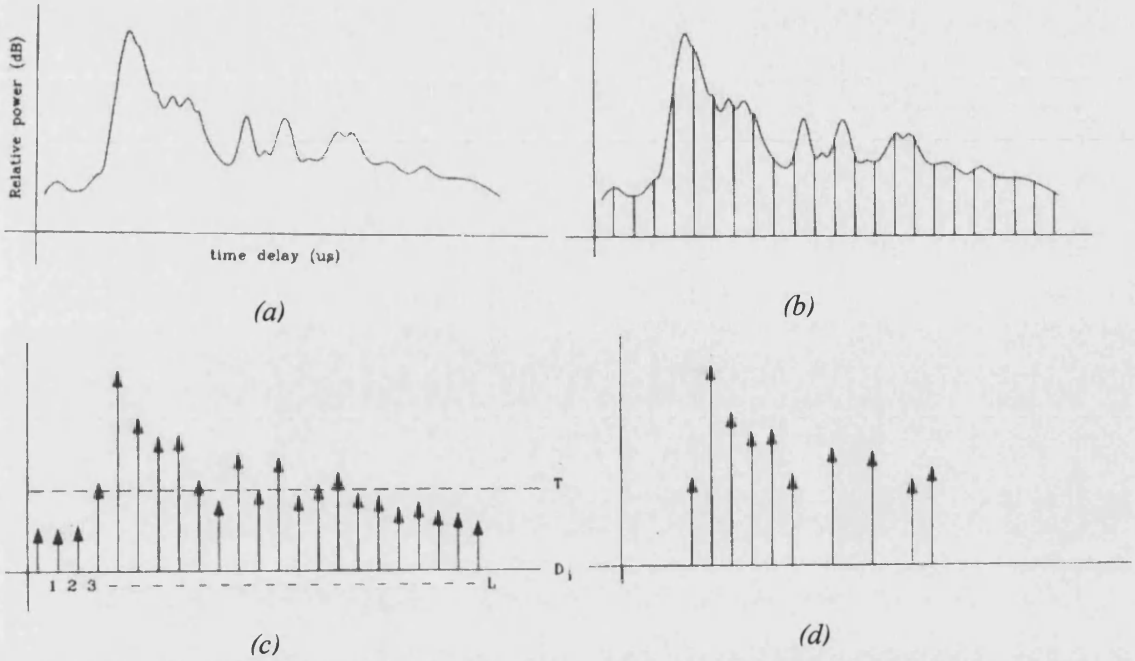

Figure 2.6: *Channel impulse response: (a) actual, (b) partitioned into equal delay bins, (c) discretised and (d) simplified discretised response, (After Steele R. [51]).*

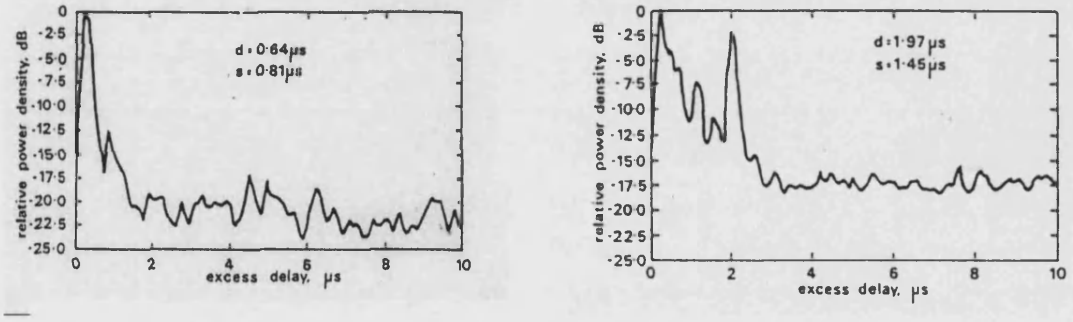

(a) Urban measurement (b) High-rise urban measurement

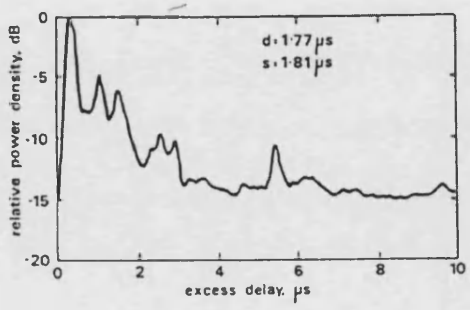

(c) Sub-urban measurement

Figure 2.7: *Power delay profiles measured in three different environments, (After Parsons et al. [63]).*

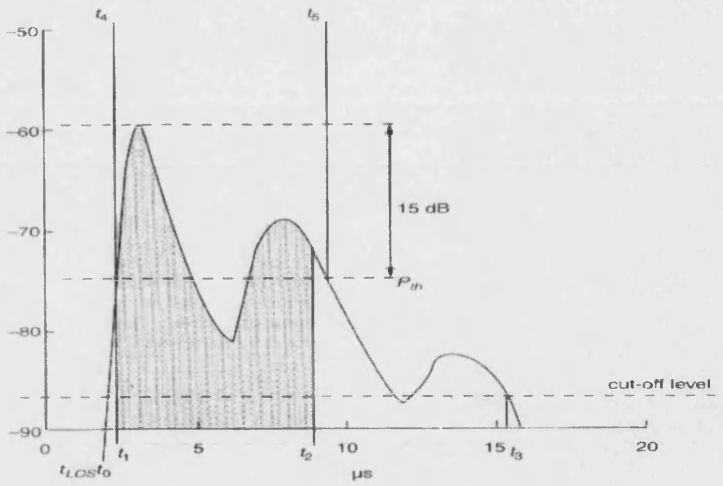

Figure 2.8: *An illustration of a typical PDP showing delay parameters, (After Barclay L. [53]).*

2.6.2 Average excess delay

The average or mean, excess delay is the first central moment of PDP, defined by:

$$\bar{\tau} = \frac{\sum_{i}^{N} \tau_i P(\tau_i)}{\sum_{i}^{N} P(\tau_i)} \tag{2.16}$$

where i is index of the PDP component and delay is measured from the LoS value. In Figure 2.8 the mean excess delay is the signal-weighted mean of the excess delays for the signal received above a cut-off level from t_{LoS} to t_3.

2.6.3 Maximum excess delay

The maximum or total excess delay is the difference between the shortest and the longest delays. In Figure 2.8 maximum excess delay is $t_3 - t_{LoS}$, where t_{LoS} is the LoS delay.

2.6.4 Delay window and delay interval

The delay window (from t_1 to t_2 in Figure 2.8) contains a stated percentage of the total PDP energy above the cut-off level. The delay interval (from t_4 to t_5 in Figure 2.8) is defined from the time when the signal level first exceeds a threshold P_{th} to the time when it drops below the threshold for the last time. In Figure 2.8, P_{th} is 15 dB below the maximum signal strength in PDP.

2.6.5 Delay spread

Delay spread is often used as a figure of merit for the quality of a multipath channel [83]. It gives a direct measure of the temporal dispersion introduced by a channel and an indication of the likely severity of inter-symbol interference (ISI)

for a given symbol rate. (The significance of ISI is that, in the absence of equalisation, this may determine a lower bound on performance in the form of an irreducible bit error rate (BER).) Several variations in its definition have been proposed, i.e.:

Absolute delay spread
This is the difference in delay between the arrival of the first and last components in the channel PDP. The delay spread obtained from measurements using this definition will depend on the sensitivity and noise floor of the measurement equipment. This is also sometimes referred to as the total excess delay.

Nth dB delay spread
This is the delay difference between the first measurable component in the impulse response and last component in the power delay profile equal to or exceeding a level N dB lower than the profile's peak value.

X% energy delay spread
This is the delay difference between the occurrence of first measurable component in the power delay profile and the delay when X% of the total energy of the impulse response has been received. (This is similar, but not identical, to the delay window defined above.)

Root mean square delay spread (RMS-DS)
The root mean square delay spread (RMS-DS), τ_{RMS}, is probably the single most important wideband radio channel parameter. It is a measure of the degree of time dispersion and is defined as the square root of the second central moment of the PDP [2], [99], [100] i.e.:

$$\tau_{RMS} = \sqrt{\frac{\sum_{i=1}^{N}(\tau_i - \bar{\tau})^2 P(\tau_i)}{\sum_{i=1}^{N} P(\tau_i)}} \tag{2.17}$$

τ_{RMS} has become widely accepted as the most appropriate statistical descriptor with which to compare the severity of multipath propagation in different channels. It does not uniquely define the PDP structure, however, and different channels with the same τ_{RMS} can have significantly different irreducible BER due to ISI. Despite this τ_{RMS} is often the figure used for a first determination of a communication system's performance in the presence of multipath propagation [83].

2.6.6 Coherence bandwidth

The maximum frequency difference for which signals are still strongly correlated is called the coherence or correlation bandwidth, B_c, [47] (Coherence bandwidth is deprecated although widely used since it implies the correlation of signal phase only.) It is also a representative parameter of the delay dispersion of the wideband channel [47], [100] – [102]. Analogous to τ_{RMS} in the time domain, B_c is used to characterise the channel in the frequency domain [2]. B_c refers to the

minimum frequency separation required for the space-frequency correlation $R_{HH}(\Delta f)$ to fall to a predefined reference level e.g., 0.5, 0.7, 0.9, 1/e [2], [103]. Two sinusoids with frequency spacing greater than the B_c therefore undergo significantly different amplitude and phase changes as they pass through a channel.

Relationship between B_c and τ_{RMS}

The exact relationship between B_c and τ_{RMS} depends not only on the precise definitions of B_c and τ_{RMS} but also on the shapes of frequency correlation function and PDP [55], [103]. The relationship between B_c and τ_{RMS} is well established for the ideal Rayleigh channel [55]. A number of different relationships to describe the dependence of B_c and τ_{RMS} have been reported in the literature e.g. [55], [56], [59] - [63], [66], [67], [103] - [105]. It is important to note that an exact relationship between B_c and τ_{RMS} does not exist [2]. For B_c defined by a correlation reference level of 0.5, an exponential power delay profile and a classical Doppler spectrum the B_c and τ_{RMS} are related by [55]:

$$B_c = \frac{1}{3.6\tau_{RMS}} \tag{2.18}$$

If the definition is relaxed so that the frequency correlation function is somewhere between 0.5 and 0.9, then the B_c is given approximately [2] by:

$$B_c = \frac{1}{5\tau_{RMS}} \tag{2.19}$$

If B_c is defined as the bandwidth over which the frequency correlation function is above 0.9 then the B_c is approximately given by [58]:

$$B_c = \frac{1}{50\tau_{RMS}} \tag{2.20}$$

B_c and τ_{RMS} are inversely proportional to each other, such that [395] – [398], [405]:

$$B_c = \frac{1}{\alpha\tau_{RMS}} \tag{2.21}$$

where α is constant. For an exponentially distributed PDP, $\alpha = 2\pi$. However, in practical situations the value of α is not a constant, it depends on the impulse response [405]. It is important to note that an exact relationship between B_c and τ_{RMS} is a function of the specific PDP profile and Eq. 2.18 to Eq. 2.21 are 'ball-park' estimates [2].

B_c and τ_{RMS} incorporate most of the information from the PDP and express it as a single value whose magnitude allows direct comparisons between different environments. In this thesis, $\alpha = 2$ is used to determine B_c from τ_{RMS}.

2.6.7 Doppler spread and coherence time

It has already been stated that τ_{RMS} and B_c are the most widely used parameters to describe time dispersive and frequency selective natures of the radio channel. They do not offer information, however, about the time varying nature of the channel caused either by relative motion between the transmitter and receiver or by the movements of objects in the environment. Doppler spread and coherence (or correlation) time are the parameters which describe the time varying nature of the channel caused by the Doppler effect [2].

Doppler spread, D_s is a measure of the spectral broadening caused by the time rate of change of the channel and is defined as the range of frequencies over which the received Doppler spectrum is essentially non-zero [2].

Correlation time (or decorrelation time or coherence time – although the latter is deprecated), T_c, is the time domain dual of D_s and is used to characterise the time varying manifestation of the frequency dispersion. $1/D_s$ is a measure of the time duration over which two received signals have strong amplitude correlation. D_s and T_c are clearly inversely proportional [2]. The constant of proportionality is of the order of unity, i.e.:

$$T_c \propto \frac{1}{D_s} \tag{2.22}$$

As with coherence bandwidth, B_c, and RMS-DS, τ_{RMS}, however, the exact relationship depends on the definitions of the quantities and the shape of the functions involved.

2.6.8 Mean Doppler shift

Mean Doppler shift is defined analogously to mean excess delay, i.e.:

$$\overline{\nu} = \frac{\int_{-\infty}^{\infty} \nu S(\nu) d\nu}{\int_{-\infty}^{\infty} S(\nu) d\nu} \tag{2.23}$$

where $S(\nu)$ is the Doppler power spectral density.

2.6.9 Doppler width

This is the width of the Doppler spectrum, $S(\nu)$, i.e. the width of the received signal spectrum when a single spectral line is transmitted. Many mathematical definitions are possible e.g. 3 dB width, RMS Doppler width etc. (equivalent to those outlined for delay spread).

2.7 Fading statistics

2.7.1 Rayleigh fading channels

In case of NLoS scenarios, if each multipath component in the received signal is statistically independent of the others then the probability density function (PDF) of its envelope is Rayleigh distributed [51]. The Rayleigh distribution is commonly used to describe the statistical time varying nature of the received signal. Such channels are commonly known as *'Rayleigh-fading channels'* or simply Rayleigh channels. The Rayleigh distribution has a PDF given by [2], [4], [54], [47], [66], [68]:

$$p(r) = \begin{cases} \frac{r}{\sigma^2} e^{\left(-\frac{r^2}{2\sigma^2}\right)} & (0 \le r \le \infty) \\ 0 & (r < 0) \end{cases} \tag{2.24}$$

where σ^2 is the mean received power. The cumulative distribution function (CDF) of the Rayleigh distribution, which determines the probability of r not exceeding a specific value R, is given as [2], [4]:

$$P(R) = P(r \le R) = \int_0^R p(r)dr = 1 - e^{\left(-\frac{R^2}{2\sigma^2}\right)} \tag{2.25}$$

In microcellular mobile radio a dominant path (which may be a LoS path) is often present. This dominant path may significantly decrease fading depth and the resulting signal envelope is said to be Rician.

2.7.2 Ricean fading channels

The effect of a dominant signal arriving with many weaker multipath signals gives rise to the Rician distribution given by [2], [4], [54], [66], [68]:

$$p(r) = \begin{cases} \frac{r}{\sigma^2} e^{\left(-\frac{r^2+A^2}{2\sigma^2}\right)} \mathrm{I}_0\left(\frac{\mathrm{Ar}}{\sigma^2}\right) & \text{for } (r \ge 0) \\ 0 & \text{for } (r < 0) \end{cases} \tag{2.26}$$

where A is the peak amplitude of the dominant signal and $\mathrm{I}_0(\bullet)$ is the modified Bessel function of the first kind and zero order. The Rician distribution is often described in terms of the parameter $K = A^2/(2\sigma^2)$ which can be interpreted as the ratio of power in the dominant components to that in the other components. The Rician distribution expressed in terms of K is given by [4]:

$$p(r) = \frac{r}{\sigma^2} e^{\left(-\frac{r^2}{2\sigma^2} - K\right)} I_o\left(\frac{r\sqrt{2K}}{\sigma}\right) \tag{2.27}$$

For large values of K the PDF of r tends towards a Guassian distribution. Such a channel behaves like an additive white Gaussain noise (AWGN) channel. If the value of K approaches to zero, the PDF reduces to a Rayleigh distribution. The Rayleigh and Rician PDFs are shown in Figure 2.9.

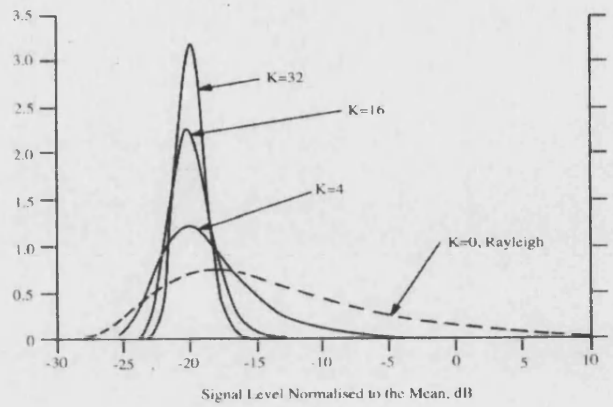

Figure 2.9: *PDFs of the Rayleigh and Rician with K= 0, 4, 16, 32, (After Steels R. [51]).*

2.8 Conclusion

In this chapter a range of channel concepts which lie at the core of the design of mobile radio communication systems have been presented and reviewed. In particular the quantities most frequently used to describe channel degradation have been defined and discussed. These concepts and quantities form a pre-requisite to much of the material that follows in later chapters.

Chapter 3: Propagation modelling and ray tracing

3 Introduction

Radio propagation is the physical process by which (RF) electromagnetic energy is transported from one location in space to another. The precise prediction of the spatial distribution of energy at a given point in time involves the solution of Maxwell's equations subject to the boundary conditions imposed by the physical environment. For all but the simplest of problems this approach is unrealistic both in terms of the level of detail (resolution and accuracy) required in the description of the environment and the computing resources necessary to complete the solution. Finite-difference time-domain (FDTD) methods have been applied, however, to directly solve Maxwell's equations in the time domain for simplified two-dimensional (2D) indoor environments [106] - [111].

Fortunately, a prediction of the exact energy distribution is not usually required and approximate methods can therefore be applied.

3.1 Radio propagation models

As described in Chapter 2, the propagation channel is the physical medium that supports electromagnetic wave propagation between transmit and receive antennas. The channel is time-variant due to the movement of the mobile terminal and/or scattering obstacles.

Several approaches exist to predicting radio propagation. These can be divided into empirical (or statistical), theoretical (or analytical) and physical (or deterministic) [112] -115], [399], [401]. Empirical models are based on measured data which is site and frequency specific and, therefore, lack generality. They are, however, easy to implement. Physical models are based on some (usually approximate) method of solving Maxwell's equations. The most widely used approximation in this context is geometrical optics (GO) and the resulting technique is referred to as ray-tracing. These deterministic models generally provide accurate prediction but are usually computationally expensive and time consuming. They also require detailed topographical databases which are not always readily available.

3.1.1 Empirical models

Empirical models rely on the data collected from measurements. Each set of measured data contains large number of received field strength (amplitudes or power) and/or CIRs in conjunction with concurrently recorded qualitative and/or quantitative environmental descriptors. (An example of a qualitative descriptor is the classification of an environment as dense urban, urban, suburban, etc. and an example of a quantitative descriptor is the distance between transmit and receive antennas.) The data are typically divided into independent sets (usually selected intuitively on the basis of the qualitative environmental descriptors) and correlation analysis is used to derive statistically valid relationships between the

environmental descriptors and the quantities required to be predicted. If the relationships derived are constrained by a requirement that they satisfy some independently known physical law or principle then the resulting model is usually called semi-empirical.

Empirical models implicitly take into account all the propagation factors of the environment, both known and unknown. They are easier to apply (generally requiring only trivial computational effort) but are insensitive to the environment's detailed topography [115], [399]. They are also relatively application specific. Empirical models developed for macro-cells environments, for example, cannot usually be used in micro-cells.

3.1.2 Physical models

Any method of calculating the distribution of electromagnetic energy that is based on well-established physical principles and is precisely repeatable represents a physical (or deterministic) model [4], [116]. FDTD, the parabolic equation method (PEM) and ray-tracing clearly fall into this category. The latter two have been applied extensively in recent years to a variety of outdoor microwave propagation problems [90], [112], 115], [117].

In recent years the increased availability of high resolution geographic databases and increased computer processing power and memory has made deterministic site-specific models attractive. In cellular systems this usually implies ray-tracing based on GO. Diffraction is often incorporated using geometrical theory of diffraction (GTD) and its variant, uniform theory of diffraction (UTD) [90], [112], [115], [117].

Unlike empirical models, deterministic site-specific ray-tracing propagation prediction models do not rely on measurements (other than those normally used in model validation) but do require a site-specific database containing detailed information on the terrain and ground cover (most notably buildings). They require significant computational resources but provide more precise propagation predictions than empirical models. Ray-tracing models are generally suitable for micro- and pico- cell environments where empirical or statistical models perform poorly as the channel is highly sensitive to environment detail [116]. The computational resources required by physical models for macro-cell propagation are probably still prohibitive for routine planning of macro-cells, although this may change rapidly as such resources become cheaper and more widely available. Deterministic site-specific ray-tracing propagation prediction models have also been used for indoor environments [2], [4], [47], [101], [118]. The limitation in this context is not computing power but the scarce nature of suitable, and reliable, databases describing indoor topographies.

3.1.3 Theoretical models

Theoretical, or analytical, models are derived physically assuming a (sometimes unrealistic) set of ideal conditions. For example, the over-rooftop diffraction model is derived using physical optics (PO) assuming uniform heights and spacing of buildings. Theoretical models are more efficient than site-specific

models but more site-specific than the empirical models [119]. They can also give important physical insights which neither empirical nor deterministic models are capable of.

3.2 Narrowband and wideband propagation models

The approaches to characterise the mobile radio propagation channels can be divided into narrowband and wideband modelling [2], [23], [47], [51], [53], [54], [64], [66], [67], [120], [399]. The fundamental concepts related to these characterisation methods were described in Chapter 2. Here we look at some examples of both model types.

3.2.1 Narrowband models

Narrowband characterisation is necessary and important for the radio network design, planning and coverage. It is used to describe the methods for predicting mean or median signal strength, path losses and other large scale fading parameters (e.g. average fade duration and level crossing rate). The mean signal strength and path loss information is especially important for the determination of coverage. Since the deployment of mobile radio communication systems in 1960s, numerous narrowband models have been developed based on extensive continuous wave (CW) measurements at a variety of VHF and UHF frequencies and for a variety of environments (urban, sub-urban, rural, hilly, mountainous, etc.) [54], [59], [121] – [128].

These models are based on empirical or semi-empirical methods resulting in a set of curves, formulas or both, derived from extensive field measurements.

The first study based on empirical methods was reported by Young in 1952 [129]. Young made an important series of measurement in New York at different frequencies. Whilst he did not develop a specific propagation prediction method, his findings proved to be influential and have been widely quoted. It could have been inferred from Young's results that the propagation losses were proportional to the fourth power of the range between transmitter and receiver, that the mean signal strength in a given area was log-normally distributed, and that the losses depended on the extent of urban clutter. In Young's study terrain features were neglected.

In 1968 Okumara et al. [130], reported an extensive and influential set of measurements at different frequencies in, and around, Tokyo [130], [131]. They presented an empirical propagation prediction method for field strength and path loss in LoS, urban, suburban, open, regular, irregular and hilly terrains. They also presented methods for handling mixed land/sea paths. The Okumura model is limited to a specific range of distances and frequencies but probably remains the most widely quoted of the narrowband propagation models.

In 1977, Allsebrook and Parsons [121], reported a series of measurements in British cities (Birmingham, Bath and Bradford). They estimated the diffraction loss of buildings close to the receiver but neglected terrain features. They

reported that the fourth power range law provided a good fit to the experimental data.

In 1980, in an attempt to make the Okumura method easy to apply, Hata [131] established empirical mathematical formulas to describe the graphical information given by Okumura. Hata's model predicts path loss between isotropic antennas is limited to certain ranges of input parameters and is applicable only over quasi-smooth terrain. The definition of building environments used by Okumura and Hata is subjective, and it is still not entirely clear how well the results for Tokyo apply to other cities [54]. To overcome the frequency limitation of Hata's model the European COST 231 program produced an extended version called the COST 231 model [52].

Ibrahim and Parsons [132] reported measurement and analysis for a number of antenna heights and frequencies in London. They observed that as the frequency increase, the path loss increases, and signal attenuates fast with the increase in range.

The above activities were primarily focussed on signal strength, path loss, and finding a path loss exponent for various environments. In general they showed that mean path loss is proportional to the nth power of range, where n lies between 3 and 4. They also confirmed that the variability in the signal slow fading can be described by a log-normal distribution. The influence of physical parameters of the environment, such as shapes and heights of buildings and street widths, were accounted for (when considered at all) using ad hoc correction factors. The limitations of these models resulted in considerable interest being focussed on physical models, especially such as ray-tracing. In [133], Ikegami uses a deterministic approach to predict field strength in urban environments. Ray-paths between transmitter and receiver were traced using a detailed map of heights, shapes and positions of building with the restriction that only single reflections from building walls were considered. The reflection losses were assumed to be constant and single edge diffraction was applied for the calculation of diffraction loss arising from the building nearest the receiver.

In 1988, Walfisch and Bertoni [134] reported a classic theoretical model for diffractions over buildings using knife-edge diffraction theory. They reported the impact of mobile terminal shadowing by a series of buildings in urban city streets. A novel aspect of their work was the consideration of building heights within the vertical propagation plane. In their study path loss was predicted on the basis of three factors: the path loss between the transmitter and the receiver under LoS and NLoS conditions, the multiple-edge diffraction loss up to the rooftop closest to the mobile receiver and the diffraction and the scatter loss from that point to the mobile receiver. The path geometry is shown in Figure 3.1.

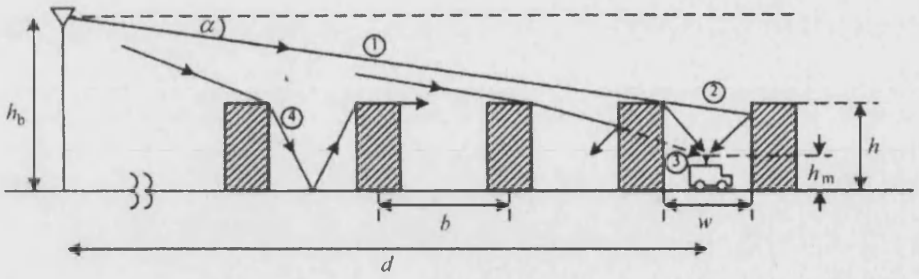

Figure 3.1: *Geometry of rooftop diffraction, (After Walfisch J. [119]).*

They showed that the primary path to the mobile terminal lies over the tops of the buildings with the buildings closest to the mobile being the most important, (see path 1, Figure 3.1). Other propagation mechanisms exists, but although the total field strength at the receiver may have multipath components due to reflection and diffractions (path 4) and building penetration (path 3), these multipath were generally neglected in their study.

Several models were subsequently developed which incorporate rooftop diffraction based on Walfisch-Bertoni approach [26], 135] – [139]. For example, in [138], [139], Xia et. al. estimates path loss due to multiple diffractions over rooftops. Walfisch and Bertoni considered that outside of the high-rise urban core, a city's buildings are of nearly uniform height and spacing and are organised by street systems in rows [119].

The Walfisch-Bertoni and Ikegami models were combined in the COST-Walfisch-Ikegami model [52] which considered four environmental factors; namely, building heights, building separation, roads widths and roads orientations with respect to the LoS path. It also includes some empirical correction factors to improve agreement with the measurements but is restricted in frequency range and parameters. More detailed discussions of narrowband propagation prediction models are available in the literature e.g. [2], [47], [51], [53], [54], [56], [58], [59], [61] – [63], [66], [67].

3.2.2 Wideband models

As discussed in Chapter 2, the multipath mobile radio propagation environment places fundamental limitations on the performance of any mobile radio communication systems. Signals arrive at the receiver via different propagation mechanisms, and existence of multiple propagation paths (multipath) with different time delays, attenuations and phases gives rise to a highly complex, time-varying dispersive propagation channel.

Wideband models are necessary, therefore, for the design of any system with a data rate that is significant with respect to the correlation bandwidth of the channel [23] and numerous wideband models have been developed.

The first general analytical treatment was presented by Zadeh [140], who dealt with time-variant linear filters. Subsequently, Kailath [141] presented similar

work with an emphasis on modelling of channel characteristics dealing with some canonical sampling models of time-variant channels and some theorems on measurability. In a seminal paper, Bello [72] extended the work of his predecessors and presented it in a form which readily showed the compactness and application of the characterisation approach to radio channels developing symmetrical relationships between system functions in the time and frequency domains employing duality and Fourier transformations. He subsequently generalised the concept of time-frequency duality and channel measurability. Bello's systems functions were described in Chapter 2.

With the advent of MCRC systems several wideband propagation prediction studies were initiated. The pioneers in this context include [50], [72], [127], [140] – [151]. The most vital of these studies was to explain the dynamic (time-variant) nature of the multipath channel.

Ossanna [150] was the first to attempt an explanation of the statistical character of the channel in terms of a set of interfering waves. His explanation was based on the interference of wave's incident and reflected from the flat sides of randomly located buildings. Although Ossanna's model predicted power spectra that were in good agreement with measurements in suburban areas, it assumes the existence of a LoS path and is limited to a restricted range of reflection angles. It is therefore rather inflexible and inappropriate for urban areas where the LoS path is often obscured.

In 1965, Gilbert [145] reported a study of energy reception in mobile radio. He examined several scattering models and established a number of important relationships between them. One feature common to all of them, was the uniform distribution of waves in angle, although he briefly mentioned the effect of a single strong component arriving directly from the transmitter.

In 1968, Clark [143] developed a model in which the statistical characteristics of the received signal at the mobile terminal were deduced from scattering. It was developed from a suggestion by Gilbert [145] and assumes that the field incident on the mobile antenna is composed of a number of horizontally travelling plane waves of random phase. The model assumes a fixed transmitter with a vertically polarised antenna. The principal constraint of Clark's model was its restriction to the case when the incoming waves are travelling horizontally, i.e. it was a 2D model. (In practice, reflection and diffraction from oblique surfaces creates waves that do not travel only horizontally.)

As previously stated, measurement of the mobile radio channels was first initiated by Young [129]. His (narrow-band) measurements at 450 MHz were made in New York. In the early 1970s, Young's mobile radio channel measurement trend was followed by Cox [77], [153] who made wideband measurements of the complex band-pass channel impulse response at 910 MHz in New Jersey and New York, using a spread-spectrum type channel sounder. This work can be regarded as a seminal study for modelling and characterisation of the wideband mobile propagation channel. Drawing upon the extensive work of Bello [72] on the statistical characterisation of random, time-variant, linear filters, Cox was able to fully characterise the mobile radio channel in terms of

parameters that provided a physical insight into the problems caused by multipath propagation [77], [153], [154].

In 1972, Turin conducted wideband experiments in urban areas of San Francisco at 488, 12880 and 2920 MHz, with a fixed transmitter and a mobile receiver. Turin reported a statistical analysis of multipath propagation which is commonly used as the basis for wideband propagation models, see Eq. 2.14 (repeated here for convenience):

$$h_b = \sum_{i=0}^{N(t)-1} \tilde{A}_i(t,\tau_i)\delta[\tau_o - \tau_i(t)]e^{j\phi_i(t,\tau_i)} \tag{3.1}$$

$\tilde{A}_i(t,\tau_i)$ is complex amplitude, $\delta[\tau_o - \tau_i(t)]$ is the delay and $e^{j\phi_i(t,\tau_i)}$ is the phase shift of the *ith* component at time *t*, respectively, and τ_i, is given by:

$$\tau_i = \frac{l_i}{c} \tag{3.2}$$

where l_i is the length of the *ith* path and *c* is the speed of propagation [155]. The principal objective of Turin's statistical model was to generate representative delay profiles (i.e. PDPs) by investigated the statistics of path arrival times in urban radio propagation environments.

In 1979, Bajwa and Parsons [33], [77], [83], [84], [153], [154], [156], [157], followed the work of Cox and conducted wideband measurements in urban and suburban areas of Birmingham. This was the first reported study of wideband propagation in the UK. In order to identify the influence of multipath propagation on channel characteristics, they proposed a scattering model (see Figure 3.2). If the scattering is assumed to result in vertically polarised horizontally travelling electromagnetic waves, the constant time delay surface becomes an ellipse in the azimuth plane. Thus each time delay between the Tx and Rx defines a con-focal ellipse. The different path lengths introduce relative phase shifts depending on the carrier wavelength. Identification of individual scatterers can only be accomplished if the angles of arrival are discernible.

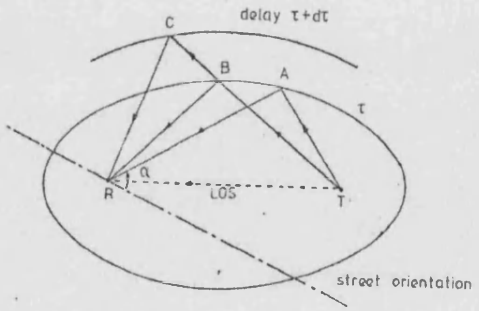

Fig 3.2: *Single scattering model for multipath propagation, (After Parsons J.D. [47]).*

Parson's et al., used a wideband channel sounder and estimated the wideband parameters relevant to system design such as average power delay profiles (APDPs), frequency correlation functions (FCFs) and 2D delay-Doppler functions. It was demonstrated that, in urban areas, the uniform distribution of locally scattered paths often leads to a homogenous scattering function, whereas, in suburban areas, one or two large scatterers can often lead to strong paths with long delays and give the multipath propagation an inhomogeneous character. Consequently, assumptions were made about the appropriate propagation model for USA and UK cities. (It was observed that the propagation characteristics in the UK cities are different from USA cities due to wide variations in street geometries.) In 1989, Demery [158] reported a similar wideband measurement study based on a medium sized urban city in the UK, using a swept time-delay cross-correlator channel sounder, having a time resolution of 0.1 μs.

Since the early 1980s considerable research has been focused on the design and development of high-performance, high-resolution, channel sounders. Many research groups, individual authors and commercial vendors have proposed new designs and developed sounders suitable for wide range of applications and environments.

Many measurements using these instruments have been conducted at various frequencies in different environments, e.g. [43], [75], [78], [89], [93], [155], [159] – [177]. Figure 3.3 shows some typical PDPs obtained from channel sounding measurements.

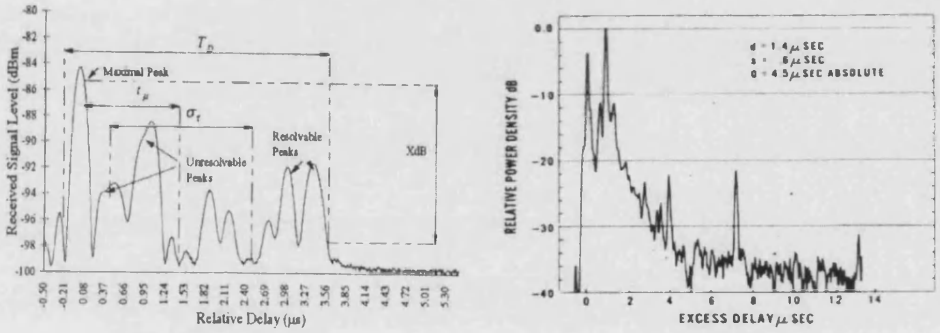

Figure 3.3: *Typical PDPs (a) After Jorgensen J. [89], (b) After Cox D.C [154].*

3.3 Review of measurement-based wideband models

This section presents a brief review of wideband measurement-based empirical propagation prediction models proposed for the microcellular environments.

In [178], Patwari et al. reports urban measurements at 1.8 GHz. The transmitting and receiving antennas were maintained at 1.7 m above the ground level. A spread spectrum channel sounder was used with 10 ns resolution. They found that RMS-DS increased exponentially with increasing path loss. RMS-DS up to 200 ns were reported.

In [179], Bohdanowicz et al. reported short range measurements in a campus environment at 17 GHz. The transmitting and receiving antenna heights were 1.8 m above ground level. The outdoor measurements were conducted in car parks. They showed that the dimensions of the environment influence RMS-DS. In the outdoor environments the average RMS-DS upto 53 ns was reported.

In [180], Domazetovic et al. report measurements in a car park at 5.3 GHz and an associated stochastic model. The receiver antenna was mounted at a height of 1.8 m, while the transmitter antenna was mounted at three different heights, ranging from 2 to 3.5 metres. Both temporal and spatial channel characteristics were analysed.

The influence of the antenna heights on delay spread has been investigated in [95], [96], [181] - [185]. In [181], Feurstein et al. presents measurement results for five microcellular environments in San Francisco, Oakland and California, at 1.9 GHz. The measurements were made using a wideband radio channel sounder with resolution of 100 ns. Three transmitter heights of 3.7, 8.5, and 13.3 m were used with a mobile receiver height of 1.7 m. The RMS-DS was calculated as a function of antenna height (Table 3.1).

In [184], Son and Myung report a quasi 3D ray-tracing model for city centre of Ottawa, Canada, at 1.9 GHz. Two transmitter heights of 3.7 and 8.5 m were used with a mobile receiver height of 1.7 m. The RMS-DS was calculated as a function of antenna height. Simulated results were compared with the measured results in [181]. In [181] and [184], it was found that RMS-DS increases with increasing antenna height. Table 3.1 shows RMS-DS found as a function of antenna height.

Table 3.1: *RMS-DS as function of the antenna heights.*

Author (Ref., Year)	Environment	Antennas heights (m)		F (GHz)	τ_{RMS} (Mean) (ns)
		Rx	Tx		
Feurstein ([181], 1994)	Urban San Francisco	1.7	3.7	1.9	136.8
			8.5		176.8
			13.3		275.9
Son ([184], 1999)	Urban- Ottawa	1.7	3.7	1.9	134.6
			8.5		173.1

3.4 Ray-tracing

With reduction in the costs of computing and the recent availability of detailed terrain database, there is an increased demand and interest in propagation prediction models that are able to provide location-specific predictions of channel characteristics. Ray-tracing has emerged as the most successful and practical technique, at least for terrestrial cellular radio applications [88]. If site-specific field prediction is needed, and the necessary detailed databases are available, then ray-tracing is probably now the technique of first resort and, in many cases, can be considered as an alternative to time consuming, and expensive, measurements. Several studies have shown that the ray-tracing models are capable of greater prediction accuracy when compared to empirical and semi-empirical models [112], [186], [189] - [195], [400], [401]. Ray-tracing

can also serve as a starting point for statistical modelling [196] - [199], virtual measurements using the ray-tracing software substituting for real measurements in the physical environment. Ray-tracing models are now widely used to predict narrowband and wideband mobile radio channel characteristics, such as field strength, path-loss, CIRs, PDPs, RMS delay spread, coherence bandwidth, Doppler-spread, angle-of-arrival (AoA) and angle-of-departure (AoD) statistics, etc.

Despite the emergence of practical ray-tracing packages their computationally intensive nature still typically restricts the range for which they can be used to a few kilometres [53]. Ray-tracing possesses disadvantages other than their sheer computational complexity. In particular they are not capable of modelling non-geometrical optic processes such as diffuse reflection and/or scattering from rough surfaces, and propagation through disordered media such as vegetation. Many implementations also suffer (at least potentially) from spatial aliasing [200] which arises in regions where the density of rays is insufficient to capture interaction with the rapidly changing component(s) of the environment.

3.4.1 Geometric optics (GO)

The propagation of electromagnetic (EM) waves is governed by Maxwell's equations. The direct numerical solution of Maxwell's equations is computationally intensive, however, and is not usually feasible for complex real life environment [54]. Geometric optics (GO) and the uniform theory of diffraction (UTD) are used, therefore, to approximate this solution. Because GO uses ray concepts it is also referred to as ray optics (RO).

GO was originally developed to study the propagation of light. It assumes that EM power propagates in infinitely small tubes known as rays. To conserve the energy in a tube of rays, the power associated with each ray must be inversely proportional to the square of the distance that it travels [201].

According to GO, the rays between any two points follows a path that makes the optical distance between them an extremum (usually a minimum) [201], [202]. In addition, the light intensity and power per unit solid angle between the two points are governed by conservation of energy flux in a tube of rays [4]. The basic equation of GO, known as the eikonal equation, can be derived from Maxell's equations and is given as [4], [201], [202]:

$$\left\{\frac{\delta\psi}{\delta x}\right\}^2 + \left\{\frac{\delta\psi}{\delta y}\right\}^2 + \left\{\frac{\delta\psi}{\delta z}\right\}^2 = n^2(x,y,z) \qquad (3.3)$$

where ψ is the real scalar function of position known as eikonal surfaces and n is the refractive index of the medium. If the medium of wave propagation is homogenous, then the rays are straight lines. The eikonal surfaces, also called the geometrical wave surfaces or the geometrical wave fronts, are normal to each of the radial rays as shown in Figure 3.4. The eikonal surfaces for plane waves are planar surfaces perpendicular to the direction of wave travel.

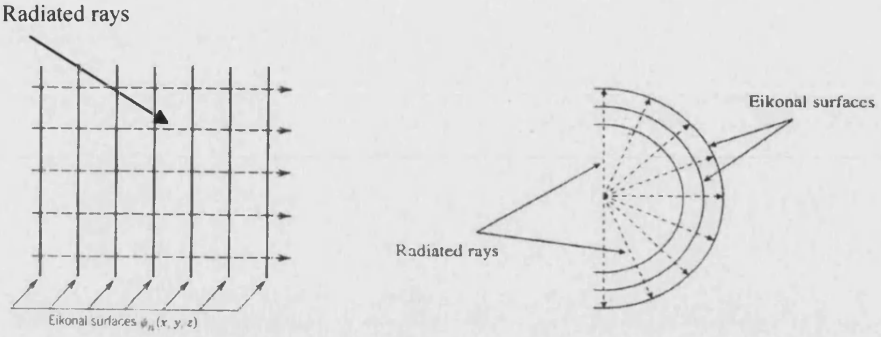

(a) (b)

Figure 3.4: Eikonal *surfaces (a) Plane radiated wave, (After Balanis C.A. [201] and (b), Spherically radiated wave, (After Lee B.S. [4]).*

[201], gives a detailed discussion on GO and Eikonal surfaces and develops the relationship between the electric fields associated with radiated rays and the eikonal surfaces.

3.4.2 Propagation mechanisms

The interaction of EM energy with the physical environment can be described in terms of four fundamental mechanisms:

1. Reflection
2. Refraction
3. Diffraction
4. Attenuation

It is useful to add two additional mechanisms which represent a specialised case and a generalised case of the fundamental mechanisms, i.e.:

5. Free-space propagation
6. Scattering

Reflection occurs when a radio wave is incident on an object such as ground surface with dimensions that are large compared to wavelength. Refraction occurs when a wave moves between regions of different dielectric constant but can usually be neglected in mobile radio communications applications [99].

Diffraction can be defined as an apparent bending of radio waves round obstacles [212]. Diffraction occurs when the radio path between the transmitter and receiver is obstructed by a surface that has sharp or irregular edges [2], [23], [115]. In the context of ray-tracing, diffraction occurs when a ray passes close to (within about one Fresnel zone of) a boundary between regions of the same or different electrical characteristics (permittivity and conductivity) [23].

The diffracting waves produced by the obstructing surface are present throughout space and even behind the obstacles, giving rise to the bending of waves around

the obstacle, even when the LoS path does not exist between the transmitter and receiver [115].

Diffraction has a rich lengthy history of theoretical investigation. It has been applied with different levels of success in the prediction of the radio wave propagation in terrestrial and cellular radio communications. It occurs from the terrain and urban or suburban topographies such as the surface of the ground, hills, mountains or ridges, exterior building walls, building rooftops, interior building walls, partitions within the building, furniture and vertices. Diffraction is an important propagation mechanism whether for outdoor (urban or suburban) or indoor (office buildings or home) environments. In this thesis diffraction for outdoor environments is taken into account. Several analysis methods and approximation theories are available for diffraction problems. For example, the finite wedge diffraction is the most common and practical approach to approximate diffracting surfaces [230]. It deals with a wedge (an edge and its two adjacent surfaces). The two surfaces forming the edge may be convex, concave or plane. The term "curved wedge" is used when both surfaces forming the edge may be convex, both surfaces may be concave, or one surface may be plane and the other convex or concave. While the term "plane wedge" is used when both surfaces forming the edge are plane. The complete solutions for these canonical problems have been addressed in the uniform theory of diffraction (UTD) in [230], [231], [260].

The effects of the terrain profile of the diffracting hills or ridges can be viewed as smooth curved surfaces with finite curvature such as circular, parabolic or elliptical cylindrical or spherical edges. While the effects of the urban or residential suburban topographies such as exterior building walls and building rooftops can be viewed as plane surfaces with infinite curvatures such as straight edges. In this thesis wedge diffraction by straight edges of the buildings is taken into account. The detailed discussion on diffraction theory and its mathematical formulations are described in Section 3.4.2.3.

Attenuation (in the sense of dissipative loss) occurs whenever the conductivity of the propagation medium is non-zero.

Strictly, free-space propagation represents the special case of propagation in a vacuum but is used in practise to describe propagation in any (approximately) attenuation free medium of constant dielectric constant in which objects are sufficiently distant from the propagation path as to cause negligible reflection, refraction or diffraction. In micro- and pico-cellular radio, where ground reflections can often be neglected, a LoS path between transmitter and receiver is usually considered to exist in free-space. Scattering is said to occur when the propagation environment contains objects with dimensions that are on the order of, or smaller than, the wavelength. Scattering, which follows the same physical principles as, and is a generalisation of, reflection and diffraction, causes energy to be radiated in many different directions. In mobile cellular radio examples of scattering objects include foliage, street furniture (lampposts, road signs, etc.) and rough surfaces (the random irregularities of the surface satisfying the wavelength condition). The physical (deterministic) prediction of scattering generally requires a level of environmental detail that is unknown. Even if this

level of detail is available it adds an unreasonable burden on the required computational resources. It can be taken account of by adding an empirical (statistical) scattering model to an otherwise deterministic one but this is rare. In practice scattering is usually neglected in mobile cellular radio applications with little deterioration in the quality of field strength prediction [99], [115].

Figure 3.5 illustrates a range of different propagation mechanisms.

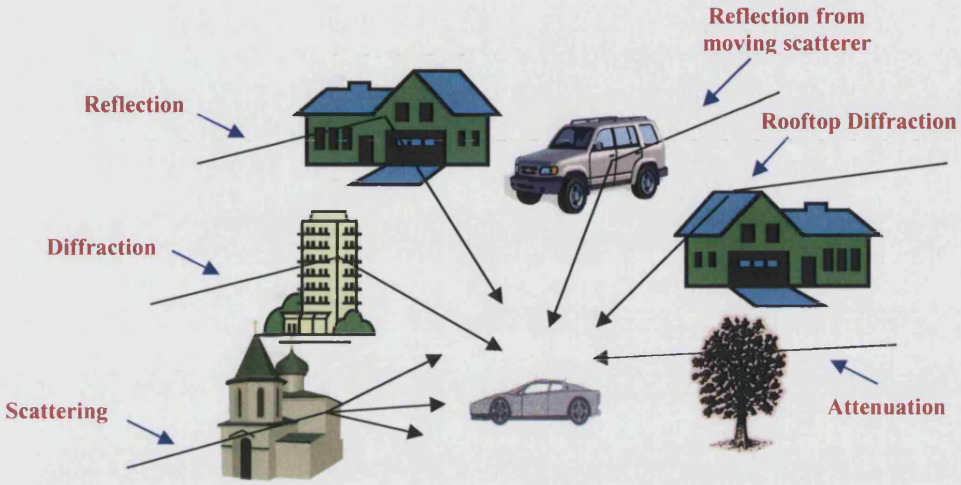

Figure 3.5: *Illustration of the propagation mechanisms.*

3.4.2.1 Free-space (LoS) propagation

The simplest case to which deterministic analysis can be applied to radio wave propagation is the case where the radio wave propagates in free-space. A free-space model characterises the contribution to the signal at the receiving antenna due to the direct ray or line-of-sight (LoS) path. Assuming that the transmitting and the receiving antennas are located in free-space, i.e. remote from any objects that might absorb, reflect or diffract radio frequency energy, the received power density S_R at a distance R from the transmitter is given [4] by:

$$S_R = \frac{P_T G_T}{4\pi R^2} \tag{3.4}$$

where P_T is the transmitted power and G_T is the gain of the transmitting antenna (relative to an isotropic source) in the direction of the receiver. The received power is:

$$P_R = A_e S_R \tag{3.5}$$

where A_e is the effective area of the receiving antenna:

$$A_e = \frac{\lambda^2}{4\pi} G_R \tag{3.6}$$

Substituting Eq. (3.4) and Eq. (3.6) into Eq. (3.5) the received power can be expressed as:

$$P_R = P_T G_T G_R \left(\frac{\lambda}{4\pi R}\right)^2 \tag{3.7}$$

Eq. (3.7) is known as the free-space or Friis propagation formula [4], [47] and represents the minimum loss in a mobile radio channel. Equation (3.7) shows that free-space propagation obeys an inverse square law with distance R, so the received power falls by 6 dB per octave of range (20 dB per decade of range) [47].

Equation (3.7) can be expressed in terms of received voltage as:

$$\frac{V_R^2}{Z_L} = P_R \tag{3.8}$$

$$\frac{V_R^2}{Z_L} = P_T G_T G_R \left(\frac{\lambda}{4\pi R}\right)^2 \tag{3.9}$$

where Z_L is the receiving antenna load (assumed matched in the maximum power transfer sense to the lossless antenna radiation impedance) and:

$$V_R = \sqrt{P_T G_T G_R \left(\frac{\lambda}{4\pi R}\right)^2 Z_L} \tag{3.10}$$

3.4.2.2 Reflection and transmission

When a wave propagating in one medium is incident on another having different electrical properties, the wave is partially reflected and partially transmitted (refracted). If medium 2 is a perfect conductor, then all incident energy is reflected back into the medium 1 without loss of energy [66]. Figure 3.6 shows a plane wave incident onto a plane boundary between two lossless media with different permeabilities, μ, and permitivities, ε. The orientation of the electric fields (i.e. polarisation) of the incident, reflected and transmitted waves is perpendicular to the plane of incidence. The plane of incidence is defined as the plane containing the normal vector to the reflecting interface and the vector in the direction of incident propagation [201] (see Figure 3.7). An incident wave with general polarisation can be split into perpendicular and parallel polarised components. The total reflected and transmitted field is then the vector sum of the perpendicular and parallel, reflected and transmitted, components [2], [66], [201].

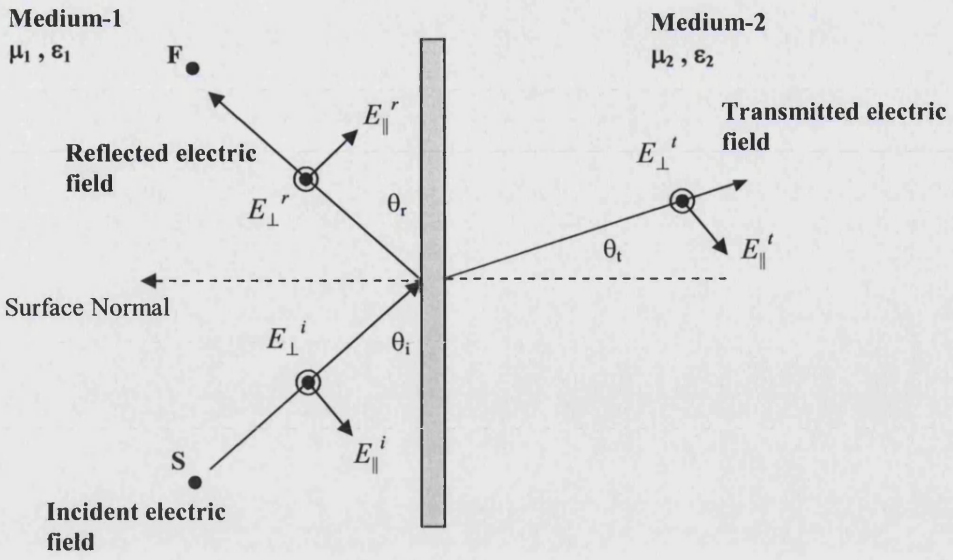

Figure 3.6: *Illustration* of *perpendicular polarised uniform plane wave incidence at an oblique angle on a boundary.*

3.4.2.2.1 Fresnel formula

The Fresnel reflection and transmission coefficients determine the reflected and transmitted fields. These coefficients are functions of the material properties, and depend on wave polarisation, angle of incidence, and the frequency of the propagating wave [2]. Fresnel reflection and transmission coefficients are, in general, complex quantities.

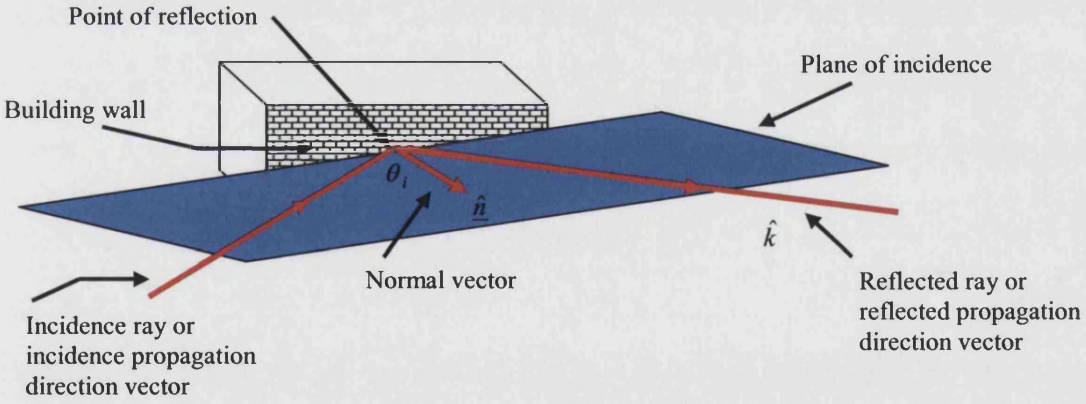

Figure 3.7: *3D illustration of the normal vector to the reflecting interface and the vectors in the direction of incidence and reflection are in the plane of incidence.*

For a plane wave incident on a plane boundary the Fresnel reflection ($\widetilde{R}$) and transmission ($\widetilde{T}$) coefficients for perpendicular ($\perp$) and parallel ($\parallel$) polarisations are given [66] by:

$$\tilde{R}_{\perp} = \frac{E_{r\perp}}{E_{i\perp}} = \frac{Z_2 \cos\theta_i - Z_1 \cos\theta_t}{Z_2 \cos\theta_i + Z_1 \cos\theta_t} \tag{3.11}$$

$$\tilde{T}_{\perp} = \frac{E_{t\perp}}{E_{i\perp}} = \frac{2Z_2 \cos\theta_i}{Z_2 \cos\theta_i - Z_1 \cos\theta_t} \tag{3.12}$$

$$\tilde{R}_{\parallel} = \frac{E_{r\parallel}}{E_{i\parallel}} = \frac{Z_2 \cos\theta_i - Z_1 \cos\theta_t}{Z_2 \cos\theta_i + Z_1 \cos\theta_t} \tag{3.13}$$

$$\tilde{T}_{\parallel} = \frac{E_{t\parallel}}{E_{i\parallel}} = \frac{2Z_2 \cos\theta_i}{Z_2 \cos\theta_i - Z_1 \cos\theta_t} \tag{3.14}$$

where Z_1 is the intrinsic impedance of free space (medium 1 in Figure 3.6) equal to 377 Ω, [47] and Z_2 is the impedance of medium 2. Z_2 is a function of the permittivity, ε, permeability, μ, conductivity σ and the angular frequency ω [66], i.e.:

$$Z_2 = \sqrt{\frac{j\omega\mu}{\sigma + j\omega\varepsilon}} \tag{3.15}$$

If medium 2 is lossy then Z_2 will be a complex quantity. The angles of reflection θ_r and transmission θ_t are related to the angle of incidence θ_i by *Snell's laws* [66]:

$$\theta_i = \theta_r \tag{3.16}$$

$$\frac{\sin\theta_i}{\sin\theta_t} = \sqrt{\frac{\varepsilon_2\mu_2}{\varepsilon_1\mu_1}} \tag{3.17}$$

Conservation of energy dictates that the transmission coefficient is related to the reflection coefficient by:

$$\left|\tilde{T}_{\perp}\right|^2 + \left|\tilde{R}_{\perp}\right|^2 = 1 \tag{3.18}$$

For perpendicular polarisation the reflected field is given by:

$$\tilde{E}(R) = \left|E_o\right|\tilde{R}_{\perp} A(R_i, R_r) e^{-j\phi_r} \tag{3.19}$$

where $\left|E_o\right|$ is the incidence field at the reflection point, $A(R_i, R_r)$ is the spreading factor and $e^{-j\phi_r}$ is the phase of the reflected ray. The spreading factor is given by:

$$A(R_i, R_r) = \frac{R_i}{R_i + R_r} \tag{3.20}$$

where R_i is the incidence distance from source point (S) to the reflection point, and R_r is the distance from the reflection point to field point (F) (see Figure 3.6).

3.4.2.2.2 Ground reflections

A 2-ray model is often considered in LoS situation where the only other path arises from ground reflection, Figure 3.8. If separation between transmitter and receiver is sufficiently small enough to consider the Earth's surface plane but sufficiently large (with respect to transmitter and receiver heights) to ensure small grazing then the LoS and ground reflected waves can be assumed to be of equal amplitude but 180^{o} out of phase. This 2-ray model has been applied in a variety of cellular environments [2], [66], [181].

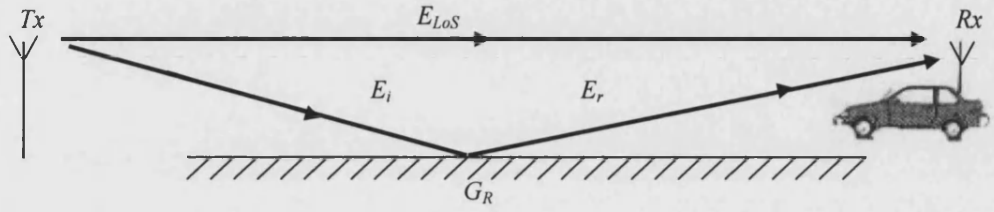

Figure 3.8 *Illustration of 2-Ray propagation model over a flat reflecting surface.*

Once, the ground reflection point, *GR* is determined, the reflected field is given by:

$$\widetilde{E}(R) = |E_o|\widetilde{R}_{\parallel} A(R_i, R_r) e^{-j\phi_r} \tag{3.21}$$

where $\widetilde{R}_{\parallel}$ is the complex, parallel polarised (for vertically polarised antennas), Fresnel reflection coefficient. All other parameters are defined earlier in Eq. (3.20). The total field at the receiver is the sum of the LoS field E_{LoS}, and reflected field, $\widetilde{E}_r$:

$$\widetilde{E}_{Total} = E_{LoS} + \widetilde{E}_r \tag{3.22}$$

3.4.2.3 Diffraction

Simple GO alone fails to account for energy diffracted into a shadow region when a wave encounters an edge, vertex, or corner of objects such as buildings, Figure 3.9.

In practice energy does propagate into the shadow region via diffraction [66].

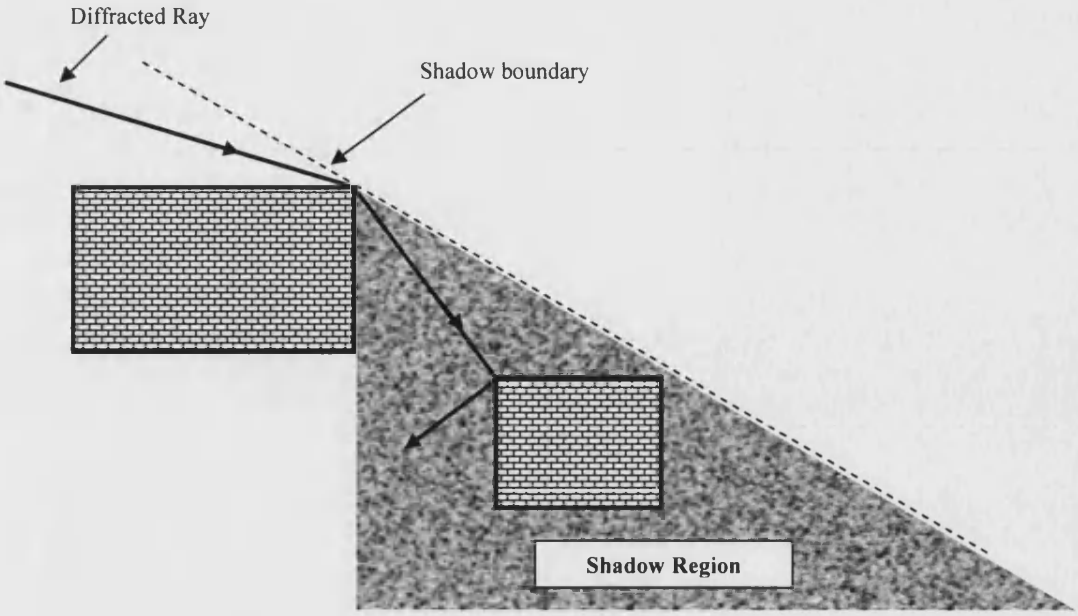

Figure 3.9: *Geometrical optics incorrect in the shadow region.*

3.4.2.3.1 Huygens' principle

In 1690, Huygens made a major contribution to understanding diffraction. His elementary-wave principle stated that a new secondary wavefront (BB) was the envelope of elementary waves emanating from the primary wavefront (AA), see Figure 3.10. Although he could not explain diffraction or how the elementary waves added up, he was able to provide this qualitative assessment. It was 150 years later that Sir George Stokes noted that no backwards propagating wave (CC in Figure 3.10) was created from the primary wave. This led to the familiar cardioid representation of the radiation pattern of each secondary source [203].

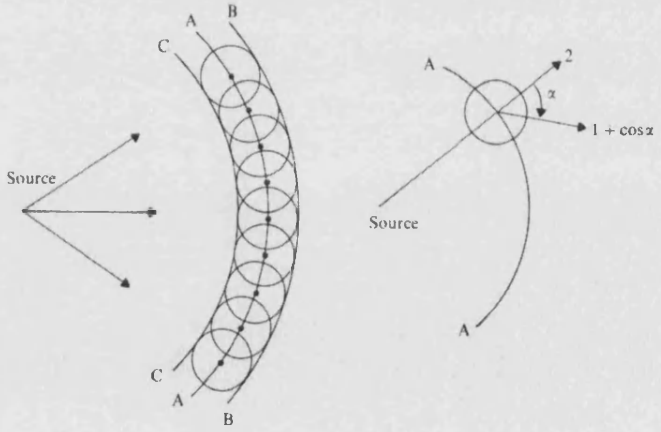

Figure 3.10: *Huygens elementary-wave principle, (After Griffiths, [204]).*

3.4.2.3.2 Young's two wave interpretation

In 1802, Thomas Young made a fundamental step in the interpretation of diffraction. He stated that diffraction was the result of the interference of two waves. The first one exists only in the lit region and follows free space propagation laws, while the second, the diffracted wave, originates at the illuminated geometrical discontinuity. Young assumed that the first wave was discontinuous at the boundary of the geometrical shadow and the diffracted wave was continuous everywhere.

3.4.2.3.3 Huygens-Fresnel principle and knife edge-diffraction

In 1815 Fresnel A. J. combined Huygens' Principle with interference. He suggested that the phase of the elementary wave be taken into account when calculating the secondary wavefront. This becomes known as the Huygens-Fresnel principle [27], [203] and explained the cardioid pattern of secondary wavelets.

In order for no backward wave (CC in Figure 3.10) to be created, the secondary wavelets cannot have uniform amplitude in all directions. If α is the angle between the propagation direction of energy in a secondary wavelet and the propagation direction of the energy at that point of the primary wavefront on which the wavelet is located, then the relative amplitude of the secondary wavelet in the direction α is given by (1 + cos α). Consider Figure 3.11(a).

Wavelet Y contributes an amplitude at W proportional to $1 + \cos 0^0 = 2$ (phase reference 0^0). Wavelet V's amplitude is proportional to $(1 + \cos \alpha) < 2$ with a phase lag of $k\pi$ radians where $0 < k < 1$. Wavelet X's amplitude is proportional to $1 + \cos \alpha'$ with a phase lag of π radians. This process is repeated over the entire wave front.

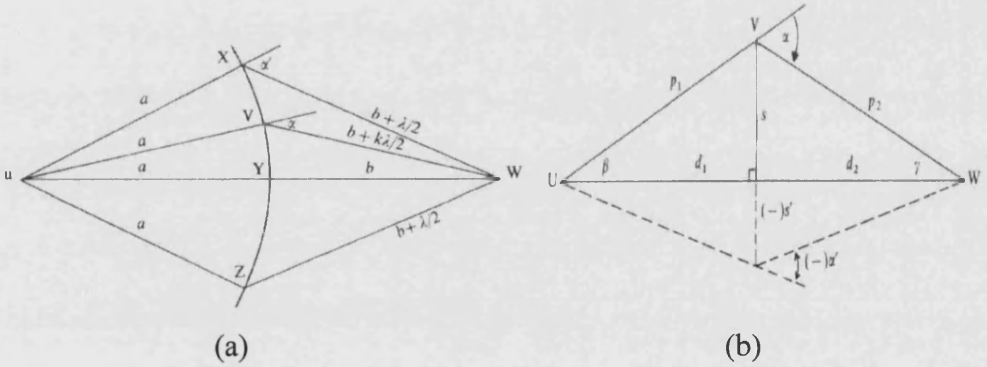

Figure 3.11: *Geometry of Huygens-Fresnel principle, (After Griffiths [204]).*

Assuming $s << d_1, d_2$ and $s >> \lambda$, (see Figure 3.11(b)) the difference between the direct and diffracted paths, the "excess path length", is [27], [204]:

$$\Delta = \frac{s^2}{2}\frac{d_1 + d_2}{d_1 d_2} \tag{3.23}$$

and the corresponding phase difference is [27], [204]:

$$\phi = \frac{2\pi}{\lambda}\Delta = \frac{\pi}{2}\frac{2(d_1 + d_2)s^2}{\lambda d_1 d_2} = \frac{\pi}{2}v^2 \tag{3.24}$$

where

$$v = s\sqrt{\frac{2(d_1 + d_2)}{\lambda d_1 d_2}} \tag{3.25}$$

v is known as an auxiliary parameter [204] or the Fresnel-Kirchhoff diffraction parameter [2], [47], and can also be expressed in terms of the geometrical parameters as [66]:

$$v = h\sqrt{\frac{2(d_1'+d_2')}{d_1' d_2' \lambda}} = \alpha\sqrt{\frac{2d_1' d_2'}{(d_1'+d_2')\lambda}} \tag{3.26}$$

where *h*'(Figure 3.12) is the excess height of the edge above the straight line from source to field points. For most practical cases, d_1, d_2 >> *h*, so that diffraction parameter, v can be approximated in terms of distances measured along the ground.

The diffraction loss is calculated by evaluating the complex "*Fresnel integral*", F(v) [2], [47], [66]:

$$F(v) = \frac{(1+j)}{2}\int_{\upsilon}^{\infty} e^{((-j\pi t^2)/2)}dt \tag{3.27}$$

which has been extensively tabulated in [2], [47], [63], [66].

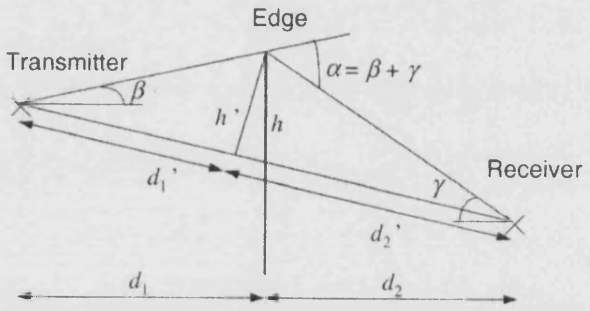

Figure 3.12: *The geometry of knife-edge diffraction, (After Parsons J. D., [47] and Saunder S. R. [66]).*

3.4.2.3.4 Knife-edge diffraction and Fresnel zones

Another useful way to consider knife-edge diffraction is in terms of the obstruction of Fresnel zones around the direct ray [2], [66]. Consider a transmitter and a receiver separated in free-space as shown in Figure 3.13. The n^{th} Fresnel zone is the region inside an ellipsoid defined by the locus of points where distance (*a* + *b*) is larger than the direct path between transmitter and

receiver (d_1 +d_2) by n half-wavelengths. Hence the radius of the n^{th} zone, r_n, is given by applying the condition:

$$a+b=d_1+d_2+\frac{n\lambda}{2} \tag{3.28}$$

If we assume that $rn << d_1$ and $r_n << d_2$, then to a good approximation [66]:

$$r_n=\sqrt{\frac{n\lambda d_1 d_2}{d_1+d_2}} \tag{3.29}$$

The first Fresnel zones can be thought of (loosely and to a first approximation) as containing all the propagated energy in the wave. Contributions within the first zone are all in phase, so any absorbing obstructions which do not enter this zone will have little effect on the received signal. The Fresnel zone clearance (h/r_n) can be expressed in terms of the Fresnel -Kirchhoff diffraction parameter ν [47], [66] as:

$$v=h\sqrt{\frac{2(d_1+d_2)}{\lambda d_1 d_2}}=\frac{h}{r_n}\sqrt{2n} \tag{3.30}$$

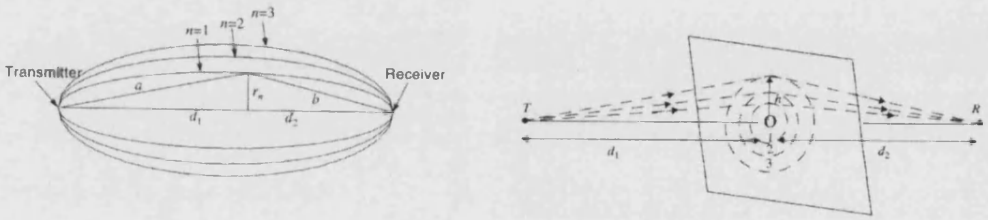

(a) (b)

Figure 3.13: (a) *Fresnel zones, (After Saunders S. R. [66]), (b) Family of circles defining the limits of the Fresnel zones at a given point on the radio propagation path, (After Parsons J.D. [47]).*

3.4.2.3.5 Multiple knife-edges

In many practical situations and real environments, the propagation path may consists of more than one obstruction, in which case the total diffracted field along the ray-path due to all of the obstacles must be computed. The extension of single-knife-edge diffraction theory to two or more obstacles is not an easy task. The problem is complicated mathematically but reduces to a double integral of the Fresnel form over a plane above each knife-edge. Several multiple knife-edge diffraction approaches have been proposed e.g. [205] – [208] which account for knife-edge diffraction by successive obstructions. Solutions for the case of two knife-edges were proposed in [209] and [210]. In [211], Vogler proposed an expression for the attenuation over multiple knife-edges. Probably the best known of the multiple diffraction models are Deygout's and Bullington's

constructions. Bullington [205] suggests that the series of obstacles can be replaced by a single equivalent obstacle so that the diffracted field can be obtained using single knife-edge diffraction theory, Figure 3.14.

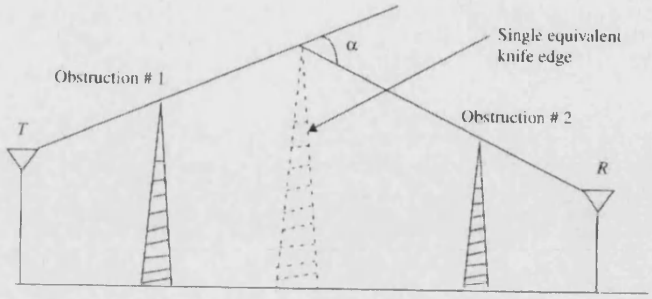

Figure 3.14: *Bullington's construction of an equivalent knife-edge, (After Rappaport T.S. [2]).*

More detailed discussions and comparisons of multiple diffraction models are available in the literature, e.g. [47], [66], [67]. All these models were proposed in the context of essentially single path propagation for applications such as radio relay and broadcasting [212]. Several authors have developed geometrical methods for modelling multiple building obstructions as knife-edges for cellular applications, e.g. [54], [99], [120], [135] - [139], [213] - [215].

Most models assume the knife-edge to be perfectly absorbing. In [215], however, the knife-edge is considered to be perfectly conducting. In [217] it is shown that a perfectly conducting building cannot, in general, be replaced by one or more perfectly conducting knife-edges. This conclusion was based on theoretical simulations and measurements using a reduced scale model.

3.4.2.3.6 Diffraction from real objects

In many modelling situations, propagation prediction of diffraction over buildings and ridges may be treated as absorbing knife-edges [66] and is commonly estimated using Fresnel knife-edge diffraction, as described above. This approach has the advantage of simplicity, and for many geometries yields accurate results. However, it can, in some cases yield results which are in serious disagreement with field measurements [218]. It is important to note, however, that in the context of urban cellular environments the knife-edge(s) approximation has usually been applied only to diffraction over buildings (i.e. roof-tops) and not to diffraction around buildings (i.e. the building's vertical edges).

Wedge diffraction has also been applied to propagation over roof-tops. (Knife edge solutions approach wedge solutions as wedge angle tends to zero.) Wedge diffraction solutions have been available since the beginning of the 19th century, but have not been widely used for radio propagation prediction modelling due to their computational complexity [219] – [225]. The most common approach to

calculating the diffraction field of a wedge is Keller's geometrical theory of diffraction.

3.4.2.3.7 Geometrical theory of diffraction

In 1953, Joseph Keller developed the geometrical theory of diffraction (GTD) [232], which is a numerically simple and elegant solution to wedge diffraction. Keller applied a modified version of Fermat's principle and observed that high frequency diffraction is a local phenomenon. In doing so, he reduced the solution of scattering of EM waves from arbitrarily shaped objects to a superposition of simple canonical problems (wedges, Figure 3.15) [27], [203], [226].

The central idea of GTD is that an extended version of Fermat's principle may be used to predict the existence of diffracted rays, which may then be treated with the ease of any other ray in GO. Figure 3.15 (a) shows a ray obliquely incident upon the edge of an obstacle at an angle θ_o to the edge. Fermat's principle for edge diffraction predicts that a cone of diffracted rays will be produced, where the cone has semi-angle θ_o [66]. This contrasts with reflected and transmitted rays, where only a single ray is produced at each interaction. In the simpler case of normal incidence, $\theta_o = \pi/2$ and the cone reduces to a disc.

A diffraction coefficient is used to adjust the value of the incident field and arrive at the initial value of the diffracted ray's field strength. The diffraction coefficient is simply multiplied by the incident field value. The following points are central to GTD:

1 Since diffraction is a local phenomenon, only the immediate vicinity of the point of diffraction affects the value of the diffraction coefficient. Factors affecting the coefficients are direction of incidence and diffraction, wavelength and geometrical and physical properties of the media
2 As $\lambda \rightarrow 0$ the diffraction coefficients tend towards zero, as does the diffracted field. In this case, only the geometrical optics field remains

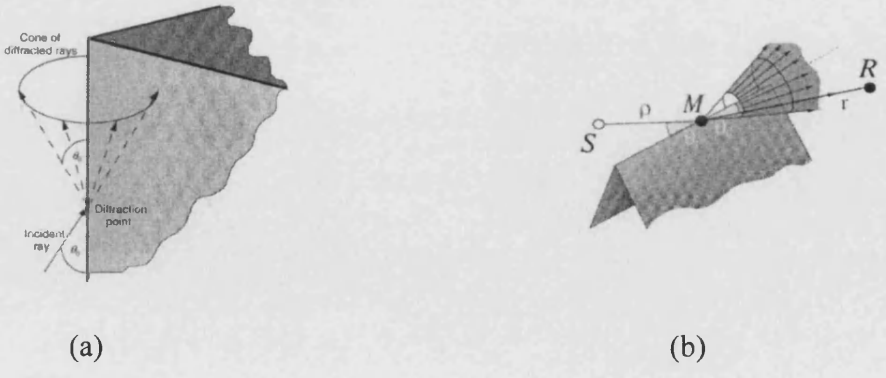

(a) (b)

Figure 3.15: *(a) Keller's cone generation of edge-diffracted rays from a wedge according to GTD, (After Saunders S.R. [66]), (b) Rays diffracted by a 3D wedge. At oblique incidence, an incoming ray gives rise to a cone of diffracted rays whose central axis is the edge, (After Tsinggos N. [227]).*

Point 1 means that diffraction due to a curved edge can be well approximated by a simple wedge with its edge tangential to that of the curved edge at the point of diffraction. Simple, wedge solutions can therefore be used to determine the diffraction coefficients and superposition subsequently applied to solve more complicated (and realistic) problems.

GTD has enjoyed remarkable success in the engineering community. Its application to antenna engineering has 'transformed antenna design from mostly art to mostly engineering' [228]. Among other applications, GTD has been widely applied to the modelling of terrains, hills, mountains, buildings and ridges etc. [218], [229] - [231]. A detailed analytical treatment of GTD is outlined e.g. in [27], [218], [232].

Classical GTD overcame the principal shortcoming of GO, i.e. the prediction of a zero field in the shadow region. Keller developed his theory using wedge diffraction as a numerically simple canonical problem but the theory remained incomplete because:

1 it predicts a singular diffracted field in the vicinity of the shadow and reflection boundaries when the source, diffracting edge and receiving point lie on a straight line
2 it considered only perfectly conducting wedges [47], [66]

To overcome the limitations of the GTD, numerous approaches were proposed. One of the best known was suggested by Kouyoumjian and Pathak [230] who set out the uniform theory of diffraction (UTD). This is valid at shadow and reflection boundaries where classical GTD fails.

3.4.2.3.8 Uniform theory of diffraction

In 1974, Kouyoumjian and Pathak [233] developed UTD, a wedge diffraction solution that is valid across the shadow and reflection boundaries. The UTD solution is obtained by adjusting the GTD formulation to remain continuous in the transition regions (the region of rapid field change adjacent to the shadow and reflection boundaries). This is accomplished applying '*transition functions*' or correction factors to the diffraction coefficient. The formulation is only slightly more involved than simple knife-edge diffraction since it is also based on the Fresnel integral. The effect of the transition functions appears in the argument of the Fresnel integral [234], [235], (see Eq. (3.27), and Section 3.4.2.3.3).

In summary, UTD is an extended version of the GTD, which is valid everywhere in space as long as the incident fields are ray optical and reflection and diffraction events can be considered to be local phenomena [47], [234] - [236].

To illustrate GTD/UTD consider a wedge (Figure 3.16). It is conventional to label the faces of the wedge, as the (zero) 0-face and the n-face. Angles are measured from 0-face [47], [53], [54]. Figure 3.16 shows the GTD/UTD geometry for calculating the field over a wedge-shaped obstacle in the plane normal to the diffracting edge; *E*. (The detailed GTD/UTD formulas are not

given here since they are given exhaustively in the context of Luebber's UTD (Section 3.4.2.3.10). Luebber's UTD has been used as the diffraction element of the ray-tracing software developed as part of this thesis.

The diffracted ray travels distance R_1 from the source, S to the diffracting edge E, and then a further distance R_2 to the field point P. The internal angle of the wedge is Ψ. The incident ray angle, Φ_1, and diffracted ray angle, Φ_2, are measured externally from 0-face. The 3D geometry of UTD is outlined in literature e.g. [4], [101], [237], [238].

The detailed formulation of UTD for perfectly conducting wedge is outlined in [47], [54], [66], [67], [100], [230], [236].

UTD has been successfully employed in a variety of microcellular propagation prediction models e.g. [23], [100], [220], [239], [240]. The solutions of UTD are restricted, however, to the case of surfaces that are smooth and perfectly conducting. These restrictions have promoted an extensive literature. It has been found that surface impedance boundary conditions may provide a useful model in analyzing the influence of material properties of wedges (e.g. building walls) for radio propagation prediction models.

Many authors have contributed to this subject and proposed numerous extensions to UTD, e.g. [23], [222], [229], [234], [235], [241] - [259]. One approach which has earned wide recognition is Leubber's extended version of UTD.

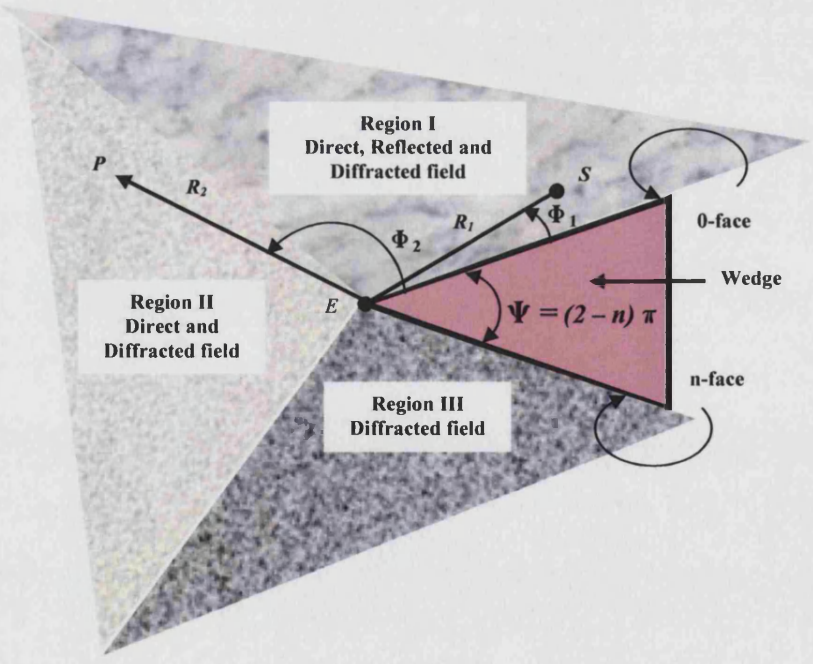

Figure 3.16: *The geometry of GTD/UTD wedge diffraction.*

3.4.2.3.9 Leubber's UTD

In 1984, Leubbers [260] proposed an enhancement to UTD which allows finite conductivity and local surface roughness effects to be catered for. The

formulation is based on single 2D wedge diffraction but the method can be extended to 3D multiple wedges [27], [236], [258].

Comparative studies of knife-edge and wedge diffraction, knife-edge diffraction and GTD, Maliuzhinet's and Luebbers' wedge diffraction formulations and non-perfectly conducting wedge diffraction using UTD and FDTD appear in [2], [47], [53], [54], [66], [67], [120], [204], [218], [236], [258], [261], [262].

Leubber's UTD diffraction coefficients are recommended by ITU-R P.526-8. They are widely quoted and extensively applied in radio propagation prediction modelling. For example, the 2D and 3D Luebber's UTD diffraction coefficients are used for non-perfectly conducing wedges in [227], [263], [234], [235], [264], and used for radio propagation prediction models in [4], [101], [120], [213], [217], [218], [237], [238], [265] - [274].

3.4.2.3.10 Luebber's heuristically enhanced UTD

The Luebber's enhanced UTD formulation of diffraction coefficient for non-perfectly conducting wedge [218], [231], [261] was obtained by modifying heuristically the perfect conducting UTD diffraction coefficient of Kouyoumjian and Pathak [240]. The approach is to include reflection coefficients in Kouyoumjian-Pathaks results to compensate discontinuities of the GO field at the reflection shadow boundaries. With the assumption that propagation through the wedge can be neglected [261]. The Luebber's heuristically enhanced UTD diffraction coefficients are easy, straight forward to implement and recommended by the ITU-R. It has been widely or almost exclusively used for the radio channel modelling.

It is these coefficients that have been used in the implementation of the ray tracer presented later in this thesis and the algorithmic details are therefore given below in full.

Consider a wedge with straight edges (Figure 3.17).

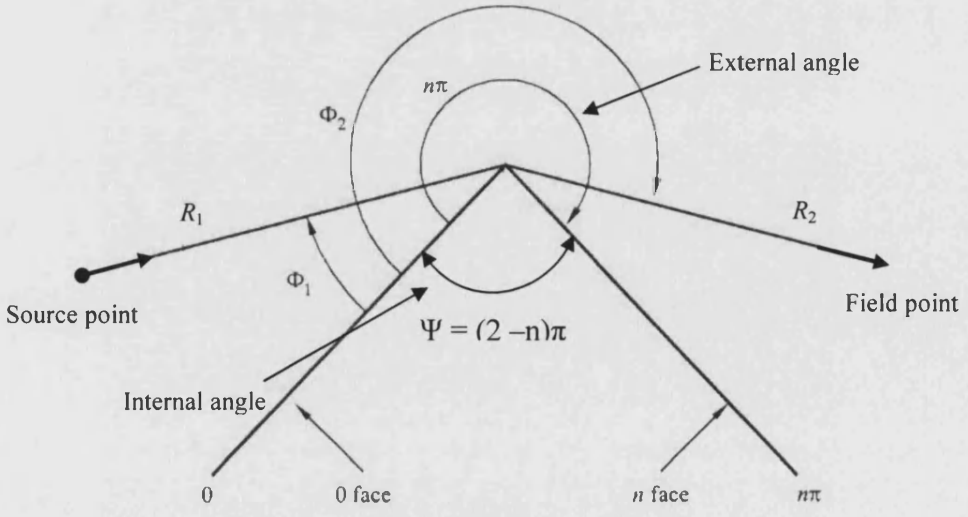

Figure 3.17: *Ray geometry for diffraction by a non-curved wedge.*

The 3D Luebber's diffraction coefficients for a non-perfectly conducting wedge are given [236] by:

$$\tilde{D}_{\parallel}^{\perp} = \frac{-\exp[-j(\pi/4)]}{2n\sqrt{2\pi \cdot k}\sin\beta_0} \times \left[\cot\left(\frac{\pi+(\Phi_2-\Phi_1)}{2n}\right)F\left[kLa^{+}(\Phi_2-\Phi_1)\right]+\cot\left(\frac{\pi-(\Phi_2-\Phi_1)}{2n}\right)F\left[kLa^{-}(\Phi_2-\Phi_1)\right]\right] \pm \left\{\begin{array}{l} R_{0,\parallel}^{\perp}\cdot\cot\left(\frac{\pi-(\Phi_2+\Phi_1)}{2n}\right)F\left[kLa^{-}(\Phi_2+\Phi_1)\right] \\ +R_{n,\parallel}^{\perp}\cdot\cot\left(\frac{\pi+(\Phi_2+\Phi_1)}{2n}\right)F\left[kLa^{+}(\Phi_2+\Phi_1)\right] \end{array}\right\} \tag{3.31}$$

where (see also Figure 15):

$\tilde{D}^{\parallel}, \tilde{D}^{\perp}$: are the diffraction coefficients for horizontal (soft) and vertical (hard) polarisation, respectively

R_1: is the distance from the source point to the diffracting wedge

R_2: is the distance from the diffracting wedge to the field point

k: is the wave number $2\pi/\lambda$

Φ_1: is the incidence angle, measured from the 0-face

Φ_2: is the diffraction angle, measured from the 0-face

n: is the external wedge angle as a multiple of π radians (actual angle = $n\,\pi$ (rad))

Ψ: is the internal angle of the wedge, $\Psi < 180^{\circ}$

L is a distance parameter that can be expressed, [4], [230] as:

$$L = \begin{cases} R_2 \sin^2\beta_0 & \text{plane wave incidence} \\ \dfrac{R_2 \sin\beta_0 R_1 \sin\beta_0'}{R_2\sin\beta_0 + R_1\sin\beta_0'} & \text{cylindrical wave incidence} \\ \dfrac{R_1\cdot R_2}{R_1+R_2}\sin^2\beta_0 & \text{spherical wave incidence} \end{cases} \tag{3.32}$$

$$a^{\pm}(\beta) = 2\cos^2\left(\frac{2\cdot\pi\cdot n\cdot N^{\pm}-\beta}{2}\right) \tag{3.33}$$

where:

$$\beta = \Phi_2 \pm \Phi_1 \tag{3.34}$$

In Eq. (3.33), $N^{\pm}$ is the integer that satisfies more closely the relations:

$$2 \cdot \pi \cdot n \cdot N^{+} - \beta = \pi \text{ and } 2 \cdot \pi \cdot n \cdot N^{-} - \beta = -\pi \tag{3.35}$$

The approximate solutions of Eq. (3.35) are cumbersome and not easy to compute accurately. Accurate solutions of the Eq. (3.33) are given in [227] i.e.:

$$N^{+} = \begin{cases} 0 \text{ for } \beta \le \pi(n-1) \\ 1 \text{ for } \beta > \pi(n-1) \end{cases} \tag{3.36}$$

$$N^{-} = \begin{cases} -1 \text{ for } \beta < \pi(n-1) \\ 0 \quad \text{for } \pi(1-n) \le \beta \le \pi(1+n) \\ 1 \quad \text{for } \beta > \pi(n+1) \end{cases} \tag{3.37}$$

$\tilde{R}_{0,\parallel}^{\perp}$, $\tilde{R}_{n,\parallel}^{\perp}$ are reflection coefficients of the (zero) 0-face and n-faces respectively. Several expressions have been proposed for these coefficients [212], [238], [241], [270]. ITU-R P.526-8 [212] recommends the use of:

$$\tilde{R}^{\perp} = \frac{\sin(\Phi) - \sqrt{\eta - \cos(\Phi)^2}}{\sin(\Phi) + \sqrt{\eta - \cos(\Phi)^2}} \tag{3.38}$$

$$\tilde{R}^{\parallel} = \frac{\eta.\sin(\Phi) - \sqrt{\eta - \cos(\Phi)^2}}{\eta.\sin(\Phi) + \sqrt{\eta - \cos(\Phi)^2}} \tag{3.39}$$

where:

$$\Phi = \Phi_1 \text{ for } R_0 \text{ and } \Phi = (n\pi - \Phi_2) \text{ for } R_n$$

$$\eta = \varepsilon_r - \mathrm{j} \times 18 \times 10^9 \, \sigma / f \tag{3.40}$$

Here:

ε_r:	is the relative dielectric constant of the wedge material
σ:	is the conductivity of the wedge material (S/m)
f:	is frequency (Hz)

If necessary the two faces of the wedge may have different electrical properties. If $R_{0,n}$ is set to -1 (horizontal polarisation) or +1 (vertical polarisation) then the Eq. (3.31) reduces to diffraction for a perfectly conducting wedge. For the same settings, if the wedge angle reduces to 0^0 then the UTD formulations of Eq. (3.31) gives the same results as Fresnel knife-edge diffraction [234], [235], [230], [240].

The function $F[.]$ in Eq. (3.31) is a Fresnel transition function which involves the Fresnel integral. $F[.]$ can be expressed as: [54], [227], [230].

$$F(x)=2j\sqrt{x}\cdot\exp(jx)\cdot\int_{t=\sqrt{x}}^{\infty}\exp(-t^2)\cdot dt \tag{3.41}$$

Several approximations exist for Eq. (3.41) in the literature e.g. [53], [54], [67], [212], [216]. Kawai [227], [275] gives approximate expressions that are simple and easy to implement [227] i.e.:

$$\text{for } X<0.8:\ F(X)=\sqrt{\pi X}\left(1-\frac{\sqrt{X}}{0.7\sqrt{X}+1.2}\right)e^{j\frac{\pi}{4}\sqrt{\frac{X}{X+1.4}}} \tag{3.42(a))}$$

$$\text{for } X\geq 0.8:\ F(X)=\left(1-\frac{0.8}{(X+1.25)^2}\right)e^{j\frac{\pi}{4}\sqrt{\frac{X}{X+1.4}}} \tag{3.42(b))}$$

It should be noted that the cotangent terms in Eq. (3.31) result in a singularity at shadow and reflection boundaries and cannot, therefore, evaluated numerically at these boundaries. $D_{\parallel}^{\perp}$, however, remains finite, and can be readily evaluated. The term containing the singular cotangent function is given for small ε as [212], [218], [227], [230]:

$$\cot\left(\frac{\pi\pm\beta}{2n}\right)\cdot F\left(kLa^{\pm}(\beta)\right)\cong n\cdot\left[\sqrt{2\pi kL}\cdot sign(\varepsilon)-2kL\varepsilon\cdot\exp\left(j\frac{\pi}{4}\right)\right]\cdot\exp\left(j\frac{\pi}{4}\right) \tag{3.43}$$

with ε defined by:

$$\varepsilon=\pi+\beta-2\pi nN^{+} \qquad \text{for } \beta=\Phi_2+\Phi_1 \tag{3.44}$$

$$\varepsilon=\pi-\beta+2\pi nN^{-} \qquad \text{for } \beta=\Phi_2+\Phi_1 \tag{3.45}$$

The resulting diffraction coefficient is continuous at shadow and reflection boundaries provided that the same reflection coefficient is used when calculating reflected rays [212]. Eq. (3.43) incorporates the advance which the UTD makes over GTD and is accurate close to the boundaries [53].

The Luebber's formulation of UTD described above can be used to predict the diffraction loss due to a finitely (non-perfectly) conducting wedge. The method is suitable for diffraction around buildings edges or over roof-tops. The method requires the conductivity and dielectric constant of the obstructing wedge, and assumes that no transmission occurs through the wedge material. It takes into account diffraction in both the shadow and LoS region and provides for a smooth transition between the two. Once the diffraction point is determined, the diffracted field is given by:

$$E^{d}(R)=|E_o|\tilde{D}_{\perp}A(R_i,R_D)e^{-j\phi_D} \tag{3.46}$$

where $|E_o|$ is the incidence field at the diffraction point, $\widetilde{D}_\perp$ is the complex perpendicularly polarised diffraction coefficient, $A(R_i, R_D)$ is the spreading factor and $e^{-j\phi_D}$ is the phase angle of the diffracted ray. The spreading factor $A(R_i, R_D)$ is given by:

$$A(R_i, R_D) = \begin{cases} \dfrac{1}{R_D} & \text{plane wave} \\ \dfrac{1}{R_D \sin\beta_0} & \text{cylinderical wave} \\ \sqrt{\dfrac{R_i}{R_D(R_i + R_D)}} & \text{spherical wave} \end{cases} \qquad (3.47)$$

where R_i is the incidence distance (from source point to the diffraction point), and R_D is the diffracted distance (from the diffraction point to field point), see Figure 3.17.

3.4.2.3.11 Multiple wedge diffraction

In practice successive multiple diffractions often occur. If the diffracted field generated by one wedge is incident on a second wedge it will, in turn, produce diffracted fields that can be found by repeating the UTD algorithm. Figure 3.18 shows the geometry of multiple wedge diffraction with unequal height and spacing between the wedges. Multiple wedge diffraction is implemented by considering the second wedge vertex as the field point for the first diffraction, the third diffracting wedge vertex as the field point for the second diffraction (the second wedge vertex being the source point for the third diffraction), and so on.

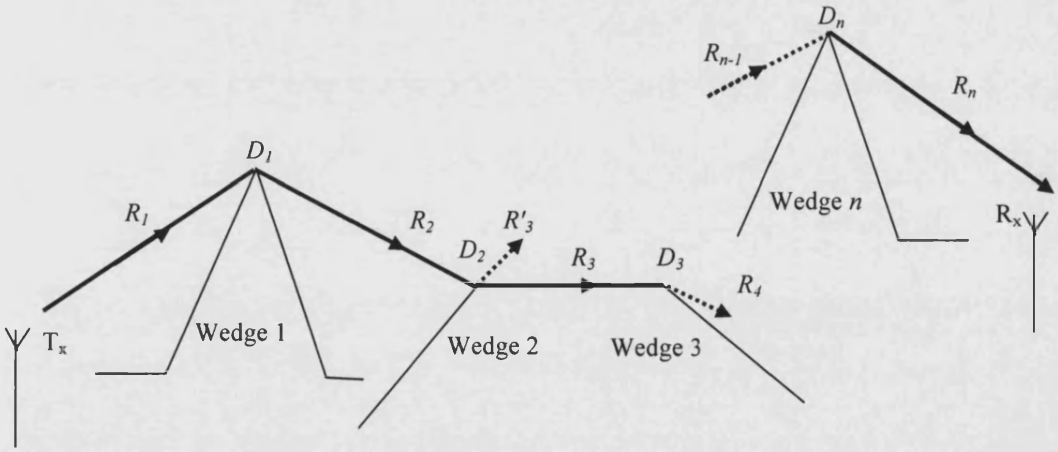

Figure 3.18: *Ray geometry of multiple wedge diffraction.*

Referring to Figure 3.18, computation of multiple diffracted fields using UTD requires the calculation of diffraction coefficient for each diffraction wedge of the ray-path. For example, computation of double diffracted fields requires the evaluation of diffraction coefficients for wedge1 and wedge 2, with wedge 3

eliminated and with R'_3 being redefined as the distance from the vertex of wedge 2 to the field point. (In Figure 3.18 wedge 2 and wedge 3 are two joined wedges.)

Several authors proposed alternative models for double, multiple and higher-order wedge diffraction, e.g. [120], [201], [212], [213], [231], [234], 235], [270]. In [213], Arablouei and Ghorbani proposed a model for multiple wedge diffraction for buildings. In this study, each building was considered to be two joined wedges (Figure 3.19). More detailed discussions of multiple wedge diffraction are given in [54], [120], [213], [231], [234], [236], [261].

The formulations of the diffraction coefficient and diffracted field defined above (see Eq. (3.31 and Eq. 3.46) are valid for single wedge diffraction. In the case of multiple wedge diffraction, UTD theory is not valid and requires further adjustment [277] of the spreading factor A[.] in Eq. 3.46 and the distance parameters L in Eq. 3.32. All the other parameters of the UTD diffraction coefficients remain same as for the single diffraction case [231].

Several expressions are available for double, and higher-order diffracted fields, e.g. [213], [234], 235], [270].

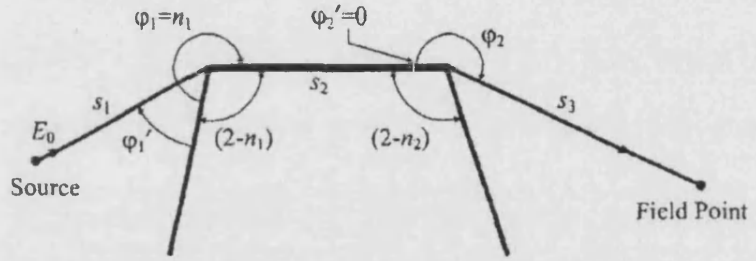

Fig. 3.19: *Ray geometry for diffraction by a two joined non-curved wedges, (After Arablouei R. [213]).*

In [234], [235], and [231] expansions of analytical expressions for the spreading factor A[.] and the distance parameters L for double, triple and higher order wedge diffracted fields, respectively, are proposed. Referring to the geometry of multiple wedge diffraction (Figure 3.18) the spreading factor A[.] and the distance parameters L for multiple diffracted rays emanating from a spherical wave source are given [231], i.e.:

$$A(R_1, R_n) = \sqrt{\frac{R_j + R_{j+1} + ... + R_n}{R_n(R_j + R_{j+1} + ... + R_n)}} \tag{3.48}$$

and:

$$L = \frac{R_j \cdot R_{j+1}}{R_j + R_{j+1}} \sin^2 \beta_0 \tag{3.49}$$

where R_j is the ray-segment (RG).

3.4.3 Ray-tracing algorithms

Ray-tracing models are usually based on one of the two ray construction techniques; ray launching or the method of images [52], [53], [10], 101], [115], [117], [200], [278], [279].

3.4.3.1 Ray-launching

Ray-launching [181] is also known as shooting-and-bouncing ray (SBR) or beam tracing [4], [54], [200], [281], [282].

Rays are launched from the transmitting antenna at (usually regular) angular intervals. They are then allowed to propagate in the environment according to the laws of GO and GTD (or UTD).

To determine points of reflection requires the intersection of a ray with an object to be established. This is a classic problem in computational geometry. The simplest (but computationally inefficient) approach tests all environmental objects against each ray.

Figure 3.20 and Figure 3.21 illustrates the concept of ray-launching, intersection with objects and reception, respectively.

Rays are traced until some criterion is satisfied, whereupon they are terminated. The criterion is, typically, either that a maximum permitted number of interactions (reflections, diffractions and/or transmissions) has occurred or that the field strength of the ray has fallen to some predetermined (absolute or relative) value.

After all rays have been terminated the field strength at a particular observation point is found by summing the fields associated with each ray at that point. Since the probability of a ray in a complex environment passing precisely through the observation point is very small (the exact probability depending on the spatial quantisation of the simulation) an important issue is how to assess which rays contribute to the field at that point and which do not. Many criteria have been proposed e.g. [193], [281], [283] - [287], almost all employ the concept of a collection sphere (for 3D ray tracers) or circle (for 2D ray tracers), see Figure 3.20. In reality this is a zone of influence associated with each ray, the radius of which is an increasing function of the optical distance along a ray from its source, Figure 3.21(a). A ray then contributes to all field observation points that fall within its zone of influence. A commonly adopted formula for the collection radius is $\alpha R/\sqrt{3}$ where R is the ray optical distance.

Figure 3.20 illustrates the use of a reception sphere [115], [193]. For each receiver location, the perpendicular distance r, from the receiver to the ray is computed, together with the total ray path length R, from transmitter to the perpendicular projection point. The principle disadvantages of ray-launching are that:

1. It suffers from spatial aliasing

2. It does not calculate exact paths (in the Fermat's principle sense) between transmitter and receiver (or field observation point)
3. There is no unambiguously correct radius of the collection sphere

3.4.3.2 Tube-tracing

Tube-tracing associates some fraction of the transmitted power with a discrete and non-zero planar angle (in the case of 2D tracing) or solid angle (in the case of 3D tracing). The shapes traced out are tessellating triangles (2D) or tessellating conical pentagons (3D). The 'rays' that are traced become the sides of the triangle or the edges of the pentagonal cone, Figure 3.21(b). All field observation points lying within the triangular area (2D) or within the conical volume (3D) benefit from the associated power.

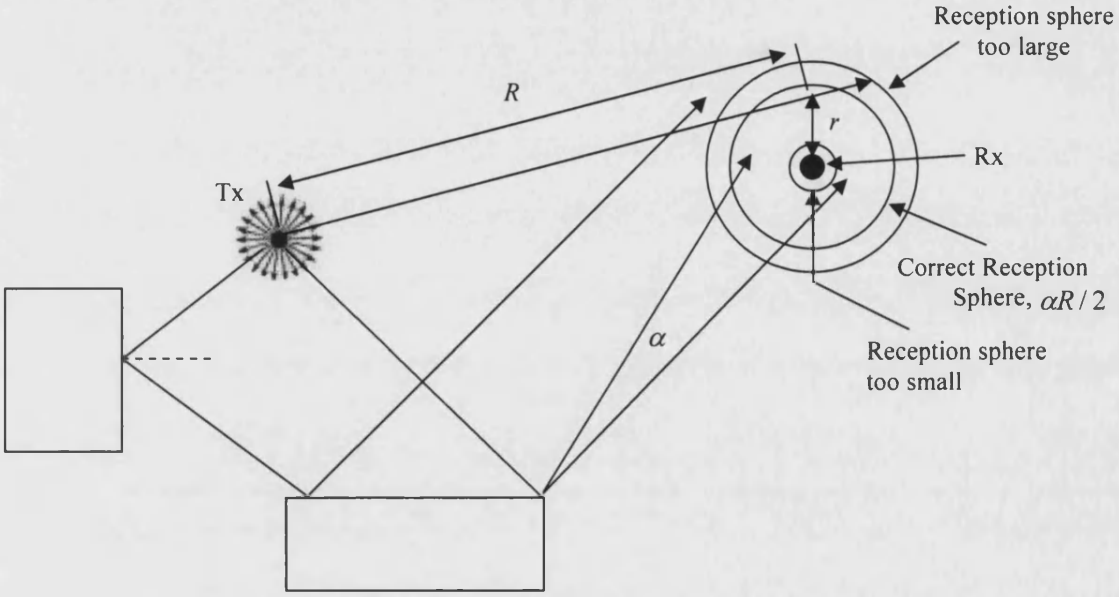

Figure 3.20: 2D *illustration of ray-launching and reception.*

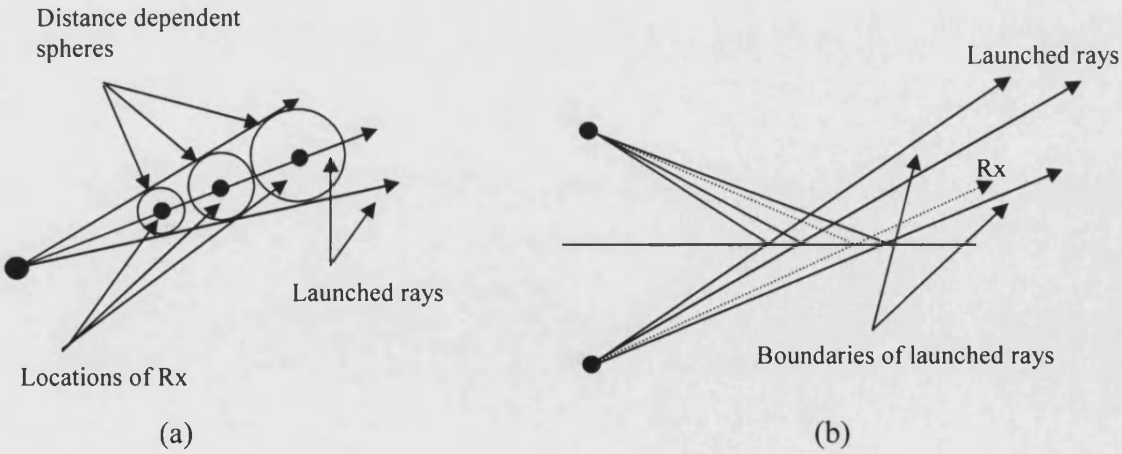

Figure 3.21: *Illustration of methods used to determine a path from the Tx to the Rx. (a) the use of distance dependent reception spheres, (b) the use of the angular information at the virtual transmitter, (After Lee B. S. [280]).*

3.4.3.3 Method of images

The method of images [112] is a classical ray-tracing technique based on the EM image theory [4], [100], [288] - [294]. It is geometrically simple and, within the approximations of GO, is exact (unlike ray-launching and tube-tracing). It locates the image of the transmitter in all plane facets of the environmental scatterers and then identifies precise points of geometrical reflection from intersections of the straight lines connecting image and receiver and the facet producing the image. (If the straight line does not intersect the physical facet then no GO path exists.) This process is repeated using the images of images as many times as desired until some criteria (e.g. maximum permitted number of interactions) has been reached. Figure 3.22 illustrates the method in 2D with a second order image. (The direct, LoS, path in Figure 3.22 needs no explanation.)

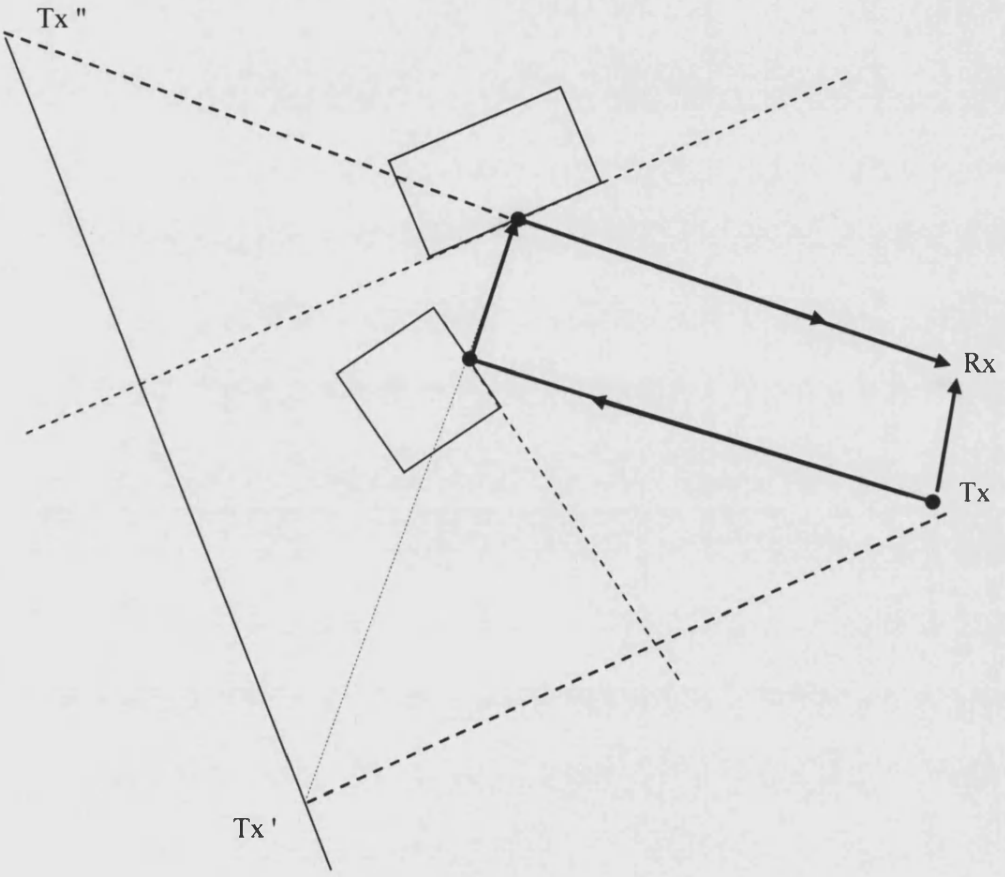

Figure 3.22: *2D illustration of first and second order images (Tx' and Tx") of a Tx.*

The image method is geometrically exact and so spatial aliasing is avoided. It is less computationally efficient than ray-launching, however, when the number of reflecting facets becomes large and number of interactions consequently high. The computational complexity increases as n^m where m and n are, respectively, the number of reflections and the number of facets considered [278], [295]. Complexity growth (assuming illumination zones are not applied) is therefore exponential. Mixed reflected-diffracted paths produce further difficulties, [279], [292]. For practical applications in complex environments special acceleration

and/or hybrid techniques must generally be employed to reduce the computational resources required to manageable levels [112], [278].

3.4.3.3.1 Image-trees

Image-trees are useful in implementing the method of images. One such tree can be constructed for each transmitter location [4], [100], [101], and holds all the images for a defined order of reflections. The tree eliminates the need to repetitively generate images for the same transmitter location and increases the speed of path-searching algorithms. The test to establish whether an image is capable of providing a path starts from the highest order and works backwards towards the transmitter. Figure 3.23 illustrates an image-tree schematically.

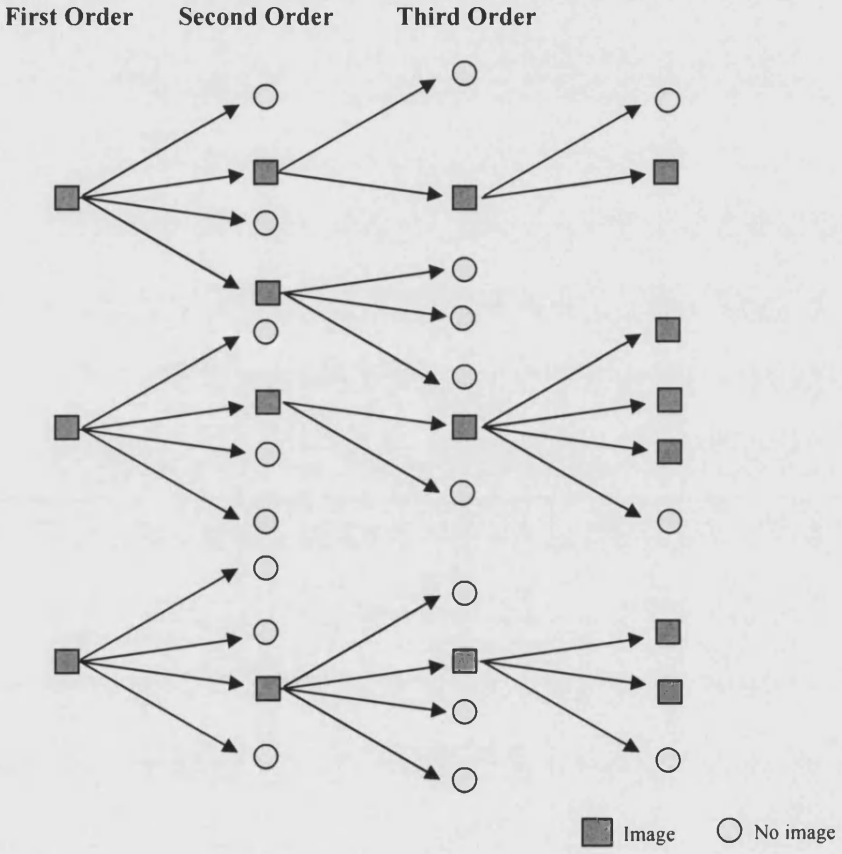

Figure 3.23: *An image-tree diagram.*

In Chapter 4, (Section 4.4.3) a new visibility technique is developed to search possible ray-paths. The new technique is a path-search algorithm which reduces the computation time compared to a classic image-tree.

3.4.3.4 2D and 3D ray-tracing

Ray-tracing can be implemented in either two dimensions (2D) or three dimensions (3D).

2D ray-tracing models may be vertical plane models (i.e. represent rays propagating over the roof-tops of buildings) or horizontal plane models (i.e.

represent rays propagating around the corners of buildings) [47], [54], [216], [249], [291], [296] - [301], [305] - [307].

Many 2D models have been proposed, e.g. [47], [120], [216], [291], [299], [302] - [304], [307] and have been reported to provide excellent prediction results for a variety of urban and suburban environments if both transmit and receive heights are well below the average roof-top level [115], [268], [308]. A comparison of 2D ray-tracing with empirical models is reported e.g. in [296], [309].

Recently, due to the availability of high-resolution databases and hugely improved computing power, 3D ray-tracing models have become practical and many have been described in the literature for a range of different environments [99], [100], [115], [117], [120], [186] - [188], [276], [279], [281], [282], [288], [290], [305], [310], [319] - [325]. 3D models, which take account of ground reflections and the overall shapes of individual buildings, obviously give better predictions than the 2D models. This is especially so when basestation antennas are located above the surrounding building clutter whilst mobile terminals are immersed in it.

Detailed comparisons between 2D and 3D models are presented in [115], [186], [310], [313].

3D ray-tracing obviously requires much greater computing resources than does 2D. Some authors have proposed combined (hybrid) 2D and 3D models e.g. [288].

3.4.3.5 Computational complexity and acceleration techniques

Computation efficiency is the biggest obstacle to the application of any ray-tracing technique. It is therefore important to make any legitimate assumptions, and choose algorithmic approaches, which can increase computational efficiency. Several such *'acceleration techniques'* have been proposed, e.g. [4], [101], [112], [115], [288], [318], [326] - [328].

The first, most obvious, technique is to reduce the number of objects or building facets on which actual ray-object intersection will be performed. The second is to accelerate the calculation of the intersection test requiring pre-processing of the propagation environments and/or the positions of transmitter and receiver. The acceleration techniques are described in the following sections. The detailed discussion of the acceleration techniques is outlined in [112].

3.4.3.5.1 Vertical plane launch model

Liang and Bertoni [187], [188] proposed the vertical plane launch (VPL) model, appropriate for microcellular environments where the building walls are predominantly vertical planar polygons [115]. 2D ray-tracing is used in the horizontal plane but each 2D ray is interpreted as representing propagation throughout the corresponding vertical plane. When a ray intersects a vertical wall specular reflection from the vertical wall occurs. When the ray hits a vertical

building edge, vertical diffraction occurs. When the ray hits a building roof-top, horizontal diffraction occurs. The over-rooftop diffraction creates two vertical propagation planes, one in the same direction as the incident ray and the other in the direction of reflection. Diffraction from the vertical edge creates a new source and many new rays in 2D planes should be launched. These rays are further traced in a similar manner until some criteria are reached. Figure 3.24 and Figure 3.25 shows schematic illustrations of the VPL method and ray-launching procedure, respectively.

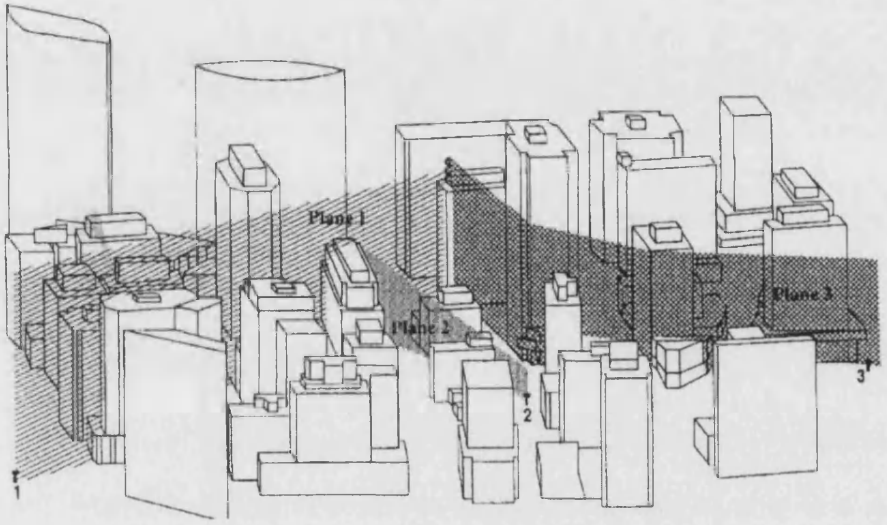

Figure 3.24: *Approximate 3D ray-tracing method using vertical planes, (After Liang G. [187]).*

3.4.3.5.2 Space-division

Space-division is widely used in computer graphics. The basic idea is to first create a grid (usually rectangular) in the propagation environment and then establish a lookup table registering objects residing in each grid cell. When a ray is launched, it is traced in the grid. For each grid the ray traverses the lookup table is checked to see if any object resides in that grid. If so the ray is tested for intersection with these objects. If the ray intersects an object reflected and transmitted (or multiple diffracted) rays are created. Space-division results in generally faster, more efficient, ray-tracing since in each grid interactions are limited to a small number. Space-division methods can be divided into *rectangular division* and *triangular division* varieties. A detailed description of both is outlined in [112]. The methods are applied in [329] – [331].

3.4.3.5.3 Angular Z-Buffer

The Angular Z-Buffer (AZB) [112], [313] is based on the light buffer used in computer graphics. Space is divided into angular regions according to a source point. The source point can be a transmitter or a transmitter image (of any order) related to a reflection plane. When a ray is launched from the source only those objects located in the angular region containing the ray are tested for ray intersection. The AZB is quite efficient when a large number of observation

points are illuminated by the source. It is suited to treat diffraction more efficiently than the ray-launching (or shooting-and-bouncing (SBR)). The efficiency of AZB depends on the environment and the size of database. Further details of the AZB algorithm are given in [112], [310], [313].

3.4.3.5.4 Ray-path search algorithms

The purpose of a ray-path search method is to find all possible ray-paths from the transmitter to a receiver (or field observation point) within whatever constraints have been applied (e.g. those paths containing not more than a certain number and type of interactions).

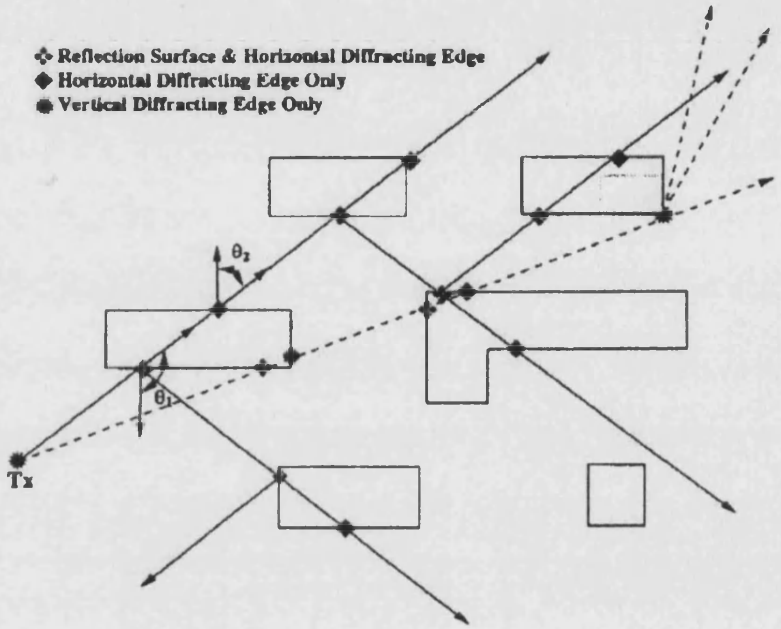

Figure 3.25: *Schematic illustration of the ray-launching procedure in the VPL method, (After Liang G. [187]).*

A ray-path search technique is based on the visibility criteria that describes what (other) potential interaction elements (building facets or edges) are visible to any (particular) interaction element. A building facet, F, is visible from the transmitter, Tx, if no object in the environment obstructs the Tx – F LoS.

A number of visibility approaches have been proposed as acceleration techniques for finding the ray-paths, e.g. [112], [117], [194, [297], [300], [310], [312], [316], [321], [332] – [336], all of them performing well under some conditions, but less well under others [336]. Comparisons of acceleration techniques are presented in [112], [117], [285], [310], [336]. Acceleration techniques coupled with parallel computing are discussed in [194], [300].

3.4.3.5.4.1 Visibility graphs technique

The visibility graph technique is used to identify all possible ray-paths between the transmitter and the receiver, either directly or via intermediate interaction points: wall reflection, edge diffractions, transmission through walls, multiple

reflections, multiple diffractions, combinations of reflections and diffractions, etc. [117].

The starting reference point for the generation of the visibility graph is the transmitter position. The visibility graphs contain several layers. The first layer includes all objects visible to the transmitter (for LoS rays). The second layer contains objects visible to the first layer. Further layers have a similar recursive relationship.

Visibility is symmetrical, i.e. if interaction element A is (totally or partially) visible to element B then element B is visible to A. Visibility relationships may be represented by undirected graphs [310]. Figure 3.26 shows an example of a visibility graph for diffracting edges in a hypothetical environment. Edges in the graph corresponding to adjacent walls are omitted.

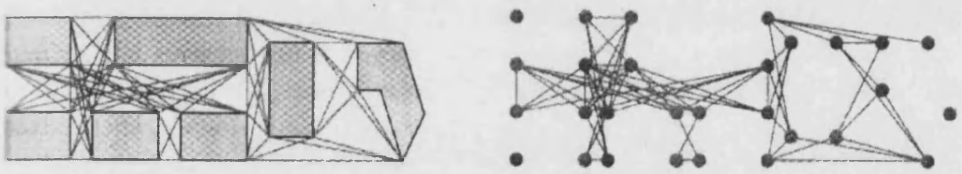

(a) (b)

Figure 3.26: *Example of visibility graph (a) physical (diffracting) ray-paths, (b) corresponding graph, (After Technical Committee, [310]).*

Algorithms to construct the visibility graph in the 2D plane are described in [117], [310]. Extensions to cope with dynamic visibility due to movement along a line are described in [337], [338].

Visibility graphs can be generated either prior to the ray-path search in a pre-processing step (and stored) or dynamically during the path search; the best approach depending on the size of the environment to be investigated and on the type and number of interactions to be analysed. The usage of a dynamic generation and data structure to store the visibility graph is described in [339]. In [340] a tree-like data structure is suggested, but no solution to the visibility problem is presented. The visibility graph is implemented in a number of propagation prediction models e.g. [117], [297], [332], [339]. A more detailed discussion of visibility graphs is given in [117], [310]. In order to generate the visibility graph, a polar sweep technique is commonly used [117], [310].

3.4.3.5.4.2 Polar sweep technique

The polar sweep (or sweep-line) technique [310], originates from computational geometry [316], [334]. The term plane sweep is used to characterize a paradigm employed to solve geometric problems by sweeping a line across the plane and halting at points where the line makes the first or last intersection with any of the objects being processed. At these points, the solution is partially computed, so that at the end of the sweep, a final solution is available. In other words, the polar sweep technique used to calculate the visible areas in such a way that the data

structures maintained during the iteration always reflect a consistent topological view of the environment [332], [310].

The polar sweep technique scans all objects contained in the different layers of the visibility graph to generate the objects in the next higher order layer. It is applied first from the transmitter position to find all objects it "sees" within the modelled environment (first layer). Then the process is repeated with the objects in the first layer using their respective reference points (as explained below) to compute the objects in the second layer, and so on. Figure 3.27 shows 2D illustration of the polar sweep algorithm.

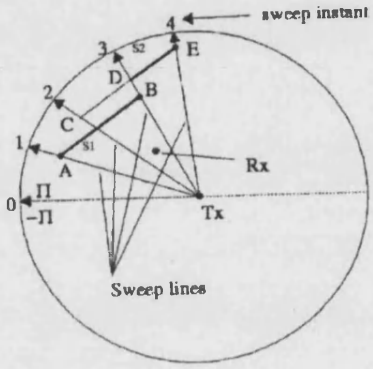

Figure 3.27: *2D illustration of polar sweep technique, (After Agelet F. A. [117]).*

In Figure 3.27, two linear segments (A – B and C – E) representing walls, and their corresponding endpoints (A, B, C, E) representing vertical edges, are shown. In order to produce an ordered list of visible interaction objects, a clockwise circular sweep is performed.

The first endpoint found is A (sweep-line 1), which belongs to segment S_1. This means that S_1 begins to be visible from this angular position. The next endpoint found is C, belonging to segment S_2. At this angular direction (sweep-line 2), a decision must be taken on which of the two segments is visible. In the case of Figure 3.27, it is decided that S_1 continue to be visible, since sweep-line 2 hits S_1 before S_2.

As the scan process continues, the next endpoint found is B. Since both ends of S_1 are visible, segment S_1 is deemed to be completely visible and is stored in the visibility graph. Now a decision must be taken on which object in the environment starts to be visible at sweep-line 3. In this case, segment S_2 begins to be visible (point D). The sweep process will end at point E, where segment S_2 ends. S_2 is partially visible, and thus it is stored in the visibility graph. The polar sweep technique continues to find the objects in the second layer of the visibility graph and so on [117]. A major drawback of the polar sweep method is that it does not account for the two adjacent edges of buildings [310] because the sweep line cannot perform in a full circle around the point of interest [339]. For instance, if the visibility area of a diffractive edge has to be calculated, the polar sweep is confined by two adjacent walls of the edge [310]. Detailed discussions of the polar sweep method are given in [117], [310, [316], [332], [334]. The running time of the polar sweep method is proportional to n log (n), where n is

the number of facets or edges. The memory requirement varies linearly with the number of facets or edges. The polar sweep algorithm is applied for propagation prediction modelling in [117], [332]. The polar sweep technique has similar drawbacks to the AZB method, i.e., when interaction levels are high, the establishment of the visibility graph will be much more time consuming and complicated [112].

3.4.3.5.5 Image illumination zone

First proposed by Athanasiadou et al. [288] the use of illumination zones [112], [288], [342], [343] reduces the number of images and computation time required to search for valid ray-paths by restricting each image to an '*illumination region*'. The illumination zone is the area for which an image can give a valid ray-path. In this technique each image is associated with a specific illuminated area, which is calculated and stored [288].

Only scattering surfaces within the illumination zone can be used for the formation of a new image and hence only objects inside this region are tested as to their ability to support a valid path. The basic concept of the illumination zone is extensively described in [100], [112], [288]. The illumination zones tend to become narrower as the images order increases [112]. Figure 3.28 illustrates the illumination zone concept. Tx' is the image of the transmitter, Tx, with respect to facet 1 and Tx" is a second-order image of Tx' with respect to facet 2. The receiver, Rx, is in the illumination zone of Tx".

3.4.3.5.6 Concluding comments and a new acceleration technique

Several visibility algorithms and modified sweeping techniques have been proposed to reduce computational complexity, time consumption and the memory requirements using pre-processing of the propagation environments [4], [112], [117], [285], [310], [321]. Other methods using visibility between transmitter, receiver and environmental objects can reduce the number of candidate objects to be tested [117], [291], [344]. These visibility based methods are usually transmitter/receiver location specific and the pre-processing procedure needs to be repeated for each transmitter/receiver location.

In Chapter 4 a new visibility-based acceleration technique is proposed. The technique is based on the formation of visibility matrices, which take into account all interaction elements (facets and edges) in the environment, and is independent of transmitter and receiver locations. The visibility matrix avoids unnecessary overlapping and interaction tests and is more efficient, and computationally faster, than those described above. To further minimise run time and avoid memory deadlocks, a distributed segmentation technique is applied. To the best of the author's knowledge this approach is not reported elsewhere in the literature.

The accelerating solutions related to ray-path searching described above are based on the idea that ray-tracing routines should be applied only to those areas where rays are likely to exist.

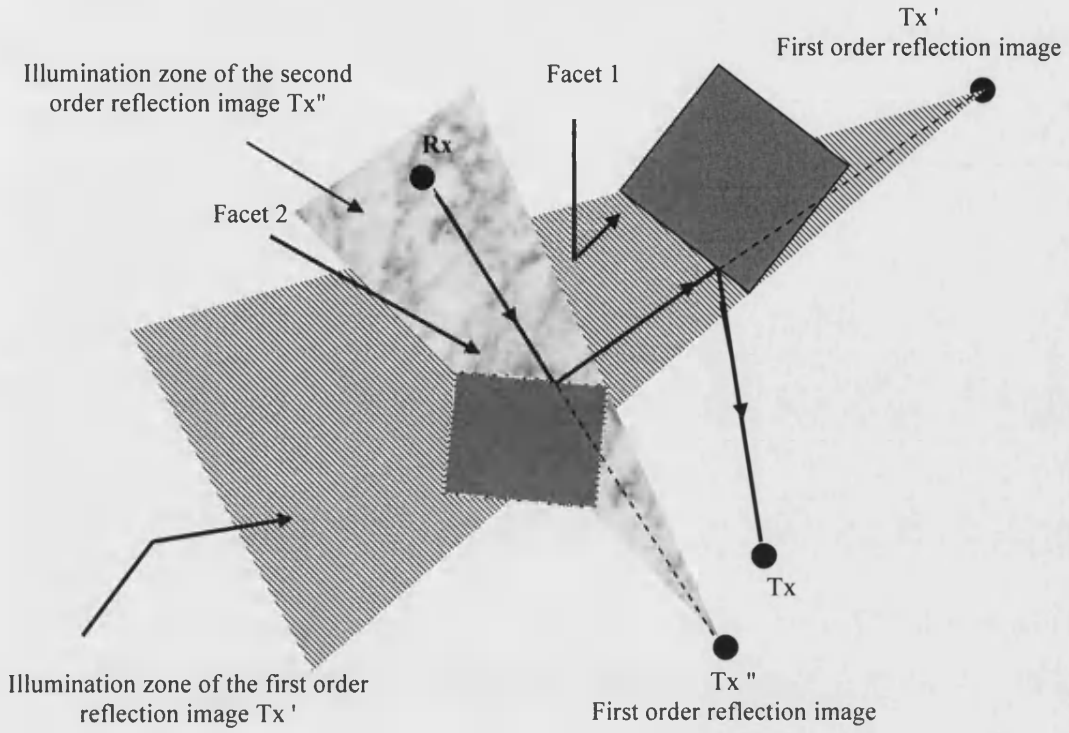

Figure 3.28: *Illustration of the illumination zones of the images: image generation and path tracing.*

3.5 Terrain and building databases

The performance of any deterministic propagation model depends on the accuracy and resolution of terrain and building database that it uses [120].

A detailed survey of high-resolution databases and host of commercial products is reported in [200]. In [2], several commercial graphical software packages, (e.g. SitePlanner, AutoCAD-drawing exchange format (DXF), geographical resources analysis support system (GRASS)) are described. These packages are able to include accurate representation of the building and terrain features and can be used as database managers for site-specific propagation prediction. Many packages are based on high-resolution data derived from USGS (United States Geological Survey) maps. In the UK digital ODSV (Ordinance Survey) maps are available.

Methods used to obtain raw information for databases include aerial photography, satellite remote sensing and photogrammetric techniques [2]. Photogrammetry was used, for example, to convert aerial and satellite photographs of the environment into usable 3D databases for the models reported in [185], [292], [325]. In [325], digital terrain models (DTMs) with superimposed building heights were used for propagation prediction [346]. Figure 3.29(a) shows a street map of a residential area in Malvern, UK, used in both ray-tracing simulations and a channel measurement campaign reported later in this thesis. Figure 3.29(b) shows the corresponding database. This is referred to as a pseudo-3D representation since the building elevations are set at their estimated mean height rather than accurately portrayed.

3.5.1 Database limitations

Terrain and building databases can never be a completely accurate representation of reality [2], [47], [53], [304], [333]. Limitations include:

1. Out of date information (databases are rarely completely up to date)
2. Coarse elevation information (poor building height precision and/or accuracy)
3. Limited spatial resolution generally
4. Coarsely estimated electrical parameters (dielectric constant and conductivity)
5. Absence of building detail (e.g. roof shapes, doors, windows, garden vegetation)
6. Absence of street furniture (lampposts, road-signs etc.)
7. Absence of mobile scatterers (principally road traffic but in some cases, e.g. crowded concourses, pedestrian traffic)

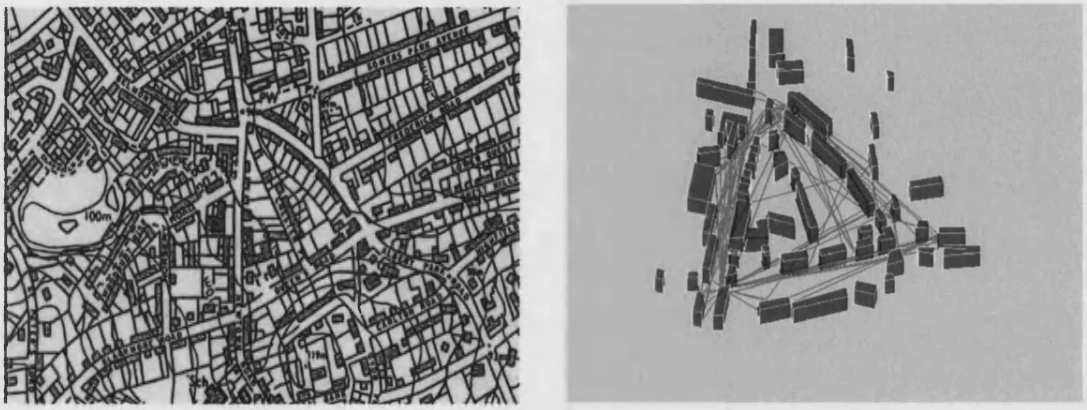

(a) (b)

Figure 3.29: *A residential suburban area of Malvern, UK*
(a) *Street map, (b) Corresponding pseudo-3D database.*

The effect of database accuracy on path loss predictions has been investigated by [291], [303], [323], [347]. These studies showed that predictions are more sensitive to errors in the location of buildings than to errors in building size. They also showed that errors were sensitive to electrical properties and, on occasion, building detail.

With respect to the specific question of required resolution [53] suggests that, as a rule of thumb, environment features of about an order of magnitude greater than the wavelength must be represented.

In [47], Parsons J. D. found that errors of up to 15 dB in microcells could be attributed to database inaccuracies.

3.5.2 Terrain and building modelling methods

Many site-specific propagation models have assumed a flat, underlying, terrain. Vu-Dinh and Lampard [348], and Parsons [47], however, have shown that even

moderate terrain undulation (valleys and hills) can modify channel characteristics significantly.

There are two fundamentally different ways to represent terrain. The first, easiest and most popular, is to use an array of elevations on a regularly spaced grid of points. This is known as a *digital elevation model* (DEM). The second is to use a set of triangular planar surfaces. This is referred to as a *triangulated irregular network* (TIN) [200].

One of the earliest attempts to incorporate the terrain (underlying building data) was made by Tameh et al. in 1997 [325] who used a DEM with superimposed building heights to make propagation predictions.

3.5.2.1 Digital elevation models

In [200], much information related to digital elevation models (DEMs) are reported, including a detailed survey of products and vendors. The DEMs described are derived from United States Geological Survey (USGS) maps. Their applicability and availability for the UK, therefore, is questionable.

The DEM data format is simple and easy to manipulate. DEMs suffer, however, from data redundancy when representing slowly changing terrain. (If spatial sampling is sufficiently high to avoid aliasing in rapidly changing parts of the terrain then it is over-sampled in more slowly changing regions.) DEMs do not usually include ground cover (either manmade or vegetation) and this must normally be added separately. Furthermore, DEM data is stored in raster format whilst most of the site-specific propagation prediction models require terrain to be represented in vector format.

3.5.2.2 Triangular irregular network models

The triangular irregular network (TIN) model was developed in the early 1970s as a simple way to build a terrain from a set of irregularly spaced points. It consists of a tessellating network of planar triangles based on irregularly spaced nodes [200]. Ideally no three nodes in a TIN model are collinear. The TIN is a vector topological structure since it is the node location vectors that are stored. The TIN implementation places a larger number of nodes in the areas of rough terrain and fewer nodes in smooth terrain. The areas with relatively flat terrain are thus modelled by large triangles and areas of rougher terrain are modelled by smaller triangles. This makes the TIN model very efficient in terms of database size. As the number of surfaces must be modelled to represent the terrain decrease, the computational complexity of the propagation model also decreases. The TIN model is, therefore, a good candidate for the site-specific propagation prediction software [200].

Unlike DEM data, which is readily available from different vendors (e.g. UK Ordinance Survey maps) terrain data is not readily available in TIN format. Typically TIN data must therefore be converted from DEM data. [200] gives an evaluation of the different conversion techniques available.

3.5.2.3 Conversion from DEM to TIN format

Several algorithms for converting DEMs into TINs have been proposed [200]. Firstly, the '*significant*' points are selected from the DEM which then become the nodes of the TIN. Significant points are those that are especially useful in describing the terrain, bringing out its salient topological features. (A variety of algorithms have been proposed to do this with minimal loss of information about the terrain e.g. the Fowler and Little algorithm and the very important point (VIP) algorithm [200].

Secondly, the significant points are interconnected to form the triangles of the TIN. This process is called *triangulation*. Several triangulation algorithms are reported in the literature e.g. [200]. The Delaunay, radial sweep, iterative Delaunay and hierarchical triangulation are probably the most widely used. Different triangulation algorithms differ from each other in the number, and quality, of triangles created for a given set of points and in their computational complexity. The quality of the triangles is generally measured by the maximum distance of any point inside a triangle from a vertex [200]. The resultant network should ideally contain short fat triangles (as close to equilateral as possible) as opposed to long thin triangles. Since the computational complexity of the propagation model increases exponentially with the number of triangular surfaces, the number of triangles should also be minimised. Figure 3.30 shows the TIN representation of terrain.

3.5.2.4 Data formats for buildings

Like terrain, buildings can be represented in raster or vector formats. The raster format typically requires greater memory than the vector format and most ray-tracing software implementations have therefore used the latter [200], [320], [349].

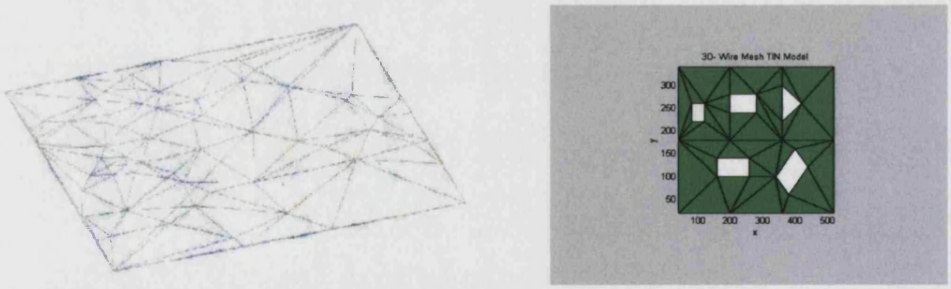

(a) (b)

Figure 3.30: *(a) The TIN representation of a real terrain using Delaunay based triangulation algorithm, (After Sheethalnath P.T. [200]), (b) Plan top view of example TIN terrain model.*

The vector format specifies the boundaries of a vector space used. Edges, for example, are specified by the location vectors of a pair of point (one start point and one end point) and surfaces are specified by location vectors of its (polygonal) vertices.

A detailed description and comparison of the raster and vector formats is contained in [200].

3.6 Review of ray-tracing tools

The Wireless System Engineering (WISE) tool represents one of the first ray-tracing tools for operational design of cellular and indoor systems. It was originally developed as a 2D model by AT&T's Bell laboratories in 1994, [289], [330]. The model is capable of up to 10 reflection and 2 diffraction interactions respectively. The prediction errors for an outdoor environment have been reported to be within 6 dB for both mean and standard deviation [318]. WISE was later enhanced for 3D propagation by [330], [350]. Different heights of the vertical buildings were considered with flat terrain and roof-tops. The model accounts for multiple reflection by building walls and roofs, and multiple diffracted rays by vertical and horizontal edges of buildings.

The FiPre model [351], developed at Eindhoven University of Technology (EUT), is a 3D model similar in capability to WISE.

The research group of the University of Karlsruhe have reported a number of ray-tracing models including 3D-IHE for macro-cells [320], 2D-URBAN-PICO [352] and 3D-IHE-URBAN-MICRO [353]. The 3D-IHE-URBAN-MICRO model was developed for urban microcellular environments in the 300 MHz to 3 GHz frequency range and can handle transmit antenna heights above, as well as below, roof-top level. It predicts field strength and CIRs for arbitrary selected receiver locations. Comparison between simulated and measured results showed generally good agreement although the model was found to be deficient in accounting for some, occasionally significant, ray-paths.

Rizk et al. of the Swiss Federal Institute of Technology, have reported a number of 2D and 3D ray-tracing models, based on method of images [120], [291], [249], [303], [304] [323], [347]. These models assumed flat terrains and flat roof-top of the buildings and capable of multiple reflection by the vertical walls of the building, and multiple vertical and horizontal diffraction from the building edges. For example, in [120], the effects of varying the reflection coefficient and the influence of various diffraction coefficients were analysed.

In [23], [354] – [358], El-Sallabi et al. reported 3D VPL wideband ray-tracing models based on method of images for urban microcellular street grids such as parallel, perpendicular and crossing streets.

Roof-top diffraction was not considered in the models. Omni-directional antennas were used with vertical and horizontal polarisations. The transmitting and receiving antennas were maintained at the heights of 13 m and 1.8, respectively. In order to predict the multipath mobile radio channel, each path is characterised in terms of its amplitude, phase, power, time delay, and angular information, respectively. The ray characteristics were given in terms of complex amplitude for both vertical and horizontal polarisations, path length, angle-of-arrival (AoA) and angle of departure (AoD). Their models provide information

of mean field strength, complex channel impulse response (CIR), power and RMS-DS.

The measurements were carried out in the city centre of Helsinki, Finland at six different routes. Their models were validated through comparison between the measured and simulated results. The measured and simulated CIRs were obtained with a spatial resolution of 0.5 m. Their comparison results show better agreement between measurements and simulations. Figure 3.31(a) and Figure 3.31(b) shows comparison plots of measured and simulated power and RMS-DS for parallel streets along the route, respectively. The maximum received power along the route 2 (crossing street) was -39 dBm in the LoS region, with a minimum value of about -80 dBm in the deep shadow region. The measured and simulated results are shown in Table 3.2.

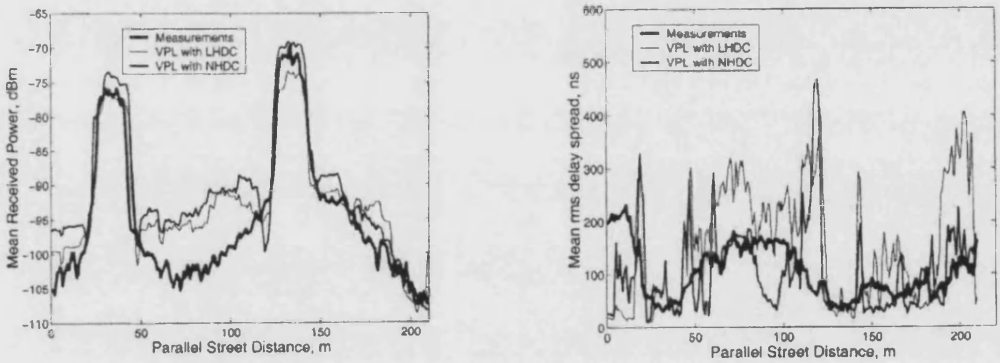

Figure 3.31 :*(a) Power and (b) RMS-DS, (After El-Sallabi H.M. [355]).*

In [357], it is shown that as the reflection interactions increases the probability of its occurrence decreases. Higher values of RMS-DS were observed at locations when Tx and Rx were close to each other. It is also observed that the ray-tracing model can predict RMS-DS to acceptable accuracy statistically but not at every Rx location. In [23], [355], [356], reported the influence of different diffraction coefficients and different electrical properties of building walls on power and RMS-DS. They showed that the prediction of RMS-DS has no statistically significant difference with different diffraction coefficients; however, it is shown that the propagation characteristics changes with different electrical properties of building walls. They also showed that the building shapes (vertical edge shapes) have an important role in accurately predicting both received power and RMS-DS.

To the best of authors knowledge, the centre for communication research (CCR) of the University of Bristol, is the leading research group active in the development of site-specific ray-tracing models [4], [100], [101], [265] - [267], [280], [288], [289], [325], [342], [343], [359] – [361].

Anderson and McGeehan have reported 2D ray-tracing models at 1.870 GHz frequency band. Their models are based on method of images [101], [265], [266].

In [266], Anderson and McGeehan have examined the influence of number of ray-paths (reflected or diffracted) and electrical properties of the building walls on the received signal and RMS-DS. They observed that the number of reflected and diffracted ray-paths significantly affect the signal variability, RMS-DS and computational efficiency of the ray-tracing models. They suggests that if the computational time for more reflected and/or diffracted ray-paths only produces marginally better results, then it may not be worth to incur the additional computational burden. They have also analysed the influence of different combinations of the electrical properties (conductivity and permittivity) and shown that the signal can vary by more than 30 dB from the signal level of reference material. The reference conductivity and relative permittivity was chosen as σ= 0.01 S-m and ε_r = 10, respectively. It was observed that the direct (LoS) ray-path from the Tx dominates the signal strength. The most pronounced changes in RMS-DS values occurred at some locations in the LoS areas where the RMS-DS values were found low under the reference conditions of the electrical properties. It was shown that at these locations the relative amplitude of long-delayed, low amplitude ray-paths is insignificant to the RMS-DS value which is controlled by the few strong amplitude ray-paths. Discontinuities in the generated ray-paths were observed in deep shadow areas. At some points the simulated plots were artificially set to zero when no ray-paths were available to compute RMS-DS values.

In [343], Lawton and McGeehan have reported a 2D ray-tracing model for small cell environment (British Telecom Labs). Reflection, diffraction and transmission were taken into account. The model was validated with the three field trial measurements. Variations in the peaks of measured and simulated PDPs were observed along the routes. Inaccuracies in the simulated results were observed as the Rx has moved into deep shadow areas because the model is unable to generate enough ray-paths to produce accurate RMS-DS values. In addition, inaccuracies also exist between the measured and simulated results which have arisen as a result of the simplifications of the modelled database of the environment. The comparison between the measured and predicted RMS-DS demonstrated reasonably fair agreement (see Table 3.2).

Athanasiadou et al., reported 2D and 3D ray-tracing models [100], [288], [342], [344], [362]. For example, in [288] Athanasiadou et al. reported 3D ray-tracing model for microcellular university campus environments at 1.823 GHz frequency band. These models were based on a hybrid technique where the building database was held in 2D but the ray-tracing engine was operated in 3D. The models used '*illumination zones*', which drastically reduced the size of the image tree. The concept of the illumination zones was described in Section 3.4.3.5.5. The test environment was considered flat. The building database was extracted from the UK Ordinance Survey landline database. The simulated area was approximately 500 x 500 m^2 with 438 external walls. All building walls were assumed same electrical properties (εr = 5, σ = 0.005 Sm-1). Anthanasiadou et al. have examined: 1) the sensitivity of the model to the input database, 2) the sensitivity of the model to the maximum permitted orders of reflection and diffraction interactions, 3) the sensitivity of the model to the electrical properties of the wall material, 4) the sensitivity of the model to the antenna positions at the

boundaries of the LoS, NLoS, and deep shadow locations, and 5) the statistics of the number of rays.

The simulated results were shown for 5 reflection interactions and 1 diffraction interaction. In order to investigate the sensitivity of the model, results were compared for 3, 5, 7 and 9 interactions of reflections and 1 diffraction interaction. The models produced the complex CIR, received power, and RMS-DS for three Rx locations (one LoS and two NLoS) and along the route in the environment. Figures 3.32 and 3.33 shows simulated plots of the valid ray-paths and PDPs for the Rx locations 1 and 2.

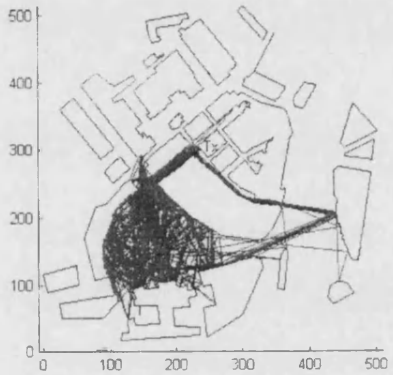

Figure 3.32: *Graphical display of the simulated ray-paths for the Rx location 2, (After Athanasiadou G. E. [288]).*

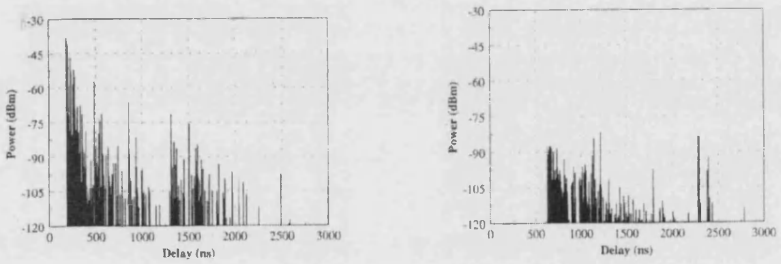

(a) (b)

Figure 3.33: *Simulated PDPs (a) LoS Rx location 1 (~ 55 m away from the Tx, (b) NLoS Rx location 2 (~ 155 m away from the Tx), (After Athanasiadou G. E. [288]).*

Three successive measurements were taken at the three Rx locations and along the route. Anthanasiadou et al. showed that, it is not necessary to obtain the same shape of PDPs and same values of RMS-DS of successive measurements along the same route. Each set of measurement shows considerable variability in the shape of PDPs and values of RMS-DS from point-to-point along the route, due to the fact that the measurements were taken at same location at slightly different times. They observed several disagreements between the set of measurements with differences in the values of RMS-DS up to 54.83 ns. Based on their observations they proclaimed that it is not true to assume the measured data to be 'correct' and attributes all errors to the modelling process. They suggest that only

repeatable characteristics of the radio channel can be predicted and only feasible agreement can be achieved between the results through the average measured and simulated values.

The measured and simulated results were obtained at the spatial resolution of 0.5 m. In order to evaluate the accuracy of the model comparisons, measurements were performed for a variety of scenarios. The received power at the Rx Location 1 was found -32.96 dBm, approximately 6 dB higher than the power of the direct path, since the strong reflected ray-paths also contributed to the total signal level. The received power at the Rx Location 2 was found between -69.59 dBm to -150 dBm, approximately 13.5 dB higher than the power of the strongest ray. The RMS-DS was calculated within a 30 dB power window from the strongest ray-path of the PDP. The power window is used in order to prevent long delayed ray-paths raising significantly the RMS-DS values, when in reality they are too weak to impact the system's performance. The plots of RMS-DS were obtained, which showed significant fluctuations in the RMS-DS values. The higher values of RMS-DS in the NLoS locations (deep shadow areas) were found due to the significant contributions of all the relatively strong ray-paths of the PDP. Figure 3.34 shows the plot of the measured and simulated RMS-DS values along the route. The measured and predicted values of RMS-DS are shown in Table 3.2.

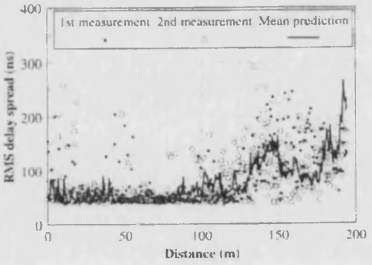

Figure 3.34: *Measured and simulated RMS-DS, (After Athanasiadou G.E. [288]).*

Similar models were also developed by Lee et al. at 2 GHz frequency band [4], [280], [363]. They showed that the shape of the PDP varies significantly due to phase variation of each individual ray-path for small displacement of the Rx location. It was also shown that, since the ray models cannot accurately predict arrival phase, perfect agreement between measured and simulated PDP cannot be achieved. For accurate predictions, the average PDPs and channel statistics along the short routes were performed. They also reported a general weakness of the ray-tracing model, i.e., the model failed to simulate the most significant ray-paths, if the Tx is placed in the shadow areas of large building(s). Comparisons between measured and simulated results were made; good agreement was obtained in terms of relative received power versus time of arrival.

In [216], [305], Zhang et al. proposed a 2D ray-tracing diffracting model in the horizontal plane for propagation prediction in a microcellular urban street grid environment. Their results showed that an increase in the number of rays may not enhance the accuracy of ray-tracing models. A number of measurements were performed in the city centre of Helsinki at 900.5 MHz and 1.8 GHz, respectively. The Tx height was 13.3 m and Rx height was 1.5 m. Comparison between measurements and simulation of published results validate the model. They

showed that the 2D model reduces the computation time significantly and overcomes the limitation and difficulty of existing techniques for multiple diffraction.

Tan et al. have reported ray-tracing models [276], [293], [294], [364], [365]. In [276], [364], Tan et al. reported ray-tracing models. In [364], Tan and Chua reported 3D ray-tracing model in a microcellular campus environment at 1.3 to 1.7 GHz bands. The building heights were assumed 16 m and 9.2 m, respectively. The transmitting antenna was placed on over roof-top (11 m and 18.3 m above the ground level) and receiving antenna height was maintained at 1.5 m above ground level. A network analyser was used to measure the frequency response of the channel. Multipath channel statistics were obtained. Comparison between measured and simulated RMS-DS was obtained for two receiver locations.

In [276], Tan et al. reported a 3D ray-tracing model that included double diffraction ray-paths from orthogonal edges i.e. roof-top edges followed by vertical edge of the buildings. Comparison between measured and simulated PDPs confirms the validity and applicability of the model.

Rossi et al. reported ray-tracing models [279], [292], [324]. In [279], Rossi and Gabillet reported a 3D model, 'geometrical ray implementation for mobile propagation modelling' (GRIMM) for urban microcellular environment. Due to the processing time and simplicity, the model can be considered for large areas typical of a cellular environment (3-km radius). The model accounts for reflection and diffraction. The predictions were made at 900 MHz, field strength, PDPs and RMS-DS were obtained. The comparison between measured and simulated results showed that the model can correctly estimate the channel parameters in about 76% of cases.

In [183], Rautiainen et al. reported a 3D ray-tracing model at 2.125 GHz. The maximum numbers of reflections and diffractions interactions for each ray-path were 3 and 2, respectively. It is observed that the number of interactions has a strong influence on the accuracy of the RMS-DS. The RMS-DS was found for two different Tx location, the one above roof-top level and the other below the roof-top level. The dependency of the accuracy on the number of reflection and diffraction intersections shows that consideration of double diffractions in 3D modelling is very important and leads to best accuracy. The measurements were carried out at 2 GHz by using a wideband radio channel sounder. Comparisons between measurements and simulations were made.

Durgin et al. reported ray-tracing models [123], [281], [317], [366]. In [366], Durgin et al. proposed a 3D ray-tracing model at 1.92 GHz frequency band. The modelled environment consists as the irregular terrain of Virginia Tech. campus, which includes hills, multi-story buildings and trees. Their prediction models account for reflection only. The position and amplitudes of multipath components were predicted very well with slight perturbations due to the accuracy of the computer database. A spread spectrum channel sounder was used with 140 MHz of bandwidth and 10 ns resolution. The measurement was conducted at 1.92 GHz in the environment at twelve different Rx locations.

Comparisons between measured and simulated results were made. Their results show good agreement between measured and simulated results (see Table 3.2).

In [300], Coco proposed a novel 2D ray-tracing procedure for the localisation of electromagnetic (EM) sources in microcellular urban environment in the presence of multipath propagation channel. Reflection and diffraction mechanisms were taken into account. A numerical experiment is also presented in order to show the applicability of the ray-tracing procedure to realistic situations.

In [299], Chen et al. proposed a 2D ray-tracing model based on progressive and approximate techniques at 900 MHz. The transmitting and receiving antenna heights were maintained at 10 m and 1.5 m above the ground level. The maximum numbers of reflection and diffraction interactions for each ray-path were 8 and 1, respectively. It was shown that diffracted rays are the main contributors to the received powers for shadow areas.

In [393], Chaves J. et al. reported a comparison study of propagation models for small urban environments at 900 MHz and 1.8 GHz. The influence of crossroads on the received power was analysed. The main aim of their study was to test the behaviour of received power at the two frequency bands. The average difference between the mean measured and simulated power values of the two bands was 7.8 dB and 9.3 dB.

In [309], an efficient combination of 2D and simple 3D ray-tracing was proposed. This approach can handle any distribution of buildings and vehicles in an urban environment. The prediction tool can investigate how vehicles affect the propagation loss and examine the effects of size, number, and location of the vehicles. (For most measurements of the propagation characteristics, Whitteker [367] and Xia et al. [135] - [138], such environmental effects were lumped together in the statistical characteristics of the data).

Several authors have reported specific studies, in order to examine the influence of various propagation mechanisms on the channel characteristics in urban LoS and NLoS environments [139], [185, [322], [368] - [372]. In [369], Rustako et al. conducted LoS propagation measurements at 900 MHz and 11 GHz to characterise micro-cell channel employing various antennas in different environments. They proposed measurement based 2-ray and 6-ray models to investigate the propagation mechanisms i.e. LoS (direct) path, ground reflected path, 2-rays with single wall reflection, and 2-rays with double reflections. The worst RMS-DS around 20 ns was predicted. It was shown that this low RMS-DS of LoS micro-cell may facilitate communications at higher digital signalling rates. Similar studies were conducted by [370], Xia et al. reported a model for LoS scenarios. They showed that when the heights of traffic (parked vehicles) and some obstacles are included in the model, better accuracy can be obtained compared with the experimental results. In case of urban NLoS areas, Papadakis et al. [322] showed that the urban rectangular street grid pattern has two important characteristics. The first characteristic is that after turning the corner, a sudden drop in received signal is observed. The second characteristics are that

there are significant distributions attributed to diffraction over roofs and building edges and to multiple reflections through the buildings.

Table 3.2 compares a range of microcellular propagation prediction models.

Similar studies in relation to the development of site-specific ray-tracing and measurement-based models for the microcellular urban and suburban environments appear in [75], [122], [133], [165], [181], [186], [195], [268], [290], [297], [312] - [314], [318], [320], [353].

3.7 Other deterministic methods

Several other deterministic propagation prediction methods have been proposed for a variety of different environment types.

3.7.1 Finite-difference time-domain

The finite-difference time-domain (FDTD) method has been proposed for application to cellular systems as an alternative to GO and UTD [110], [115]. FDTD is numerical method capable of the direct solution of Maxwell's equations in the time domain. It fully accounts for the effects of reflection and diffraction. The advantages of the FDTD method are its accuracy and generality, and that it simultaneously provides a complete solution for all points in the simulated space. It requires large amounts of memory, however, to keep track of the solution at all locations. Its application to anything but pico-cells is problematic (because of the computational resources required). Nor is it appropriate for open areas containing few scattering objects [115]. FDTD has often been applied to simplified 2D indoor environments [109], [110], [386]. Some limited work on the application of FDTD to microcellular environments is reported in [109], [387], [388].

3.7.2 Method of moments

Models based on the method of moments (MoM) are reported in [388] - [390]. The solutions determined by MoM are numerically exact as long as the spatial segmentation used for the objects is small enough. Due to limitations of computer memory and CPU time, MoM is usually applied in environments comprising objects that are tens of wavelengths in size. By choosing structures with dimensions around a few wavelengths, however, MoM can be used to validate a ray-tracing program. A comprehensive review of MoM (and hybrid) models is given in [115].

3.7.3 Vector parabolic equation model

The vector parabolic equation (VPE) model allows a full treatment [115] of 3D electromagnetic scattering and has been applied to propagation modelling in urban environments. It is particularly useful for accurate modelling of scattering by a single building or by a group of buildings. Examples of its application in this context are presented in [115].

Table 3.2: *Comparison of microcellular propagation prediction models.*

Author (Ref., Year)	(Environment – Features)	Antennas heights (m)	f (GHz)	Results	
				Power (dBm)	τ_{RMS} (ns)
Anderson ([101],1994)	Urban - 2D ray-tracing Reflection, Diffraction	Tx = 7.6 Rx = 1.6	1.870	-	Meas. 150 (Mean) Sim. 200 (Max.)
Lawton ([343], 1994)	British Telecom Labs- 2D ray-tracing Reflection, Diffraction	Tx = 2.5 Rx = 1.5	-	-	Meas. Site 1, 3: 60 – 250, Site 2 : 40 – 130 Site 1: 130 (Med) Site 2: 70 Med) Site 3: 120 (Med)
Athanasiadou ([288], 2000)	Campus- 3D ray-tracing 5-Reflection, 1-Diffraction	Tx = 3 Rx = 1.5	1.823	Meas. - Sim Min: -69.59 Max: -150 Rx 1: -32.96 Rx 2: -69.36	Meas. 54 to 289 Sim. 900 (Max.) Rx 1: 43.92 (LoS) Rx 2: 624.59 (Max.-NLoS)
Lee ([4], 2002)	Urban-3D ray-tracing 5-Reflection, 2-Diffraction	Tx = 1.6 Rx = 1.7	1.920	Meas. - Sim. Rx 1: 29.34	Meas. - Sim. Rx 1: 19.88
Schaubach ([185], 1992)	Campus- Virginia Tech Reflection only	Tx = 10 Rx = 1.7	0.914	-	Sim. 127. 8 (LoS) T-R = 170 m
Seidel ([194], 1993)	Campus- Virginia Tech Refection, Diffraction	Tx = 7.6 Rx = 1.7	1.9	-	Meas. 23.2 Sim. 44.8
Durgin ([281], 1997)	Campus- Virginia Tech 3D ray-tracing Reflection only	Tx = 3 Rx = 1.5	1.9	Sim. -56.8 dBm	-
El-Sallabi ([354], 2003)	Urban-street 3D ray-tracing Reflection, Diffraction	Tx = 13 m Rx = 1.8 m	2.154	Sim. Max. -39 (LoS) Min. -80(NLoS)	Meas. Route 2: 41.3 (Mean) Route 6: 251.2 (Max.) 100.5 (Med)

3.7.4 Waveguide model

In large metropolitan areas containing many tall buildings where transmitting and receiving antennas are located well below roof-top height the city streets form a waveguide-like structure. The analytical modelling of street propagation as a 3D multislit waveguide has, therefore, been proposed [115]. Assuming the screens and slits are Poisson distributed, the statistical propagation characteristics in such a waveguide can be expressed in terms of multiple ray fields. Algorithms for path-loss have been presented, and compared with experimental data, in the previous reference.

3.7.5 Hybrid methods

Hybrid techniques combine ray-tracing with the other methods. The objective is improved accuracy without undue sacrifice of computational efficiency [391]. In [365], Tan et al. a hybrid method combining method of images with ray-launching is proposed. Ray-launching is used to quickly identify possible ray trajectories. When these approximate trajectories are found the set of objects

involved can be determined. More precise ray trajectories are then found using the image method.

In [391], a hybrid method based on combining a ray-tracing with FDTD is proposed. Ray-tracing is used to model open areas and FDTD is used to model the regions close to structures with complex material properties.

A hybrid model based on MoM and ray-launching is described in [392].

3.8 Conclusion

This chapter has presented a comprehensive review and literature survey of existing work relevant to propagation prediction modelling and methods with an emphasis on wideband modelling using ray-tracing.

Chapter 4: A Ray-Tracing Tool: 3D MRT-1

4 Introduction

Ray-tracing is a deterministic propagation prediction method. Its routine use has been made possible, relatively recently, by advances in the power of personal computers. If site-specific field prediction is needed, and the necessary detailed databases are available, then ray-tracing is probably now the technique of first resort and can be considered as an alternative to time consuming field trial measurements.

This chapter presents a new 3D, wideband, ray-tracing propagation prediction tool (3D MRT-1) for the characterisation of the dispersive mobile radio channel in microcellular environments. The chapter begins (Section 4.1) with a specification and description of the most important features of the tool. Section 4.2 summarises its principal capabilities. Section 4.3 defines the top-level software structure and Section 4.4 presents a description of the individual algorithms and subroutines. A small number of the subroutines at the periphery of 3D MRT-1 remains incomplete but this does not affect the core ray-tracing functions.

4.1 The new ray-tracing tool

The model is based on geometric optics (GO) and the uniform theory of diffraction (UTD). A novel format has been developed for the 3D representation of the environment (terrain plus buildings). A transmitter and receiver can be arbitrarily located anywhere within this environment. The method of images is used to find ray-paths between a transmitter and receiver that satisfy (precisely) Snell's laws of reflection and a transmitter rotation rule based on Fermat's theorem is used to find diffracted paths. A *'visibility matrix'* is used to avoid the calculation of obscured ray-paths. The visibility matrix algorithm runs once only for each environment.

In order to reduce computational complexity, reduce processing time and avoid memory deadlocks, a new accelerated distributed partitioning and segmentation technique has been developed and implemented. A novel *'filter paths'* algorithm is used to identify and eliminate any invalid ray-paths and an *'equivalent sources'* algorithm is used to find the amplitude, phase, polarisation, angle-of-departure (AoD), angle-of-arrival (AoA), optical path length and received field strength for each valid reflected or diffracted ray-path.

The ray-tracing tool is demonstrated using Matlab. (An operational/commercial version of the tool would, of course, be implemented in a more efficient programming language such as C.)

4.2 Model capability

The model can be applied to:

1. Any terrain (consistent with being synthesised by a set of plane, tessellating, triangles)
2. Any building heights, shapes and orientations (consistent with being synthesised from a set of plane tessellating polygons)
3. Any terrain and building electrical properties
4. Any frequency (consistent with the fundamental approximations inherent in GO)
5. Any antenna types and polarisations (as defined by their radiation patterns)
6. Any antenna locations (in x, y, z)
7. Any antenna orientation (θ, φ)

3D MRT-1 output includes received power (RP), transmission loss (TL), channel impulse response (CIR), power delay profile (PDP), average delay spread (AV-DS) and RMS delay spread (RMS-DS).

4.3 Software structure

The top-level structure is shown in Figure 4.1. The ray-tracer is composed of several procedures, sub-procedures and functions. The structure is divided into two parts; one for reflected paths and the other for diffracted paths. A breakdown of the most important procedures and their corresponding sub-procedures is shown in Figures 4.2 - 4.5. The subsequent sections of this chapter describe individual algorithms.

4.4 Algorithm descriptions

The principal algorithms and subroutines used in 3D MRT-1 are described below.

4.4.1 Modelling of physical environment

Two environment definition formats (raster and vector) have been reviewed in Chapter 3 (Section 3.6.4). Site-specific ray-tracers usually use a vector format because these are more economical in storage requirements compared to raster formats. In this thesis a new vector format is developed and implemented to model the environment. The new format is conceptually simple (and therefore easy to use) and flexible. The following sections describe the software routines used to model the terrain and building databases.

4.4.1.1 POLY_ENV

POLY_ENV (Block 1, Figure 4.1) is a collective name of the physical environment containing natural terrain database and the building database.

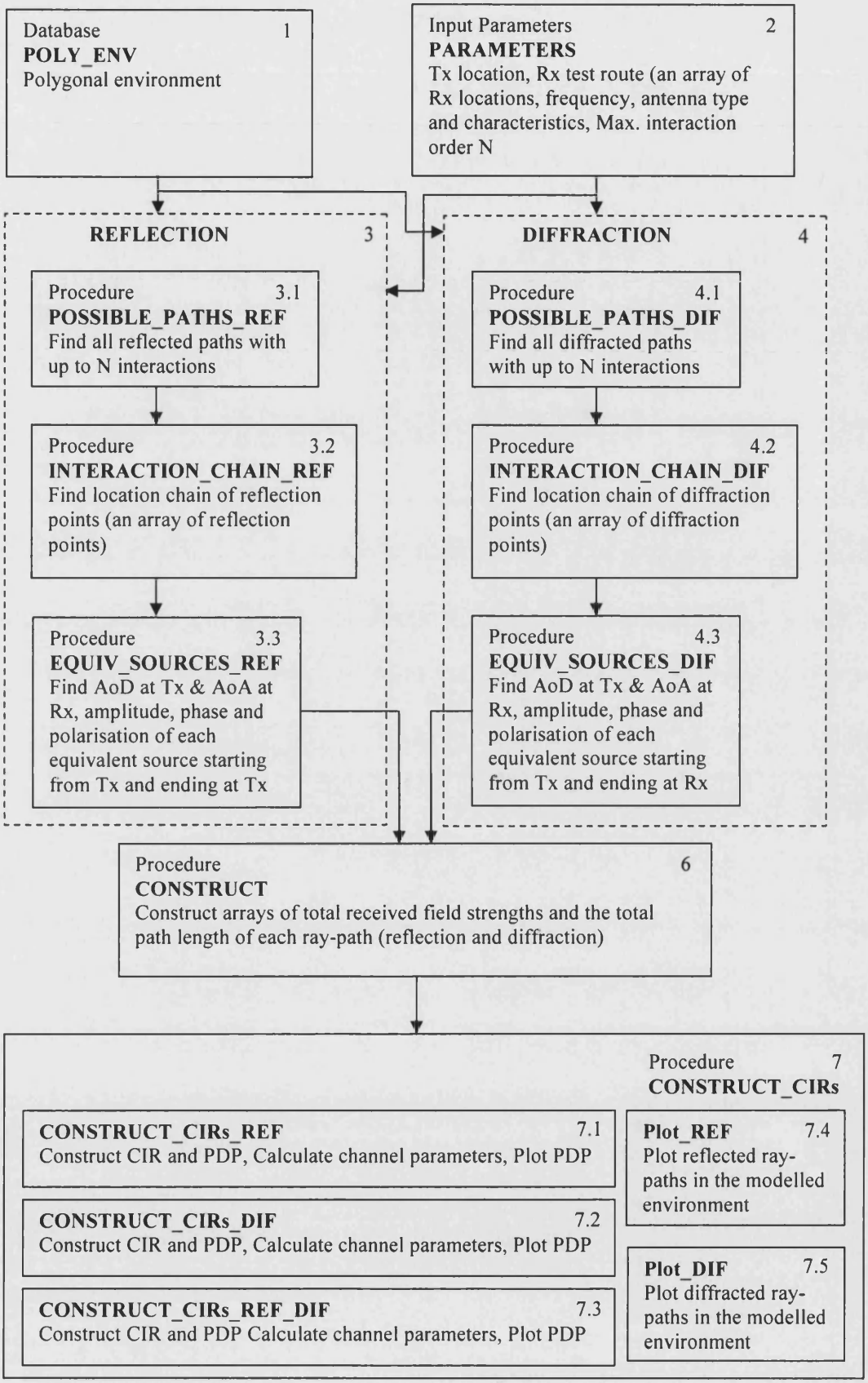

Figure 4.1: *Top-level structure of the ray-tracing model.*

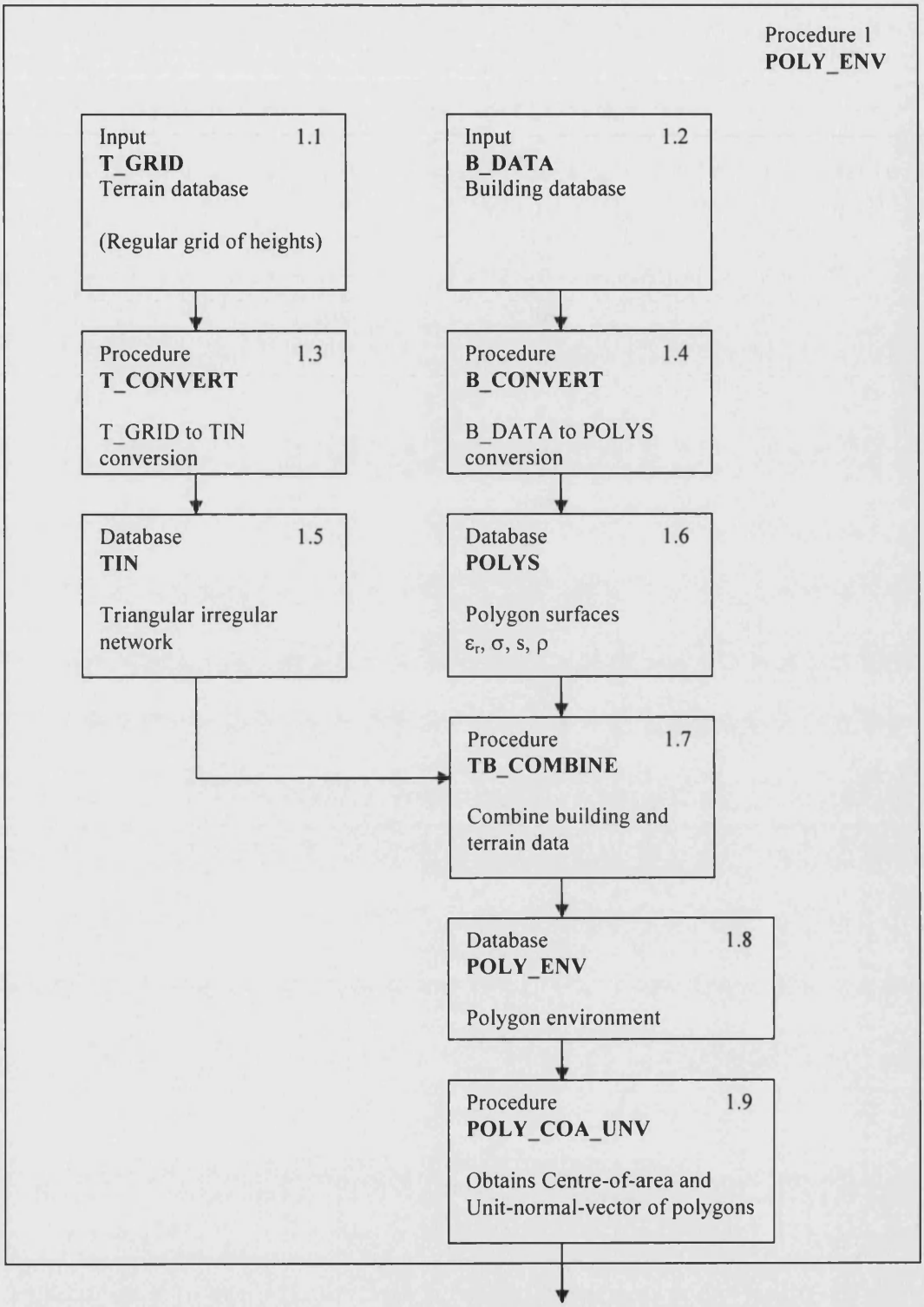

Figure 4.2: *Poly_ENV sub-structure.*

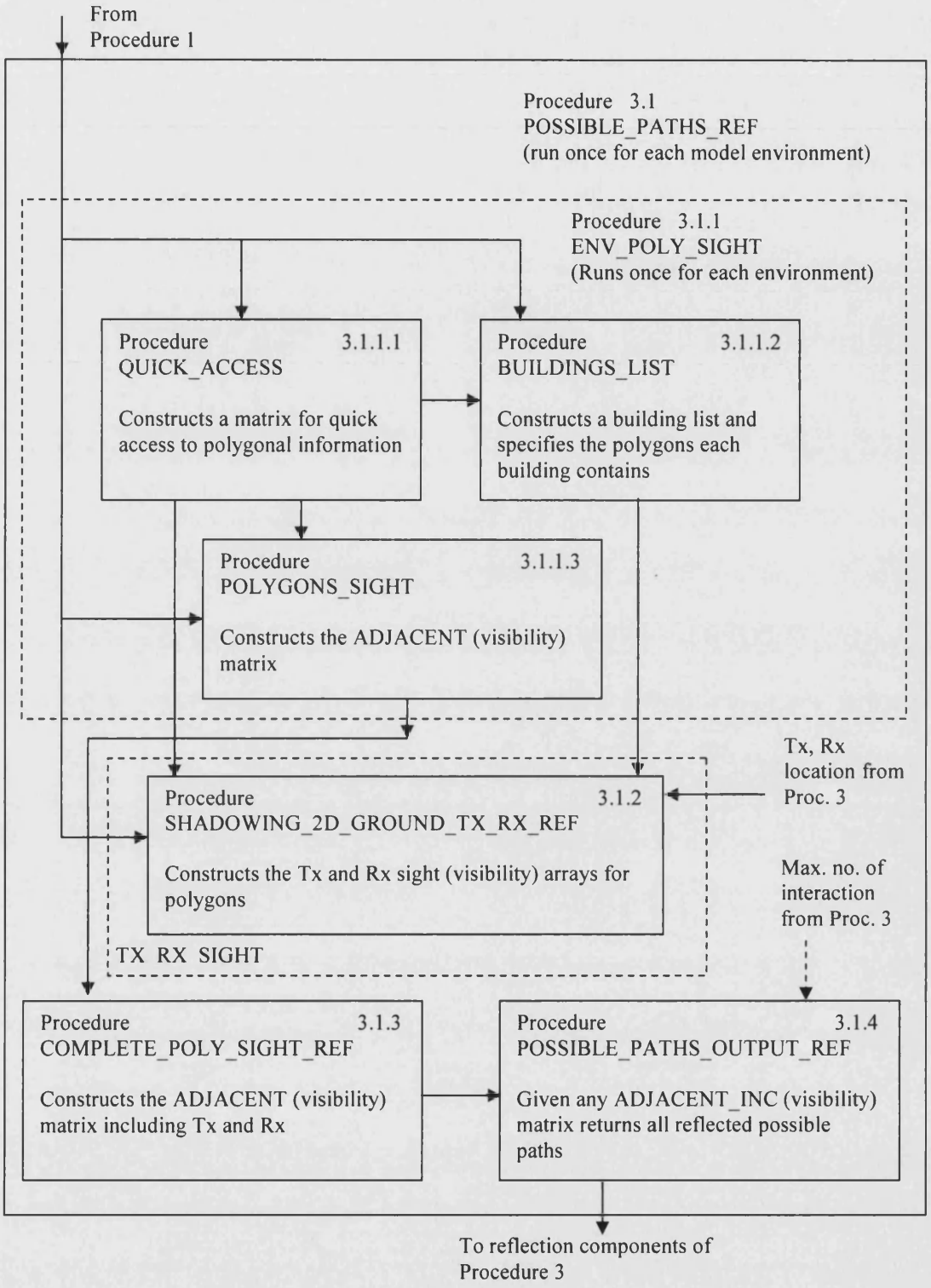

Figure 4.3: *POSSIBLE_PATHS_REF sub-structure.*

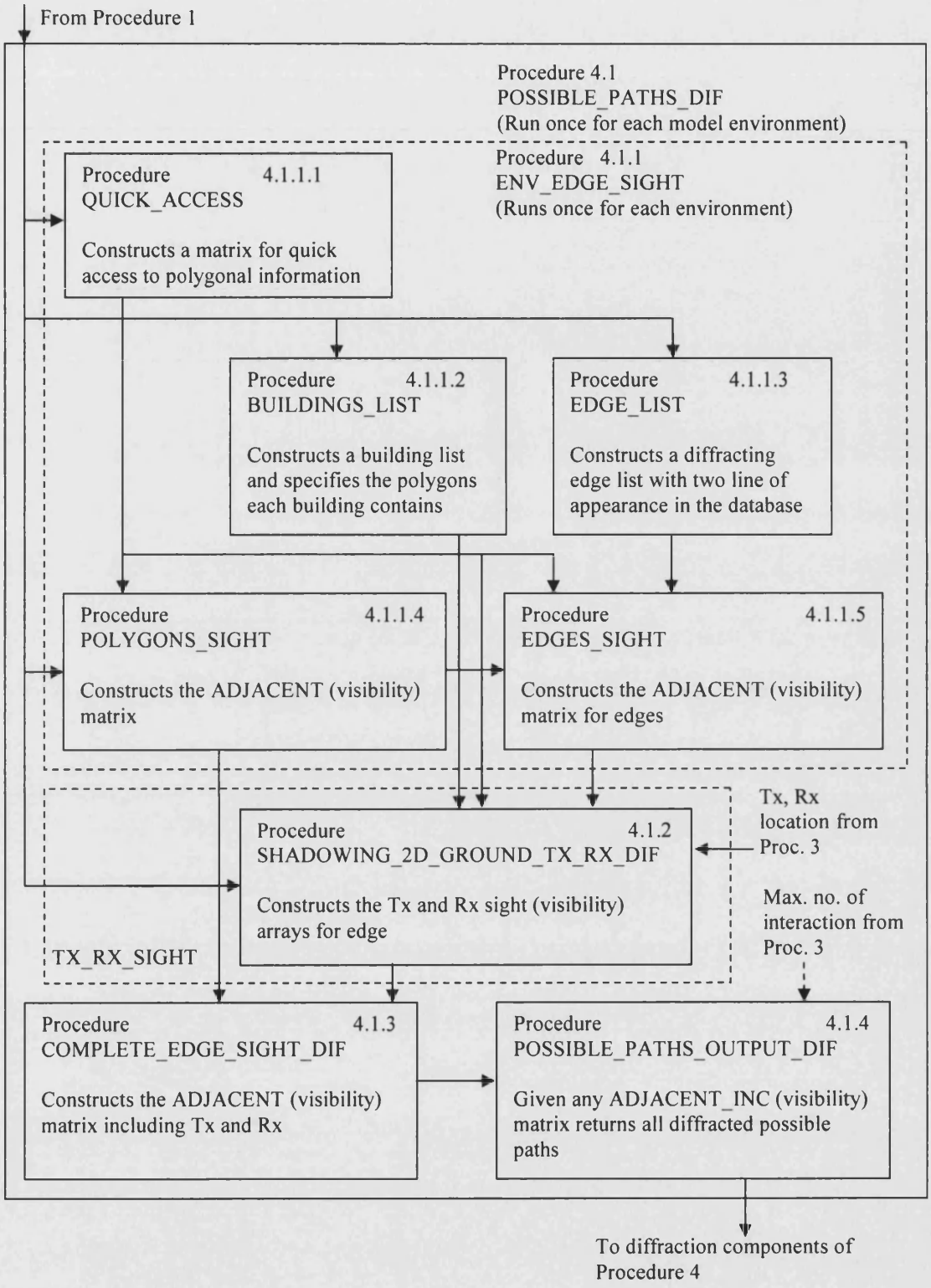

Figure 4.4: *POSSIBLE_PATHS_DIF sub-structure.*

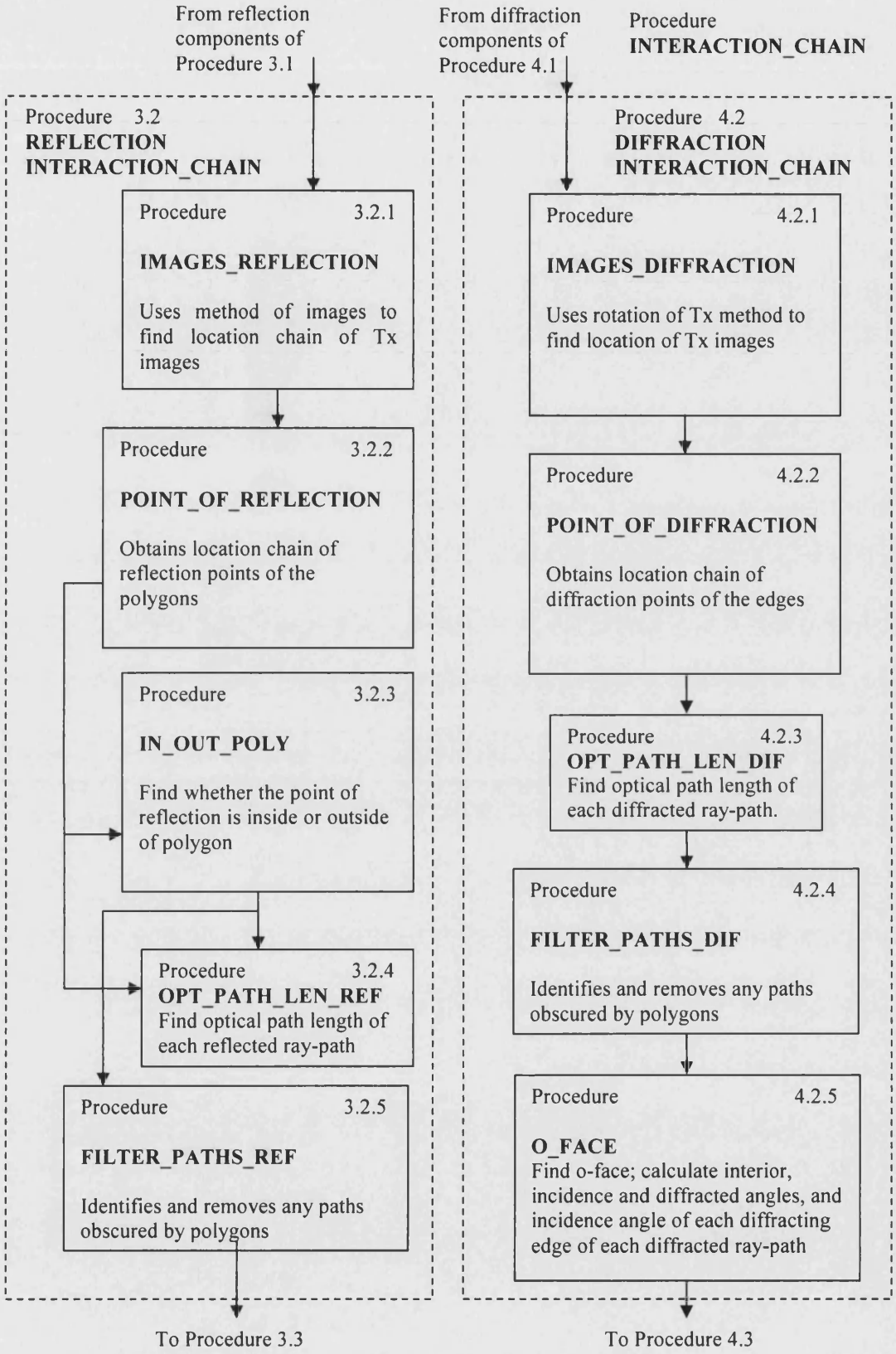

Figure 4.5: *INTERACTION_CHAIN sub-structure.*

4.4.1.2 T_GRID

T_GRID (Block 1.1, Figure 4.2) is a commercial variety of DEM (digital elevation model) or digital terrain model (DTM) database. DEMs, DTMs and their corresponding data formats have been described in Chapter 3 (Section 3.6.2.1).

4.4.1.3 T_CONVERT

T_CONVERT (Block 1.3, Figure 4.2) is a procedure which converts raster T_GRID data into a triangular irregular network (TIN) format. TIN is an irregularly spaced set of terrain heights that form the corners of a set of tessellating triangles and is a common method for model natural terrains (see Chapter 3, Sections 3.6.2.2 and 3.6.3). The implementation of T_CONVERT is incomplete.

4.4.1.4 TIN

TIN (Block 1.5, Figure 4.2) is a database containing the environment terrain model. It is composed of a set of tessellating triangular facets. Each facet is defined by three edges. Each edge is defined by a pair of points; one start point and one end point. The physical and electrical characteristics of each facet are defined in the database. Table 4.1 specifies the TIN database file format.

Table 4.1: *TIN database format (modelling terrain.)*

1	2	3	4	5	6	7	8	9
DT	N_P	N_E						
0	1	0	ε_r	σ	S	ρ	-	-
0	1	1	x_1	y_1	z_1	x_2	y_2	z_2
0	1	2	x_1	y_1	z_1	x_2	y_2	z_2
0	1	3	x_1	y_1	z_1	x_2	y_2	z_2
0	1	-1	x_1	y_1	z_1	x_n	y_n	z_n
0	2	0	ε_r	σ	S	ρ	-	-
0	2	1	x_1	y_1	z_1	x_2	y_2	z_2
0	2	2	x_1	y_1	z_1	x_2	y_2	z_2
0	2	3	x_1	y_1	z_1	x_2	y_2	z_2
0	2	-1	x_1	y_1	z_1	x_n	y_n	z_n
0	3	0	ε_r	σ	S	ρ	-	-
0	3	1	x_1	y_1	z_1	x_2	y_2	z_2
0	3	2	x_1	y_1	z_1	x_2	y_2	z_2
0	3	3	x_1	y_1	z_1	x_2	y_2	z_2
0	3	-1	x_1	y_1	z_1	x_n	y_n	z_n
etc.	-	-	-	-	-	-	-	-

In Table 4.1, column 1 represents data type (DT), 0 indicating a terrain triangular facet, column 2 is facet number (N_P) and column 3 is facet edge number (N_E). The special edge number 0 indicates that columns 4 to 7 contain the facet's relative permittivity, ε_r, conductivity (S/m), thickness (m), and surface roughness (m), respectively. The default thickness for a terrain facet is 1000 m. The surface roughness is the standard deviation (m) of terrain surface measured normally from the facet plane. Edge numbers 1 to 3 (column 3) indicate that columns 4 to 6 contain the cartesian coordinates (x_1, y_1, z_1) in metres of the edge-start-point

and columns 7 to 9 contain the cartesian coordinates (x_2, y_2, z_2) in metres of the edge-end-point. The special edge number –1 (column 3) indicates that columns 4 to 6 contain the cartesian components (x_l, y_l, z_l) in metres of the facet location vector (i.e. the position vector defining the facet's centre-of-area). Columns 7 to 9 contain the cartesian components, (x_n, y_n, z_n) in metres of the facet's surface unit normal vector.

The following algorithm is used for uniquely ordering the terrain facets making up the TIN database.

(i) **Ordering of terrain facets**
Choose that (those) containing edge-end-point with minimum value of z. If more than one facet exists with same minimum value of z then choose that (those) with minimum value of y. If more than one facet exists with the same minimum values of z and y then choose that (those) with the same minimum value of x.

(ii) **Ordering of facet edges**
Choose the facet corner with a minimum value of z. If more than one corner exists with the same minimum value of z then choose that (those) with a minimum value of y. If more than one point exists with the same minimum values of z and y then choose that with the minimum value of x. Number the corners 1, 2, 3 starting at the chosen corner and moving anti-clockwise looking in the direction of the facet unit normal (i.e. using a right hand rule around the facet normal vector). Edge 1 is that connecting corner 1 and 2. Edge 2 is that connecting corner 2 and 3. Edge 3 is that connecting corner 3 and 1 (see Figure 4.6).

(iii) **Ordering of edge points**
The start point (Point 1) of edge 1 is at corner 1. The end point (Point 2) of edge 1 is at corner 2. The start point (Point 1) of edge 2 is at corner 2. The end point (Point 2) of edge 2 is at corner 3. The start point (Point 1) of edge 3 is at corner 3. The end point (Point 2) of edge 3 is at corner 1.

Figure 4.6 illustrate an example of a single triangular terrain facet.

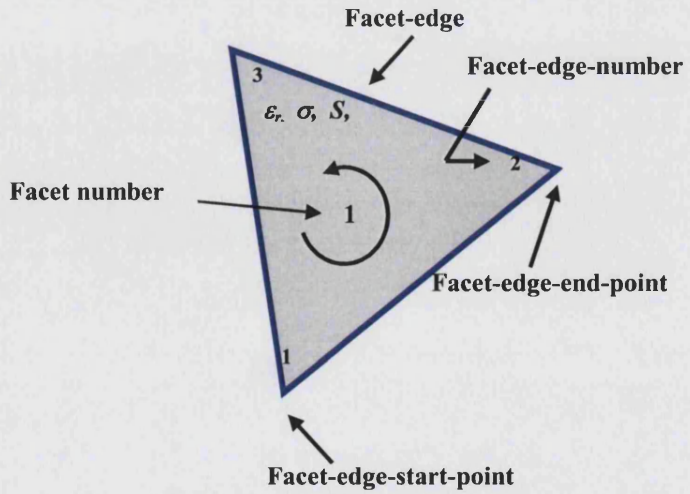

Figure 4.6: *Example triangular terrain facet.*

4.4.1.5 B_DATA

B_DATA (Block 1.1, Figure 4.2) is a commercial building database. It is, typically, raster formatted (e.g. AutoCAD-DXF).

4.4.1.6 B_CONVERT

B_CONVERT (Block 1.4, Figure 4.2) is a procedure which converts commercial raster building database format into vector building database format. This implementation of B_CONVERT is incomplete.

4.4.1.7 POLYS

POLYS (Block 1.6, Figure 4.2) is the database containing the model of buildings of the terrain cover, which specifies the walls and roofs of buildings as polygons. The buildings are represented by the external walls and roofs only (i.e. no internal structure of buildings is considered). Each wall is represented by a set of plane polygons defined by the coordinates of the polygon vertices. Each polygon is defined by a set of edges. Each edge is defined by a pair of points; one start point and one end point. The physical and electrical characteristics of each polygon are also defined in the database. Table 4.2 specifies the POLYS database file format.

Table 4.2: *POLYS database format (modelling buildings database.)*

1	2	3	4	5	6	7	8	9
DT	N_P	N_E						
1	1	0	ε_r	σ	S	ρ	-	-
1	1	1	x_1	y_1	z_1	x_2	y_2	z_2
1	1	2	x_1	y_1	z_1	x_2	y_2	z_2
1	1	3	x_1	y_1	z_1	x_2	y_2	z_2
1	1	-1	x_1	y_1	z_1	x_n	y_n	z_n
1	2	0	ε_r	σ	S	ρ	-	-
1	2	1	x_1	y_1	z_1	x_2	y_2	z_2
1	2	2	x_1	y_1	z_1	x_2	y_2	z_2
1	2	3	x_1	y_1	z_1	x_2	y_2	z_2
1	2	-1	x_1	y_1	z_1	x_n	y_n	z_n
1	3	0	ε_r	σ	S	ρ	-	-
1	3	1	x_1	y_1	z_1	x_2	y_2	z_2
1	3	2	x_1	y_1	z_1	x_2	y_2	z_2
1	3	3	x_1	y_1	z_1	x_2	y_2	z_2
1	3	-1	x_1	y_1	z_1	x_n	y_n	z_n
etc.	-	-	-	-	-	-	-	-

In Table 4.2, column 1 represents data type (DT); 1 indicating a building polygonal facet, column 2 is polygon number (N_P) and column 3 is polygon edge number (N_E). The special edge number 0 (column 3) indicates that columns 4 to 7 contain polygon relative permittivity, conductivity (S/m), thickness (m), and surface roughness (m). The surface roughness is the surface standard deviation (m) measured normally from the polygon plane. Edge numbers that are positive, non-zero, integers (column 3) indicate that columns 4 to 6 contain the cartesian coordinates (x_1, y_1, z_1) in m of the polygon edge start point and columns 7 to 9 contain the cartesian coordinates (x_2, y_2, z_2) in m of the polygon edge end point. The special edge number –1 (column 3) indicates that columns 4 to 6 contain the

cartesian components (x_l, y_l, z_l) in m of the polygon location vector (its location being defined by the polygon's centre-of-area), columns 7 to 9 contain the cartesian components (x_n, y_n, z_n) (m) of the polygon's unit surface normal vector.

The following algorithm is used to uniquely order the building and their associated polygons (walls and roof-tops of buildings).

(i) **Ordering of buildings**
Choose the building(s) containing points with minimum value of z. If more than one building exists with the same minimum value of z then choose that (those) with the minimum value of y. If more than one building exists with the same minimum values of y and z then choose that (those) with the minimum vale of x. If more than one building exists with the same minimum values of x, y and z then repeat this algorithm using the second highest value of z, y and x. Continue with the third highest values and so on until building order is fully and uniquely resolved.

(ii) **Ordering of building polygons facets**
Choose the building polygon containing edge-end-points with a minimum value of z. If more than one polygon exists with same minimum value of z then choose that (those) with minimum value of y. If more than one polygon exists with the same minimum values of z and y then choose that with the minimum value of x.

(iii) **Ordering of polygon edges**
Choose the building polygon's corner with a minimum value of z. If more than one corner exists with the same minimum value of z then choose that (those) with a minimum value of y. If more than one point exists with the same minimum values of z and y then choose that with the minimum value of x. Number the corners 1, 2, 3, ... starting at the chosen corner and moving anti-clock-wise looking in the direction of the polygon's unit normal (i.e. using a right hand rule around polygon normal vector). For an N-sided polygon, edge 1 is that connecting corners 1 and 2. Edge 2 is that connecting corners 2 and 3, edge 3 is that connecting corners 3 and 4, ... and edge N is that connecting corners N and 1 (see Figure 4.7).

(iv) **Ordering of edge points**
For an N-sided polygon, the start point (point 1) of edge 1 is at corner 1. The end point (point 2) of edge 1 is at corner 2. The start point (point 1) of edge 2 is at corner 2. The end point (point 2) of edge 2 is at corner 3. The start point (point 1) of edge 3 is at corner 3. The end point (point 2) of edge 3 is at corner 4, ... The start point (point 1) of edge N is at corner N. The end point (point 1) of edge N is at corner 1.

Figure 4.7 illustrates the numbering of edges, corners, start point and end points for a simple cuboid-shaped building. Pitch-roofs can be accommodated.

4.4.1.8 TB_COMBINE

TB_COMBINE (Block 1.7, Figure 4.2) is a procedure which merges the TIN and POLYS databases into the single database POLY_ENV_DATABASE (Block 1.8, Figure 4.2).

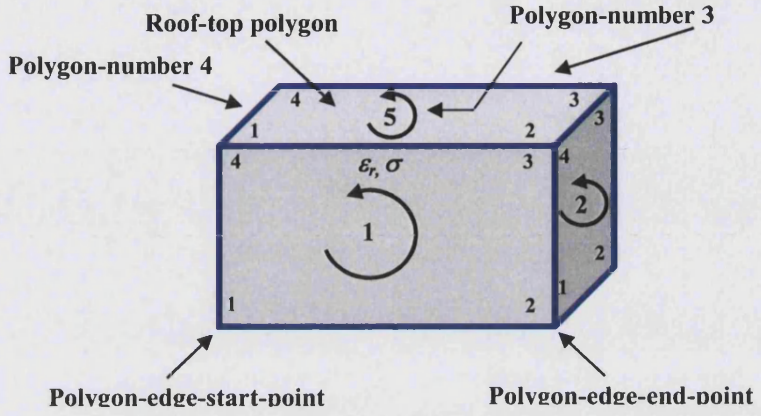

Figure 4.7: *Illustration of building polygon, edges and point numbering in POLYS.*

4.4.1.9 POLY_ENV

POLY_ENV (Block 1.8, Figure 4.2) is a database containing the complete specification of the physical environment to be modelled. It is a combination of the terrain database TIN and building database POLYS. Table 4.3 shows an example of the combined natural terrain TIN and building database POLYS.

Table 4.3: *TIN and POLYS databases, extract from example POLY file format.*

0	1	0	4.44	0.1	1000	0		
0	1	1	40	20	0	160	100	0
0	1	2	160	100	0	40	180	0
0	1	3	40	180	0	40	20	0
0	1	-1	80	100	0	0	0	1
0	2	0	15	0.1	1000	0		
0	2	1	200	20	0	260	100	0
0	2	2	260	100	0	160	100	0
0	2	3	160	100	0	200	20	0
0	2	-1	206.67	73.34	0	0	0	1
1	1	0	3	0.01	0.3	0		
1	1	1	380	60	0	440	120	0
1	1	2	440	120	0	440	120	30
1	1	3	440	120	30	380	60	30
1	1	4	380	60	30	380	60	0
1	1	-1	410	90	15	0.7071	-0.7071	0
1	2	0	3	0.01	0.3	0		
1	2	1	440	120	0	400	160	0
1	2	2	400	160	0	400	160	30
1	2	3	400	160	30	400	120	30
1	2	4	400	120	30	400	120	0
1	2	-1	400	140	15	0.7071	0.7071	0
-	-	-	-	-	-	-	-	-

4.4.1.10 POLY_COA_UNV

This algorithm is used to find the polygon centre-of-area (COA) and unit-normal-vector (UNV). POLY_COA_UNV (Block 1.9, Figure 4.2) consists of two subroutines, namely COA and UNV. The first, COA, calculates the location of a polygon as defined by its centre-of-area and is required to construct the TIN and POLY databases. The polygon is a triangle if it represents a facet of the ground plane (terrain) and can have any number of sides if it represents a building facet (polygon). COA is the mean value of the polygon corner coordinates, i.e.:

$$\underline{r} = \hat{x}\left(\frac{x_1 + x_2 + \cdots + x_n}{N}\right) + \hat{y}\left(\frac{y_1 + y_2 + \cdots + y_n}{N}\right) + \hat{z}\left(\frac{z_1 + z_2 + \cdots + z_n}{N}\right) \tag{4.1}$$

where $\underline{r}$ is the location vector, x_i, y_i and z_i are the coordinates of the polygon corners and N is the number of sides. Figure 4.8 shows the location vector, $\underline{r}$.

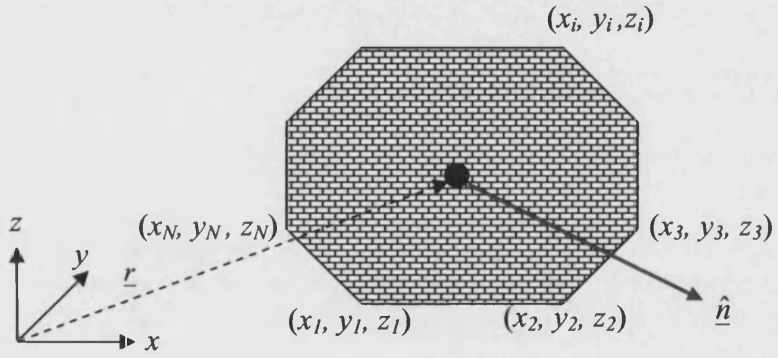

Figure 4.8: *Location vector of polygon centre-of-area (COA) and polygon unit-normal -vector (UNV).*

UNV, calculate the *unit-normal-vector,* $\hat{\underline{n}}$ of each polygon. UNV is obtained as the normalised *cross product* of its first and last edges. (The vector sense of each edge is from its start point (Point 1) to its end point (Point 2). In Figure 4.8 (x_1, y_1, z_1) is point 2 of edge N and point 1 of edge 1, (x_2, y_2, z_2) is point 2 of edge 1 and point 1 of edge 2, …, and (x_N, y_N, z_N) point 2 of edge N-1 and point 1 of edge N.

4.4.1.11 Example databases

A test environment comprising terrain (TIN) data and building (POLYS) data is shown in Figures 4.9 and 4.10, respectively.

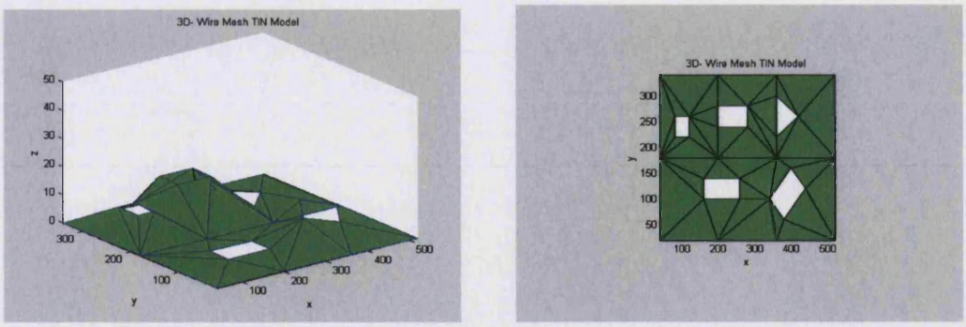

(a) (b)

Figure 4.9: *Example terrain (TIN) model, (a) isometric view, (b) plan view.*

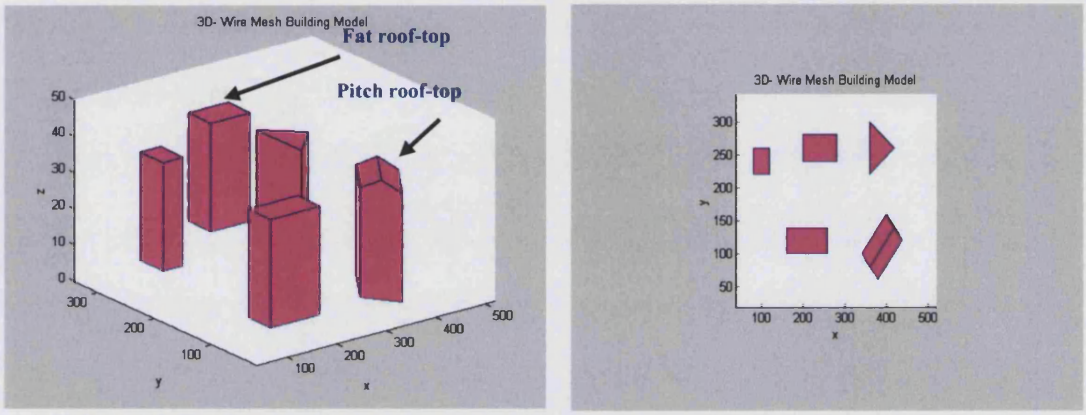

(a) (b)

Figure 4.10: *Example building (POLYS) model, (a) isometric view, (b) plan view.*

Figure 4.11 shows 3D view combined terrain, TIN and building, POLYS databases.

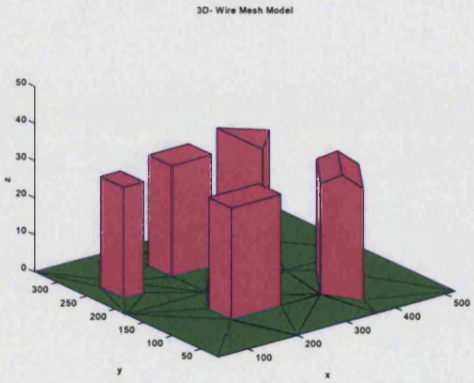

Figure 4.11: *Example environments (POLY_ENV_DATABASE) model.*

4.4.1.12 Reference environment model

A test database containing a hypothetical reference environment model was developed for use in validation tests of subroutines and functions. It contains seven buildings on flat ground plane and covers an area of 800 × 800 m^2, Figure 4.12.

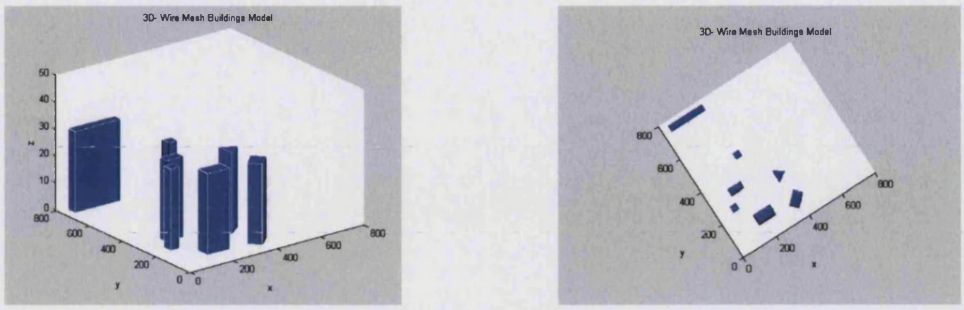

(a) (b)

Figure 4.12: *Test environment.*

4.4.2 PARAMETERS

PARAMETERS (Block 2, Figure 4.1) is a file containing model input parameters such as frequency, antenna type and characteristics, electrical properties of building walls and ground plane, maximum number of interactions (reflections or diffractions), and locations of transmitter and receiver.

4.4.3 Ray-path search algorithm: The Visibility Matrix

The visibility-matrix is a computationally efficient technique used to accelerate ray-path searching. It avoids unnecessary overlapping and interaction tests and is more efficient and computationally faster than the polar sweep algorithm described in Chapter 3, Section 3.4.3.5.4.2.

4.4.3.1 The visibility matrix

The visibility-matrix facilitates a search for all possible ray-paths from the transmitter to the receiver (or field observation point). It is based on the visibility criteria between polygon facets or edges in the modelled environment. (The concept of visibility criteria was described in Chapter 3, Section 3.4.3.5.4) The structure of the visibility matrix is described in Section 4.4.4.4 POLYGONS_SIGHT.

It is developed in four steps as follows:

1. An environment visibility-matrix is constructed once for the chosen environment. The purpose of visibility-matrix is to search which polygon or edges of the buildings can see each other

2. A transmitter visibility-matrix is constructed for each transmitter location of interest. The purpose of the matrix is to search which polygon or edges of the buildings can see the transmitter

3. The receiver visibility-matrix is constructed for each receiver location of interest. The purpose of the matrix is to search which polygon or edges of the buildings can see the receiver

4. The visibility-matrices obtained from 1 - 3 are combined. Sections 4.4.4.6 and 4.4.5.5 describe construction of complete or combined visibility-matrix for reflection and diffraction, respectively

All the visibility-matrices described above are symmetrical. (The physical interpretation of this symmetry is that if polygon or edge A is visible to polygon or edge B then polygon or edge B is visible to polygon or edge A. Once the visibility-matrix is formed a search is made for all possible (unobstructed) ray-paths from transmitter to receiver. Figure 4.13 shows two unobstructed (or valid) ray-paths. For example, in Figure 4.13, a reflected ray-path exists due to LoS between transmitter, polygon-3 (P3), polygon-7 (P7) and receiver-Rx and a diffracted ray-path exit due to LoS between transmitter, edge-11 (E11), edge-13 (E13) and receiver.

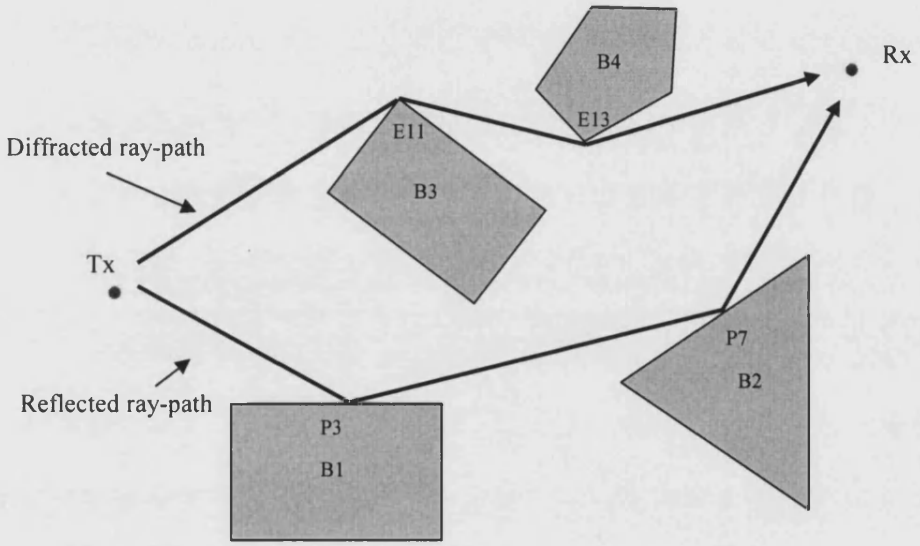

Figure 4.13: *2D plain view of valid reflected and diffracted ray-paths from transmitter to receiver based on visibility criteria.*

To simplify the ray-path search algorithm two separate visibility-matrices have been developed, one for reflection and the other for diffraction. The reflection visibility-matrices contain information relating to building facets while the diffraction visibility-matrices relate to facet edges.

4.4.4 POSSIBLE_PATHS_REF

The procedure POSSIBLE_PATHS_REF (Block 3, Figure 4.1 and Block 3.1, Figure 4.3) is the reflection visibility-matrix implementation. The purpose of this procedure is to find all possible paths that might support a valid, reflected, ray. POSSIBLE_PATHS_REF generates a $P \times N_b$ matrix, where P is the number of reflected possible ray-paths found and N_b is the maximum number of interactions

specified by the user. Each row of this matrix represents a possible reflected ray-path given as a sequence of building polygon numbers.

The input to this procedure is the database POLY_ENV and the output is the matrix of all possible reflected ray-paths (Block 3.1.4, Figure 4.3). A detailed breakdown of POSSIBLE_PATHS_REF into its component subroutines is given in Figure 4.3.

4.4.4.1 ENV_POLY_SIGHT

ENV_POLY_SIGHT (Block 3.1.1, Figure 4.3) is a procedure to calculate the visibility-matrix. The inputs to this procedure are the database POLY_ENV, QUICK_ACCESS and BUILDINGS_LIST matrices and the output is the reflection visibility-matrix. The subroutines of this procedure are as follows:

4.4.4.2 QUICK_ACCESS

QUICK_ACCESS is a matrix which has a rapid access to the environment database. It constructs an $N \times 4$ matrix, where N is the number of all polygons of all buildings in the environment database. Each row of the matrix corresponds to a building polygon. For row i the columns contain the number of the row of the environmental database 'POLY_ENV' where the following data can be found:

Column 1: the electrical properties of polygon i
Column 2: the first edge of polygon i
Column 3: the last edge of polygon i
Column 4: the COA and the UNV of polygon i

The QUICK_ACCESS algorithm is based on the object ordering rules applied earlier in the environment database 'POLY_ENV' (see Section 4.4.1.9). This allows every polygon of the buildings to be called by its row number in the QUICK_ACCESS matrix and its properties to be obtained without reading the whole of environmental database. The input to this procedure is environmental database POLY_ENV and the output is the $N \times 4$ matrix.

4.4.4.3 BUILDINGS_LIST

BUILDINGS_LIST (Block 3.1.1.2, Figure 4.3) constructs an $N \times 2$ matrix (where N is the number of buildings in environment database) which contains the information of all the buildings in the environment database. Each row of the matrix corresponds to one building. The columns in row i contain the numbers of the rows in QUICK_ACCESS matrix where the following can be found:

Column 1: the first polygon of building i
Column 2: the last polygon of building i

The input to this procedure is the QUICK_ACCESS matrix and the output is the $N \times 2$ BUILDINGS_LIST matrix.

4.4.4.4 POLYGONS_SIGHT

POLYGONS_SIGHT (Block 3.1.1.3, Figure 4.2) is a kernel procedure of the reflection visibility-matrix. It generates an $N \times N$ matrix POLYGONS_SIGHT (where N is the number of all polygons of all buildings in the environment database). Each row and each column of the matrix represents a polygon according to the order of QUICK_ACCESS matrix. If polygon i has unobstructed LOS to polygon j then element (i, j) of the POLYGONS_SIGHT matrix is set equal to 1. Otherwise it is set equal to 0. The algorithm used takes account only of the orientations of the polygons. It does not take account of the shadowing of some polygons by others. (One polygon is said to see another if any part of one is visible to any part of the other.) The POLYGONS_SIGHT algorithm starts by assuming that all polygons of all buildings of the environment database can see all other polygons in the environment. It then applies a two-tier elimination process as follows:

1 Tier 1 elimination: *Polygons behind P_{ref}*

The first step of the POLYGONS_SIGHT algorithm is to eliminate all those polygons of the environment which are behind the reference polygon or polygon under test, P_{ref}. The algorithm is based on the comparison of the UNV, $\hat{\underline{nr}}$ of the P_{ref} and the *position vectors*, $\underline{Vi}$ of all other polygons in the environment database. Figure 4.14 illustrates the vector quantities used. In Figure 4.14 P_{ref} is the reference polygon.

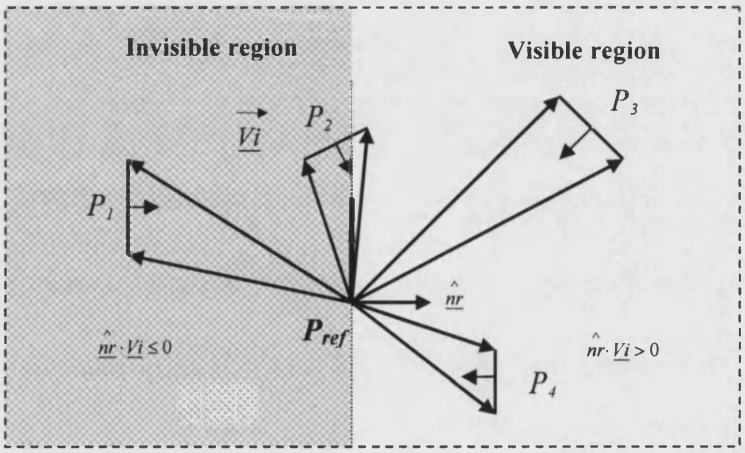

Figure 4.14: *Visibility test for polygon P_{ref} with polygons P_1, P_2, P_3 and P_4* with the reference polygon P_{ref}.

For polygon P_{ref} every dot product $\hat{\underline{nr}} \cdot \underline{Vi}$ is calculated. If the dot product is negative for all points on a given polygon P_i (which generally means considering four points in 3D), then this polygon is not seen by P_{ref}. In Figure 4.14 for example, polygon P_1 is not seen by P_{ref}. All the other polygons (i.e. P_2, P_3, and P_4) are seen by P_{ref}.

2 Tier 2 elimination: *Polygons not looking toward P_{ref}*
The second step of the POLYGONS_SIGHT algorithm is to eliminate all those polygons of the environment database which are not seen by the reference polygon or polygon under test, P_{ref}. The algorithm is based on the orientation of a polygon P_i with respect to its location vector, $\underline{Vi}$ from P_{ref}. Since P_{ref} has spatial extension, all (extreme) points that define P_{ref} (typically four points in 3D),) are tested. Figure 4.15 illustrates the concept in 2D. Once again, the algorithm is based on the comparison of the UNV, $\hat{\underline{nr}}$ of the P_{ref} and the *position vectors,* $\underline{Vi}$ of all other polygons in the environment database. Figure 4.15 illustrates the vector quantities used. In Figure 4.15 P_{ref} is the reference polygon. If all the dot products $\hat{\underline{n}}_i \cdot \underline{V}_{1i}$ and $\hat{\underline{n}}_i \cdot \underline{V}_{2i}$ are positive then P_i is not seen from P_{ref}. Thus, for example, P_1 is not seen by P_{ref} but P_2 and P_3 are visible from P_{ref}.

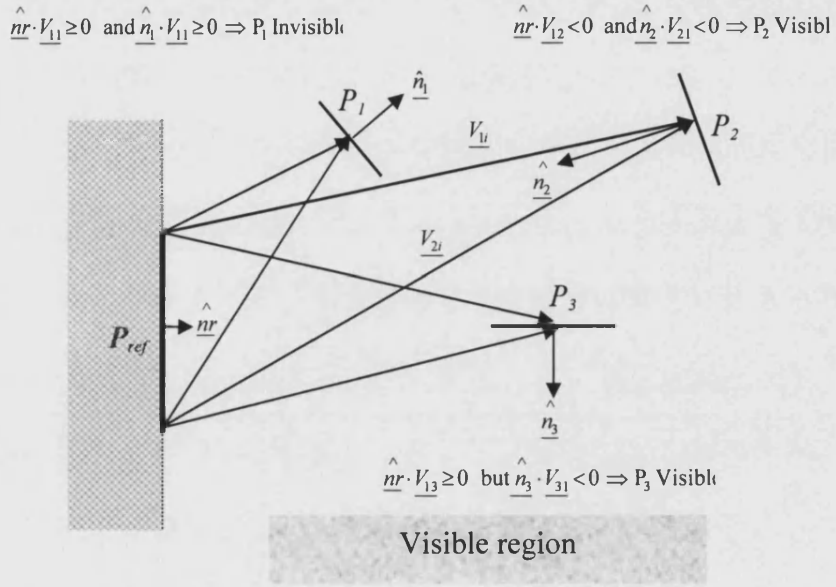

Figure 4.15: *Visibility test for polygon P_{ref} with polygons P_1, P_2 and P_3.*

The inputs to POLYGONS_SIGHT are the environment database POLY_ENV and QUICK_ACCESS matrices. The output of POLYGONS_SIGHT is the $N \times N$ POLYGONS_SIGHT matrix. This matrix is filled with 0s and 1s representing visible and non-visible conditions respectively. This is the environment visibility matrix described in section 4.4.3.1.

Limitations of the POLYGONS_SIGHT algorithm
The POLYGONS_SIGHT algorithm does not include the shadowing of some polygons by others. Thus cases as in Figure 4.16 can occur where P_2 is said to be seen by P_{ref} but in reality the LoS is obscured by an intervening polygon (e.g. P_1). This is addressed by the procedure FILTER_PATHS (The FILTER_PATHS procedure is described in the subsequent section).

4.4.4.5 SHADOWING_2D_GROUND_Tx_Rx_REF

The procedure SHADOWING_2D_GROUND_Tx_Rx_REF (Block 3.1.2, Figure 4.3) is an implementation of reflection visibility-matrices for the transmitter and receiver described in Section 4.4.3.1. It generates the equivalent of the POLYGONS_SIGHT matrix for transmitter and receiver. This algorithm is constructed in several steps as follows.

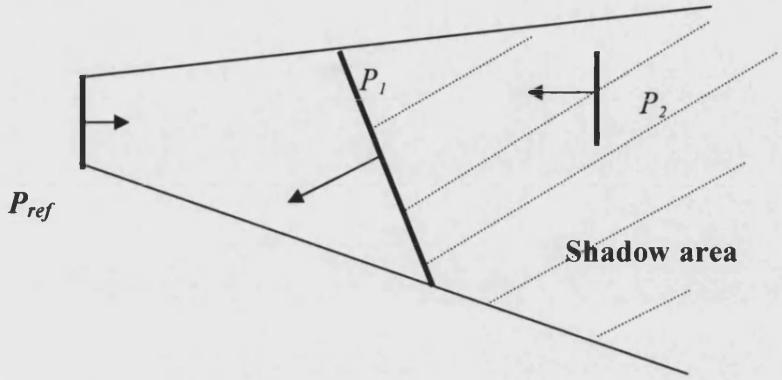

Figure 4.16: *Illustration of shadowing of polygon P_2 with polygon P_{ref}.*

1 Simplification of the problem

We start by reducing the number of polygons considered. We proceed exactly as the tier 2 elimination process described in the POLYGONS_SIGHT algorithm, but instead of having a complete polygon sight, we consider the single point representing the location of the transmitter.

2 Construction of shadow area

The shadow area is not necessarily defined by a single polygon of a building, but may be defined by two (or more) contiguous polygons belonging to the same building, Figure 4.17.

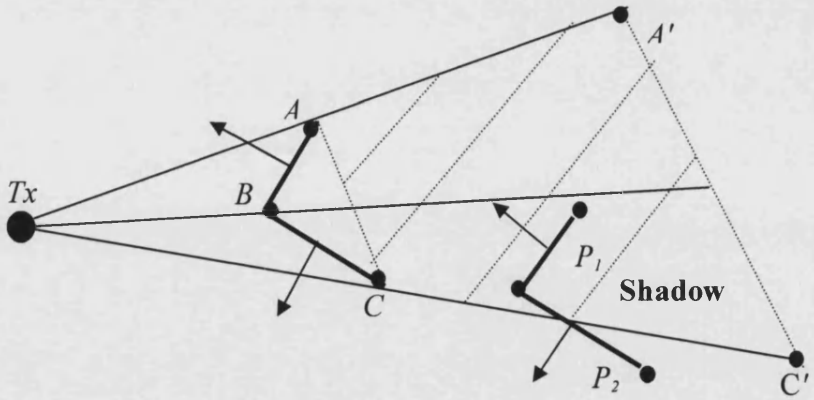

Figure 4.17: *Shadowing from more than one polygon.*

The algorithm selects the buildings of the environment database and takes the polygons that can still be seen from Tx. It then builds the list of the extremity of these polygons {*A, B, B,* and *C*} and simplifies it to obtain the real extremities to be considered: {*A, C*}. It is now possible to calculate *A′* and *C′* using the Tx coordinates. These two points are constructed so that they include the complete

area of the environment database. The shadow area is now perfectly defined by the four points $\{A, C, C', A', A\}$, representing a '2D ground polygon'.

3 Testing the polygons

This part of the algorithm uses the *in-polygon* subroutine which can test the 2D ground polygon described above. The purpose of *in-polygon* is to establish whether a point lies inside, outside, or on, a closed polygon, $\{A, C, C', A', A\}$. Thus for a polygon P_i which is still seen by Tx, we test its two ground points. If they both lie in the shadow area, then this polygon is not seen by Tx. In Figure 4.17, for example, P_1 will not be seen by Tx whereas P_2 will be seen.

SHADOWING_2D_GROUND_Tx_Rx_REF currently works in 2D only. Since a large majority of buildings have vertical walls, and since ray-paths supported by the possible paths but erroneously neglected due to this limitation are unlikely to link Tx and Rx, this limitation is thought to have no practical engineering impact. (The limitation may be more significant if Tx or Rx is located on the roofs of buildings.) The same techniques and testing procedures are applied to find the visibility-matrix for the receiver location, Rx.

The inputs to SHADOWING_2D_GROUND_Tx_Rx_REF are the environment database POLY_ENV, QUICK_ACCESS and BUILDINGS_LIST matrices and the location of Tx and Rx. The outputs of the procedure are two $1 \times N+2$ visibility matrices, one for Tx and the other for Rx. They are filled with 0s and 1s following the same rules used for the POLYGONS_SIGHT_REF matrix described earlier.

4.4.4.6 COMPLETE_POLY_SIGHT_REF

COMPLETE_POLY_SIGHT_REF (Block 3.1.3, Figure 4.3) is a complete or combined visibility-matrix of reflecting polygons of the building, the visibility-matrices for the Tx and Rx, respectively, of the modelled environment. A schematic illustration of the complete visibility-matrix for reflections, filled with 1s and 0s, is shown in Figure 4.18.

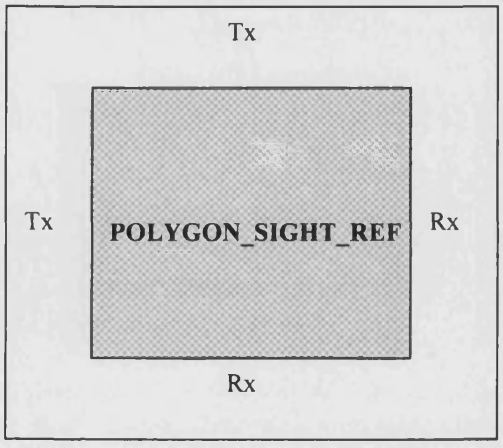

Figure 4.18: *Schematic illustration of the COMPLETE_ POLY SIGHT_ REF matrix.*

The inputs to COMPLETE_POLY_SIGHT_REF are the outputs of POLYGONS_SIGHT and SHADOWING_2D_GROUND_Tx_Rx_REF. The output of COMPLETE_POLY_SIGHT matrix is an *(N+2) × (N+2)* matrix, where *N* is the number of reflecting polygons in the modelled environment. It is a complete visibility matrix for all possible reflected ray-paths from the transmitter to the receiver as described in Section 4.4.3.1.

4.4.4.7 Distributed partitioning and segmentation technique for reflection

To reduce computational complexity, reduce processing time and avoid memory deadlocks, an accelerated distributed partitioning and segmentation technique has been developed and implemented. The algorithm is used to make partitions and segments of the COMPLETE_POLY_ SIGHT_REF matrix described earlier for reflection case (see Block 3.1.3, Figure 4.3). This matrix is a complete visibility-matrix for the modelled environment. The distributed partitioning and segmentation algorithm is outlined and explained below.

1. Take the first column, say C1 of the complete sight matrix. The column C1 is actually the visibility-matrix of Tx *(1 × N+2)*, where *N* is the number of the building polygons in the modelled environment. The column C1 contains 1s and 0s (1 means Tx can see the polygon and 0 means Tx can not see the polygon). Eliminate all 0s and keep 1s i.e. the information of those polygons in column C1 which can see the Tx.
2. Make segments of column C1, say $S1_n$, where the subscript *n* is the number of segments of column C1. As the size of column C1 increases the number of segments increase.
3. For example, take the i^{th} segment $S1_i$. The element of the segment indicates the polygon numbers $P1_1$ to $P1_k$, where the subscript k indicates the number of polygons in $S1_i$. Take the first element of the segment, P_1 and look for its corresponding column number in the complete sight matrix, $C2_j$. Repeat step 2 and step 3 for the number of interactions required, in this case 3 interactions (e.g. S1, S2 and S3), see Figure 4.19.
4. If the last element of the first n^{th} segment ($S1_n$) is 1, then Tx can see Rx and a LoS ray-path exits. The algorithm stores this information as a LoS case.
5. If the last element of the second n^{th} segment ($S2_n$) is 1, then the corresponding polygon can see Rx and only 1 reflection interaction occurs. The algorithm stores this information as an array of building polygon numbers, e.g., [8 0 0]. This array indicates that there a path possibly exists between Tx, the polygon number 8 and Rx. Similarly, if the last element of third n^{th} segment ($S3_n$) is 1, that means the corresponding polygon can see Rx and only 2 reflection interactions occur. The algorithm stores this information as an array of building polygon numbers, e.g., [45 52 0]. This array indicates that a path possibly exists between Tx, the polygon numbers 45 and 52, and Rx.
6. Finally, all the elements of all the segments of the third segment (S3) need to be checked in order to find the 3^{rd} interaction. In this case, for example, consider the i^{th} segment ($S3_i$) (see Figure 4.19). If the element e.g. $P3_1$ can see Rx then its corresponding column number, $C3_j$ in the complete sight matrix needs to be checked. If the last element of $C3_j$ is 1,

then $P3_1$ can see Rx and the algorithm stores this information as an array of building polygon numbers, e.g. [33 38 41] representing a 3 reflection interaction. If any element (i.e. polygon) of the segment S3 does not see Rx, then no path exists between Tx and Rx.

Figure 4.19 illustrates the distributed partitioning and segmentation process for 3-order reflection, where P indicates building polygon number.

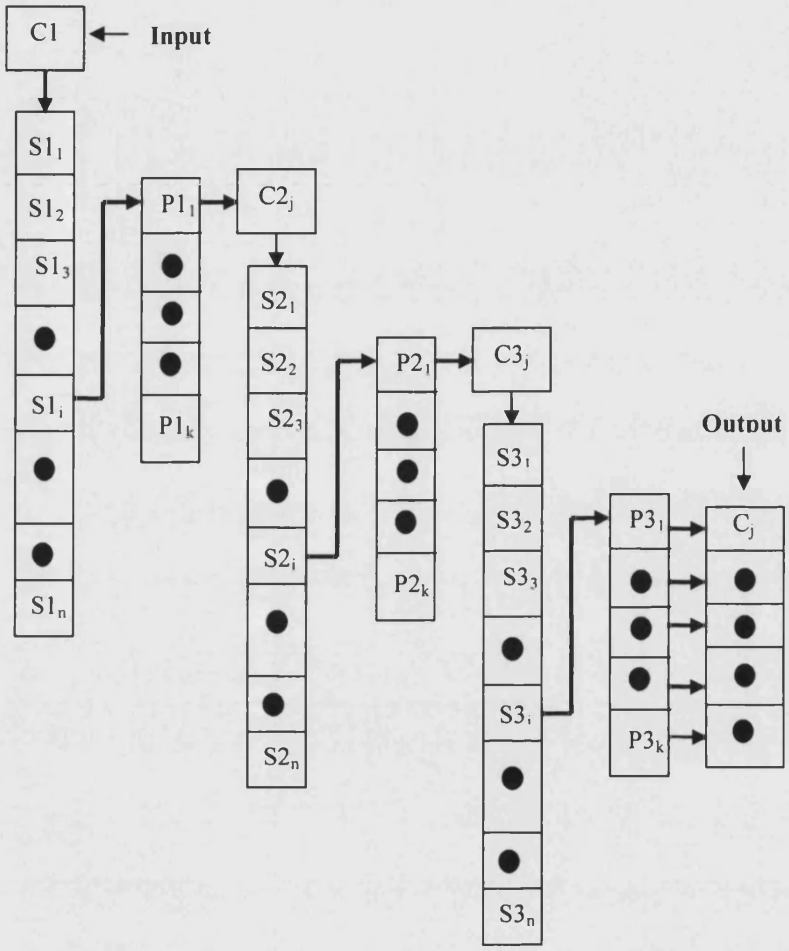

Figure 4.19: *An illustration of the distributed partitioning and segmentation process.*

The output array, called POSSIBLE_PATHS_OUT_REF, contains a sequence of successive reflecting building polygon numbers.

4.4.4.8 INTERACTION_CHAIN_REF

INTERACTION_CHAIN_REF (Block 3.2, Figure 4.5) represents the GO kernel of the ray-tracing reflection calculations. Once an array of polygons possibly supporting a reflected ray-path has been generated, the next step is to find the interaction chain (or matrix) of images and corresponding points-of-reflection (PORs), optical path length of the ray-paths and finally find a valid, unobstructed or filtered reflected ray-path from the Tx to the Rx.

The input to this procedure is an array of possible reflected paths and the location of the transmitter and receiver from the PARAMETER database described in Section 4.4.2. The output is an array containing a location chain of unobstructed (i.e. valid) PORs from Tx to Rx. The following sections describe the software structure and the corresponding subroutines used in the INTERACTION_CHAIN_REF procedure.

4.4.4. 9 IMAGES_REFLECTION

IMAGES_REFLECTION (Block 3.2.1, Figure 4.5) finds the successive image locations of the transmitter for each reflecting polygon along the ray-path. The vector geometry on which IMAGES_REFLECTION is based is described below.

The first order Tx image, $\underline{Tx}'$, is derived from the location of $\underline{Tx}$, the centre-of-area (COA) location of the polygon, $\underline{L}$, and unit normal vector (UNV), $\hat{\underline{n}}$. The COA and UNV are contained in the environment database POLY_ENV (Block, 1.8, 1.9, Figure 4.2). Figure 4.20 shows the vector geometry used to derive the image coordinates. The origin of the *x, y, z* coordinate system is denoted by *0*, $\hat{\underline{n}}$ is the UNV of the reflecting polygon, $\underline{L}$ is location vector (i.e. COA) of the reflecting polygon, $\underline{Tx}$ is the location vector of the transmitter and $\underline{Tx}'$ is the location vector of the transmitter image.

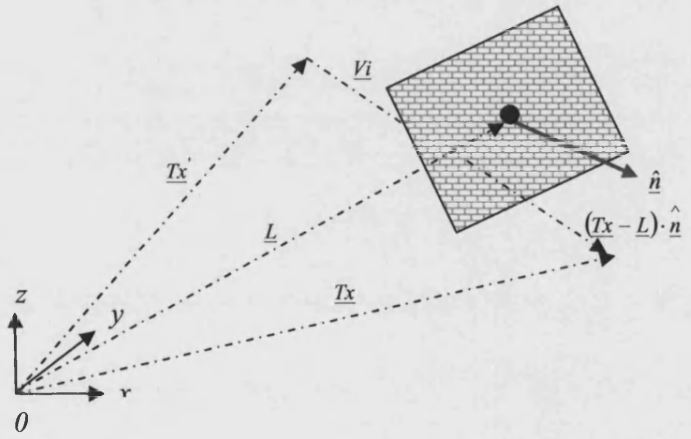

Figure 4.20: *Vector geometry for the calculation of a transmitter image (Tx') from the location of the transmitter (Tx), the location vector of the reflecting polygon (L) and the reflecting polygon unit normal vector ($\hat{n}$).*

In Figure 4.20, $\underline{Tx}'$ is given by:

$$\underline{Tx}' = \underline{Tx} - \underline{Vi} \tag{4.2}$$

where

$$\underline{Vi} = \underline{Tx} - \underline{Tx}' \cdot \underline{Vi} \tag{4.3}$$

$\underline{Vi}$ is parallel to the reflecting polygon's UNV, i.e.:

$$\underline{Vi} = \lambda \hat{\underline{n}} \tag{4.4}$$

where λ is a constant scalar given by:

$$\lambda = 2\left[\left(\underline{Tx} \cdot \hat{\underline{n}}\right) - \left(\underline{L} \cdot \hat{\underline{n}}\right)\right] \tag{4.5}$$

Identifying $\hat{\underline{n}}$ as a common factor in Eq. (4.5):

$$\lambda = 2\left[\left(\underline{Tx} - \underline{L}\right) \cdot \hat{\underline{n}}\right] \tag{4.6}$$

and substituting Eq. (4.6) in Eq. (4.4) gives:

$$\underline{Vi} = 2\left[\left(\underline{Tx} - \underline{L}\right) \cdot \hat{\underline{n}}\right]\hat{\underline{n}} \tag{4.7}$$

Finally, substituting Eq. (4.7) in Eq. (4.2) gives the location of the transmitter image, $\underline{Tx}'$ explicitly.

The inputs to this procedure are the location vector of the transmitter, $\underline{Tx}$, an array of polygons forming a possible path and the location vector of the receiver, $\underline{Rx}$. The input format of the procedure for the nth reflection interaction is:

$$\begin{bmatrix} P_1 \\ P_2 \\ \cdots \\ P_n \end{bmatrix} \tag{4.8}$$

where, P_n is the reflecting polygon and the subscript n is the number of interactions along the possible path. The IMAGES_REFLECTION algorithm can be summarised as follows:

1. Select location vector of the transmitter, $\underline{Tx}$
2. Select the first element of the input array (i.e. the first polygon number in the array, e.g. P_1)
3. Find the first order image, $\underline{Tx}_1'$
4. Select $\underline{Tx}_1'$
5. Select the next element of the input array (i.e. the second polygon number in the array, e.g. P_2)
6. Find the second order image, $\underline{Tx}_2'$
7. Repeat steps 4 through 6 each time a new location of the image is obtained

The output of IMAGES_REFLECTION is a chain of transmitter image location vectors:

$$\begin{bmatrix} \underline{Tx}_1' \\ \underline{Tx}_2' \\ \cdots \\ \underline{Tx}_n' \end{bmatrix} \tag{4.9}$$

4.4.4.10 POINT_OF_REFLECTION

The procedure POINT_OF_REFLECTION (Block 3.2.2, Figure 4.5) is used to find all point-of-reflections (PORs) on reflecting polygons along the ray-path. The vector geometry used by this procedure is described below.

Figure 4.21 shows the vector geometry used to derive the coordinates of POR of a reflecting polygon.

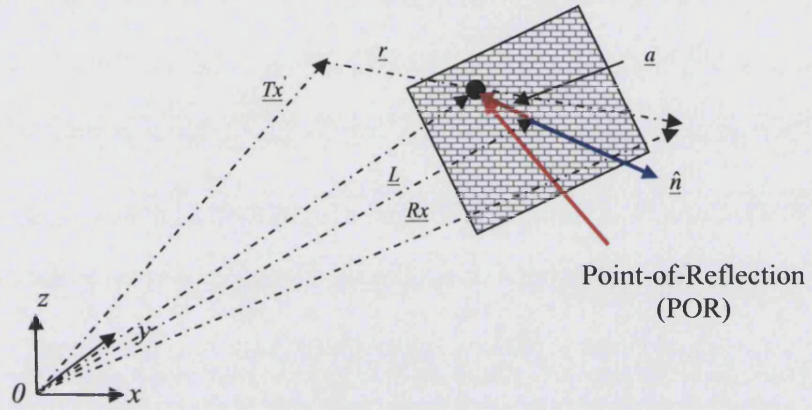

Figure 4.21: *Vector geometry for the calculation of a Point-of-reflection, POR, $\underline{P}$ from the location of the transmitter image, $\underline{Tx}'$, the location vector of the reflecting polygon, $\underline{L}$, the reflecting polygon UNV, $\hat{\underline{n}}$, and location vector of the receiver, $\underline{Rx}$.*

In Figure 4.21 the origin of the *x, y, z* coordinate system is denoted by *0*, $\hat{\underline{n}}$ is the UNV of the reflecting polygon, $\underline{L}$ is location vector (i.e. COA) of the reflecting polygon, $\underline{Tx}'$ is location vector of the transmitter image, and $\underline{Rx}$ is the location vector of the receiver. $\underline{r}$ is given by:

$$\underline{r} = \underline{Rx} - \underline{Tx}' \tag{4.10}$$

and POR vector $\underline{P}$ is given by:

$$\underline{P} = \underline{Tx}' + k\hat{\underline{r}} \tag{4.11}$$

The vector $\underline{a}$ is given by:

$$\underline{a} = \underline{P} - \underline{L} \tag{4.12}$$

where $\underline{a}$ is the vector from $\underline{P}$ - $\underline{L}$ and:

$$\underline{a} \cdot \hat{\underline{n}} = 0 \tag{4.13}$$

Therefore,

$$(\underline{P} - \underline{L}) \cdot \hat{\underline{n}} = 0 \tag{4.14}$$

Similarly,

$$\left(\underline{P} \cdot \hat{\underline{n}}\right) - \left(\underline{L} \cdot \hat{\underline{n}}\right) = 0 \tag{4.15}$$

Substituting the Eq. (4.11) into Eq. (4.15) gives:

$$\left[\left(Tx' + k\hat{\underline{r}}\right) \cdot \hat{\underline{n}}\right] - \underline{L} \cdot \hat{\underline{n}} = 0 \tag{4.16}$$

Identifying $\hat{\underline{n}}$ as a common factor:

$$Tx' \cdot \hat{\underline{n}} + k\left(\hat{\underline{r}} \cdot \hat{\underline{n}}\right) - \underline{L} \cdot \hat{\underline{n}} = 0 \tag{4.17}$$

and rearranging the values in Eq. (4.17) gives:

$$k\left(\hat{\underline{r}} \cdot \hat{\underline{n}}\right) = \left(\underline{L} \cdot \hat{\underline{n}}\right) - \left(Tx' \cdot \hat{\underline{n}}\right) \tag{4.18}$$

Finding the value of k from Eq. (4.18):

$$k = \frac{\left(\underline{L} \cdot \hat{\underline{n}}\right) - \left(Tx' \cdot \hat{\underline{n}}\right)}{\hat{\underline{r}} \cdot \hat{\underline{n}}} \tag{4.19}$$

Finally, substituting Eq. (4.19) into Eq. (4.11) gives the location of the POR vector $\underline{P}$ explicitly.

The POINT_OF_REFLECTION procedure works recursively in reverse order i.e. the POR of the last reflecting polygon of the possible ray-path is found first and so on. The input to POINT_OF_REFLECTION is the location vector of the receiver, $\underline{Rx}$, and the inverse of the output matrix of the IMAGES_REFLECTION procedure. The input format of the procedure for n^{th} reflection interaction is:

$$\begin{bmatrix} \underline{Rx} \\ \underline{Tx}_n' \\ \underline{Tx}_{n-1}' \\ \cdots \\ \underline{Tx}_1' \end{bmatrix} \tag{4.20}$$

where, $\underline{Rx}$ is the location vector of the receiver, $\underline{Tx}_n'$ is the last transmitter image and the subscript n is the number of transmitter images of the possible ray-path. The POINT_OF_REFLECTION algorithm can be summarised as follows.

1. Select the first element of the input array (i.e. the $\underline{Rx}$ location)
2. Select the next element of the input array (i.e. the last Tx image, Tx_n')
3. Find the point-of-reflection, POR_n (i.e. the POR of the n^{th} polygon of the possible ray-path array)
4. Select POR_n
5. Select the second element of the input array (i.e. the second last Tx image, Tx_{n-1}')
6. Find POR_{n-1}
7. Repeat steps 4 through 6 each time a new location of the POR is obtained

The output format of POINT_OF_REFLECTION is a location chain of PORs of the corresponding polygons of the possible ray-path.

$$\begin{bmatrix} \underline{POR}_1 \\ \underline{POR}_2 \\ \cdots \\ \underline{POR}_n \end{bmatrix} \tag{4.21}$$

where $\underline{POR}_n$ is the location vector of the point-of-reflection (POR) and the subscript n is the number of PORs of the reflecting polygons along the possible ray-path.

4.4.4.10.1 Example output

Figure 4.22 shows an example ray-path found by INTERACTION_CHAIN_REF (i.e. an output array of POSSIBLE_PATHS_REF (see Block 3.1, Figure 4.3). One drawback of the POINT_OF_REFLECTION procedure is that there are cases in which the location vector of POR is outside the reflecting polygon, which means no valid ray-path from Tx to Rx exits. In these cases the possible ray-path array is eliminated. In order to test whether the POR is inside or outside of the reflecting polygon, the following techniques was developed.

4.4.4.11 IN_OUT_POLY

IN_OUT_POLY (Block 3.2.3, Figure 4.5) procedure is a component of INTERACTION_CHAIN_REF. It is used to test whether the intersection of a ray segment with the plane of a reflecting polygon lies inside or outside the polygon boundary (i.e. to test whether the POR is inside or outside of the reflecting polygon). Figure 4.23 shows a 'ray' with POR, outside its reflecting polygon (and therefore this ray-path should be discarded).

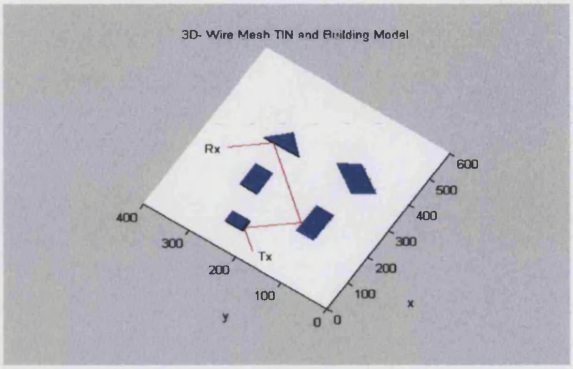

Figure 4.22: *Plan view of test database showing example ray-path between transmitter (Tx) and receiver (Rx).*

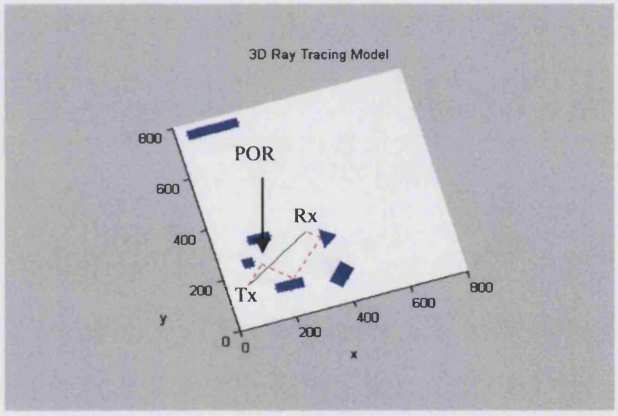

Figure 4.23: *2D plan view of reference database showing an erroneous ray (dashed curve) with POR outside its reflecting polygon boundary and a direct (LoS) ray (solid curve).*

The input to IN_OUT_POLY is the location vector of the POR, the building polygon number, the location vector of COA, and the UNV of the polygon. The algorithm can be summarised as follows:

1. For the convex reflecting polygon number in question label each corner, e.g. P_1, P_2, P_3, ..., P_n. (The corners may be labelled in a clockwise or counter-clockwise direction)
2. Construct the triangles formed by the point, P and the corners of the polygon (see Figure 4.24)
3. Given the three points forming the corners of each triangle, e.g. $P_1 = (x_1, y_1, z_1)$, $P_2 = (x_2, y_2, z_2)$, and $P = (x_P, y_P, z_P)$ calculate the determinant:

$$A = \begin{vmatrix} x_1 & y_1 & z_1 \\ x_2 & y_2 & z_2 \\ x_P & y_P & z_P \end{vmatrix} \tag{4.22}$$

4. *P* is inside the polygon boundary if the sgn(A) is equal for all triangles, otherwise *P* is outside the polygon boundary.

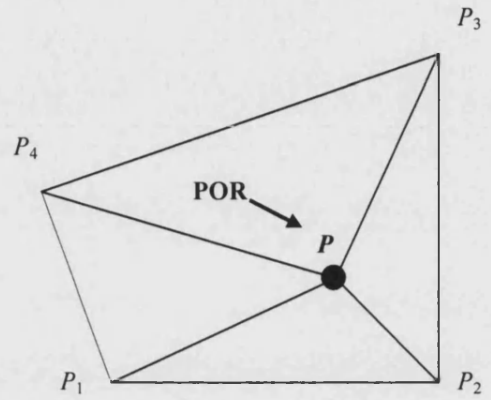

Figure 4.24: *Four sided (convex) polygon with point P (i.e. POR) inside the polygon boundary.*

For point *P* to be inside the polygon, trace around in a counter-clockwise direction from P_1 to P_2 to P_3 to P_4 and back to P_1, the determinant of the triangles P_1P_2P, P_2P_3P, P_3P_4P, and P_4P_1P must all be negative. If the orientation of the polygon is unknown, then they must either all be positive or all be negative. For point *P* to be outside the polygon then the determinant of the triangles P_1P_2P, P_2P_3P, P_3P_4P, and P_4P_1P must not all be negative. If the point *P* is on a polygon edge (or boundary) then one of the determinants must be zero. If the point *P* is at a corner of the polygon then two determinants must be zero. If the first POR is outside the reflecting polygon then the corresponding possible ray-path should be discarded and the algorithm looks for the next output array of possible ray-path. The output of the IN_OUT_POLY procedure is 1 or 0 (zero), 1 indicating that POR is inside the reflecting polygon and 0 means that the POR is outside of the reflecting polygon.

4.4.4.12 OPT-PATH_LEN_REF

The procedure OPT-PATH_LEN_REF (Block 3.2.4, Figure 4.5) is used to find the total optical path length of the ray-path. The inputs to this procedure are the location vector of the transmitter, the output matrix of POINT_OF_REFLECTION and the location vector of the receiver. The input format of the procedure for the n^{th} reflection interaction is:

$$\begin{bmatrix} \underline{Tx} \\ \underline{POR_1} \\ \cdots \\ \underline{POR_n} \\ \underline{Rx} \end{bmatrix} \tag{4.23}$$

The output format of OPT-PATH_LEN_REF is a location chain of distances of ray-segments (i.e. the distance from transmitter, Tx to first POR, the distance from first POR to second POR and so on). The output format is:

$$\begin{bmatrix} RG_1 \\ RG_2 \\ \cdots \\ RG_n \end{bmatrix} \tag{4.24}$$

where RG_n is the ray-segment (RG) and the subscript n is the number of RGs of the possible ray-path.

It is often the case that a ray-path is blocked by the intervening building polygon(s). In order to cope with this problem a technique was developed and implemented to find unobstructed (or valid) ray-paths from the transmitter to the receiver. The following section describes the technique.

4.4.4.13 FILTER_PATHS_REF

Many calculated ray-paths are obscured by intermediate building(s). In order to cope with these situations, a filtering algorithm has been developed to 'filter out' such obscured (and therefore invalid) ray-paths. This section describes the most important procedures or subroutines used in the FILTER_PATHS_REF procedure.

FILTER_PATHS_REF (Block 3.2.5, Figure 4.5) is a component of the INTERACTION_CHAIN_REF procedure, which is used to find unobstructed ray-paths from the transmitter to the receiver (i.e. to select those ray-segments where the LoS between the transmitter, Tx, reflecting polygons and the receiver, Rx, exits) and discard those ray-paths which are blocked by intervening building polygon(s). The inputs to this procedure are the output of OPT-PATH_LEN_REF (see Eq. 4.23, described earlier) and the output of IN_OUT_POLY procedure (i.e. 1 or 0 (zero)) as an input. Figure 4.25 shows an example layout of six buildings and the locations of transmitter, Tx, and receiver, Rx, to illustrate the operation of the FILTER_PATHS_REF algorithm. There are two ray-paths from Tx to Rx. The first ray-path from Tx reaches Rx via reflections from Building 3, Building 1 and Building 2. The second ray-path from Tx reaches Rx via a reflection from Building 6. The first ray-segment of the second ray-path is from Tx to Building 6 and the second ray-segment of the second ray is from Building 6 to Rx. The first ray-segment of the second ray-path

is obscured by two polygons of Building 4 and the second ray-segment of the second ray-path is obscured by two polygons of Building 5. This ray-path is thus invalid is to be discarded.

The FILTER_PATHS_REF algorithm can be summarised as follows:

The algorithm FILTER_PATHS_REF constructs rectangles, the diagonals of which coincide with each ray-segment. (In the case of path 2; from Tx to the POR (building 6) and from POR (building 6) to Rx. Four rectangles are constructed from the first ray-path and two rectangles are constructed from the second-ray path. The algorithm FILTER_PATHS_REF first detects if one or more polygons lies wholly or partly inside a rectangle. If one or more polygons are found inside a rectangle then the algorithm determines if the ray intersects any of these polygons. After the first intersection is found the corresponding possible ray-path is discarded. (No further search is necessary since multiple intersections are irrelevant.) The first ray-path in Figure 4.25 nearest Tx, therefore, is un-obscured and is retained but the second ray-path is obscured by the polygon of Building 4. No further search is carried out (so the shadowing effect of Building 5 will not be established) but the entire ray (comprising both segments) is discarded.

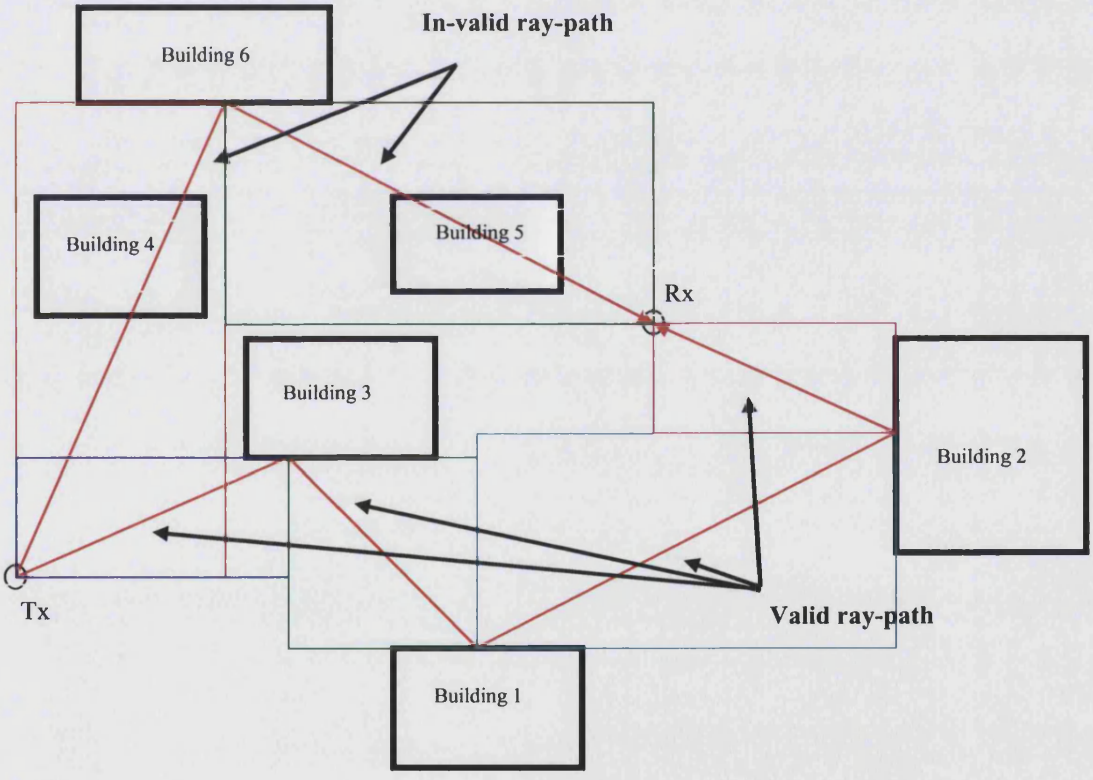

Figure 4.25: *FILTER_PATHS principle.*

The algorithm FILTER_PATHS_REF thus identifies all obscured paths and eliminates them. The algorithm also identifies those paths where the point-of-reflection, POR, is outside the reflecting polygon and eliminates these too. The output of the FILTER_PATHS procedure is an $(N + 2 \times 3)$ matrix, where N is the

numbers of valid PORs, containing the PORs, the location vector of the transmitter and the location vector of receiver, i.e.:

$$\begin{bmatrix} \underline{Tx} \\ \underline{POR_1} \\ \underline{POR_2} \\ \cdots \\ \underline{POR_n} \\ \underline{Rx} \end{bmatrix} \tag{4.25}$$

The output of the algorithm contains only un-obscured, geometrically valid ray-paths.

4.4.4.13.1 Examples output

Figure 4.26(a) shows an example of LoS and three possible ray-paths from the transmitter (Tx) to the receiver (Rx). Tx and Rx are denoted by green asterisks. The dashed (magenta) line is the direct (LoS) path. The first ray-path (red solid line) is an un-obstructed (valid) ray-path. The second ray-path (black dashed-dot line) is an obscured (in-valid) ray-path. The third ray-path is an obscured (in-valid) ray-path with a point-of-reflection, POR outside of the reflecting polygon (blue dashed line). The output arrays of these possible ray-paths have been applied as the input to the FILTER_PATHS procedure. Figure 4.26(b) shows un-obscured (or valid) ray-paths between Tx and Rx (the solid red line).

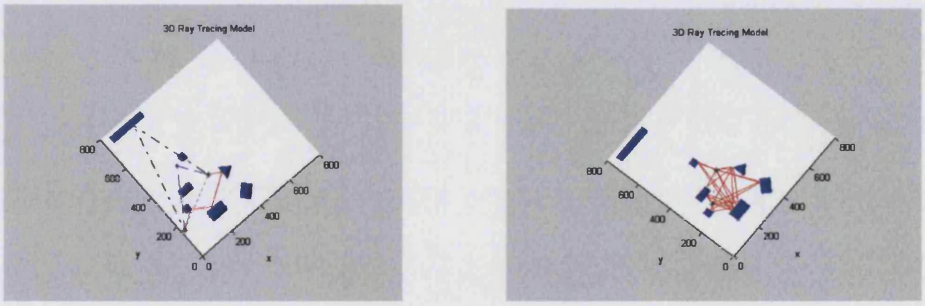

(a) *(b)*

Figure 4.26: *(a) Plan view of reference database showing example ray- paths between transmitter (Tx) and receiver (Rx), (b) Plan view of reference database showing all filtered (or valid) ray paths between transmitter(Tx) and receiver(Rx).*

4.4.4.14 EQUIV_SOURCES_REF

In order to find the field strength at the receiver of each valid reflected or diffracted ray, a new, efficient, reliable and accurate Equivalent-Sources algorithm has been developed and implemented. This section describes in brief the most important procedures or subroutines used to in this algorithm.

In order to simplify the problem, two separate sequences of equivalent-source procedures were developed; one for reflections and one for diffractions. The procedure EQUIV_SOURCES_REF finds the equivalent sources for the reflection case.

EQUIV_SOURCES_REF (Block 3.3, Figure 4.1) finds the amplitude, phase, polarisation, angle-of-departure (AoD), angle-of-arrival (AoA), optical path length, and received field strength of each valid reflected ray-path. Table 4.4 shows the input parameters (PARAMETERS Block 2, Figure 5.1) used to find the components of the EQUIV_SOURCES_REF for the reference model.

Table 4.4: *Input Parameters for the reference model.*

	Parameter	**Values**	**Specifications**
1	b_t	8.2 (m)	Building heights
2	Z_1	377 (Ω)	Free-space impedance (medium-1)
3	v	3×10^8 (m/s)	Velocity of light
4	f	2.38 (GHz)	Frequency
5	λ	0.1261 (m)	Wavelength
6	L_{DP}	$\lambda/2$ (m)	Length of dipole antenna
7	Z_L	73.53 (Ω)	Antenna load impedance
8	P_T	1 (W)	Transmitted power
9	K	$2\pi/\lambda$ (m^{-1})	Wave number
10	σ	0.1 (S/m)	Conductivity (buildings and ground)
11	ε_r	4.44	Relative permittivity of building material
12	ε_{rG}	15	Relative permittivity of ground

Vertically polarised half-wave dipole transmitting and receiving antennas have been assumed. The characteristics of the dipole are given in Appendix 1. The input to EQUIV_SOURCES_REF procedure is the output matrix of FILTER_PATHS_REF; see Block 3.2.5, Figure 4.5 and Equation (4.25) reproduced here for ready reference:

$$\begin{bmatrix} \underline{Tx} \\ \underline{POR}_1 \\ \underline{POR}_2 \\ \cdots \\ \underline{POR}_n \\ \underline{Rx} \end{bmatrix} \tag{4.26}$$

where, $\underline{Tx}$ is the location vector of the transmitter, $\underline{Rx}$ is the location vector of the receiver and $\underline{POR}_n$ is the location vector of the point-of-reflection (POR). The subscript n is the PORs number of the corresponding polygons of the valid ray-path. We call this input matrix a valid-ray-path-matrix (VRPM). Figure 4.27 shows the vector geometry of the equivalent sources for reflection case.

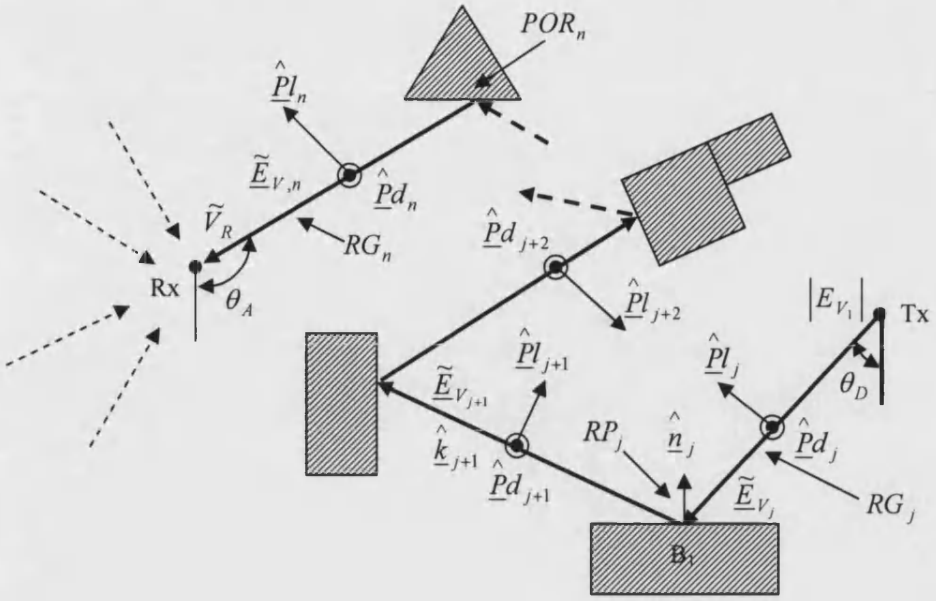

Figure 4.27: *2D illustration of vector geometry of equivalent sources for reflection.*

The EQUIV_SOURCES_REF algorithm can be summarised as follows:

1. Using the database POLY_ENV and procedure POLY_COA_UNV obtain a matrix of UNVs of the reflecting polygons (RPs) along the ray-path:

$$\hat{\underline{n}}_M = \begin{bmatrix} \hat{\underline{n}}_1 \\ \hat{\underline{n}}_2 \\ \cdots \\ \hat{\underline{n}}_n \end{bmatrix} \tag{4.27}$$

where $\hat{\underline{n}}_n$ is the UNV and subscript *n is* the number of reflecting polygon along the ray-path.

2. Using the VRPM matrix (see Eq. 4.26) find the propagation direction vector for the j+1[th] ray-segment (RG_{j+1}). The j+1[th] unit propagation direction vector $\hat{\underline{k}}_{j+1}$ is calculated by subtracting the vector element in row j, from that in row j+1:

$$\underline{k}_{j+1} = \underline{POR}_{j+2} - \underline{POR}_{j+1} \tag{4.28}$$

and

$$\hat{\underline{k}}_{j+1} = \frac{\underline{k}_{j+1}}{\left|\underline{k}_{j+1}\right|} \tag{4.29}$$

3. Find the matrix of unit propagation direction vectors, $\hat{\underline{k}}_M$ of each RG along the ray-path:

$$\hat{\underline{k}}_M = \begin{bmatrix} \hat{\underline{k}}_1 \\ \hat{\underline{k}}_2 \\ \cdots \\ \hat{\underline{k}}_n \end{bmatrix} \tag{4.30}$$

where $\hat{\underline{k}}_n$, is the unit propagation direction vector and the subscript n is the number of propagation direction vectors of each RG along the ray-path.

4. The phase, $e^{j\phi_1}$ from transmitter, Tx, to the first point-of-reflection, POR_1 of the first ray-segment (RG1) of the ray-path is found using:

$$e^{j\phi_1} = e^{j2\pi\left[\frac{R_1}{\lambda} - Int\left(\frac{R_1}{\lambda}\right)\right]} \tag{4.31}$$

where R_1 is the length of RG_1 (i.e. the distance from Tx to POR_1), λ is wavelength and *Int* is the integer value of the bracket.

5. ***Electrical properties of building walls***
Using the database POLY_ENV (described in section 4.4.1.9) obtain an array of electrical properties of the j^{th} reflecting polygon (RP_j):

$$\lfloor \sigma_j \quad \varepsilon_{r,j} \rfloor \tag{4.32}$$

where, σ_j is conductivity (S/m) and $\varepsilon_{r,j}$ is relative permittivity.

6. ***Angle-of-departure (AoD)***
Assuming vertical transmitting and receiving antennas the AoD at the transmitting antenna, θ_D is found using:

$$\theta_D = \cos^{-1}\left(\hat{\underline{k}}_1 \cdot \hat{\underline{z}}_T\right) \tag{4.33}$$

where $\hat{\underline{z}}_T$, is the unit direction vector of the transmitting antenna, $\hat{\underline{k}}_1$ is the propagation direction vector of RG_1.

7. ***Radiation pattern of the transmitting antenna***
The radiation pattern of the transmitting antenna (i.e. field strength gain), $E'_{\theta T}$ is given by [404]:

$$E'_{\theta_T} = \left[\frac{\cos\left(\frac{kL_{DP}}{2}\cos\theta_D\right) - \cos\left(\frac{kL_{DP}}{2}\right)}{\sin\theta_D} \right] \tag{4.34}$$

where k is wave number, L_{DP} is the dipole length and θ_D is the AoD.

8. ***Incident electric field strength***

The incident electric field strength of the first ray-segment, RG_1 is found as follows:

(i) The received power density, S_R is:

$$S_R = \frac{P_T G_T}{4\pi R_1^2} \tag{4.35}$$

where P_T is the transmitted power, G_T is the gain of the transmitting antenna and R_1 is the length of RG_1.

The electric field strength is related to power density by:

$$\frac{|E_{V_1}|^2}{Z_o} = S_R \tag{4.36}$$

where $|E_{V1}|$ is the magnitude of the vertically polarised component of the incident field and Z_o is the intrinsic impedance of free space.

Substituting Eq. (4.36) in Eq. (4.35), we get:

$$|E_{V_1}| = \sqrt{\frac{P_T G_{\max} Z_1}{4\pi R_1^2}} \tag{4.37}$$

where $G_{\max}$ is the maximum gain of the transmitting antenna given as [404]:

$$G_{\max} = G_T = \frac{2}{Q} \tag{4.38}$$

where Q is defined in Appendix 1(see Eq.(A.11).

The vertically polarised incident electric field strength at RP_1 is then given by:

$$\tilde{E}_{V_1} = |E_{V_1}| e^{j\phi} E'_{\theta_D} \tag{4.39}$$

where $\tilde{E}_{V_1}$ is the complex vertical incident field.

9. The unit horizontal (polarisation) vector, $\underline{\hat{H}}_1$ for RG_1 is given by:

$$\underline{\hat{H}}_1 = \hat{\underline{k}}_1 \times \hat{\underline{z}} \tag{4.40}$$

where $\hat{\underline{k}}_1$ is the unit propagation direction vector of RG_1 and $\hat{\underline{z}}$ is the unit direction vector of surface.

10. The unit vertical (polarisation) vector, $\underline{\hat{V}}_1$ for RG_1 is:

$$\underline{\hat{V}}_1 = \underline{\hat{H}}_1 \times \hat{\underline{k}}_1 \tag{4.41}$$

and the complex vertically polarised incident electric field strength vector, $\underline{\tilde{E}}_{V_1}$ for RG_1 is:

$$\underline{\tilde{E}}_{V_1} = \tilde{E}_{V_1} \underline{\hat{V}}_1 \tag{4.42}$$

11. The complex horizontally polarised incident electric field strength vector, $\tilde{E}_{H_1}$ for RG_1 is:

$$\underline{\tilde{E}}_{H_1} = \tilde{E}_{H_1} \underline{\hat{H}}_1 \tag{4.43}$$

4.4.4.14.1 EQUIV_SOURCES_REF algorithm

This section describes the kernel of the EQUIV_SOURCES_REF algorithm. The algorithm proceeds as follows:

1. Find the unit perpendicular vector for the j^{th} ray-segment, RG_j (see Figure 4.27):

$$\underline{\hat{P}d}_j = \frac{\hat{\underline{n}}_j \times \hat{\underline{k}}_j}{\left| \hat{\underline{n}}_j \times \hat{\underline{k}}_j \right|} \tag{4.44}$$

where $\hat{\underline{n}}_j$ is the UNV of the j^{th} reflecting polygon (RP_j) and $\hat{\underline{k}}_j$ is the propagation direction vector of the j^{th} ray-segment, RG_j.

Using the $\hat{\underline{n}}_M$ and $\hat{\underline{k}}_M$ matrices (see Eq. 4.27 and Eq. 4.30), obtain a matrix of unit perpendicular vectors for each ray-segment (RG) along the ray-path:

$$\hat{\underline{P}}d_M = \begin{bmatrix} \hat{\underline{P}}d_1 \\ \hat{\underline{P}}d_2 \\ \cdots \\ \hat{\underline{P}}d_n \end{bmatrix} \tag{4.45}$$

where $\hat{\underline{P}}d_n$ is unit vector perpendicular to the plane of incidence and the subscript n is the number of ray-segment (RG) along the ray-path.

2. Find the unit parallel vector for the j^{th} ray-segment (RG_j) as:

$$\hat{\underline{P}}l_j = \hat{\underline{k}}_j \times \hat{\underline{P}}d_j \tag{4.46}$$

where $\hat{\underline{k}}_j$ is the propagation direction vector, $\hat{\underline{P}}d_j$ is the unit perpendicular vector and $\hat{\underline{P}}l_j$ is the unit vector parallel to the plane of incidence for the j^{th} ray-segment RG_j).

Using $\hat{\underline{k}}_M$ and $\hat{\underline{P}}d_M$ and matrices Eq. 4.30 and Eq. 4.45, obtain a matrix of unit parallel vectors for each ray-segment (RG) along the ray-path as:

$$\hat{\underline{P}}l_M = \begin{bmatrix} \hat{\underline{P}}l_1 \\ \hat{\underline{P}}l_2 \\ \cdots \\ \hat{\underline{P}}l_n \end{bmatrix} \tag{4.47}$$

where $\hat{\underline{P}}l_n$ is the parallel vector and the subscript n is the ray-segment number.

3. Using the $\hat{\underline{k}}_M$ matrix (see Eq. 4.30), obtain the unit horizontal vector and unit vertical vector for each RG:

$$\hat{\underline{H}}_j = \hat{\underline{k}}_j \times \hat{\underline{z}} \tag{4.48}$$

$$\hat{\underline{V}}_j = \hat{\underline{H}}_j \times \hat{\underline{k}}_j \tag{4.49}$$

Obtain the unit vertical vector matrix, $\hat{\underline{V}}_M$ and unit horizontal vector matrix, of each RG along the ray-path as:

$$\underline{\hat{V}}_M = \begin{bmatrix} \underline{\hat{V}}_1 \\ \underline{\hat{V}}_2 \\ \cdots \\ \underline{\hat{V}}_n \end{bmatrix} \tag{4.50}$$

$$\underline{\hat{H}}_M = \begin{bmatrix} \underline{\hat{H}}_1 \\ \underline{\hat{H}}_2 \\ \cdots \\ \underline{\hat{H}}_n \end{bmatrix} \tag{4.51}$$

where $\underline{\hat{V}}_n$ is the unit vertical vector, $\underline{\hat{H}}_n$ is the unit horizontal vector and the subscript n is the ray-segment number.

4. ***Electric field components***

(i) ***Incidence electric field components***

The complex perpendicularly polarised component of incident electric field to the plane of incidence for the j^{th} ray-segment, RP_j of the ray-path is found using (see Figure 4.27):

$$\tilde{E}d_j = \underline{\tilde{E}}_{V_j} \cdot \underline{\hat{P}}d_j + \underline{\tilde{E}}_{H_j} \cdot \underline{\hat{P}}d_j \tag{4.52(a)}$$

The complex parallel polarised component of incident electric field to the plane of incidence for the RP_j is found using (see Figure 4.27):

$$\tilde{E}l_j = \underline{\tilde{E}}_{V_j} \cdot \underline{\hat{P}}l_j + \underline{\tilde{E}}_{H_j} \cdot \underline{\hat{P}}l_j \tag{4.52(b)}$$

(ii) ***Fresnel reflection coefficient***

The Fresnel Equations (Eq. 3.11, Eq. 3.13 and Eq. 3.15) are used to find the complex perpendicular, $\tilde{R}_\perp = \tilde{R}d$ and complex parallel, $\tilde{R}_\parallel = \tilde{R}l$ reflection coefficients for each reflecting polygon in the sub-procedure FRESNEL_REF_COEFF. The output of FRESNEL_REF_COEFF is the matrices of perpendicular and parallel Fresnel reflection coefficients, i.e.:

$$\tilde{R}d_M = \begin{bmatrix} \tilde{R}d_1 \\ \tilde{R}d_2 \\ \cdots \\ \tilde{R}d_n \end{bmatrix} \tag{4.53}$$

$$\tilde{R}l_M = \begin{bmatrix} \tilde{R}l_1 \\ \tilde{R}l_2 \\ \cdots \\ \tilde{R}l_n \end{bmatrix} \tag{4.54}$$

where $\tilde{R}d_n$ is the complex perpendicular reflection coefficient, $\tilde{R}l_n$ is the complex parallel reflection coefficient and n is the number of reflecting polygons along the ray-path.

(iii) ***Reflected electric field components***

The reflected electric field for the $j^{th}+1$ ray-segment (RG_{j+1}) is found using (see Figure 4.27):

$$\tilde{E}d_{j+1} = \tilde{E}d_j \tilde{R}d_j \qquad (4.55) \qquad\qquad \tilde{E}l_{j+1} = \tilde{E}l_j \tilde{R}l_j \qquad (4.56)$$

(iv) ***Incidence and reflected electric field components***

The matrices of complex perpendicularly polarised component of electric field, $\tilde{E}d_M$ and complex parallel polarised component of electric field, $\tilde{E}l_M$ are obtained:

$$\tilde{E}d_M = \begin{bmatrix} \tilde{E}d_1 \\ \tilde{E}d_2 \\ \cdots \\ \tilde{E}d_n \end{bmatrix} \qquad (4.57) \qquad\qquad \tilde{E}l_M = \begin{bmatrix} \tilde{E}l_1 \\ \tilde{E}l_2 \\ \cdots \\ \tilde{E}l_n \end{bmatrix} \qquad (4.58)$$

where $\tilde{E}d_n$ is the complex perpendicularly polarised component of reflected electric field, and $\tilde{E}l_n$ is the complex parallel polarised component of reflected electric field. Note, for example, that the first element of the matrix, $\tilde{E}d_M$ (Eq. 4.57), i.e. $\tilde{E}d_1$ is the incidence complex perpendicularly polarised component of first reflecting polygon (RP_1), i.e. j^{th} ray-segment, RG_j, and $\tilde{E}d_2$ is the reflected complex perpendicularly polarised component of second reflecting polygon (RP_2), i.e. the reflected complex perpendicularly polarised electric field component of $j+1^{th}$ ray-segment. $\tilde{E}d_n$ is the complex reflected perpendicularly polarised component of the electric field component at the receiver, Rx, (see Figure 4.27).

(v) ***Vertically polarised components of electric field***

Equations (Eq. 4.45, 4.47, 4.50 and 4.51) are used to obtain the vertically polarised components of electric field for the $j^{th}+1$ ray-segment; RG_{j+1} (see Figure 4.27):

$$\begin{aligned} \tilde{E}_{V,j+1} &= \tilde{E}d_{j+1}\left(\hat{\underline{P}}d_{j+1} \cdot \hat{\underline{V}}_{j+1}\right) + \tilde{E}l_{j+1}\left(\hat{\underline{P}}l_{j+1} \cdot \hat{\underline{V}}_{j+1}\right) \\ &= \frac{\tilde{E}_{V,j+1}\left(e^{j\phi_{j+1}}\right)R_j}{R_j + R_{j+1}} \hat{\underline{V}}_{j+1} \end{aligned} \qquad (4.59)$$

(vi) ***Horizontally polarised components of electric field***

Similarly, the horizontal electric field vector for the $j+1^{th}$ ray-segment, RG_{j+1} is (see Figure 4.27):

$$\begin{aligned}\widetilde{E}_{H,j+1} &= \widetilde{E}d_{j+1}\left(\hat{\underline{P}}d_{j+1}\cdot\hat{\underline{H}}_{j+1}\right)+\widetilde{E}l_{j+1}\left(\hat{\underline{P}}l_{j+1}\cdot\hat{\underline{H}}_{j+1}\right)\\ &= \frac{\widetilde{E}_{H,j+1}\left(e^{\phi_{j+1}}\right)R_j}{R_j+R_{j+1}}\hat{\underline{H}}_{j+1}\end{aligned} \tag{4.60}$$

(vii) ***Vertically and horizontally polarised incidence and reflected electric field components***

The matrices of complex vertically polarised, $\widetilde{E}_{V_M}$ and horizontally polarised, $\widetilde{E}_{H_M}$, electric field components with respect to the plane of incidence (and plane of reflection) for each reflecting polygon along the ray-path is (see Figure 4.27):

$$\widetilde{E}_{V_M} = \begin{bmatrix}\widetilde{E}_{V_1}\\ \widetilde{E}_{V_2}\\ \cdots\\ \widetilde{E}_{V_n}\end{bmatrix} \tag{4.61}$$

$$\widetilde{E}_{H_M} = \begin{bmatrix}\widetilde{E}_{H_1}\\ \widetilde{E}_{H_2}\\ \cdots\\ \widetilde{E}_{H_n}\end{bmatrix} \tag{4.62}$$

where $\widetilde{E}_{V_n}$ is the complex vertical electric field component and $\widetilde{E}_{H_n}$ is the complex horizontal electric field component. $\widetilde{E}_{V_n}$ is the reflected complex vertical electric field component at the receiver (see Figure 4.27).

5. ***Phase difference***

The phase angle difference between vertically and horizontally polarised components of electric field for the j+1th ray-segment (RG^{j+1}) is:

$$e^{j\phi_{V,j+1}} = \arg\left(\widetilde{E}_{V,j+1}\right)-\arg\left(\widetilde{E}_{H,j+1}\right) \tag{4.63}$$

and the phase angle matrix, $e^{\phi_{VM}}$ for each ray-segment (RG) is:

$$e^{j\phi_{VM}} = \begin{bmatrix}e^{j\phi_{V1}}\\ e^{j\phi_{V2}}\\ \cdots\\ e^{j\phi_{Vn}}\end{bmatrix} \tag{4.64}$$

where, $e^{j\phi_{Vn}}$ is phase angle difference of the vertically polarised components and the subscript n is the number of ray-segments (RGs) along the ray-path.

6. ***Angle-of-Arrival (AoA)***

As described earlier, we assumed vertical transmitting and receiving antennas. The AoA at the receiving antenna, θ_A is found using:

$$\theta_A = \cos^{-1}\left(\hat{\underline{k}}_1 \cdot \hat{\underline{z}}_R\right) \tag{4.65}$$

where $\hat{\underline{z}}_R$, is the unit orientation vector of the receiving antenna and $\hat{\underline{k}}_n$ is the direction propagation vector of nth (i.e. last) ray-segment, RG_n.

7. ***Radiation pattern of the receiving antenna***
The radiation pattern of the receiving antenna (i.e. field strength gain) at the receiver, E'_{θ_A} is [404]:

$$E'_{\theta_A} = \left[\frac{\cos\left(\frac{kL_{DP}}{2}\cos\theta_A\right) - \cos\left(\frac{kL_{DP}}{2}\right)}{\sin\theta_A}\right] \tag{4.66}$$

where k is the wave number, L_{DP} is the length of the receiving dipole antenna and θ_A is the AoA at the receiver.

8. ***Received field strength due to reflected ray-path***
We assumed vertical polarisation. Here, we find the vertical received field strength at the receiver, Rx.

(i) The received power, P_R is given by:

$$P_R = A_e S_R = \frac{V_R^2}{Z_L} \tag{4.67}$$

where V_R is the voltage developed at the antenna terminals, Z_L is antenna load impedance, S_R is incident power density and A_e is the effective area of the receiving antenna which is related to antenna gain via:

$$A_e = \frac{\lambda^2}{4\pi} G_R \tag{4.68}$$

The gain of receiving antenna can be expressed as:

$$G_{\max} = G_R = \frac{2}{Q} \tag{4.69}$$

where $G_{\max}$ is the maximum gain of the receiving antenna and Q is defined in Appendix 1(see Eq.(A.11), [404].

The incident power density S_R is related to incident electric field by:

$$S_R = \frac{\left|\tilde{E}_{V_n}\right|^2}{Z_o} \tag{4.70}$$

where $\left|\tilde{E}_{V_n}\right|$ is the magnitude of complex vertically polarised electric field component of the last ray-segment or nth ray-segment RG_n.

Substituting Eqs. 4.64, 4.66, 4.70 and 4.68 into Eq. (4.67), we get the received (complex) voltage, i.e.:

$$\tilde{V}_{R_n} = \sqrt{\frac{\lambda^2}{4\pi}\left|E_{V_n}\right|^2 (G_{\max})\frac{Z_L}{Z_o}} e^{j\phi_n} E'_{\theta_A} \tag{4.71}$$

9. ***Received field due to direct (LoS) ray-path***
The received field strength, $V_{R,LOS}$, of the direct (or LoS) ray path can be obtain using the Equations described section 3.4.2.1 (see Eq. 3.9 and Figure 3.8), i.e.

$$V_{R,LOS} = \sqrt{P_T G_T G_R \left(\frac{\lambda}{4\pi R}\right)^2 Z_L} \tag{4.72}$$

where P_T is transmitted power, G_T is the gain of the transmitting antenna, G_R is the gain of the receiving antenna, Z_L is the load impedance, λ is wavelength and R is the distance between the transmitter and the receiver.

10. ***Received field strength due to ground reflection***
In order to find the equivalent source due to the (specular) ground reflection (GR), (see chapter 3, section 3.4.2.2.2, Figure 3.8) the sub-procedure EQUIV_SOURCES_GROUND_REF was developed. It is similar to the EQUIV_SOURCES_REF algorithm except that the Fresnel parallel reflection coefficient is found from the ground surface. Therefore:

$$\tilde{V}_{R,GR} = \sqrt{\frac{\lambda^2}{4\pi}\left|E_{V_{GR}}\right|^2 (G_{\max})\frac{Z_L}{Z_o}} e^{j\phi_G} E'_{\theta_A} \tag{4.73}$$

11. ***Output of equivalent sources***
Finally, the EQUIV_SOURCES_REF procedure executes a loop from step 1 to step 10 for each valid (or filtered) ray-path and generates a received complex received signal, $\tilde{V}_R$ and optical path length, PL for each valid ray-path from the transmitter to the receiver. The outputs of the procedure are:

$$\tilde{V}_R = \left[\tilde{V}_{R_1}\right] \tag{4.74}$$

$$PL = \left[PL_1\right] \tag{4.75}$$

In Eq. (4.74) $\tilde{V}_{R_1}$ is the complex received voltage generated by the first valid ray-path, In Eq. (4.75.) PL_1 is the optical path length from the transmitter to the receiver of the first valid ray-path. If a LOS ray-path exits, the procedure generates a LoS received field strength, $V_{R,LOS}$ and a ground reflected field strength, $\tilde{V}_{R,GR}$ (and their corresponding optical path lengths):

$$V_{R,LOS} = [V_{R,LOS}] \quad (4.76) \qquad \tilde{V}_{R,GR} = [\tilde{V}_{R,GR}] \quad (4.77)$$

$$PL_{LoS} = [PL_{Los}] \quad (4.78) \qquad PL_{GR} = [PL_{GR}] \quad (4.79)$$

In order to plot ray-paths from the transmitter to receiver, the procedure also generates the sequence number of each reflecting polygon (RP) and the associated location vectors of point-of-reflections (PORs).

4.4.4.15 Output of reflection procedure

The REFLECTION procedure (Block 3, Figure 4.1) generates matrices of received complex voltage, $\tilde{V}_{R,M}$, optical path length, PL_M , the sequence number of each reflecting polygon (RP) and their associated location vectors of point-of-reflections (PORs), $\underline{POR}_M$, for all valid reflected ray-path from the transmitter to the receiver, i.e.:

$$\tilde{V}_{R,M} = \begin{bmatrix} \tilde{V}_{R,1} \\ \tilde{V}_{R,2} \\ \cdots \\ \tilde{V}_{R,N} \end{bmatrix} \quad (4.80) \qquad PL_M = \begin{bmatrix} PL_1 \\ PL_2 \\ \cdots \\ PL_N \end{bmatrix} \quad (4.81) \qquad \underline{POR}_{n,M} = \begin{bmatrix} \underline{POR}_{1,1} \\ \underline{POR}_{2,1} \\ \cdots \\ \underline{POR}_{n,N} \end{bmatrix} \quad (4.82)$$

Figure 4.28 shows a simplified flow diagram of the reflection procedure (Block 3, Figure 4.1).

4.4.5 POSSIBLE_PATHS_DIF

The procedure POSSIBLE_PATHS_DIFF (Block 4.1, Figure 4.1 and Block 4.1, Figure 4.4) represents an implementation of the diffraction visibility-matrix. The purpose of this procedure is finding all possible paths that might support a valid, diffracted, ray. This procedure is similar to the POSSIBLE_PATHS_REF procedure described earlier in section 4.4.4, for the reflection case. The only difference is that all building polygons are replaced by the building edges.

POSSIBLE_PATHS_DIF generates a $P \times N_b$ matrix, where P is the number of diffracted possible ray-paths found and N_b is the maximum number of interactions specified by the user. Each row of this matrix represents a possible diffracted ray-path given as a sequence of building edge numbers.

The input to this procedure is the database POLY_ENV and the output is the matrix of all possible diffracted ray-paths (Block 4.1.4, Figure 4.4). A detailed

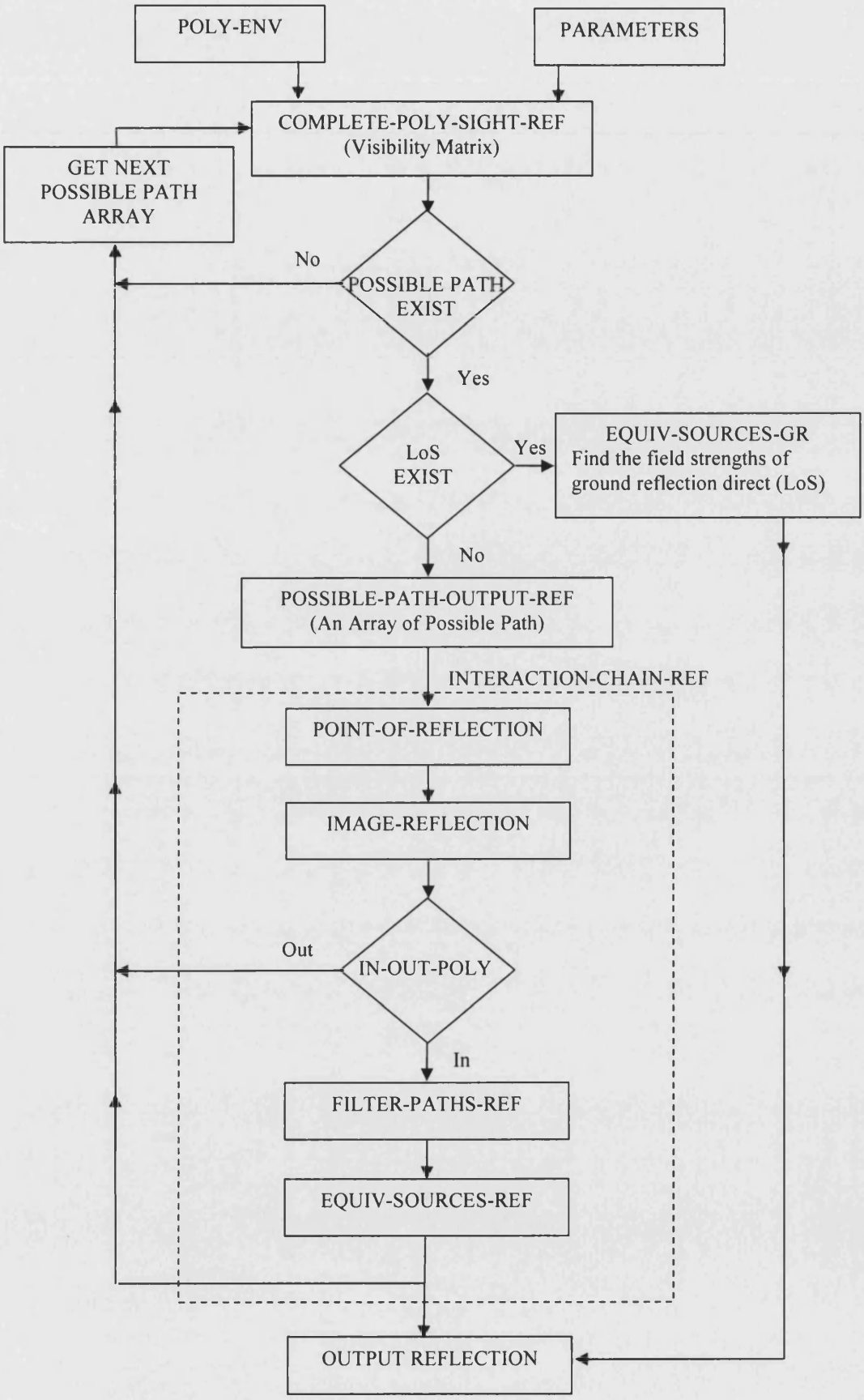

Figure 4.28: *Simplified flow diagram for REFLECTION procedure.*

breakdown of POSSIBLE_PATHS_DIFF into its component subroutines is given in Figure 4.4. The following sections briefly describe the software structure and corresponding subroutines.

4.4.5.1 ENV_EDGE_SIGHT

ENV_EDGE_SIGHT (Block 4.1.1, Figure 4.4) is a procedure to calculate the diffraction visibility-matrix. The inputs to this procedure are the POLY_ENV, QUICK_ACCESS, BUILDINGS_LIST and EDGE_LIST matrices and the output is the diffraction visibility-matrix. QUICK_ACCESS and BUILDINGS_LIST matrices were described earlier (see Sections 4.4.4.2 and 4.4.4.3). The subroutines of this procedure are as follows.

4.4.5.2 EDGES_LIST

EDGES_LIST (Block 4.1.1.3, Figure 4.4) constructs a $2 \times N$ matrix (where N is the number of building edges in environment database) and contains all information relating building edges (not part of the ground) in the environment database. The edges are ordered without ambiguity.

The input to this procedure is the database POLY_ENV and the output is the $N \times 2$ EDGES_LIST matrix.

4.4.5.3 EDGES_SIGHT

EDGES_SIGHT (Block 4.1.1.5, Figure 4.4) is a kernel procedure of the diffraction visibility-matrix. It generates the $N \times N$ matrix EDGES_SIGHT (N is the number of all edges of all buildings in the environment database). This procedure is equivalent of POLYGONS_SIGHT matrix for the building edges. The principle is to use the fact that an edge is defined as the intersection of two polygons of the building. Thus the information about the edges is contained in the POLYGONS_SIGHT matrix (see Section 4.4.4.4) and this procedure just extracts the information about building edges.

The inputs to this procedure are the outputs of QUICK_ACCESS, BUILDING_LIST, EDGES_LIST and POLYGONS_SIGHT matrices. The output of the procedure is the $N \times N$ EDGES_SIGHT matrix. This matrix is filled with 0s and 1s representing visible and non-visible conditions, respectively. This is the environment diffraction visibility matrix described in Section 4.4.3.1.

4.4.5.4 SHADOWING_2D_GROUND_Tx_Rx_DIFF

The procedure SHADOWING_2D_GROUND_Tx_Rx_DIFF (Block 4.1.2, Figure 4.3) is an implementation of diffraction visibility-matrices for the transmitter and receiver as described in Section 4.4.3.1. It determines the diffracting building edges which are visible from transmitter or receiver. It is equivalent to the SHADOWING_2D_GROUND_Tx_Rx_REF matrix, described earlier for reflections (see Section 4.4.4.5). The only difference is that the building polygons are replaced by the building edges.

The inputs to SHADOWING_2D_GROUND_Tx_Rx_ are the environment database POLY_ENV, QUICK_ACCESS, BUILDINGS_LIST, EDGES_SIGHT matrices and the location of Tx and Rx. The outputs of the procedure are two $1 \times N+2$ visibility matrices, one for Tx and the other for Rx. They are filled with 0s and 1s following the same rules as used in the POLYGONS_SIGHT and SHADOWING_2D_GROUND_Tx_Rx_REF matrices described in Sections 4.4.4.4 and 4.4.4.5, respectively.

4.4.5.5 COMPLETE_EDGE_SIGHT_DIF

COMPLETE_EDGE_SIGHT_DIF (Block 4.1.3, Figure 4.4) is a complete or combined visibility-matrix of diffracting edges of the buildings and the visibility-matrices for Tx and Rx. A schematic illustration of the complete visibility-matrix for diffraction, filled with 1s and 0s, is shown in Figure 4.29.

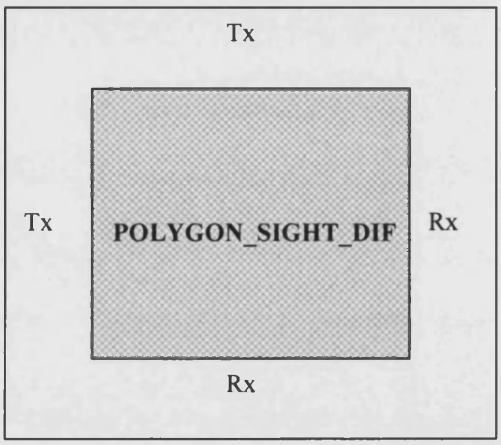

Figure 4.29: *Schematic illustration of the COMPLETE_EDGE_SIGHT_ DIF matrix.*

The inputs to COMPLETE_EDGE_SIGHT_DIF are the outputs of EDGES_SIGHT and SHADOWING_2D_GROUND_Tx_Rx_DIFF. The output of the COMPLETE_EDGES_SIGHT_DIF matrix is an $(N+2) \times (N+2)$ matrix, where N is the number of diffracting edges in the modelled environment. It is a complete visibility matrix for all possible diffracted ray-paths from the transmitter to the receiver as described in Section 4.4.3.1.

4.4.5.6 Distributed partitioning and segmentation technique for diffraction

In order to reduce computational complexity, reduce processing time and avoid memory deadlocks for diffraction, a distributed partitioning and segmentation technique has been developed and implemented. This algorithm is equivalent to that for distributed partitioning and segmentation in the reflection case (see Figure 4.19) except that the building polygons are replaced by building edges.

The algorithm is used to make partitions and segments of the COMPLETE_EDGE_ SIGHT_DIF matrix. This matrix is a complete visibility matrix for the modelled environment.

The output array, called POSSIBLE_PATHS_OUT_DIF, contains a sequence of successive diffracting building edge numbers.

4.4.5.7 INTERACTION_CHAIN_DIF

INTERACTION_CHAIN_DIF (Block 4.2, Figure 4.5) represents the UTD kernel of the ray-tracing diffraction calculations. Once an array of edges possibly supporting a diffracted ray-path has been generated, the interaction chain (or matrix) of images and corresponding point-of-diffraction (POD) are found. Finally valid, unobstructed (i.e. 'filtered'), diffracted ray-paths from Tx to Rx are found and the optical-path-length, PL, of the ray-paths are calculated.

The input to this procedure is an array of possible diffracted ray-path and the location of the transmitter and the receiver from the PARAMETER database. The output is an array containing a location chain of unobstructed (i.e. valid) points of diffraction from Tx to Rx. The following sections describe the software structure and the corresponding subroutines used in INTERACTION_CHAIN_DIF procedure.

4.4.5.8 IMAGES_DIFFRACTION

IMAGES_DIFFRACTION (Block 4.2.1, Figure 5.5) finds the successive image locations of the transmitter for each diffracting edge along the ray-path. The vector geometry on which IMAGES_DIFFRACTION is based is described below.

The algorithm is developed in such a way to construct the images of the transmitter for the multiple diffracting edges along the possible diffracted ray-path. The image of a point is constructed knowing that the next one has to be in a plane defined by two edges. Figure 4.30 shows the vector geometry used to drive the image coordinates.

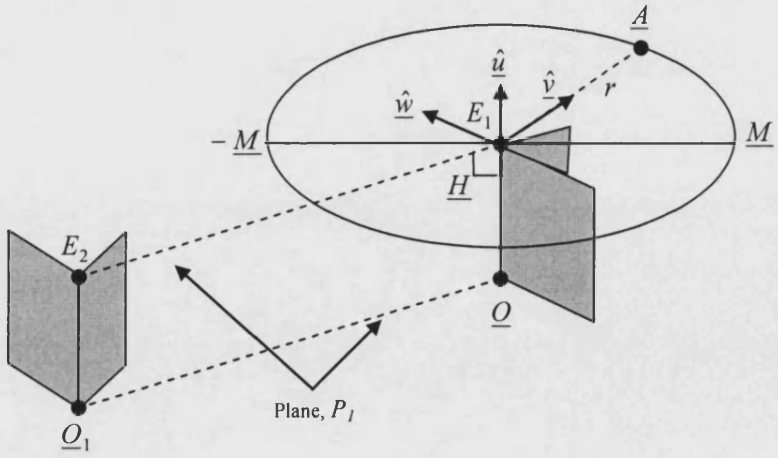

Figure 4.30: *Illustration of vector geometry used to drive the image coordinates.*

The algorithm rotates the original location vector, $\underline{A}$, around the first edge, E_1, in a plane which is orthogonal to E_1 until it lies in the plane defined by the two edges, i.e. E_1 and E_2. In order to simplify the calculation of the problem, a new

system of coordinates is used. The new system of coordinates is $\underline{H}(\hat{v}\ \hat{w}\ \hat{u})$. $\underline{H}$ is the origin vector of new system, (see Eq. 4.83) is the orthogonal projection of $\underline{A}$ onto the first edge, E_1, $\hat{v}$ is the unit vector going towards A, $\hat{u}$ is the unit direction vector of E_1 (i.e. going from the first point of E_1 towards the second point of E_1). By default the first point of E_1 is called $\underline{O}$, $\hat{w}$ is constructed such as the new system is an orthogonal system. The base of $\underline{H}$ is:

$$\underline{H} = \underline{O} + ((\underline{O} \cdot \underline{A})\hat{u})\hat{u} \tag{4.83}$$

$\hat{v}$ is:

$$\hat{v} = \frac{\underline{A} - \underline{H}}{|\underline{A} - \underline{H}|} \tag{4.84}$$

and $\hat{w}$ is:

$$\hat{w} = \hat{u} \times \hat{v} \tag{4.85}$$

Knowing the unit vectors, $\hat{v}$, $\hat{w}$ and $\hat{u}$ we can get the passage matrix, P, between the original base and the new base, i.e.:

$$P = [\hat{v}\ \hat{w}\ \hat{u}] \tag{4.86}$$

The P matrix is invertible by definition as it is the passage matrix between two orthogonal bases. We take the first point of next edge (i.e. E_2) and find the coordinates of this point, O_1 in the new base using:

$$\underline{O_1}' = P^{-1}(\underline{O_1} - \underline{H}) \tag{4.87}$$

The solution M is the location vector defined as:

$$x^2 + y^2 + z^2 = r^2 \tag{4.88}$$

where, x, y and z are the coordinates of M. M belongs to plane P_1 (see Figure 4.30), which is the plane defined by $(\hat{u}, \underline{k})$ and:

$$r = |\underline{M} - \underline{H}| \quad (4.89) \qquad k = \underline{O}'_1 = (k_1, k_2, k_3) \quad (4.90) \qquad z = 0 \tag{4.90}$$

$$\det\begin{bmatrix} \hat{u} \\ \underline{k} \\ \underline{M} \end{bmatrix} = 0 \tag{4.91}$$

Substituting, $z = 0$ in Eq. (4.88), we get:

$$x^2 + y^2 = r^2 \tag{4.92}$$

Solving Eq. (4.91) we get:

$$k_1 y - k_2 x = 0 \tag{4.93}$$

Assuming $k_1 \neq 0$ and solving Eq. (4.93), we get:

$$x = r / \sqrt{1 + \left(\frac{k_2}{k_1}\right)^2} \tag{4.94}$$

$$y = \frac{k_2}{k_1} x \tag{4.95}$$

We have two solutions of M i.e. $M_1(x, y, z)$ and $M_2(-x, -y, -z)$. We identify the solution which is furthest from Edge 2 (E_2) and then convert the coordinates of the solution M back to the original base as:

$$\underline{A}' = \underline{H} + PM \tag{4.96}$$

where $\underline{A}'$ is the image of the original location vector, $\underline{A}$. The only restriction to this method is that the four points defining the two edges have to be coplanar. This condition is thus checked each time before performing this rotation. Since the buildings have vertical walls and horizontal roofs, this limitation has nearly no effects on the accuracy of ray-tracer. A potential limitation, however, occurs when several interactions occur including both horizontal and vertical edges.

Finding the transmitter images by using the transmitter rotation method described above, is geometrically simple, exact and within the approximations of UTD. The transmitter rotation method locates the image of the transmitter in all plane facets of the environmental scatterers and then identifies precise points of geometrical diffraction from intersections of the straight lines connecting image and receiver and the facet producing in the image. (If the straight line does not intersect the physical facet then no UTD path exists.) This process is repeated using the images of images as many times ads desired until some criteria (e.g. maximum permitted number of interactions) has been reached. Figure 4.31 illustrates the method for first and second order transmitter images.

The inputs to this procedure are the location vector of transmitter, $\underline{Tx}$, an array of edges forming a possible path and the location vector of the receiver, $\underline{Rx}$. The input format of the procedure for n^{th} diffraction interaction is:

$$\begin{bmatrix} E_1 \\ E_2 \\ \cdots \\ E_n \end{bmatrix} \tag{4.97}$$

where, E_n is the diffracting edge and the subscript n is the number of interactions along the possible path.

The IMAGES_DIFFRACTION algorithm can be summarised as follows:

1. Select location vector of the transmitter, $\underline{Tx}$
2. Select the first element of the input array (i.e. the first edge number in the array, e.g. E_1)

3. Find the first order image, $\underline{Tx}_1'$
4. Select $\underline{Tx}_1'$
5. Select the next element of the input array (i.e. the second edge number in the array, e.g. E_2)
6. Find the second order image, $\underline{Tx}_2'$
7. Repeat steps 4 through 6 each time a new location of the image is obtained

The output of the IMAGES_DIFRACTION procedure is a chain of transmitter image location vectors (see Section 4.4.4.9, Eq. 4.9).

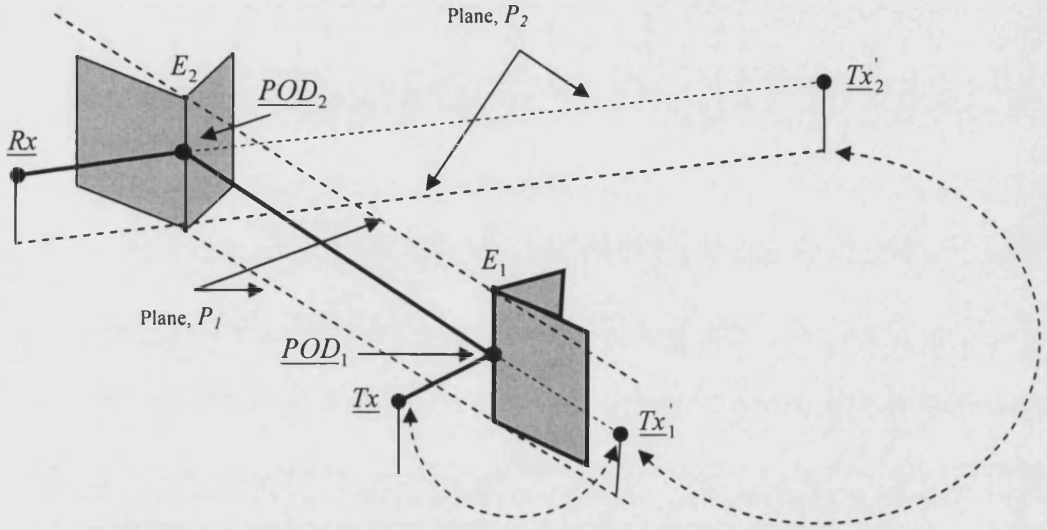

Figure 4.31: *3D illustration of first and second order transmitter images ($\underline{Tx}_1'$ and $\underline{Tx}_2'$) of a Tx, where POD is point-of-diffraction while all other parameters are apparent.*

4.4.5.9 POINT_OF_DIFFRACTION

The procedure POINT_OF_DIFFRACTION (Block 4.2.2, Figure 4.5) is used to find all point-of-diffractions (PODs) on diffracting edges along the ray-path. The vector geometry used by this procedure is described below.

The algorithm calculates the POD (i.e. intersection line between transmitter image $\underline{Tx}'$ and receiver, $\underline{R}_x$. Figure 4.32 shows the UTD vector geometry used to derive the coordinates of the POD.

The principle is to build a new coordinate system, where the problem is solvable in 2D. The new coordinate system is $\underline{O}_1\left(\hat{\underline{i}}\ \hat{\underline{j}}\ \hat{\underline{k}}\right)$. $\underline{O}_1$ is the first point of the edge, E_1, $\hat{\underline{j}}$ is the unit vector of E_1, $\hat{\underline{i}}$ is the unit vector orthogonal to $\hat{\underline{j}}$ with a specific orientation and $\hat{\underline{k}}$ is the unit vector to complete the orthogonal base. Knowing the unit vectors, $\hat{\underline{i}}$, $\hat{\underline{j}}$ and $\hat{\underline{k}}$ we can get the passage matrix, P between the original base and the new base as:

$$P = \left[\hat{\underline{i}}\ \hat{\underline{j}}\ \hat{\underline{k}}\right] \tag{4.98}$$

Note that, the P matrix is invertible by definition as it is the passage matrix between two orthogonal bases.

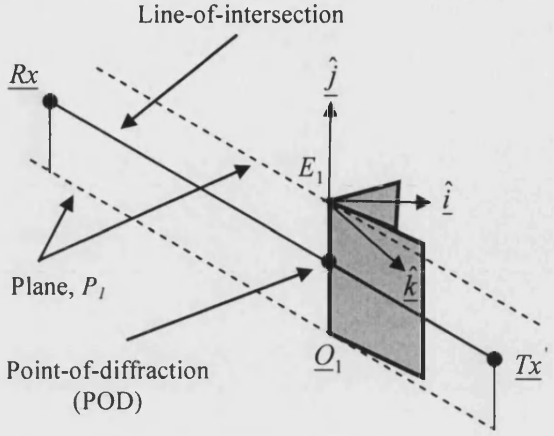

Figure 4.32: *UTD vector geometry for the calculation of a Point-of-diffraction, POD.*

The problem is then solved in the plane $(\hat{\underline{i}}, \hat{\underline{j}})$ (see Figure 4.32), because we know the expression of the coordinates of $\underline{Rx}$ and $\underline{Tx}'$ i.e. $(0, y, 0)$. We find the coordinates of the receiver ($\underline{Rx}$) and transmitter image ($\underline{Tx}'$) in the new base as:

$$\underline{Rx} = P^{-1}\left(\underline{Rx} - \underline{O_1}\right) \quad (4.99.a) \qquad \underline{Tx}' = P^{-1}\left(\underline{Tx}' - \underline{O_1}\right) \quad (4.99.b)$$

and we find the intersection point (i.e. POD) in the new base as:

$$y = \underline{Rx}(2) - \frac{\underline{Rx}(2) - \underline{Tx}'(2)}{Rx(1) - Tx'(1)}\underline{Rx}(1) \tag{4.100}$$

If y is within the first and second point of the edge, E_1 (that means the intersection point is inside the end points of E_1), then we convert the coordinates of y back to the original base giving the location vector of the POD as:

$$POD = \underline{O_1} + Py \tag{4.101}$$

The POINT_OF_DIFFRACTION procedure works recursively in reverse order i.e. the POD of the last diffracting edge of the possible ray-path is found first and so on. The inputs to POINT_OF_DIFFRACTION are location vector of the receiver, $\underline{Rx}$, and the inverse of the output matrix of the IMAGES_DIFFRACTION procedure. The input format of the procedure for the n^{th} diffraction interaction is similar to the input format of the POINT_OF_REFLECTION procedure (see Section 4.4.4.10, Eq. 4.20).

The POINT_OF_DIFFRACTION algorithm can be summarised as follows.

1. Select the first element of the input array (i.e. the $\underline{Rx}$ location)
2. Select the next element of the input array (i.e. the last Tx image, Tx'_n)
3. Find the point-of-diffraction, POD_n (i.e. the POD of the nth edge of the possible ray-path array)
4. Select POD_n
5. Select the second element of the input array (i.e. the second last Tx image, Tx'_{n-1})
6. Find POD_{n-1}
7. Repeat steps 4 through 6 each time a new location of the POD is obtained

The output format of the POINT_OF_DIFFRACTION is a location chain of valid PODs of the corresponding edges of the possible ray-path.

$$\begin{bmatrix} \underline{POD_1} \\ \underline{POD_2} \\ \cdots \\ \underline{POD_n} \end{bmatrix} \tag{4.102}$$

where, $\underline{POD_n}$, is the location chain of the point-of-diffraction (POD) and the subscript n is the number of PODs of the diffracting edges along the possible ray-path.

4.4.5.10 OPT-PATH_LEN_DIF

The procedure OPT-PATH_LEN_DIF (Block 4.2.3, Figure 4.5) is used to find the total optical length of the ray-path. The inputs to this procedure are the location vector of the transmitter, the output matrix of the POINT_OF_DIFFRACTION and the location vector of the receiver. The input format of the procedure for nth diffraction interactions is:

$$\begin{bmatrix} \underline{Tx} \\ \underline{POD_1} \\ \cdots \\ \underline{POD_n} \\ \underline{Rx} \end{bmatrix} \tag{4.103}$$

The output format of the OPT-PATH_LEN_DIF procedure is similar to the output format of the OPT-PATH_LEN_REF procedure (see Section 4.4.4.12, Eq. 4.24).

4.4.5.11 FILTER_PATHS_DIF

As described earlier, many calculated ray-paths are obscured by intermediate building(s). In order to cope with these situations, a filtering algorithm has been developed to remove such obscured (and therefore invalid) ray-paths.

The procedure FILTER_PATHS_DIF (Block 4.2.4, Figure 4.5) is the diffraction filtering algorithm. The procedure is equivalent to the reflection filtering algorithm, 'FILTER_PATHS_REF' procedure described earlier (see section 4.4.4.13, Figure 4.25). The differences are minor compared to the procedure for the reflection case.

The procedure FILTER_PATHS_DIF is a component of the INTERACTION_CHAIN_DIF procedure, which is used to find unobstructed ray-paths from the transmitter to the receiver (i.e. to select those ray-segments where the LoS between the transmitter, Tx, diffracting edges and the receiver, Rx, exits) and discard those ray-paths which are blocked by intervening building polygon(s).

The inputs to this procedure are the output of the OPT-PATH_LEN_DIF procedure (see Eq. 4.103, described earlier). The output format of the procedure is an $(N + 2 \times 3)$ matrix, where N is the numbers of valid PODs, containing the PODs, the location vector of the transmitter and the location vector of receiver, i.e.:

$$\begin{bmatrix} \underline{Tx} \\ \underline{POD_1} \\ \underline{POD_2} \\ \cdots \\ \underline{POD_n} \\ \underline{Rx} \end{bmatrix} \tag{4.104}$$

The output of the algorithm contains only un-obscured, geometrically valid ray-paths.

4.4.5.11.1 Examples output

Figure 4.33 shows diffracted, un-obstructed (i.e. filtered), and therefore valid, ray-paths between transmitter and receiver. Figure 4.33(a) shows ray-paths with a single interaction. Figure 4.33(b) shows diffracted ray-paths with two interactions. The rapid increase in the number of diffracted ray-paths as the allowed number of interactions increases is apparent.

4.4.5.12 O_FACE

As describer earlier Luebber's heuristically enhanced UTD (see Section 3.4.2.3.10, Chapter 3) is used to find the diffraction coefficients of the diffracting building edges. One of the difficult tasks of a UTD algorithm is to identify the 0-face (zero-face) and the n-face of the diffracting edges along the ray-path. This procedure identifies the 0-face of each diffracting edge along the ray-path and finds (1) the interior angles of each diffracting building along the ray-path, (2) the incidence angles of each diffracting edge of the diffracting building along the ray-path, (3) the incidence and diffracting angles with respect to 0-face of each diffracting edge along the ray-path, and (4) the UNV of each 0-faced polygon along the diffracted ray-path.

O_FACE (Block, 4.2.5, Figure 5.5) is a component of the INTERACTION_CHAIN_DIF procedure which is used to find the 0-face of diffracting building edges. The inputs to the O_FACE procedure are the database POLY_ENV, QUICK_ACCESS, OPT_PATH_LEN_DIF, EDGES_LIST matrices and the array of POSSIBLE _PATHS _OUT_DIF.

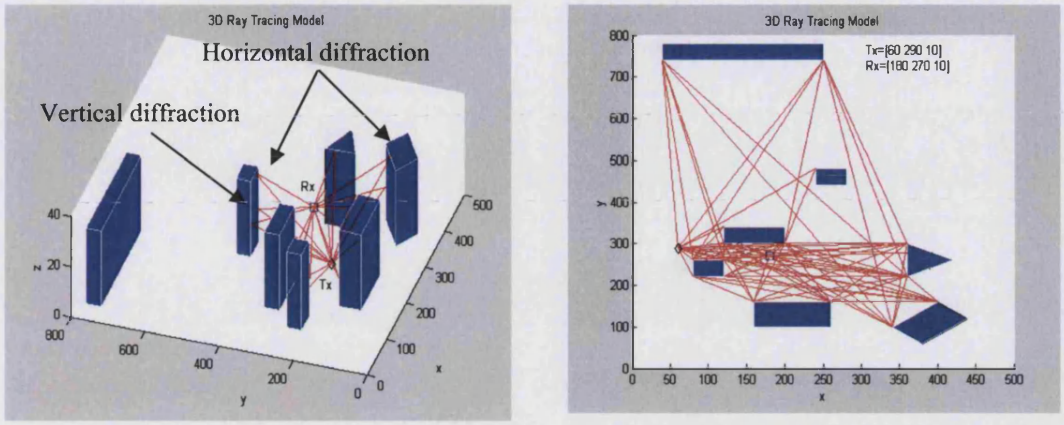

(a) (b)

Figure 4.33*: Examples diffracted un-obscured (filtered or valid) ray-paths* (a) *3D view of reference database showing diffracted ray-paths between transmitter (Tx) and receiver (Rx) with 1-interaction, (b) Plan view of reference database showing diffracted un-obscured (filtered or valid) ray-paths between transmitter(Tx) and receiver(Rx) with 2-interactions.*

As we know that an edge is associated with two polygons (i.e. we use the fact that a diffracting wedge or edge is defined as the intersection of two polygonal facets of a building). In order to find the 0-face of each diffracting edge along the ray-path we consider all possible visible scenarios of each incidence and diffracted ray-segment (RG) of the edges along the ray-path, starting from Tx and ending at Rx, (see Figure 4.34), and find the output parameters of the O_FACE procedure.

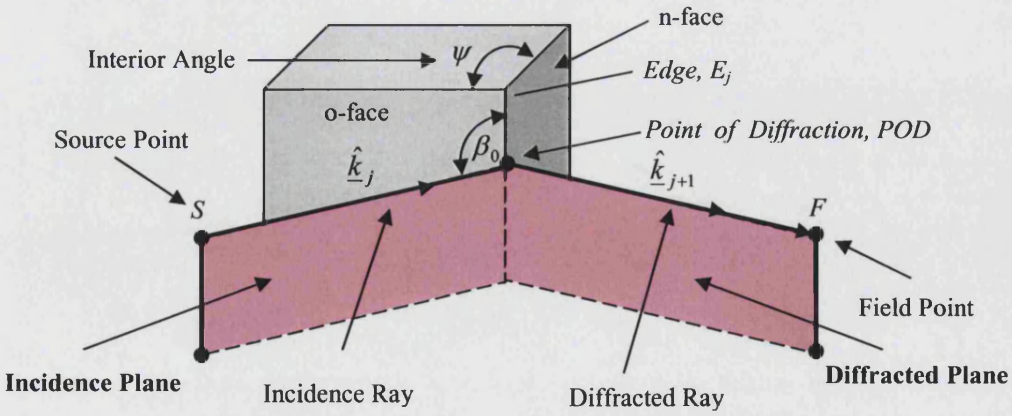

Figure 4.34: *3D UTD geometry for diffraction by a non-curved building edge.*

The O_FACE algorithm proceeds as follows:

1. We obtain a matrix of the unit-normal-vectors (UNVs) of the polygons corresponding to each diffracting edge along the diffracted ray-path as:

$$\hat{\underline{n}}_M = \begin{bmatrix} \hat{\underline{n}}_{11} & \hat{\underline{n}}_{12} \\ \hat{n}_{21} & \hat{\underline{n}}_{22} \\ \cdots & \\ \hat{\underline{n}}_{n1} & \hat{\underline{n}}_{n2} \end{bmatrix} \tag{4.105}$$

   where $\hat{\underline{n}}_{n1}$ and $\hat{\underline{n}}_{n2}$ are the UNVs of two polygons corresponds to the diffracting edge, and the subscript n is the number of diffracting edges along the diffracted ray-path.

2. We obtain the interior angle of each diffracting edge as (Figure 4.34):

$$\psi_j = \cos^{-1}\left(\hat{\underline{n}}_{j1} \cdot \hat{\underline{n}}_{j2}\right) \tag{4.106}$$

   where ψ_j is the interior angle of jth diffracting edge, E_j. Using Eq. (4.105) for each diffracting edge, we obtain a matrix of all the interior angles of all the diffracting edges along the ray-path as:

$$\psi_M = \begin{bmatrix} \psi_1 \\ \psi_2 \\ \cdots \\ \psi_n \end{bmatrix} \tag{4.107}$$

3. We obtain the matrix of unit propagation direction vectors along the ray-path using Eq. (4.29) for the reflection case and Eq. (4.104) for diffraction case, as:

$$\hat{\underline{k}}_M = \begin{bmatrix} \hat{\underline{k}}_1 \\ \hat{\underline{k}}_2 \\ \cdots \\ \hat{\underline{k}}_n \end{bmatrix} \tag{4.108}$$

   where $\hat{\underline{k}}_1$ is the incidence propagation direction vector of the first ray-segment (i.e. incidence to first diffracting edge) and $\hat{\underline{k}}_2$ is the diffracted propagation direction vector of the second ray-segment (i.e. diffracted with respect to the first diffracting edge and incident on the second diffracted edge), and $\hat{\underline{k}}_n$ is the last propagation direction vector of the ray-path as it reaches Rx (see Figure 4. 27, described earlier in Section 4.4.4.14 for reflection case).

4. We obtain the incidence angle of the diffracting edge, E_j, of the building as:

$$\sin_{\beta_{Oj}} = \cos^{-1}\left(\hat{\underline{e}}_j \cdot \hat{\underline{k}}_j\right) \tag{4.109}$$

where $\sin_{\beta_{Oj}}$ is the incidence angle of E_j of the building and $\hat{\underline{e}}_j$ is the UNV of E_j and $\hat{\underline{k}}_j$ is the propagation direction vector of the j[th] ray-segment (see Figure 4.34). Using Eq. 4.109 for each diffracting edge, we obtain the matrix of all the incidence angles for all the diffracting edges along the diffracted ray-path as:

$$\sin_{\beta_{OM}} = \begin{bmatrix} \sin_{\beta_{O1}} \\ \sin_{\beta_{O2}} \\ \cdots \\ \sin_{\beta_{On}} \end{bmatrix} \tag{4.110}$$

5. We find the 0-face polygon, its corresponding UNV, the incidence angles and diffracted angles with respect to the 0-face of each diffracting edge along the ray-path. Knowing the fact that each diffracted edge is associated with two polygons of a building, we consider all possible visible scenarios of each incidence and diffracted ray-segment along the ray-path, starting from the Tx and end at the Rx (see Figure 4.34). In order to simplify the problem and calculate the parameters mentioned above, we consider all possible visibility scenarios of diffracting edges along the ray-path.

Scenario 1:
Only one polygon facet (i.e. polygon face) of E_j can see the incidence propagation direction vector of the j[th] ray-segment (RG_j), $\hat{\underline{k}}_j$. In this case we check the visibility conditions. Figure 4.35 illustrates this scenario. The algorithm for scenario 1 proceeds as follows:

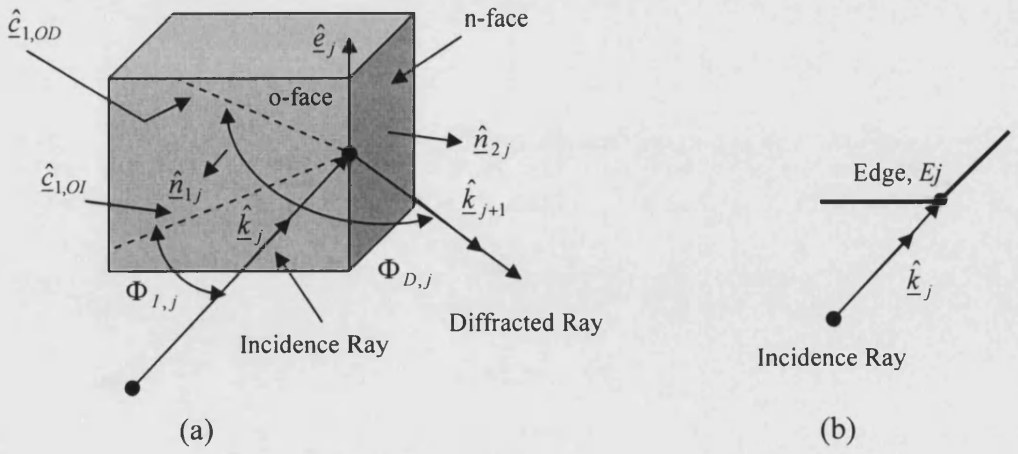

Figure 4.35: *UTD geometry of edge diffraction for scenario 1, (a) 3D- view, (b) 2D plan view.*

(i) Check the visibility conditions of both the polygon faces of E_j with respect to incidence propagation vector, $\hat{\underline{k}}_j$ of jth ray-segment (RGj):

$$\hat{\underline{k}}_j \cdot \hat{\underline{n}}_{j1} \leq 0 \qquad (4.111) \qquad\qquad \hat{\underline{k}}_j \cdot \hat{\underline{n}}_{j2} \leq 0 \qquad (4.112)$$

where $\hat{\underline{k}}_j$ is the UNV of the propagation direction vector of RGj and $\hat{\underline{n}}_{j1}$ and $\hat{\underline{n}}_{j2}$ are the UNVs of the polygon 1 and polygon 2 of E_j. If any of the dot products of Eq. (4.111) or Eq. (4.112) is ≤ 0 then the UNV associated with the polygon can see the incidence propagation direction vector, $\hat{\underline{k}}_j$ and this is the 0-face of E_j, (i.e. the UNV of the incidence polygon, $\hat{\underline{n}}_{OI,j}$ can see $\hat{\underline{k}}_j$) so we store it. In the example of Figure 4.35 polygon 1 is the 0-face of the *Ej*, therefore $\hat{\underline{n}}_{OI,j} = \hat{\underline{n}}_{1j}$ (see Eq. 4.105).

(ii) Find the direction vector of the 0-face polygon of E_j with respect to the incident propagation direction vector of the jth ray-segment, RGj, $\hat{\underline{k}}_j$ as (Figure 4.35):

$$\hat{\underline{c}}_{i,OI} = \frac{\hat{\underline{k}}_j - \left|\left(\hat{\underline{k}}_j \cdot \hat{\underline{n}}_{ij}\right)\hat{\underline{n}}_{ij}\right|}{\left|\hat{\underline{k}}_j - \left(\hat{\underline{k}}_j\right)\hat{\underline{n}}_{ij}\right|} \qquad (4.113)$$

where $\hat{\underline{n}}_{ij}$ is the ith UNV of the polygon (i.e. polygon 1 or polygon 2) and $\hat{\underline{c}}_{i,OI}$ is the direction vector of the ith polygon (i.e. polygon 1 or polygon 2) from which we need to find the incidence angle from the 0-face, $\Phi_{I,j}$ where the subscript I represents the incidence angle from the 0-face polygon and the subscript j represents the jth diffracting edge, i.e. E_j (see Figure 4.35). The problem with $\hat{\underline{c}}_{i,OI}$ is that we don't know whether it is pointing inside or outside of the 0-face polygon of the diffracting edge. Therefore we make an artificial point P_I.

(iii) We establish whether P1 is inside or outside the 0-face polygon using:

$$P_1 = POD_j + \Delta\hat{\underline{c}}_{OI,j} \qquad (4.114)$$

where POD_j is the point-of-diffraction of E_j and Δ is a small (incremental) distance. We use the procedure IN_OUT_POLY defined earlier in section 4.4.4.11 (see Block 3.2.3, Figure 4.5). If P_I is inside the polygon, the direction of vector $\hat{\underline{c}}_{i,OI}$ remains the same otherwise we set $\hat{\underline{c}}_{i,OI}$ as:

$$\hat{\underline{c}}_{i,OI} = -\hat{\underline{c}}_{i,OI} \qquad (4.115)$$

(iv) We find the incidence angle, $\Phi_{I,j}$ with respect to 0-face of E_j, as (Figure 4.35):

$$\Phi_{I,j} = \cos^{-1}\left(-\hat{\underline{k}}_j \cdot \hat{\underline{c}}_{i,OI}\right) \tag{4.116}$$

where $-\hat{\underline{k}}_j$ is the inverse of the incidence propagation direction vector of E_j and $\hat{\underline{c}}_{i,OI}$ is the direction vector of the 0-face polygon with respect to the incident ray.

(v) We find the direction vector of the 0-face polygon of the jth diffracting edge, E_j with respect to the diffracting propagation direction vector of the j+1th ray-segment, RGj, $\hat{\underline{k}}_{j+1}$ as (Figure 4.35):

$$\hat{\underline{c}}_{i,OD} = \frac{-\hat{\underline{k}}_{j+1} - \left[\left(-\hat{\underline{k}}_{j+1} \cdot \hat{\underline{n}}_{ij}\right)\hat{\underline{n}}_{ij}\right]}{\left|-\hat{\underline{k}}_{j+1} - \left(-\hat{\underline{k}}_{j+1}\right)\hat{\underline{n}}_{ij}\right|} \tag{4.117}$$

where $\hat{\underline{n}}_{ij}$ is the ith UNV of the polygon (i.e. polygon 1 or polygon 2), $-\hat{\underline{k}}_{j+1}$ is the inverse of diffracted propagation direction vector of the j+1th ray-segment, RGj and $\hat{\underline{c}}_{i,OD}$ is the direction vector of the ith polygon (i.e. polygon 1 or polygon 2) from which we need to find the diffracted angle from the 0-face, $\Phi_{D,j}$ where the subscripts D represents the diffracted angle from the 0-face polygon and the subscript j represents the jth diffracting edge, E_j . The same test is applied to establish whether the point $\hat{\underline{c}}_{i,OD}$ is inside or outside the 0-face, see Eq. (4.114).

(vi) We find the diffracted angle, $\Phi_{D,j}$ with respect to the 0-face of E_j, as (Figure 4.35):

$$\Phi_{D,j} = \cos^{-1}\left(\hat{\underline{k}}_{j+1} \cdot \hat{\underline{c}}_{i,OD}\right) \tag{4.118}$$

where $\hat{\underline{k}}_{j+1}$ is the propagation direction vector of the j+1th ray-segment, RGj+1, (i.e. the diffracted ray, see Figure 4.35) and $\hat{\underline{c}}_{i,OD}$ is the direction vector of the 0-face polygon with respect to diffracted ray.

(vii) Finally, we obtain a matrix of incidence and diffracted angles, Φ_M with respect to the 0-face of E_j along the ray-path as:

$$\Phi_M = \left[\Phi_{I,j} \quad \Phi_{D,j}\right] \tag{4.119}$$

where $\Phi_{I,j}$ and $\Phi_{D,j}$ are the incidence and diffracted angles of E_j with respect to 0-face polygon, respectively.

Scenario 2:
Both polygon faces of the j[th] diffracting edge, E_j can see the incident propagation direction vector of the j[th] ray-segment (RG$_j$), $\hat{\underline{k}}_j$. In this case we check the visibility conditions. Figure 4.36 illustrates this scenario. Algorithm for scenario 2 proceeds as follows:

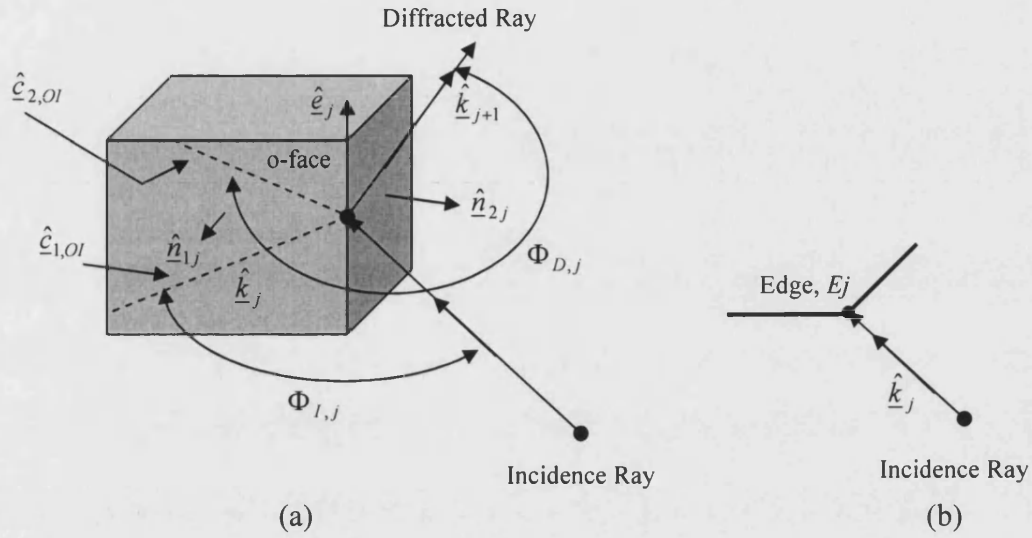

Figure 4.36: *UTD geometry of edge diffraction for scenario 2, (a) 3D- view, (b) 2D plan view.*

(i) We check the visibility conditions of both the polygon faces of E_j with respect to the incident propagation vector for each ray-segment. If the dot product of Eq. (4.111) and Eq. (4.112), described earlier, will be ≤ 0 (see step (i) Scenario 1).

(ii) Using Eq. (4.113) of step (ii) Scenario 1 we find the direction vectors of both polygon faces (i.e. $\hat{\underline{c}}_{1,Ol}$ and $\hat{\underline{c}}_{2,Ol}$) of E_j with respect to incident propagation direction vector of the j[th] ray-segment, RG$_j$, $\hat{\underline{k}}_j$.

(iii) We find the incidence angles with respect to both faces of E_j, as (Figure 4.36):

$$\alpha_1 = \cos^{-1}\left(-\hat{\underline{k}}_j \cdot \hat{\underline{c}}_{1,Ol}\right) \tag{4.120}$$

and

$$\alpha_2 = \cos^{-1}\left(-\hat{\underline{k}}_j \cdot \hat{\underline{c}}_{2,Ol}\right) \tag{4.121}$$

where $-\hat{\underline{k}}_j$ is the inverse of the incident propagation direction vector of the j[th] ray-segment, RG$_j$, and $\hat{\underline{c}}_{1,Ol}$ and $\hat{\underline{c}}_{2,Ol}$ are the direction vectors of both visible polygon faces of E_j with respect to incident propagation direction vector of the j[th] ray-segment, RG$_j$, $\hat{\underline{k}}_j$.

(iv) We obtain the matrix of both incidence angles with respect to both faces of E_j, α_M as:

$$\alpha_M = [\alpha_1 \quad \alpha_2] \tag{4.122}$$

and then test visibility conditions for both incidence angles of the α_M matrix.

Case No.1: The incidence angles of the matrix, α_M (Eq. 122), are not equal i.e. $\alpha_1 \neq \alpha_2$. Figure 4.37 illustrates scenario 2, Case 1. The algorithm for this scenario proceeds as follows:

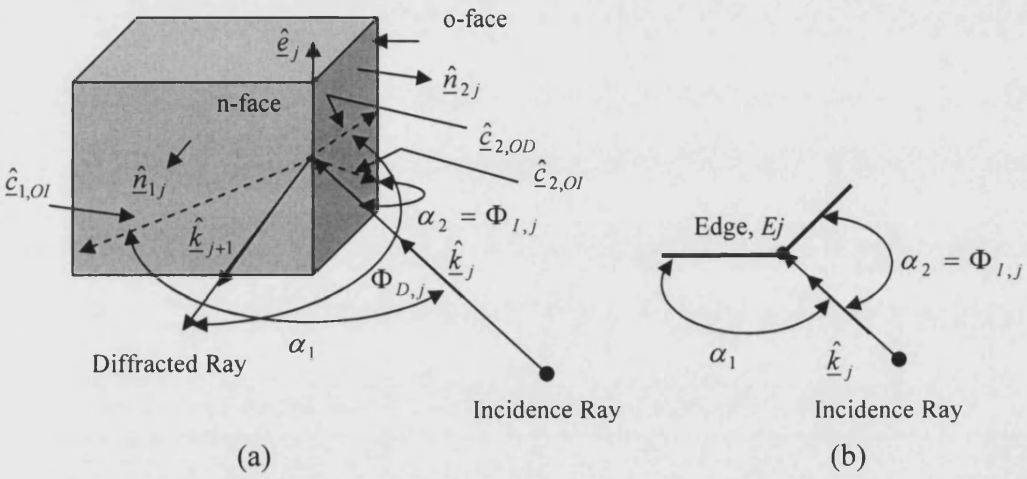

Figure 4.37: *UTD geometry of edge diffraction for scenario 2, Case No.1, (a) 3D- view, (b) 2D plain top view.*

In this case the minimum angle of α_M matrix corresponds to 0-face polygon. For example, in Figure 4.37, α_2 is the incidence angle with respect to polygon 2 of E_j. Therefore, the UNV of polygon 2 is the 0-face polygon (i.e. $\hat{n}_{OI} = \hat{n}_{2j}$) and we store it, and α_2 is the incidence angle, (i.e. $\Phi_{I,j} = \alpha_2$) of the 0-face polygon with respect to incidence propagation direction vector of jth ray-segment, RG$_j$ of E_j.

(v) We find the diffracted angle, $\Phi_{D,j}$ with respect to the 0-face of E_j, as (Figure 4.37):

$$\Phi_{D,j} = \cos^{-1}\left(\hat{k}_{j+1} \cdot \hat{c}_{i,OD}\right) \tag{4.123}$$

where $\hat{c}_{i,OD}$ is the direction vector of the 0-face polygon with respect to diffracted ray. If the inverse of the propagation direction vector, $-\hat{k}_{j+1}$ (i.e. j+1th ray-segment, RG$_{j+1}$ (i.e. diffracted ray) cannot see the 0-face polygon, i.e. $-\hat{k}_{j+1} \cdot \hat{n}_{OI,j} \geq 0$, then $\Phi_{D,j}$ is:

$$\Phi_{D,j} = 360^o - \Phi_{D,j} \tag{4.124}$$

(vi) Finally, obtain a matrix of incidence and diffracted angles with respect to the 0-face of E_j along the ray-path similar to matrix Φ_M defined in Eq. (4.119) (see step (vii), Scenario 1.)

Case No.2: The incidence angles of the matrix, α_M are equal (i.e. $\alpha_1 = \alpha_2$). This occurs when both polygon faces of E_j can see the incident propagation direction vector, $\hat{\underline{k}}_j$ of the jth ray-segment, RG$_j$. Figure 4.38 illustrates scenario 2. The algorithm for scenario 2 proceeds as follows:

In this case we always choose $\hat{\underline{n}}_{1j}$ (see Figure 4.38) as a UNV of the 0-face polygon of E_j (i.e. $\hat{\underline{n}}_{OI,j} = \hat{\underline{n}}_{1j}$) and α_1 as the angle of incidence (i.e. $\Phi_{I,j} = \alpha_1$) with respect to the 0-face of E_j. We store $\hat{\underline{n}}_{OI,j}$ and $\Phi_{I,j}$. Now the problem is to find the diffracted angle, $\Phi_{D,j}$ of the 0-face polygon with respect to diffracted propagation direction vector, $\hat{\underline{k}}_{j+1}$ of j+1th ray-segment, RG$_{j+1}$.

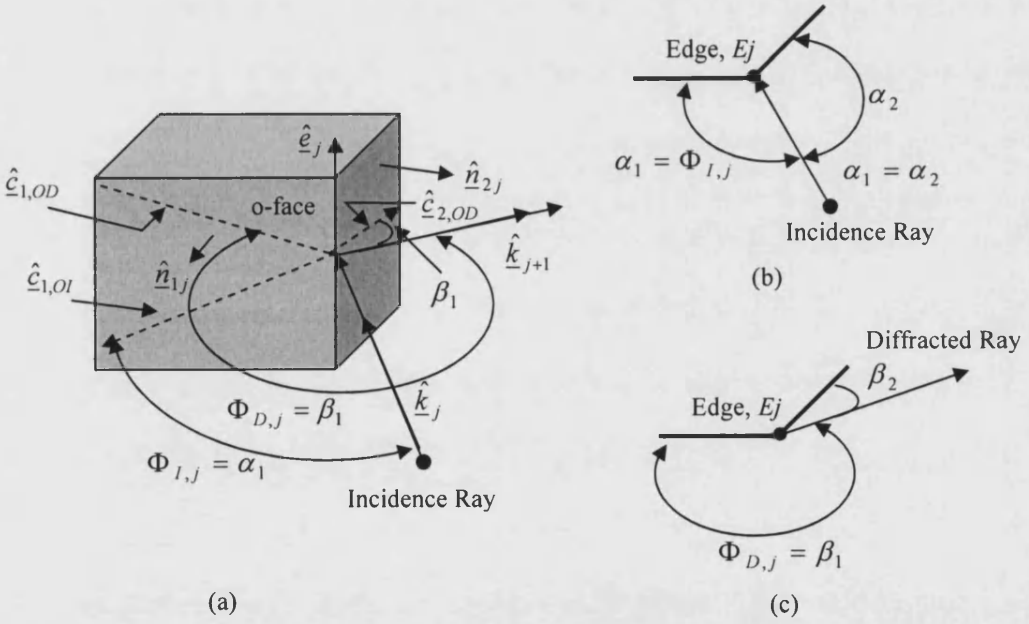

Figure 4.38: *UTD geometry of edge diffraction for scenario 2, Case No.2, (a) 3D- view, (b) 2D plain top view, (c) 2D plain top view.*

(vii) Using Eq. (4.117) of step (v) Scenario 1 we find the direction vectors of both polygon faces (i.e. $\hat{\underline{c}}_{1,OD}$ and $\hat{\underline{c}}_{2,OD}$) of E_j with respect to diffracted propagation direction vector of j+1th ray-segment, $\hat{\underline{k}}_{j+1}$ (see Figure 4.38).

(viii) We find the diffracted angles with respect to both faces of E_j as:

$$\beta_1 = \cos^{-1}\left(\hat{\underline{k}}_{j+1} \cdot \hat{\underline{c}}_{1,OD}\right) \tag{4.125}$$

and

$$\beta_2 = \cos^{-1}\left(\hat{\underline{k}}_{j+1} \cdot \hat{\underline{c}}_{2,OD}\right) \tag{4.126}$$

(ix) We obtain the matrix of both diffracted angles, β_M as:

$$\beta_M = [\beta_1 \quad \beta_2] \tag{4.127}$$

Here we test visibility conditions for both diffracted angles of β_M matrix.

Case No. 3: Both polygon faces of E_j can see incidence propagation direction vector, $\hat{\underline{k}}_j$ of the jth ray-segment, RGj, both incidence angles of α_M matrix in Eq.(4.122) are equal (i.e. $\alpha_1 = \alpha_2$, see Figure 4.38 (b)), diffracted angles of β_M in Eq. (4.127) are not equal (i.e. $\beta_1 \neq \beta_2$, see Figure 4.38 (c)) and only one face of E_j can see the inverse of the propagation direction vector (i.e. the inverse of diffracted ray). Figure 4.38(a-c) illustrates scenario 2, Case 3. The algorithm proceeds as follows:

(x) Check the visibility conditions for both polygon faces of E_j with respect to the diffracted propagation vector, $\hat{\underline{k}}_{j+1}$ of the j+1th ray-segment as:

$$-\hat{\underline{k}}_{j+1} \cdot \hat{\underline{n}}_{1j} \geq 0 \qquad (4.128) \qquad\qquad -\hat{\underline{k}}_{j+1} \cdot \hat{\underline{n}}_{2j} \geq 0 \qquad (4.129)$$

(xi) Find which polygon face (i.e. $\hat{\underline{n}}_{j1}$ or $\hat{\underline{n}}_{j2}$) of E_j cannot see the inverse of the propagation direction vector, $-\hat{\underline{k}}_{j+1}$ of the j+1th ray-segment, RGj+1, and find the diffracted angle, $\Phi_{D,j}$ with respect to that polygon face of E_j. For example, in Figure 4.38(a) and (c) polygon face 1 of E_j cannot see the inverse of propagation direction vector (i.e. $-\hat{\underline{k}}_{j+1} \cdot \hat{\underline{n}}_{1j} \geq 0$). In this case the diffracted angle $\Phi_{D,j}$ can be found from β_M matrix, (Eq. 4.127) as:

$$\Phi_{D,j} = 360^0 - \beta_1 \tag{4.130}$$

Case No. 4: Both polygon faces of E_j can see the incident propagation direction vector, $\hat{\underline{k}}_j$ of the jth ray-segment, RGj, both incidence angles of α_M matrix in Eq.(4.122) are equal (i.e. $\alpha_1 = \alpha_2$, see Figure 4.38 (b)), diffracted angles of β_M in Eq. (4.127.) are not equal (i.e. $\beta_1 \neq \beta_2$, see Figure 4.38 (c)) and both polygons of E_j can see the inverse of the propagation direction vector, $-\hat{\underline{k}}_{j+1}$ of the j+1th ray-segment, RGj+1 (i.e. Eq. (4.128) and Eq. (4.128) are ≥ 0). Figure 4.39 (a-b) illustrates Scenario 2, Case 4.

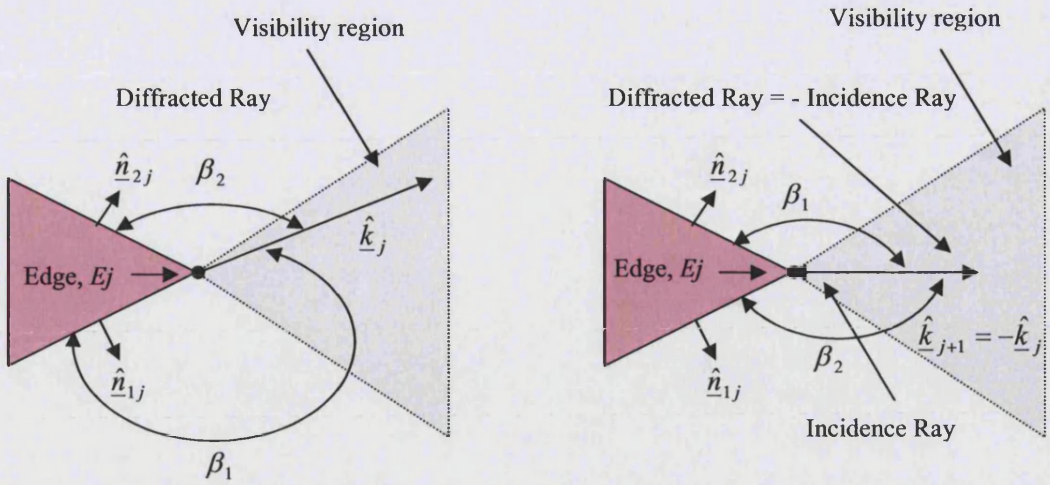

Figure 4.39: *UTD geometry of edge diffraction for scenario 2, Case No.4, (a) 2D plan view for* $\beta_1 \neq \beta_2$ *(b) 2D plan view for* $\beta_1 = \beta_2$.

The algorithm for scenario 2, Case 4 proceeds as follows.

(xii) Find the diffracted angle, $\Phi_{D,j}$ with respect to 0-face of E_j as:

$$\Phi_{D,j} = \max(\beta_M) \tag{4.131}$$

(xiii) Obtain a matrix of incident and diffracted angles with respect to the 0-face of E_j along the ray-path similar to matrix Φ_M defined in Eq. (4.119), see step (vii), Scenario 1.

Case No. 5: Both polygon faces of E_j can see the incident propagation direction vector, $\hat{\underline{k}}_j$ of the jth ray-segment, RG$_j$, both incidence angles of α_M matrix in Eq.(4.122) are equal (i.e. $\alpha_1 = \alpha_2$, see Figure 4.38 (b)), both diffracted angle of β_M in Eq. (4.127) are equal (i.e. $\beta_1 = \beta_2$, see Figure 4.39(c)) and both polygons of E_j can see the inverse of the propagation direction vector, $-\hat{\underline{k}}_{j+1}$ for the j+1th ray-segment (i.e. Eq. (4.128) and Eq. (4.129) are ≥ 0).

This is the case when the incidence angle, $\Phi_{I,j}$ and diffracted angle, $\Phi_{D,j}$ are both equal (i.e. $\hat{\underline{k}}_j = \hat{\underline{k}}_{j+1}$) which means the incident ray and the diffracted ray are both opposite to each other (see Figure 4.39 (b)). The algorithm for Scenario 2, Case 5 proceeds as follows:

(xiv) Find the diffracted angle, $\Phi_{D,j}$ with respect to the 0-face of E_j as:

$$\Phi_{D,j} = \Phi_{I,j} \tag{4.132}$$

(xv) Obtain a matrix of incidence and diffracted angles with respect to the 0-face of E_j along the ray-path similar to matrix Φ_M as defined in Eq. (4.119), see step (vii), Scenario 1.

4.4.5.12.1 Output of O_FACE

The O_FACE (4.2.5, Figure 4.5) procedure generates four output matrices: (1) interior angles, ψ_M, of each diffracting building along the ray-path (see Eq. (4.107) described earlier), (2) incidence angles, $\sin_{\beta_{O,m}}$ for each diffracting edge along the ray-path (see Eq. (4.110 described earlier), (3) incidence and diffracting angles, Φ_M with respect to the 0-face of each diffracting edge along the ray-path, and (4) the UNV of each 0-faced polygon along the diffracted ray-path:

$$\Phi_M = \begin{bmatrix} \Phi_{I,1} & \Phi_{D,1} \\ \Phi_{I,2} & \Phi_{D,2} \\ \cdots\cdots & \\ \Phi_{I,n} & \Phi_{D,n} \end{bmatrix} \tag{4.133}$$

$$\underline{\hat{n}}_{O,M} = \begin{bmatrix} \hat{n}_{O,1} \\ \hat{n}_{O,2} \\ \cdots \\ \underline{\hat{n}}_{O,n} \end{bmatrix} \tag{4.134}$$

In Eq. (4.133), $\Phi_{I,n}$ is the incidence and $\Phi_{D,n}$ is the diffracting angle with respect to the 0-face of each diffracting edge and the subscript n is the number of diffracting edges along the ray-path. In Eq. (4.134) $\underline{\hat{n}}_{O,n}$ is the UNV of the 0-faced polygon.

4.4.5.13 EQUIV_SOURCES_DIF

As described earlier, in order to simplify the problem, two separate sequences of equivalent-sources procedures were developed, one for the reflection case (see section EQUIV_SOURCES_REF) and the other for diffraction case. The procedure EQUIV_SOURCES_DIF is developed to find the equivalent sources for the diffraction case. This section describes in brief the most important procedures used.

The EQUIV_SOURCES_DIF (Block 4.3, Figure 4.1) procedure is used to find the amplitude, phase, polarisation, angle-of-departure (AoD), angle-of-arrival (AoA), optical path length and received field strength for each valid diffracted ray-path; of each equivalent source starting from the transmitter, Tx, and ending at the receiver, Rx. Table 4.4 shows the input parameters (PARAMETERS Block 2, Figure 4.1) used to find the components of the EQUIV_SOURCES_DIF for the reference model.

The input to this procedure is the output of FILTER_PATHS_DIF (Block 4.2.4, Figure 4.5) procedure (see Eq. 4.104, described earlier). The EQUIV_SOURCES_DIF algorithm is equivalent of the EQUIV_SOURCES_REF procedure, described earlier for reflection case (see

Section 4.4.4.14) and the differences are minor. The modification of the EQUIV_SOURCES_DIF algorithm is as follows:

Steps 1 to Step 11 are similar to those of the EQUIV_SOURCES_REF algorithm with the exception of Step 4(ii) to (vi).

The software modifications are described as follows:

1. ***UTD diffraction coefficient***

(i) We use the Luebber's heuristic enhanced UTD diffraction coefficient equations describe in section 3.4.2.3.10 (i.e. Eqs. 3.31 to 3.49). The complex perpendicular, $\tilde{D}_{\perp} = \tilde{D}d$ and complex parallel, $\tilde{D}_{\parallel} = \tilde{D}l$ diffraction coefficients of each diffracting edge along the ray-path are found. A sub-procedure UTD_DIF_COEFF COEFF is developed to find the UTD diffraction coefficients for each diffracting edge (DE) along the ray-path. Using the output of the UTD_DIF_COEFF COEFF, the matrices of perpendicular and parallel UTD diffraction coefficient are obtained:

$$\tilde{D}d_M = \begin{bmatrix} \tilde{D}d_1 \\ \tilde{D}d_2 \\ \cdots \\ \tilde{D}d_n \end{bmatrix} \qquad (4.135) \qquad \tilde{D}l_M = \begin{bmatrix} \tilde{D}l_1 \\ \tilde{D}l_2 \\ \cdots \\ \tilde{D}l_n \end{bmatrix} \qquad (4.136)$$

where $\tilde{D}d_n$ is complex perpendicular diffraction coefficient, $\tilde{D}l_n$ is complex parallel diffraction coefficient and the subscript n is the number of diffracting edges (DEs) along the ray-path.

(ii) **Diffracted electric field components**

The diffracted electric field (see Figure 4.34) for the j^{th}+1 ray-segment (RG_{j+1}) in terms of its complex perpendicularly polarised component of diffracted electric field, $\tilde{E}d_{j+1}$ and complex parallel polarised component of diffracted field, $\tilde{E}l_{j+1}$ can be obtained as:

$$\tilde{E}d_{j+1} = \tilde{E}d_j \tilde{D}d_j \qquad (4.137) \qquad \tilde{E}l_{j+1} = \tilde{E}l_j \tilde{D}l_j \qquad (4.138)$$

(iii) ***Vertically polarised components of electric field***

Using Equations (Eq. 4.45, 4.47, 4.50 and 4.51), we obtain the vertically polarised components of electric field (for the j^{th}+1 ray-segment, RG_{j+1}) as:

$$\begin{aligned} \tilde{E}_{V,j+1} &= \tilde{E}d_{j+1}\left(\hat{\underline{P}}d_{j+1} \cdot \hat{\underline{V}}_{j+1}\right) + \tilde{E}l_{j+1}\left(\hat{\underline{P}}l_{j+1} \cdot \hat{\underline{V}}_{j+1}\right) \\ &= \tilde{E}_{V,j+1}\left(e^{\phi_{j+1}}\right)\sqrt{\frac{R_j + R_{j+1}}{R_{j+1}\left(R_j + R_{j+1}\right)}}\hat{\underline{V}}_{j+1} \end{aligned} \qquad (4.139)$$

All other parameters are similar to those for the reflection case.

(iv) ***Horizontally polarised components of electric field***
Similarly, we obtain the horizontal electric field vector (for the j+1th ray-segment, RG_{j+1}) as:

$$\begin{aligned}\widetilde{E}_{H,j+1} &= \widetilde{E}d_{j+1}\left(\hat{P}d_{j+1}\cdot\underline{\hat{H}}_{j+1}\right)+\widetilde{E}l_{j+1}\left(\hat{P}l_{j+1}\cdot\underline{\hat{H}}_{j+1}\right)\\ &= \widetilde{E}_{H,j+1}\left(e^{j\phi_{j+1}}\right)\sqrt{\frac{R_j+R_{j+1}}{R_{j+1}\left(R_j+R_{j+1}\right)}}\underline{\hat{H}}_{j+1}\end{aligned} \tag{4.140}$$

All other parameters are similar to those for the reflection case.

The EQUIV_SOURCES_DIF procedure does not take account of direct (or LoS) and ground reflection (GR) as these scenarios are already considered in the reflection case.

4.4.5.14 Calibration of the UTD diffraction coefficient

As described above the UTD diffraction coefficients were calculated using the Luebber's heuristic enhanced UTD diffraction coefficient Equations. In order to validate the software the perpendicular diffraction coefficient, $\widetilde{D}_{\perp}=\widetilde{D}d$ was calculated for a perfectly conducting building edge as a function of diffracting angles, $\Phi_d = 0^o$ to 270^o, at 2. 38 GHz with incident angle $\Phi_I = 45$ with respect to the 0-face of the diffracting edge and incident angle $\beta_O = 90^o$ with respect to diffracting edge, and building edge interior angle $\psi = 90^o$. Figure 4.40(a) shows amplitude of the diffraction coefficients of the perfectly conducting building edge. The two peaks at 45° and 225° are due to *reflection/shadow boundaries*. Figure 4.40(b) shows the non-perpendicular diffraction coefficients, $\widetilde{D}_{\perp}=\widetilde{D}d$ with $\varepsilon_r = 3$, $\sigma = 5, 4, 3, 2, 1, 0.8, 0.6, 0.4, 0.2, 0, 0.01, 0.02, 0.04, 0.06, 0.08$.

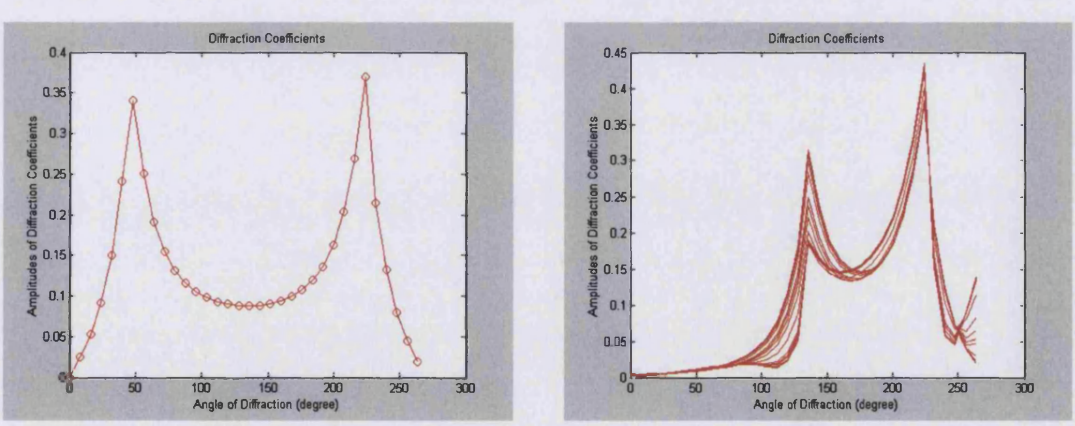

(a) (b)

Figure 4.40: *Diffraction coefficients, (a) Amplitudes of perpendicular UTD diffraction coefficients for perfecting conducting edge, (b) Amplitudes of perpendicular UTD diffraction coefficients for non-perfectly conducting edge.*

The validation of the diffraction coefficients is achieved by comparing Figure 4.40(a) with the results obtained independently in Figure 4.41 by [100], [237].

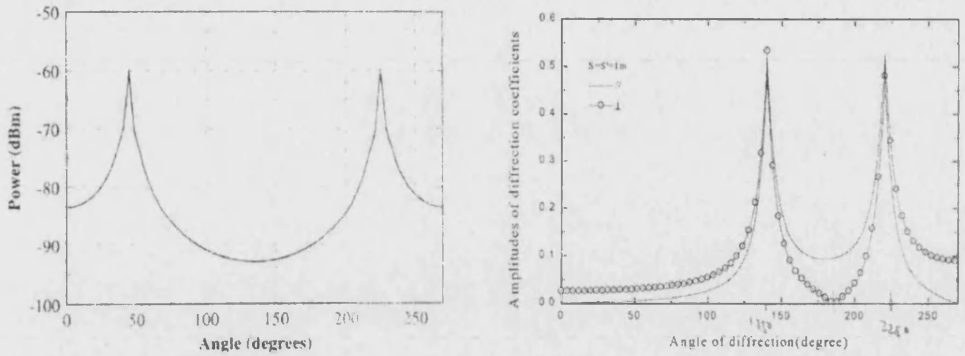

Figure 4.41: *Examples of the diffraction coefficients (a) An example of diffracted power at f = 1.823 GHz, (After Athanasiadou G. [100]), (b) An example of amplitudes of diffraction coefficients at f = 1.8 GHz, (After Ji Z. [237]).*

4.4.5.15 Output of diffraction procedure

The DIFFRACTION (Block 4, Figure 4.1) procedure generates matrices of received complex voltage, $\tilde{V}_{R,M}$, optical path length, PL_M, the sequence number of each diffracting edge (DE) and their associated location vectors of point-of-diffractions (PODs), $\underline{POD}_M$ for all valid ray-path from the transmitter to receiver. The output matrices of the diffraction procedure are similar to those of the reflection case described earlier (see Eqs. 4.80, 4.81 and 4.82) except that in Eq. 4.82 PORs are replaced with PODs.

4.4.5.16 CONSTRUCT_MERGER

The CONSTRUCT_MERGER (Block 6, Figure 4.1) procedure is used to merge the outputs of reflection and diffraction procedures (see Block 3 and Block 4, Figure 4.1).

4.4.5.17 CONSTRUCT_CIRs

The CONSTRUCT_CIRs (Block 7, Figure 4.1) procedure is effectively the output results of the ray-tracing model. The purpose of the procedure is to construct CIRs and their corresponding PDPs. The sub-procedures were developed to calculate channel parameters such as transmission loss, total received power, average delay spread and RMS delay spread for each PDP.

4.4.5.17.1 CONSTRUCT_CIRs_REF

The CONSTRUCT_CIRs_REF (Block 7.1, Figure 4.1) procedure is used to (1) construct CIRS and their corresponding PDPs for all reflected ray-paths, (2) calculate the channel parameters defined earlier, (3) plot CIRs (and/or PDPs), (4) Plot reflected ray-paths in the modelled environment. The inputs to this procedure are matrices of received complex voltage, $\tilde{V}_{R,M}$, optical path length, PL_M, the sequence number of each reflecting polygon (RP) and their associated

location vectors of point-of-reflections (PORs), $\underline{POR}_M$ for all valid reflected ray-path from the transmitter to receiver (see Eqs. 4.80, 4.81 and 4.82, Section 4.4.4.15).

4.4.5.17.2 CONSTRUCT_CIRs_DIF

The CONSTRUCT_CIRs_DIF (Block 7.2, Figure 4.1) procedure is similar to CONSTRUCT_CIRs_REF described earlier but treats diffracted rather than reflected paths.

4.4.5.17.3 CONSTRUCT_CIRs_REF_DIF

The CONSTRUCT_CIRs_REF_DIF (Block 7.3, Figure 4.1) procedure is used to construct combined CIRs and their corresponding PDPs for reflection and diffraction. The inputs to this procedure are the outputs of CONSTRUCT_MERGER procedure (Block 6, Figure 4.1). The procedure is used to (1) construct CIRS and their corresponding PDPs for all valid combined reflected and diffracted ray-paths, (2) calculate the channel parameters defined earlier, and (3) plot CIRs (and/or PDPs).

4.4.5.17.4 PLOT_REF

The PLOT_REF (Block 7.4, Figure 4.1) procedure is used to plot all valid reflected ray-paths in the modelled environment up to certain number of interactions specified by the user.

4.4.5.17.5 PLOT_DIF

The PLOT_DIF (Block 7.5, Figure 4.1) procedure is used to plot all valid diffracted ray-paths in the modelled environment up to certain number of interactions specified by the user.

4.5 Conclusion

In this chapter a 3D ray-tracing propagation prediction model for characterisation of dispersive multipath radio channel has been presented.

The new model utilises vector mathematics in order to implement the ray-tracing algorithms. The model is based on GO and its variant UTD. The new techniques are introduced in order to implement faster, reliable, efficient and accelerated ray-tracing suitable for microcellular mobile radio communication systems.

Each individual path generated by the ray-tracer is characterised in terms of its amplitude, phase, polarisation, AoD, AoA and optical path length.

The model is flexible and can accommodate variable building heights, shapes and orientations (including pitched roofs). The electrical properties of the building (and ground) can be arbitrarily assigned. Antenna radiation patterns (including polarisation) are also arbitrary in principle although only vertical electric dipoles have been implemented to date. Reflection and diffraction rays

transmitted into the interior of buildings are not traced. The software constructs channel impulse responses (CIRs) and power delay profiles (PDPs) and calculates relevant channel parameters including signal strength, transmission loss, received power, average delay spread and RMS delay spread.

The model has implemented for a suburban area of Malvern, UK, where the field trial measurements have also been conducted. Chapter 5 describes the measurement campaign and presents the measured results. Chapter 6 compares the simulated and measured results.

Chapter 5: Propagation Measurements

5 Introduction

Characterisation of the multipath channel can be achieved either by propagation measurements or by deterministic modelling (e.g. ray-tracing). Measurements implicitly take into account all the propagation factors of the environment, both known and unknown whilst physical models are always subject to both simplification and approximation. Physical models are more convenient, however, and cheaper than measurements but require some level of validation (by measurements) before they can be relied on.

This chapter presents wideband propagation measurements of the 2.38 GHz radio channel in a microcellular residential suburban area of Malvern, UK. Data in the form of time-variant complex channel impulse responses (CIRs) have been recorded and discrete multipath components extracted. The first-order statistics of these components, including exceedance curves of number of propagation paths and received power, average delay spread and RMS delay spread are presented and compared with those derived from similar measurement campaigns reported in the literature.

The chapter is organised as follows. Section 5.1 describes the measurement equipment. Section 5.2 describes the measurement campaign. Section 5.3 describes the measurement set-up. Section 5.4 describes the measurement database, including the data collection methodology, and the algorithms developed for the extraction of multipath parameters. Section 5.4.2 presents the measurement results, and Section 5.5 compares the results with those derived from measurements reported in the literature.

5.1 Measurement system: The RUSK WLL channel sounder

The channel measurements were taken using a MEDAV RUSK WLL channel sounder provided by QinetiQ, Malvern, UK. The RUSK WLL transmits a digitally generated frequency chirp. The received signal is digitised, stored and (digitally) correlated with a delayed replica of the transmitted signal. It is designed for real time measurements and can be adapted to different radio frequencies. The RF unit supports frequencies between 1.7 GHz and 2.7 GHz in increments of 2 MHz. A measurement rate of 976 CIRs per second is possible. Table 5.1 gives the instrument's principal characteristics.

5.1.1 System configuration

Applications run under the OS/2 operating system. All programs are menu based. The video output of the receiver is used for visualising menu structures and monitoring measured data. Items of the menu can be selected with the mouse or keyboard. Using the menu various measurement parameters can be selected from a list of files and modified. When the filename is confirmed, the parameters held in the file are loaded into memory and are then available for the measurement.

The measured data collection system operates such that the complex CIRs measured can be observed as the measurements are made using the sounder's monitor.

Table 5.1: *Principal characteristics of the RUSK WLL channel sounder.*

Frequency bands	1.7 ... 2.7 GHz
Bandwidth	879 kHz to 120 MHz
Number of spectral lines	769 ≅ 770
Distance of spectral lines	1.2 MHz, 156.25 kHz, 39.06 kHz
Observation time	0.8 μs..6.4 μs..25.6 μs
Number of sampling Points	256 to 1024 complex
Chip period/frequency	6.25 ns / 160 MHz
Time resolution	Max. 15 ns
Number of channels	2
Repetition rate (normal mode)	24.576 ms / 41 Hz
Repetition rate (Doppler mode)	1.024 ms / 977 Hz
SNR	Calibrated 35 dB
Modulation	DSB
Intermediate frequency	80 MHz
Storage capacity	DAT 2 GB
Storage time	6 hrs.
Digital signal processor	DSP56001-33 MHz
Display	Colour LCD
Year of make	1995

5.1.2 Operating modes

The sounder can be operated in the following three measurement modes:

1. Time grid mode
2. Distance grid mode
3. Doppler mode

Further details concerning these measurement modes are given in [402].

5.1.3 Transmitter

The transmitter is essentially conventional in design. The discrete-time, bandlimited, baseband signal represents a (frequency) chirp. The observation time (i.e. chirp signal duration) and bandwidth are downloaded from a laptop. Figure 5.1 illustrates a simplified block diagram of laptop to transmitter download conversion procedure. A read only memory (ROM) downloads the signal from 10 selectable chirp signals (i.e. test sequences). The chirp signal is then fed to a digital-to-analogue (D/A) converter, filtered and translated in frequency to the required RF passband using double sideband amplitude modulation (DSB-AM) with a high stability carrier of selectable frequency in the range 1.7 GHz to 2.7 GHz. The RF signal is then amplified and fed to the antenna for transmission. The maximum transmitter output power is 1 W within the sub-range 2.5 GHz to 2.7 GHz. The transmitted signal has a line spectrum, the magnitude of which is almost constant within the transmission bandwidth

[173]. More detailed discussion of the RUSK WLL transmitter is documented in [100], [288], [402].

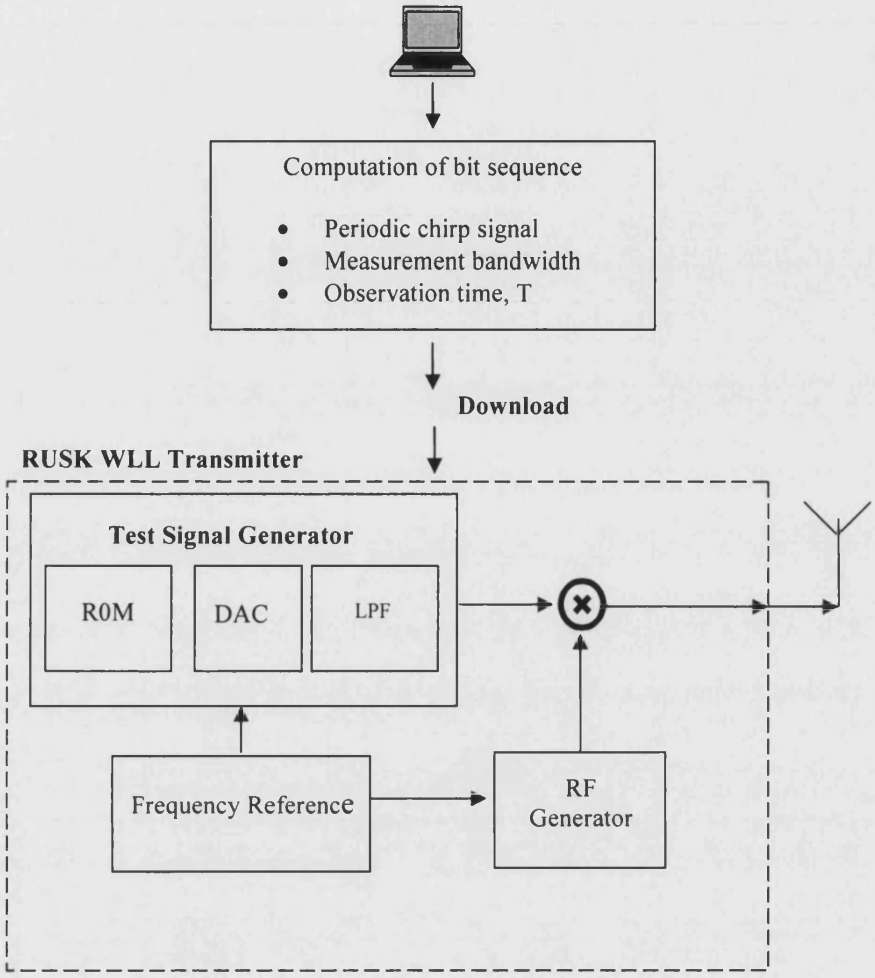

Figure 5.1: *A simplified block diagram of laptop to transmitter download conversion procedure of RUSK WLL.*

5.1.4 Receiver

Like the transmitter, the receiver is essentially conventional. Figure 5.2 illustrates a simplified block diagram of RUSK WLL receiver. The receiver extracts complex baseband CIRs from the received bandpass signal. It consists of three cascaded functional blocks, i.e. an RF-tuner, a digital signal processor (DSP) and data storage. The receiver video terminal shows the absolute value of complex CIRs in real time. The measured complex CIRs are stored to DAT tape. More details of the receiver and associated sub-systems are documented in [402].

5.2 Measurement campaign

The measurement campaign was carried out in a residential southern suburb of Malvern, U.K. The campaign was conducted jointly, on 31 July 2001, by the Radio Systems and Radio Science Research Group (now the

Telecommunications, Space and Radio Group), University of Bath, and QinetiQ. The test equipment and vehicles were provided by QinetiQ.

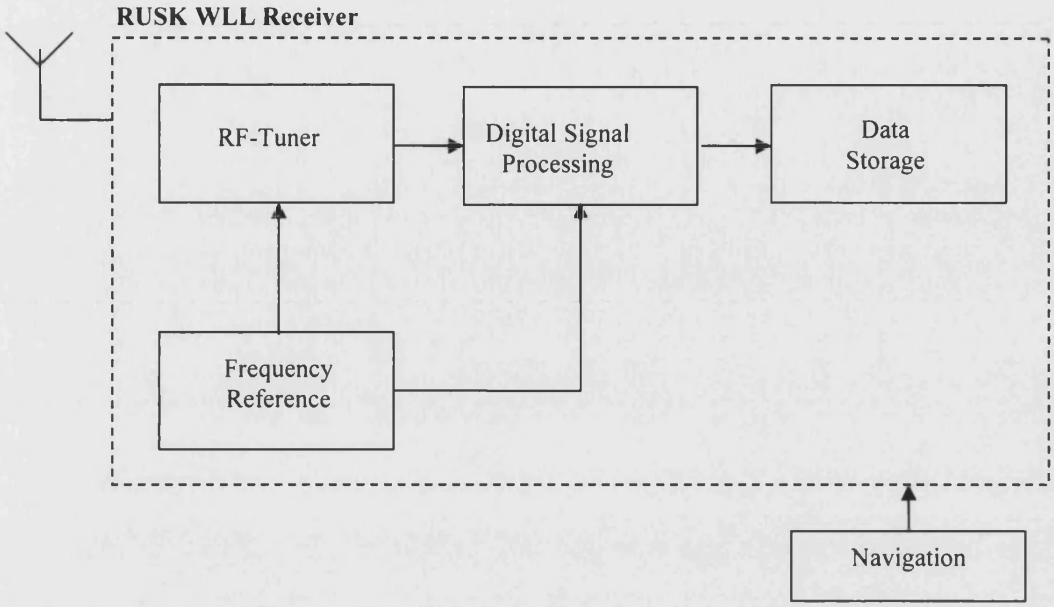

Figure 5.2: *A simplified block diagram of RUSK WLL receiver.*

The sounder transmitter and receiver were mounted in separate vehicles and the centre frequency for the measurement was set to 2.38 GHz. A closed loop route for the mobile receiver and two static locations for the transmitter were selected. Transmitter location 1 coincided with a point on the closed curve followed by the receiver. Transmitter location 2 was coincident with the approximate centre of area bounded by the closed curve.

Figure 5.3 shows the measurement area, the mobile receiver test route (ABC) and the (static) transmitter locations.

5.2.1 Receiver test routes

For Route 1, the transmitter was parked at the kerb of Albert Park Road; approximately 5 m from the intersection with Somers Park Avenue (see Figure 5.3). The vehicle carrying the receiver started each measurement from immediately in front of the transmitter, travelled along Albert Park Road for about 230 m, turned right onto Queen's Road, travelled along the Queen's Road for about 250 m, turned again right onto New Town Road, travelled along New Town Road for about 290 m, and completed a measurement by parking immediately behind the transmitter in Albert Park Road. The perimeter of the route is approximately 800 m. The transmitter maintained line-of-sight (LoS) contact with the receiver up to the intersection of Albert Park Road and Queen's Road. There was obstruction of the signal i.e. no-line-of-sight (NLoS) between transmitter and receiver for most of the route on Queen's Road and New Town Road. Approximately 75% of Route 1, therefore, had NLoS.

For Route 2, the transmitter was parked on the kerb of Chester Place and the receiver travelled an identical closed loop to that of Route 1 but starting and ending from Chester Place (see Figure 5.3). NLoS conditions prevailed for almost all measurement locations on Route 2.

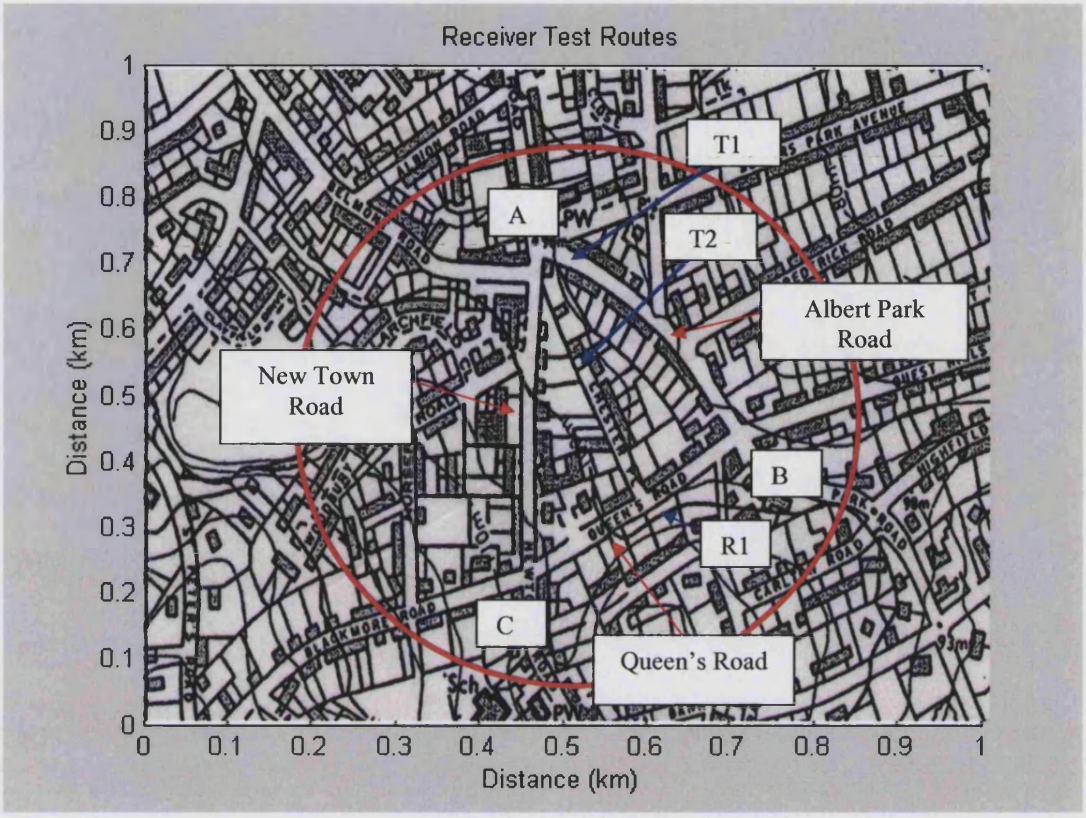

Figure 5.3: *Measurement area, transmitter locations and receiver test routes.*

5.2.2 Description of the physical environment

The terrain along the test routes was not flat but subject to gentle undulations. Figure 5.4 (a) shows a qualitative elevation of the roads along the test routes.

The residential buildings were mostly two storied with almost uniform heights. At a small number of locations there were three story buildings. Generally, the heights of the buildings were between 7.5 m and 10 m.

All the buildings had pitched roofs with chimneys projecting from the roof-top in most cases. Many houses were surrounded by vegetation in the form of bushes, hedges and small trees. Each road on the closed loop route was predominantly straight – the three roads forming the sides of an (approximately) equilateral triangle, with similar widths (see Figure 5.3 and Figure 5.4 (b)).

Thick, tall and dense rows of trees were found on the left side of Queen's road close to the mid-point, and both sides of Chester Place. A small number of newly constructed buildings are located in Chester Place which are not shown on map

of Figure 5.3. The newly constructed buildings are somewhat higher than the surrounding buildings.

Scattered trees are present on Beauchamp, Frederick and Albert roads.

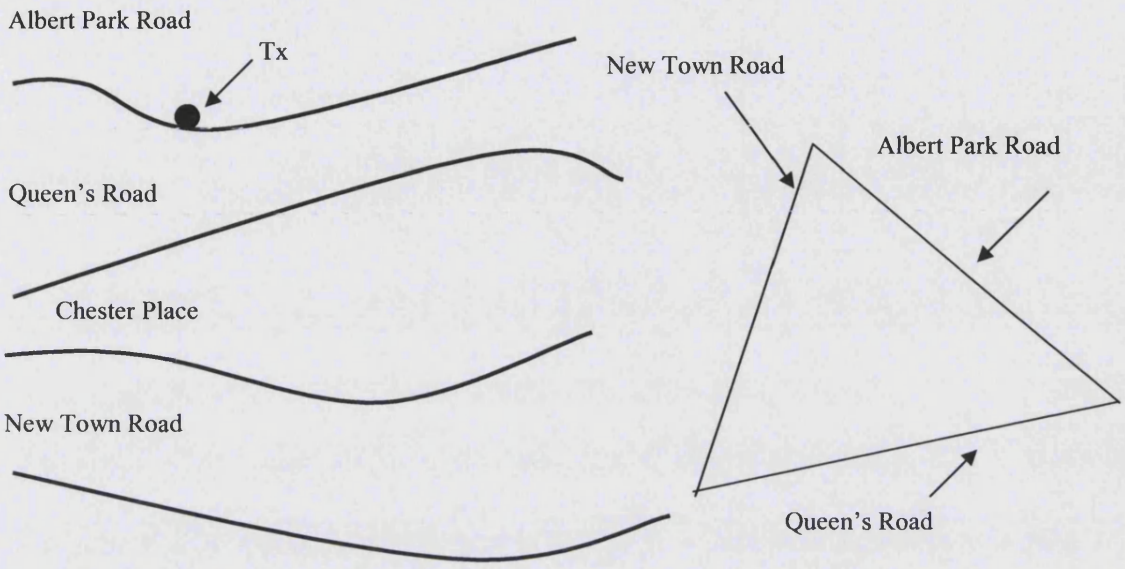

Figure 5.4: O*rientation of the roads along the Rx route.*

Figure 5.5 (a-h) are photographs of the test area taken in the March. The measurements, however, were made in the July. The photographs, therefore, under represent vegetation.

(a) Corner of Albert Park road

(b) Middle of Albert Park road

(c) Middle of Queen's road

(d) Building on Queen's road

(e): Chester Place

(f) Buildings on Chester place

(g): New Town road

(h): The Church on Somers Park road

Figure 5.5: *Photographs of the area: (a-b) Albert Park Road, (c-d) Queens Road, (e-f) Chester Place,* (g-h) *New Town Road.*

5.3 Measurement set-up

The sounder carrier frequency and bandwidth were set to 2.38 GHz and 120 MHz, respectively. The duration of the transmitted chirped signal was 1.6 μs and the temporal resolution was 6.25 ns. Two identical omni-directional, antennas were used for transmission and reception. The antennas were mounted in the centre of vehicle roofs at a height of 3.3 m above the ground. Both antennas were vertically polarized. The transmitter output power was 26 dBm. The data acquisition system was triggered by pulses from an optical encoder spliced into

the tachometer of the vehicle carrying the sounder receiver. The encoder was set to generate a CIR acquisition pulse at displacement intervals of 5 cm allowing data to be obtained free of spatial aliasing, assuming acquisition pulse rates did not exceed the maximum possible CIR measurement rate of the sounder. (This assumption imposed a maximum speed on the vehicle carrying the receiver of 2.5 m/s or 9 km/h.) The principal measurement parameters are summarised in Table 5.2.

Table 5.2: *Principal measurement set-up parameters.*

Frequency	2.38 GHz
Bandwidth	120 MHz
Transmit power	26 dBm
Antenna pattern	Omni directional
Polarisation	Vertical
Chirp duration	1.6 μs
Temporal resolution	6.25 ns
Measurement rate	976 CIR/s
Antenna heights	3.3 m

Three consecutive measurements were taken for each of the two selected receiver routes (see Figure 5.3) with the stationary transmitter and mobile receiver. During the measurement, the speed of the mobile vehicle was kept as constant as possible. A total of 96,626 complex channel impulse responses (CIRs) were recorded.

The data logging system allows real time observation of the (decimated) CIR magnitudes. The complex CIRs were stored on DAT tapes with a capacity of 14 GB. Each stored CIR consists of 256 samples of the incoming signal, corresponding to the duration of one chirp signal period (i.e. 1.6 μs).

The data was stored in six binary files; each file representing the data for one complete measurement route. The six files were then transferred to the hard disk of a personal computer (PC). A file header contains calibration and measurement parameter information. Software written in IDL was used to read each binary file, separate the file header from the data and plot CIRs. A simplified flow diagram of IDL software is shown in Figure 5.6.

All measured data was converted into MATLAB readable form. Each data file was divided into blocks of 1000 CIRs, each block representing a physical distance of 50 m. This resulted in a total of 96 data files each containing 1000 CIRs. Each CIR contains 256 delay bins, one bin corresponding to the time resolution of 6.25 ns, Figure 5.7.

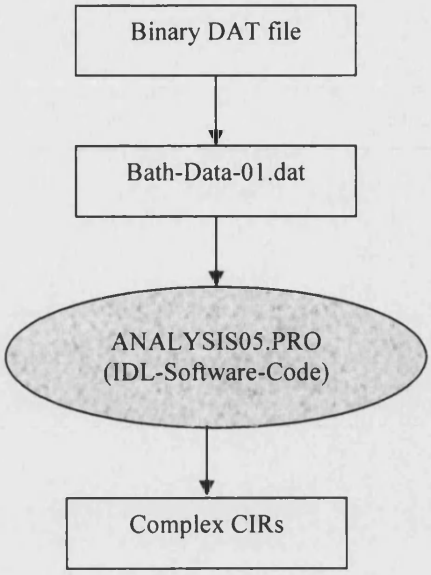

Figure 5.6: *A simplified flow diagram of IDL software code.*

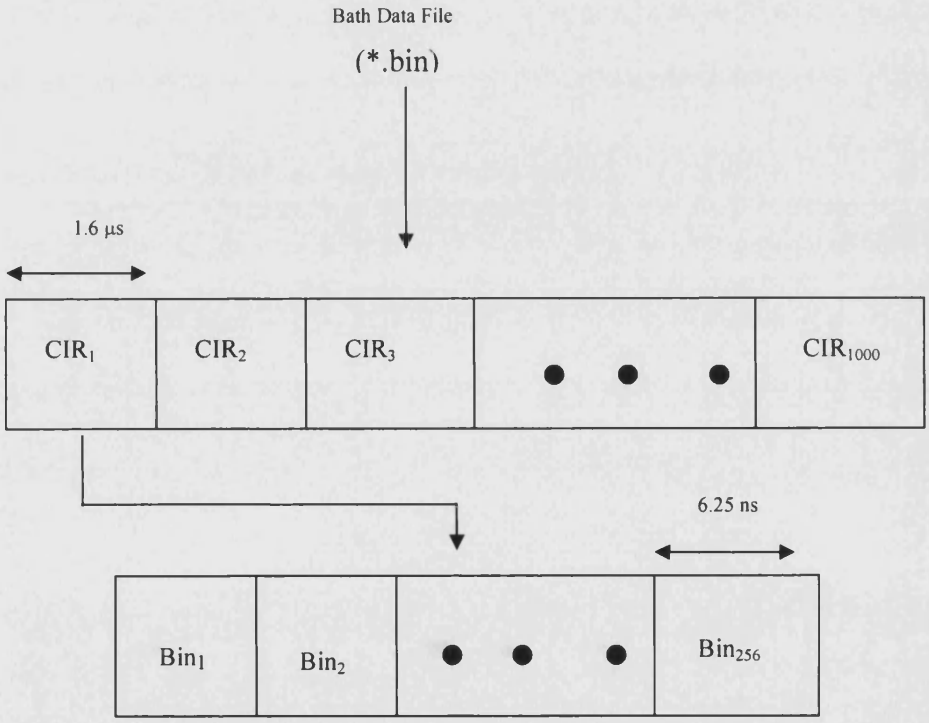

Figure 5.7: *Schematic illustration of CIR data format in the MATLAB software.*

5.4 Measurement database and data collection methodology

Three consecutive measurements were taken for each of the two selected routes with the stationary transmitter and mobile receiver. Table 5.3 summarises the six sets of measured data with their corresponding binary file names.

Table 5.3: *Number of CIRs obtained from the measurements on two different routes.*

Measurement	Database Files	Number of CIRs	Route
1	Bath-data-01	18083	T1
2	Bath-data-02	17057	T1
3	Bath-data-03	16159	T1
4	Bath-data-04	15368	T2
5	Bath-data-05	15262	T2
6	Bath-data-06	14697	T2
Total No. of CIRs:	96626		

5.4.1 Data pre-processing

This section describes the techniques and the algorithms developed to process the measured data. The algorithms were in implemented in MATLAB.

5.4.1.1 Initial data inspection

The CIR varies with the location of the transmitter, receiver and surrounding objects. When the transmitter, receiver or objects are in relative motion, therefore, the CIR or PDP become time variable. The shape of PDP can also vary depending upon the type of channel sounder and bandwidth used [100].

In order to inspect and 'sanity check' the measured data, a set of raw power delay profiles (PDPs) were plotted. The ordinate of these plots is in units of dBV (dB with respect to 1.0 V) since it is the receiver voltage that is recorded. To within a constant offset, however, this is the same as the more traditional units for a PDP (i.e. dBm). Figures 5.8(a-b) and 5.9(a-b) are example PDPs. In Figure 5.8(a-b) the receiver is at a distance from the transmitter of about 4 m and 151 m, respectively, on the Albert Park road where LoS conditions exist. In Figure 5.9(a) the receiver has travelled a distance of about 350 m from the transmitter. At this location the receiver is on Queen's road where NLoS conditions exist between transmitter and receiver. In Figure 5.9(b) the receiver has travelled a distance of about 600 m. At this location the receiver is on the intersection of Queen's and New Town roads which is in a deeply shadowed (NLoS) region.

5.4.1.2 Pseudo-colour plots

Figure 5.10 and Figure 5.11 are examples of pseudo-colour plots of the data in the distance plane.

In Figure 5.10(a) the receiver is on Albert Park Road where a LoS exists between transmitter and receiver while in Figure 5.10(b) the receiver is near the intersection of the Albert Park Road and Queen's Road where NLoS conditions exist. In Figure 5.11(a) the receiver is on Queen's Road in deep shadow and in Figure 5.11(b) the receiver is on New Town Road (NLoS conditions). They show vertical striations characteristic of discrete multiple paths but undoubtedly also due to sidelobe artefacts in the CIR measurements. The required channel PDP is thus partially obscured by the superimposed sidelobe structure originating from aggressive bandlimiting in the transmitter/receiver chain. In order to examine this

effect more closely and assess possible strategies for reducing, removing or compensating the artefacts a back-to-back transmitter/receiver calibration was performed to characterise the sidelobes effects in the context of a perfect channel.

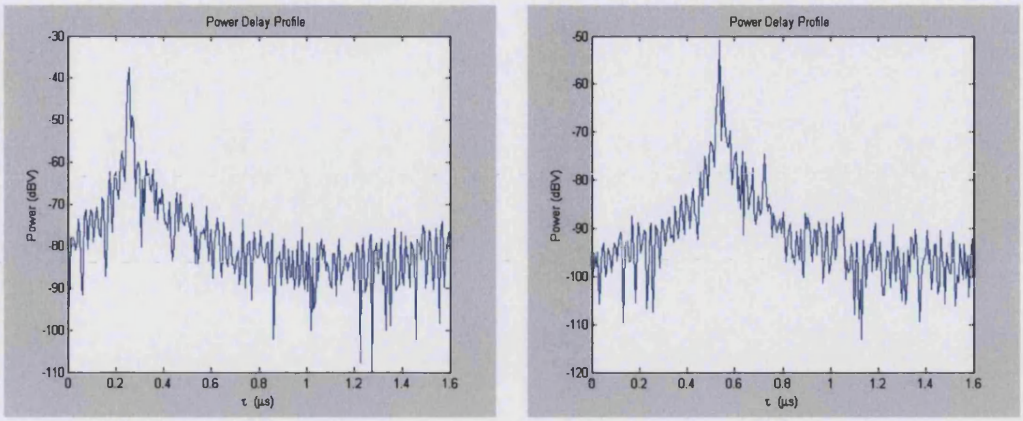

(a) *(b)*

Figure 5.8: *Examples PDPs obtained from complex CIR, (a) Mobile receiver located about 4 m from transmitter, T1 on route 1, measurement-1, (b) Mobile receiver located 151m from transmitter, T1 on route 1, measurement-2.*

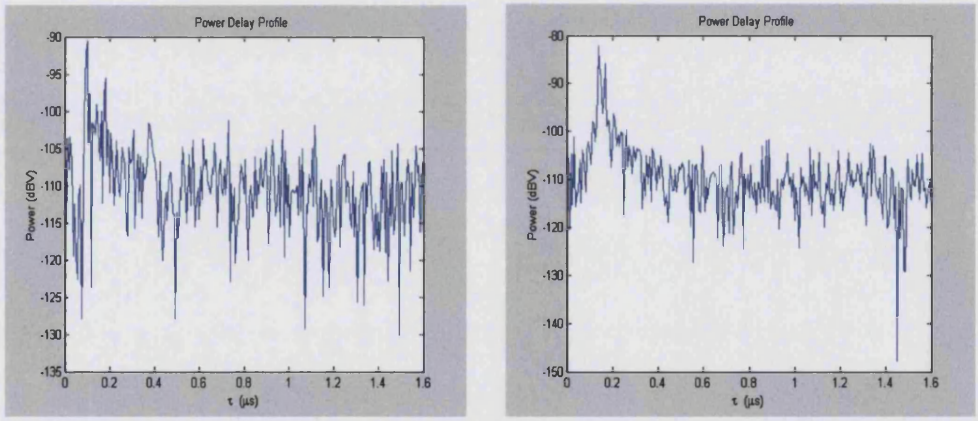

(a) *(b)*

Figure 5.9: *Examples PDPs obtained from complex CIR, (a) Mobile receiver located about 350 m from transmitter, T2 on route 2, measurement-5, (b) Mobile receiver located 600 m from transmitter, T2 on route 2, measurement-6.*

5.4.1.3 Back-to-back calibration

A back-to-back calibration was conducted in time-grid mode immediately prior to, and immediately after, all measurements. During the calibration the complete transmit-receive system (with the exception of the antennas) were cascaded via a length of coaxial cable and a 45.5 dB attenuator. The transmit power was 10.4 dBm. This allowed adjustment of variable attenuators in the front end of the receiver so that the received power was within the range expected during measurements. The transmit frequency was 2.38 GHz with a bandwidth of 120 MHz. The period of the transmit signal was 1.6 μs.

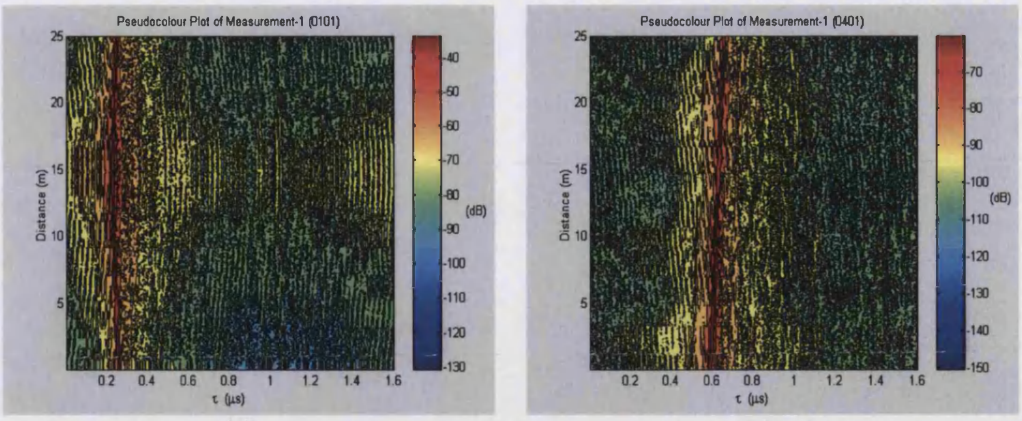

(a) (b)

Figure 5.10: *Examples pseudo-colour plots, (a) Plot of 500 CIR, mobile receiver located 25 m from transmitter, T1 on route 1, measurement-1, (b) Plot of 500 CIR , mobile receiver located 200 m from transmitter, T1 on route1, measurement-1.*

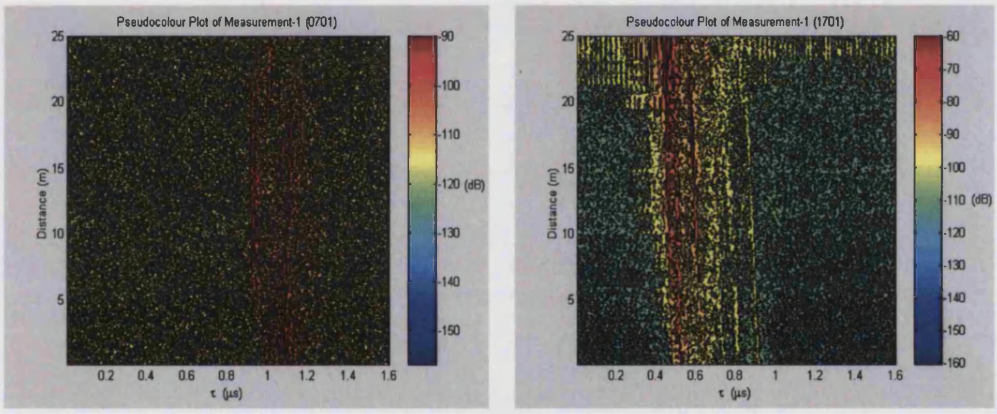

(a) (b)

Figure 5.11: *Examples pseudo-colour plots,* (a) *Plot of 500 CIR, mobile receiver located 350 m from transmitter, T1 on route 1, measurement-1, (b) Plot of 500 CIR, mobile receiver located 800 m from transmitter, T1 on route1, measurement-1.*

An example of a back-to-back calibration power delay profile (PDP) (in dBV) is shown in Figure 5.12(a). In Figure 5.12(a) 256 delay bins corresponds to 1.6 μs. The data resulting from the back-to-back measurement contains 10,067 complex CIRs. In order to assess the stability of the calibration CIR sidelobes the probability density function (pdf) of the difference between the PDP peak and the highest PDP sidelobe was calculated, Figure 5.12(b). This gives a quantitative measure of the stability and precision of the sounder measurement that is important if calibration CIRs are to be used to mitigate the effect of equipment sidelobe artefacts in measured channel characteristics.

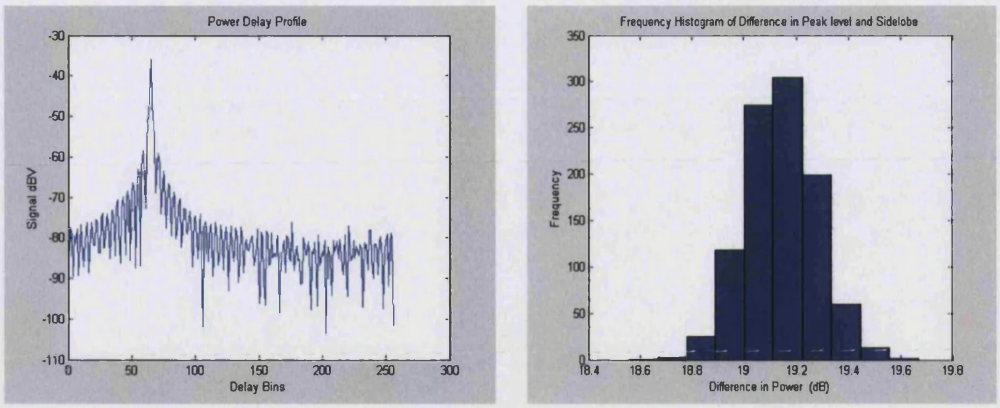

(a) (b)

Figure 5.12: *(a) An example PDP from back-to-back calibration, (b) An example Pdf plot of difference between peak level and the maximum sidelobe for first 1000 back-to-back CIRs.*

5.4.1.4 Hardware multipath simulator

A hardware multipath simulator with known multipath amplitude and delay was constructed in order to give confidence in the proper interpretation of the sounder data and also to be used to generate benchmark data for the development and testing of data-processing algorithms. Figure 5.13 shows a block diagram of the simulator. It contains a power splitter, a power combiner and a transmission line having a propagation delay of 100 ns at 2.38 GHz (as determined by a network analyser measurement). Output 1 of the splitter was connected to the delay line and output 2 was connected to the combiner, which adds the direct and delayed signals. The attenuation of the delay line was 14.22 dB.

The input of the splitter was connected to the transmitter of the sounder and the output of the combiner was connected to the receiver. The measurements, like those of the back-to-back calibration, were made at a frequency of 2.38 GHz in time grid mode. A transmit power of 10.4 dBm was set for the measurements with a channel attenuation of 45.5 dB.

The hardware simulated multipath data contains 10,141 complex CIRs. An example PDP (in dBV) is shown in Figure 5.14(a). Figure 5.14(b) shows the pdf of the CIR magnitude in dBV for the first 1000 CIRs.

The mean gain of the delayed path was found to be -14.22 dB with respect to the non-delayed path and the standard deviation of gain variation was 0.04 dB. The peak variation in gain observed (in 1000 measurements) was ±0.15 dB.

5.4.1.5 Extraction of multipath parameters

Several methods of extracting the principal multipath parameters (i.e. the strengths and delays of the discrete paths) from the CIRs were investigated as described below.

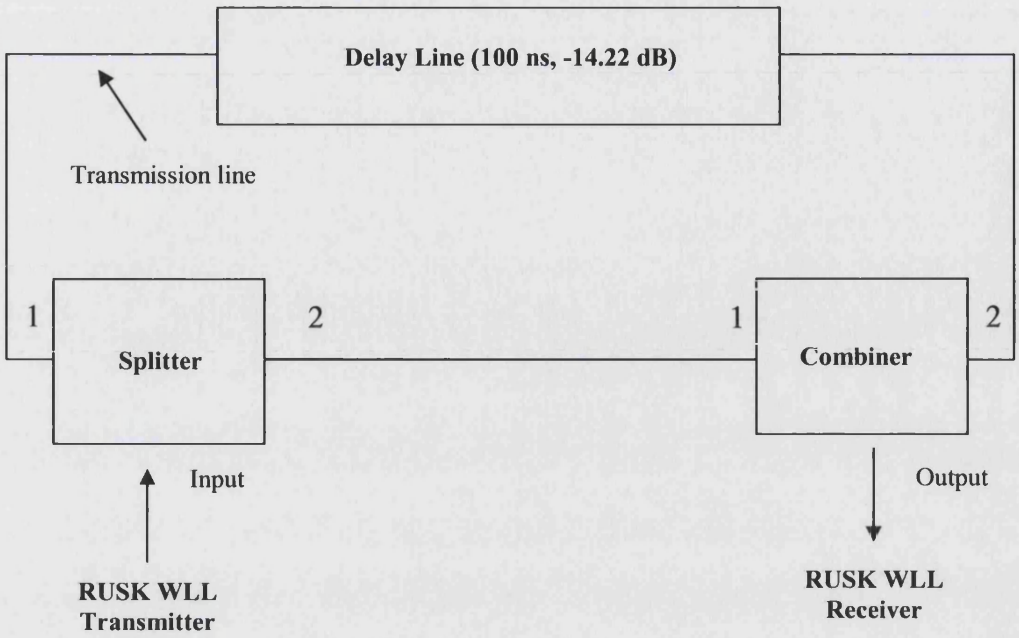

Figure 5.13: *Block diagram of the hardware multipath simulator.*

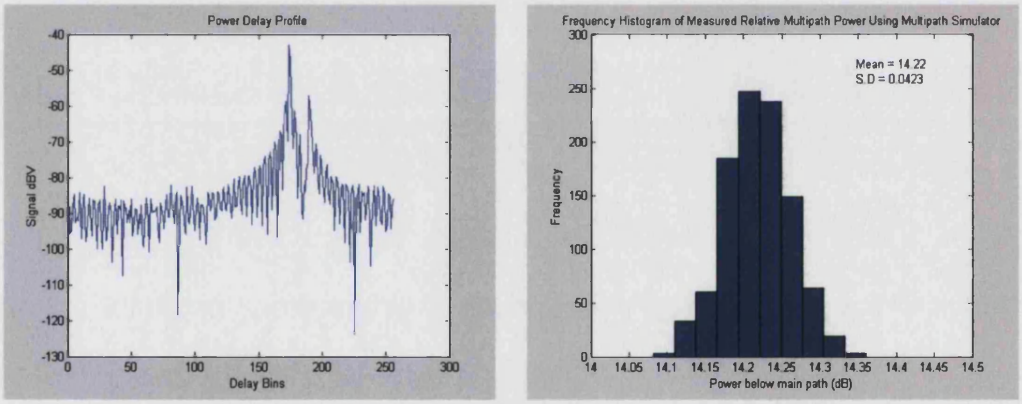

(a) *(b)*

Figure 5.14: *(a) An example of magnitude in dBV of complex CIRs from simulated multipath measurements (2-path model with delay =100 ns), (b) An example of pdf of peak difference between direct and delayed multipath signal amplitudes for first 1000 measured CIRs using hardware simulator.*

5.4.1.5.1 Largest CIR vector elements

The 50 maximum power elements in each CIR vector were identified and their delays noted. An example for 100 CIRs (covering a distance of 5 m) is shown in Figure 5.15. It was hoped that by choosing the largest power values, the signal energy would be identified without having to resort to establishing a noise threshold.

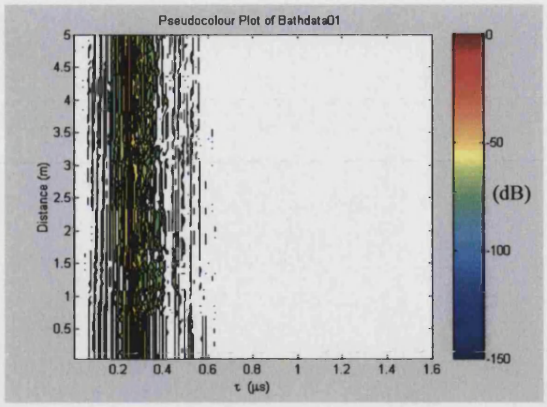

Figure 5.15: *50 maximum power elements for 100 CIRs of measurement 1, T1 on Route, measurement-1, (Mobile receiver located 5 m from transmitter.)*

Noise is essentially discarded using this elementary algorithm (providing the peak CIR signal to noise ratio is sufficiently large) but sidelobe artefacts remain. It was clear, however, after examining a number of example plots that a more sophisticated approach to parameter extraction would be required.

5.4.1.5.2 Detection of local maxima

Since convolution of the propagation path impulse response with the impulse response of the sounder smears the measured PDP in delay, it was decided that to reliably obtain the discrete multipath components of the channel, a multipath parameter extraction algorithm based on PDP local maxima detection was required. In early versions of the local maximum detection algorithm noise spikes superimposed on the CIR resulted in the spurious detection of multiple, closely spaced, propagation paths where engineering judgment (and considerations of measurement temporal resolution) suggested strongly that only one path was present. Averaging within a CIR time-window corresponding to three delay bins (18.7 ns) greatly reduced the occurrence of these spurious local maxima at an acceptable cost of reduced time-resolution. Figure 5.16 shows a plot of this, (a) before, (b) after taking 18.7 running mean.

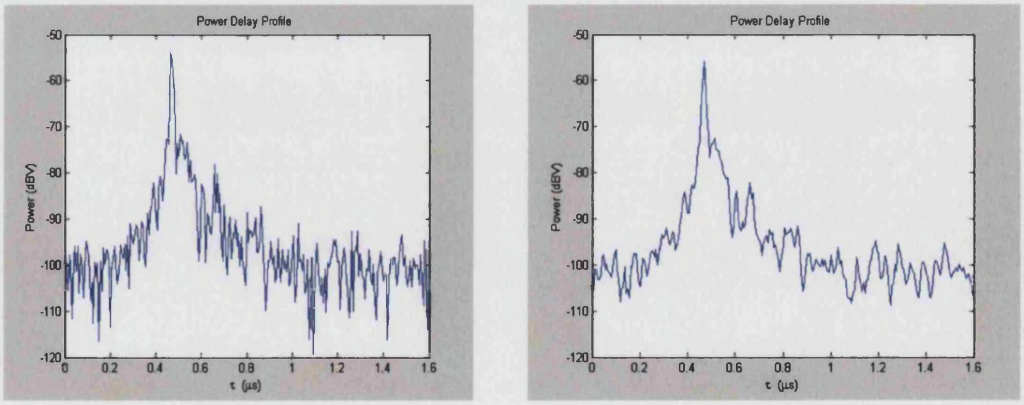

(a) (b)

Figure 5.16: PDP *(a) Before taking running mean, (b) after taking running mean.*

5.4.1.5.3 Thresholding below peak signal level

In order to mitigate the effects of CIR measurement sidelobes (i.e. to avoid identifying sidelobes as multipath signals) a threshold of -20 dB with respect to the peak level of each CIR was established. All CIR vector elements lying below this threshold were ignored. An example pseudo-colour plot of 500 CIRs of measurement 3 is shown in Figure 5.17.

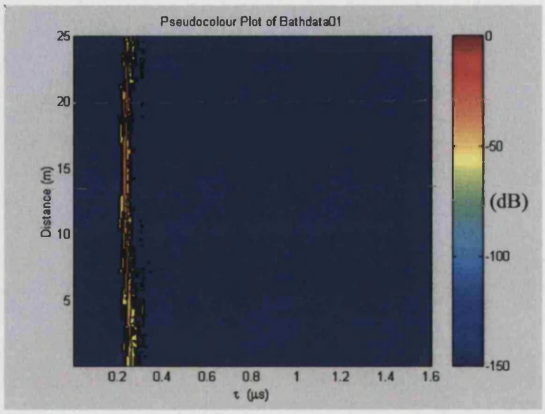

Figure 5.17: *Pseudo-colour plot thresholded at -20 dB with respect to peak level for 500 CIRs of T1 on route 1, measurement-1 (Mobile receiver located 25 m from transmitter.)*

This algorithm prevented sidelobe contamination of extracted multipath parameters but risks erroneous interpretation of noise as multipath components when the peak signal level is small (e.g. in NLoS conditions).

5.4.1.5.4 Thresholding above noise level

To avoid noise masquerading as low-level multipath a noise floor for each CIR was established by first identifying the delay corresponding to the maximum power element in the CIR vector. The corresponding (reference) delay, τ_{ref}, was noted. A 0.3 μs time window commencing 0.7 μs after τ_{ref} was then used to estimate the noise floor. (0.7 μs was judged to be a sufficient excess delay to preclude multipath signal energy from falling within the time window.) The mean noise power was found by averaging the squared amplitudes of the elements within the time window. Establishing a 'signal-free' time window with respect to the reference delay for each CIR avoided the problem of drifting absolute delay (i.e. delay wrapping around from the end of the CIR to the beginning).

5.4.1.5.5 Combined signal and noise thresholding

The preceding two strategies were combined to eliminate both noise and sidelobe contamination of multipath parameters. Potential noise and spurious responses were removed by applying two threshold levels (T1 and T2) in order to isolate the resolvable multipath components.

Threshold T1 was set at -18.5 dB with respect to the peak value of a given CIR. This value was selected after considering the probability density function (pdf) of

the back-to-back calibration measurement. (The minimum difference between the peak level and the sidelobe level was 18.55 dB).

Threshold T2 was set 10 dB above the CIR noise floor. The noise floor was established separately for each CIR by calculating the mean noise power in the time window starting 0.7 μs after the strongest PDP component and ending 1.0 μs after the strongest PDP component as described earlier in Section 5.4.1.5.4.

A two-threshold algorithm was implemented that finds both T1 and T2 threshold and then selects the highest (i.e. least negative) threshold of the two (T = max {T1, T2}).

5.4.1.5.6 Adopted parameter extraction algorithm

The parameter extraction algorithm adopted is described below.

(i) Each CIR was filtered using an 18.75 ns running mean filter.
(ii) Threshold T1 is calculated
(iii) Threshold T2 is calculated
(iv) An operating CIR threshold, T, was set using T = max {T1, T2}
(v) All local maxima of the absolute value of CIR components exceeding the threshold T, assumed to represent multipath components, were found within a window starting 1.0 μs window starting 0.3 μs prior to the occurrence of the CIR signal maximum

This algorithm was applied to all six measurements taken along the routes T1 and T2. Table 5.4 shows the total number of measured and post-thresholded CIRs of three consecutive measurements along route T1.

Table 5.4: *Number of measured and threshold CIRs of measurements along the route T1 and T2.*

Measurement No.	Number of measured CIRs	Number of threshold CIRs	Route
Measurement 1	18083	12682	T1
Measurement 2	17057	12279	T1
Measurement 3	16159	11455	T1
Measurement 4	15368	11633	T2
Measurement 5	15262	11567	T2
Measurement 6	14697	10983	T2
Total No. of CIRs:	96626	70599	

5.4.2 Post-processing

In order to analyse the discrete multipath parameters, for the entire set of field trial measurements, a number of post-processing algorithms were developed.

5.4.2.1 Multiple path exceedances

The statistics of path numbers for all six measurements have been found and summarised as (un-normalised) exceedance curves in Figures 6.18 – 6.20.

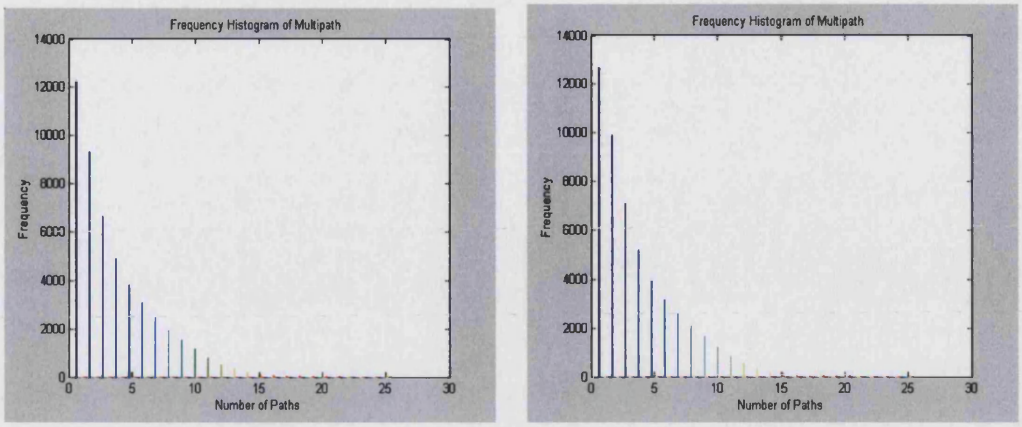

(a) (b)

Figure 5.18: *Frequency histogram of number of multiple paths exceeding n, (a) Measurement-1(Bath-data-01), (b) Measurement-2(Bath-data-02).*

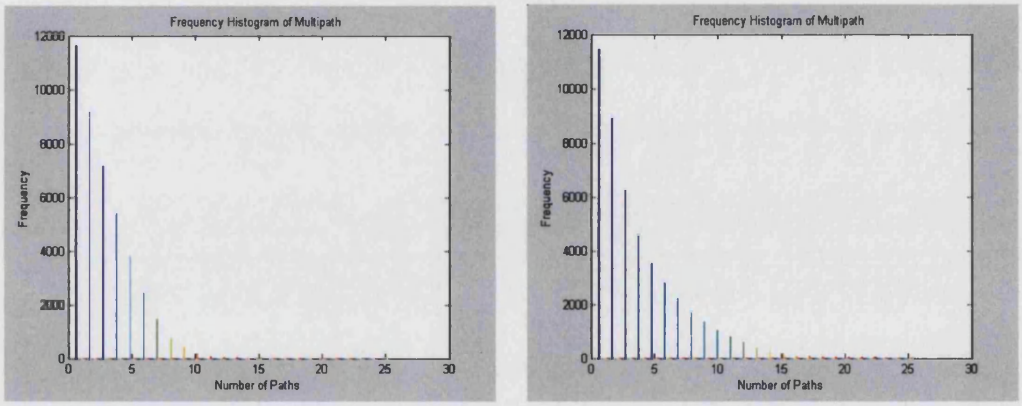

(a) *(b)*

Figure 5.19: *Frequency histogram of number of multiple paths exceeding n, (a) Measurement-3(Bath-data-03), (b) Measurement-4(Bath-data-04).*

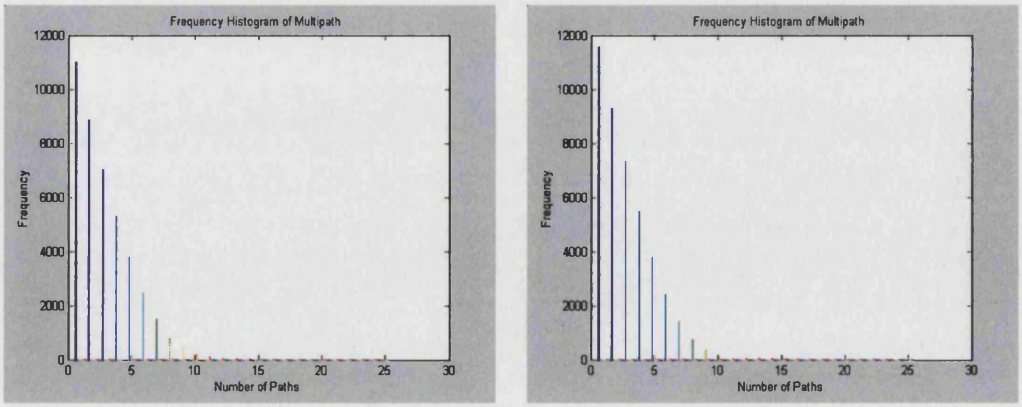

(a) (b)

Figure 5.20: *Frequency histogram of number of multiple paths exceeding n, (b) Measurement-5(Bath-data-05), (b) Measurement-6(Bath-data-06).*

5.4.2.2 Power

Total received power has been obtained for each CIR along route T1.

5.4.2.2.1 Comparison between measured power

Figure 5.21(a) is a comparison of total received power for the three consecutive measurements taken along the route T1. The red curve represents measurement 1 (Meas. 1), the blue curve represents measurement 2 (Meas. 2) and the magenta curve represents measurement 3 (Meas. 3). Figure 5.21(b) shows the corresponding cumulative distribution functions (cdfs) and Figure 5.21(c) shows the scatter diagram of measured power of Meas. 1 and Meas. 2, along the route T1. A best fit regression line is also shown.

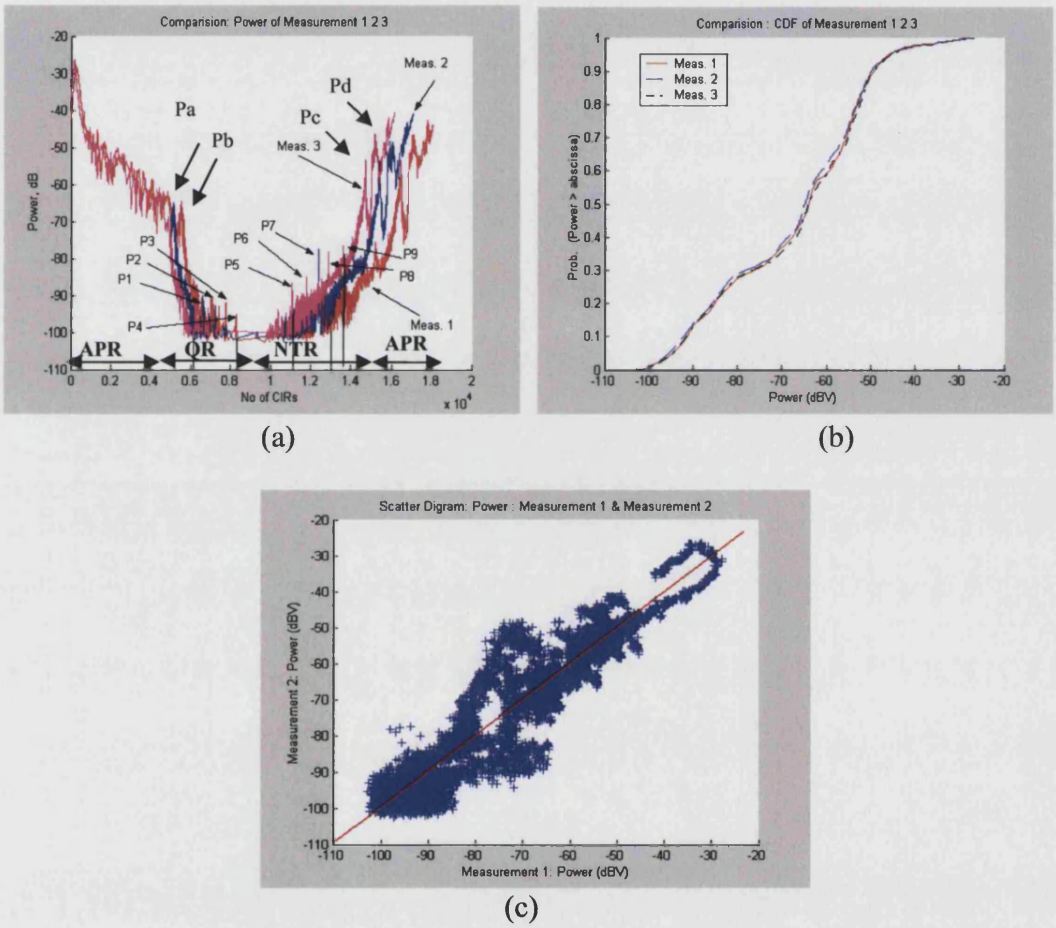

Figure 5.21: *(a) Measured power of the three measurements, (b) Cdf of the measured power, along the route T1, (c) Scatter diagram of measured power of Meas. 1 and Meas. 2, along the route T1.*

The received power from CIR 1 up to about CIR 4340 represent the LoS region in Albert Park Road (APR). CIR 4340 to CIR 9384 represent Queen's Road (QR), which is in deep shadow (and therefore a NLoS region) and the CIR 9384 to CIR 15,515 represent New Town Road (NTR), which again is in deep shadow. CIR 15,515 to CIR 18,000 represents APR (again LoS) which completes the measurement circuit.

There is a gradual, and entirely expected, reduction in received power as the receiver moves away from the transmitter and a corresponding increase as the receiver approaches the transmitter at the end of the circuit.

Table 5.5 shows the mean received power values calculated from all six measurements as a function of distance along the routes T1 and T2.

5.4.2.3 Statistical analysis

The following quantities have been calculated using the extracted multipath components for each measured CIRs:

(i) Average delay spread
(ii) RMS delay spread
(iii) Estimated coherence bandwidth

Average delay-spread (DS) and the RMS-DS statistically quantify the time-delay structure of the channel. The estimated coherence bandwidth is taken as the reciprocal of twice the RMS-DS.

The relative frequency histograms of the quantities are shown in Figures 22 - 24.

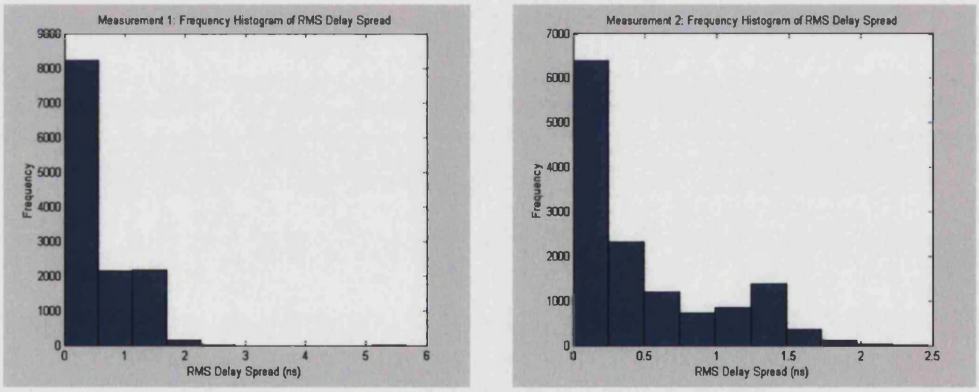

(a) (b)

Figure 5.22: (a) *Frequency histogram of RMS delay spread, transmitter located at T1 on route 1, measurement-1, (b) Frequency histogram of RMS delay spread, transmitter located at T1 on route 1, measurement-2.*

5.4.2.3.1 Comparison between measured RMS-DS

Figure 5.25(a) is a comparison between the RMS-DSs of the three consecutive measurements taken along the route T1 (see Figure 5.3). The red curve represents measurement 1 (Meas. 1), the blue curve represents measurement 2 (Meas. 2) and the magenta curve represents measurement 3 (Meas. 3). Figure 5.25(b) shows the corresponding cdfs and Figure 5.25(c) shows the scatter diagram of measured RMS-DS of Meas. 1 and Meas. 2, along the route T1. A best fit regression line is also shown.

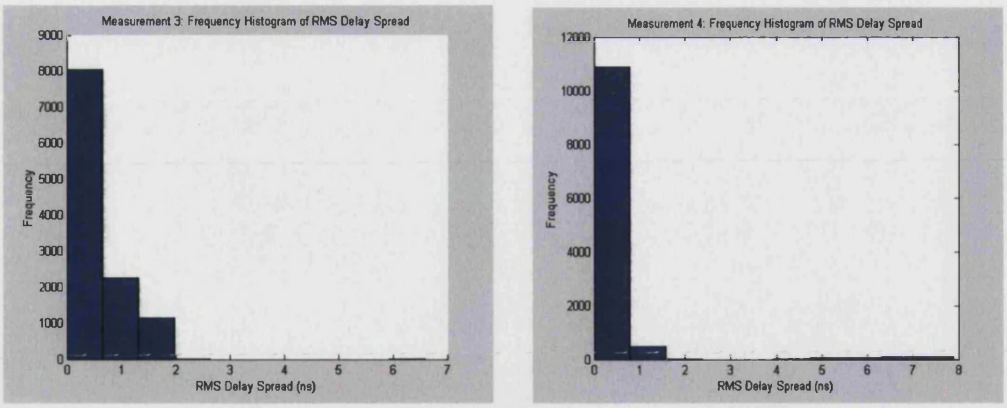

(a) (b)

Figure 5.23: (a) *Frequency histogram of RMS delay spread, transmitter located at T1 on route 1, measurement-3, (b) Frequency histogram of RMS delay spread, transmitter located at T2 on route 2, measurement-4.*

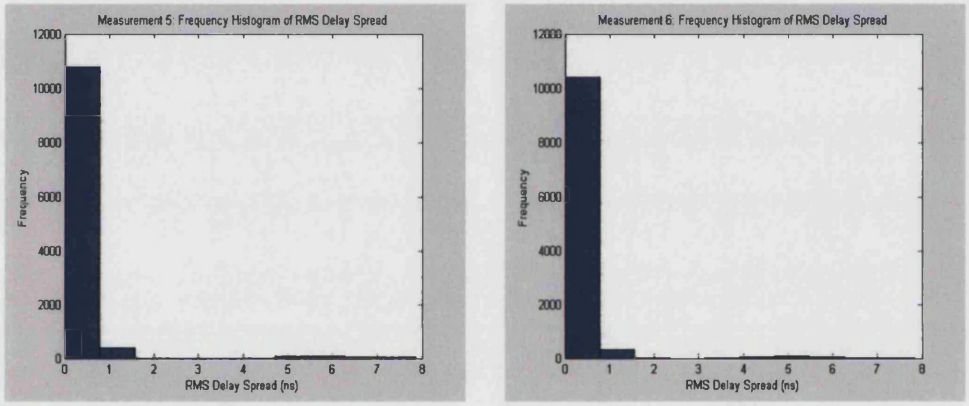

(a) (b)

Figure 5.24: *(a) Frequency histogram of RMS delay spread, transmitter located at T2 on route 2, measurement-5, (b) Frequency histogram of RMS delay spread, transmitter located at T2 on route 2, measurement-6.*

Excluding the contribution of RMS-DS due to P2 and P3 (Figure 5.25(a)) which are clearly non-physical outliers then the maximum of Meas. 1, Meas. 2 and Meas. 3 are 247 ns, 247 ns and 244 ns, respectively.

Table 5.5 shows mean RMS-DS values calculated from all six measurements along the routes T1 and T2, respectively.

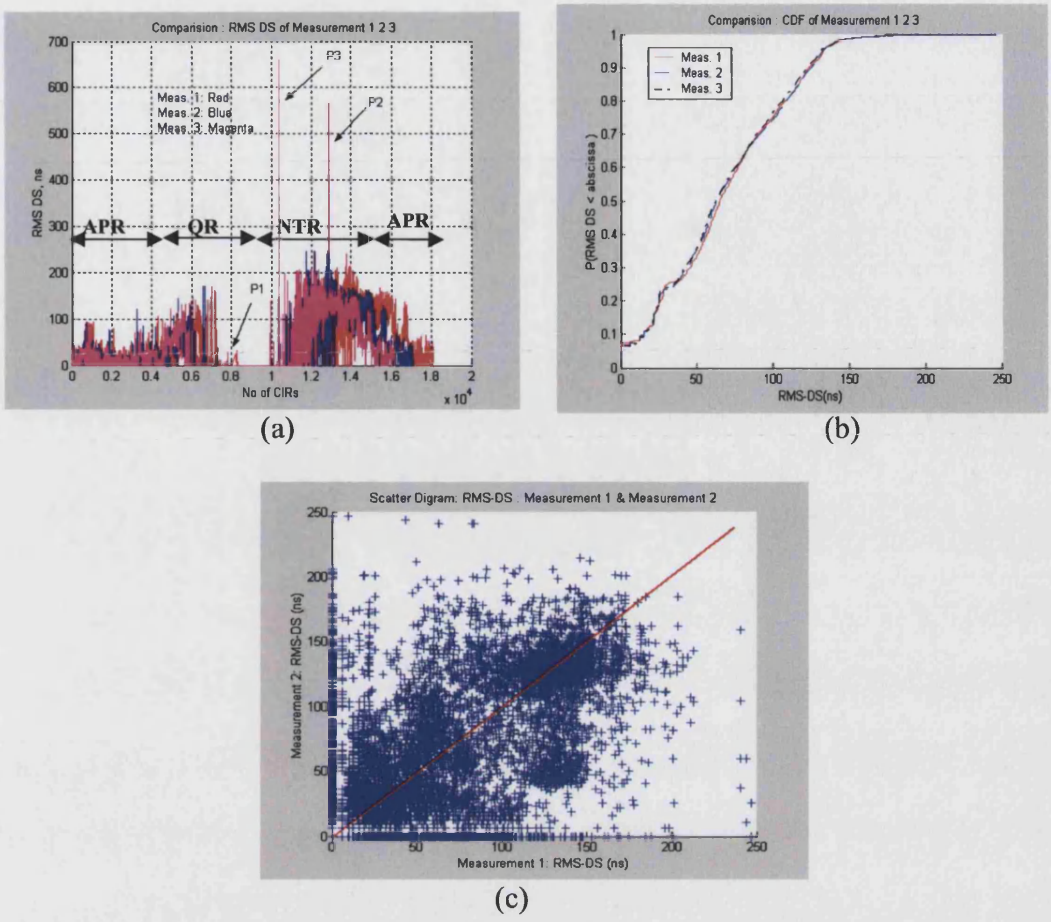

Figure 5.25: *(a) Measured RMS-DS of the three measurements, (b) Cdf of the measured RMS-DS, along the route T1, (c) Scatter diagram of measured RMS-DS of Meas. 1 and Meas. 2, along the route T1.*

5.5 Comparison with other measurements

A comparison of other measured delay spread values is presented in Table 5.6. These mostly relate conventional cellular systems, however, with one antenna elevated above the local clutter and generally greater propagation distances. Figure 5.26 shows the RMS-DS versus increasing range between the transmitter and receiver.

Table 5.5: *Measured mean values of received power, RMS-DS and corresponding coherence bandwidths.*

Meas.	Transmitter Location	Number of CIRs	Power (dBV)	Mean τ_{rms} (ns)	Estimated mean B_C (MHz)
1	T1	18083	-45.89	50.37	9.92
2	T1	17057	-45.20	49.73	10.58
3	T1	16157	-45.63	48.89	10.22
4	T2	15368	-79.75	47.81	10.45
5	T2	15262	-79.42	49.81	10.03
6	T2	14697	-79.75	44.97	11.11

Table 5.6: *Conventional RMS-DS in suburban environments.*

f (GHz)	τ_{rms} (ns)	Location: Author, ref
0.91	300 (median)	Toronto: Sousa, 1994, [403]
0.91	300 (median)	The Hague: Rees, 1987, [95]
1.9	200 – 500	Metropolitan: Jorgensen, 1997, [89]
0.91	200 – 310	Averaged typical case: Cox, 1972, [83]
0.91	1960 – 2110	Averaged extreme case: Cox, 1972, [153]

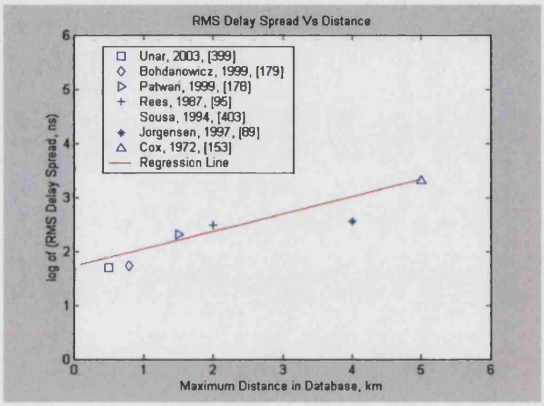

Figure 5.26: *Delay spread versus increasing maximum range between Tx and Rx. (Regression line corresponds to* $\log_{10}(\tau_{rms}) = 1.8 + 0.3R$ *where R is maximum range in km)*

5.6 Conclusion

Wideband microcellular-like radio channel sounding measurements has been reported for a residential suburban area. The measurement equipment, measurement campaign and results of the field trials have been described. Measurements were made at 2.38 GHz, in two different scenarios of the same area. The propagation measurements are needed in order to validate a deterministic site-specific ray-tracing model. Data in the form of the time-variant complex channel impulse responses (CIRs) were recorded and discrete multipath channel parameters (amplitude and delays of the principal PDP components) were extracted using an off-line data pre-processing algorithm. Exceedance curves of total received power and numbers of propagation paths along the routes were obtained. The important first-order statistics of these components such as average DS, RMS-DS and the estimated coherence bandwidth for each CIR have been calculated. RMS-DS has been compared with those derived from similar measurement campaigns reported elsewhere in the literature.

Chapter 6: Simulated Results and Comparison with Measurements

6 Introduction

Characterisation of the multipath channel can be achieved either by field trial propagation measurements or deterministic ray-tracing. In Chapter 5, we described a wideband measurement campaign and reported the resulting channel statistics.

The ray-tracing tool reported in Chapter 4, 3D MRT-1, predicts wideband channel characteristics and extracts the important multipath channel parameters needed in system design.

In this chapter comparisons are made between the predicted and measured channel characteristics. Section 6.1 describes the simulated building database. Section 6.2 summarises the data collection methodology. Section 6.3, presents description of the simulated results and Section 6.4 compares predictions with measurements.

6.1 Simulated building database

A 3D building database of the test-site was constructed. The database does not include a small number of newly constructed buildings near the test-site centre since these were not shown on the (2D) map used.

All buildings were assumed to be of equal height with flat roofs. The terrain was also assumed to be flat. These were thought to be reasonable approximations. Vegetation, garden furniture (including fences), street furniture etc. were neglected.

Initially, the test environment was modelled to a radius of half of a mile. It contained 83 buildings, 418 polygons and 669 edges. Because of the long computational time of the 3D MRT-1, the environment was reduced resulting in 55 buildings, 285 polygons and 460 edges. The reduced building database is shown in Figure 6.1.

A simulated test route was constructed identical to that used in the measurements (Route T1, Chapter 5), Figure 6.2.

6.2 Simulated database and data collection methodology

6.2.1 Pre-processing of the simulated data

The simulated test route was split into 92 locations. An average separation distance of about 8.5 m between adjacent receiver locations was maintained.

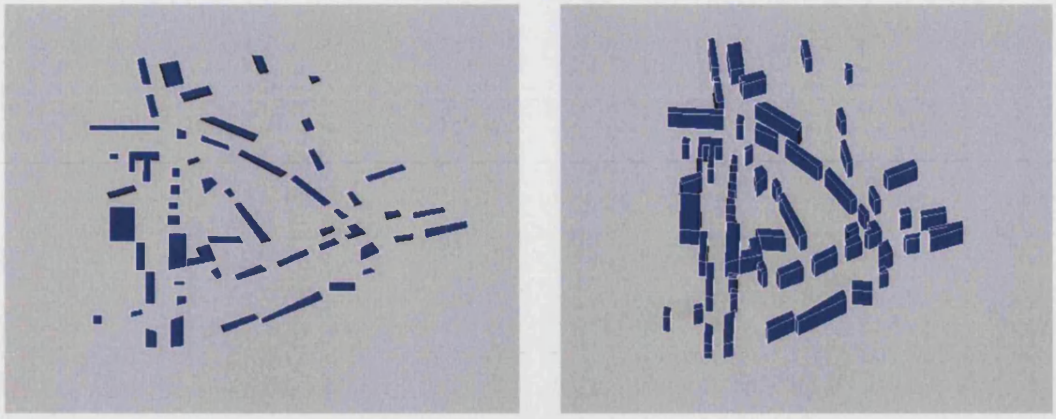

(a) (b)

Figure 6.1: *Simulated database (a) Plan view, (b) Isometric view.*

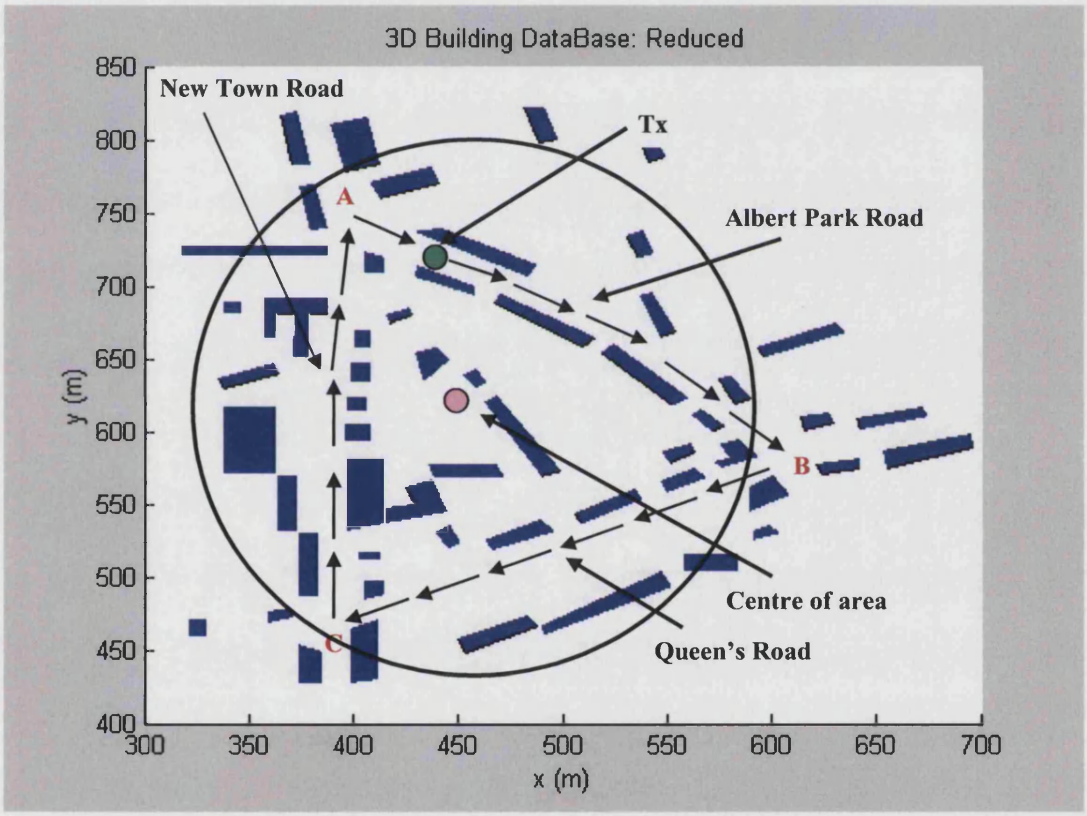

Figure 6.2: *Plan view of simulated test route.*

The main simulated test sequence was executed 184 times (92 times for reflection interactions and 92 times for diffraction interactions). The simulated data was then stored in five separate files. Each file contains the total number of filtered or valid ray-paths, field strength, optical lengths of each ray, locations of all points-of-reflection (PORs) and locations of all points-of-diffraction (PODs). The pre-processed simulated data for combined reflection and diffraction interactions were also obtained and stored in six separate files for each receiver location (see Table 6.1).

6.2.2 Noise threshold

An algorithm was developed to find derive 'noise threshold' for each simulated CIR from the noise thresholds levels present in the measured CIRs (see Chapter 5, Sections 5.4.1.5.3-5). Figure 6.3(a) shows a plot of average noise threshold levels found from the measured CIRs for three consecutives measurements taken along the route 1 (Chapter 5, Section 5.4.1). Figure 6.3(b) shows the corresponding cdfs.

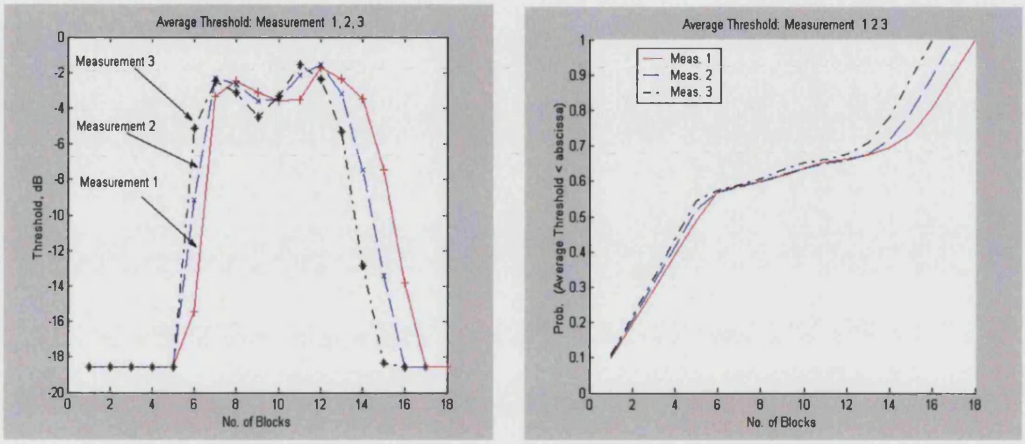

(a) (b)

Figure 6.3: *(a) Average noise threshold levels of the measured CIRs, (b) Cdf of average noise threshold levels. [+ Meas. 1, x Meas.2, * Meas.3].*

6.2.3 Post-processing of simulated data

6.2.3.1. Initial data inspection

The simulated data was executed 11 times, 3 times for reflection interaction (Sim10, Sim20, and Sim30, and 2 times for diffraction interaction Sim01 and Sim02, and 6 times for all possible combinations of reflection and diffraction interactions. Table 6.1 shows number of simulation runs, simulation types, number of receiver locations where signal received and number of receiver locations along each route. Simulation types (column 2), Sim ij can be read as i reflection interaction and j diffraction interactions.

As described earlier in Section 6.2.1, the simulated receiver test route was split into 92 distinct receiver locations. In Table 6.1 column 3 shows the number of locations where simulated signal was observed or received.

One of the major limitation or drawback of ray-tracing models is that it is not possible to observe signals at all receiver locations. This is due to the fact that deeply shadowed areas create discontinuities in received signal levels. These discontinuities are common and expected, and reported by many authors e.g. [4], [101], [228], [265] - [267], [343], [351] - [353], [363].

Authors normally set the values where ray-paths are absent to zero when calculating RMS-DS, e.g. [101], [266].

As the number of interactions increases the occurrence probability of discontinuities decreases (see Table 6.1). The inclusion of diffraction (Sim02), as might be expected, effectively eliminates these discontinuities.

Table 6.1: *Simulation types and number of receiver locations.*

No.	Simulation types	No. of Rx locations where signal received	No. of Rx locations on each road
01	Sim10	37	1-26 Albert Part Road (LoS scenario) 27-57 Queens Road (NLoS scenario) 58-89 New Town Road (NLoS scenario) 90-92 Albert Park Road (LoS scenario)
02	Sim20	40	
03	Sim30	49	
04	Sim01	89	
05	Sim02	92	
06	Sim32	49	
07	Sim31	49	
08	Sim22	40	
09	Sim21	40	
10	Sim12	37	
11	Sim11	37	
Total number of receiver (Rx) locations : 92			

6.3 Simulated results

In order to validate 3D MRT-1 model we have compared the simulated results and measured results.

The simulated data was constructed and the following channel parameters were extracted for several reflection and diffraction interaction orders:

1. Number of ray-paths
2. Transmission loss
3. Received power
4. Power delay profiles
5. Average delay spread
6. RMS delay spread

6.3.1 Ray-path statistics

Figure 6.4(a) and (b) show frequency histograms of possible ray-paths for Sim30 and Sim02. As the number of interaction (reflection or diffraction) increases the number of possible paths increases exponentially [101], [266], [288]. For example, Sim10 results in 23 possible paths, Sim20 results in 1,099 possible paths and Sim30 results in 83,316 possible paths.

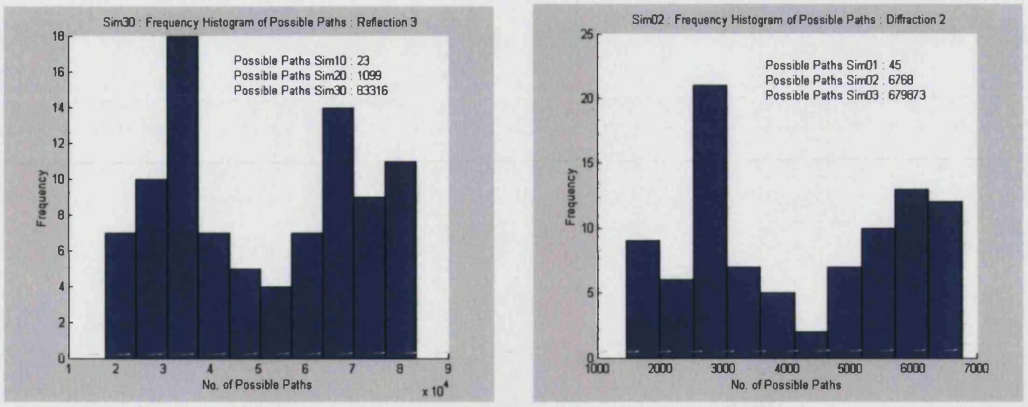

(a) (b)

Figure 6.4: *Frequency histograms of possible ray-paths (a) Sim30, (b) Sim02.*

Figure 6.5(a) and (b) shows frequency histograms of filtered or valid ray-paths for Sim30, Sim02. A similar range of filtered or valid ray-paths was observed for all reflection interactions (Sim10, Sim20, and Sim30). The reasons for this are 1) as the reflection interaction order increases the probability of its occurrence decreases [357] and 2) reflection interaction are rare in deeply shadowed areas [101], [183], [216], [265] - [267], [288], [357]. For diffraction interactions, however (Sim01, Sim02), the number of valid ray-paths increases as the number of interactions increases. Sim01, for example, results in 25 valid ray paths whilst Sim02 results in 356 valid ray-paths.

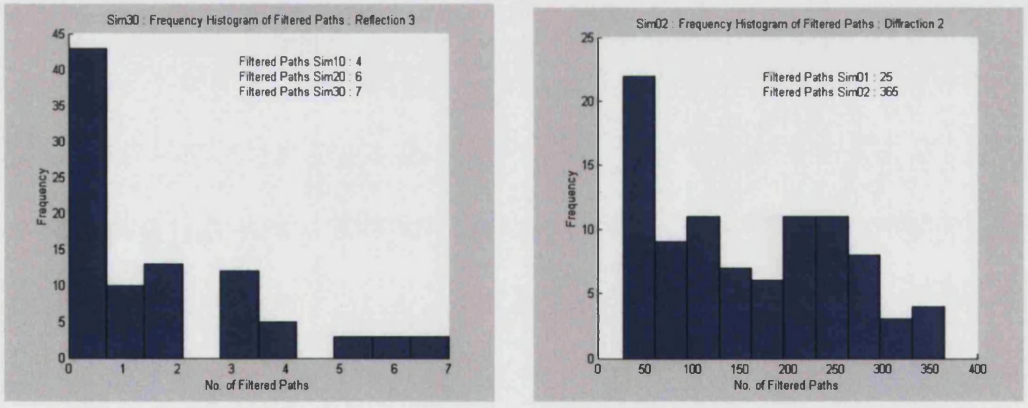

(a) (b)

Figure 6.5: *Frequency histograms of valid ray-paths, (a) Sim30, (b) Sim02.*

Figure 6.6 shows frequency histograms valid ray-paths for combined reflection-interaction-3 and diffraction-interaction-2 (Sim32).

Table 6.2 shows the maximum number of valid ray-paths computed along the receiver route. Note that as the number of interactions increases the number of the ray-paths increases.

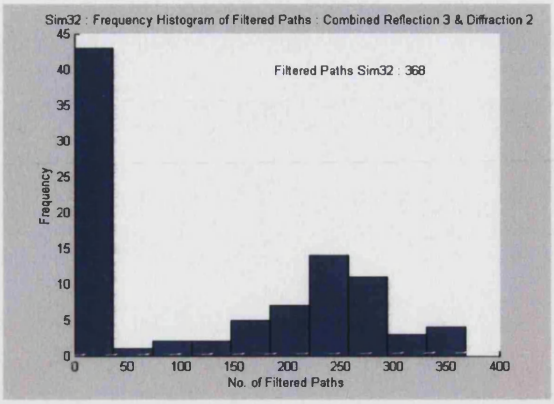

Figure 6.6: *Frequency histograms of valid ray-paths for combined reflection-diffraction interaction (Sim32).*

Table 6.2: *Possible and valid ray-paths computed along the simulated receiver route.*

Simulations	Possible Paths	Filtered or Valid paths
Sim10	23	4
Sim20	1099	6
Sim30	83316	8
Sim01	45	25
Sim02	6768	365
Sim03	679873	—

6.3.2 Simulated ray-paths

A total of 1,012 simulated propagation ray-path plots obtained for all 11 simulation types, along the simulated receiver route (see Table 6.1). Some example plots for reflected and diffracted ray-paths are shown in Figures 6.7 – 6.12.

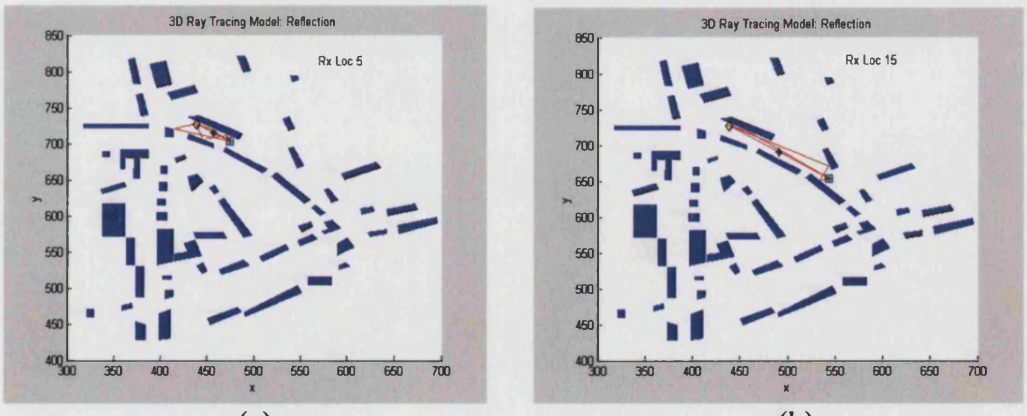

(a) (b)

Figure 6.7: *Simulated reflected valid ray-paths (Sim30), (a) Rx Location 5 at Albert Park Road, (LoS) scenario, (b) Rx Location 15 at Albert Park Road, (LoS) scenario.*

The over-riding qualitative impression is of energy predominantly following the road layout. Street canyon effects are well known, and expected, in urban areas but there is the suggestion here that similar wave-guiding phenomena also operate in residential suburban areas where building density much lower and gaps between buildings occur on a much more frequent spatial scale.

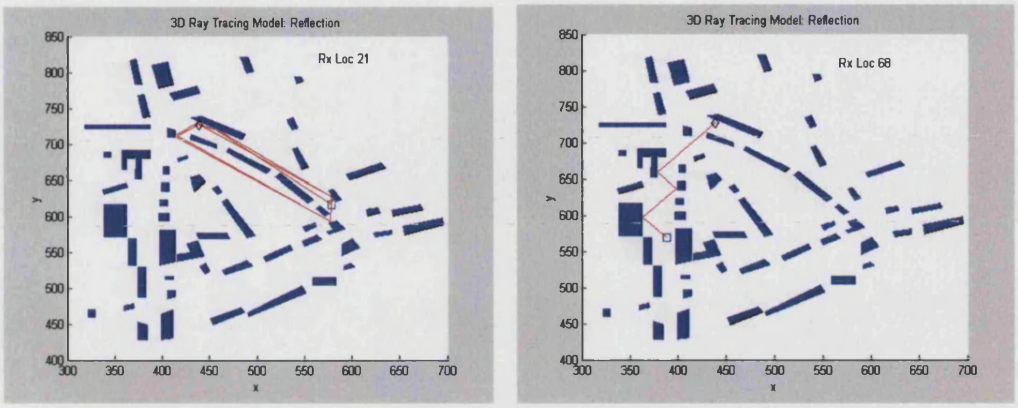

(a) (b)

Figure 6.8: *Simulated reflected valid ray-paths(Sim30), (a) Rx Location 21 at the interaction of Albert Park and Queens Road, (NLoS) scenario, (b) Rx Location 68 at New Town Road, (NLoS) scenario.*

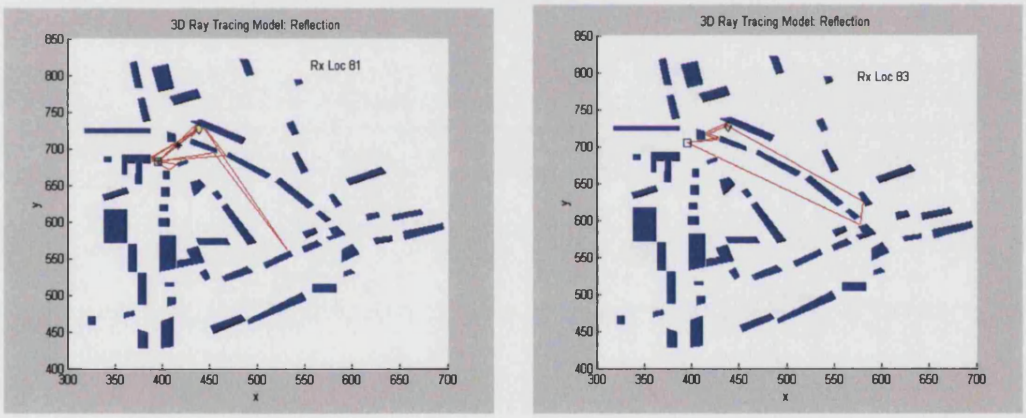

(a) (b)

Figure 6.9: *Simulated reflected valid ray-paths (Sim30), (a) Rx Location 81 at New Town Road, (LoS) scenario, (b) Rx Location 83 at New Town Road, (NLoS) scenario.*

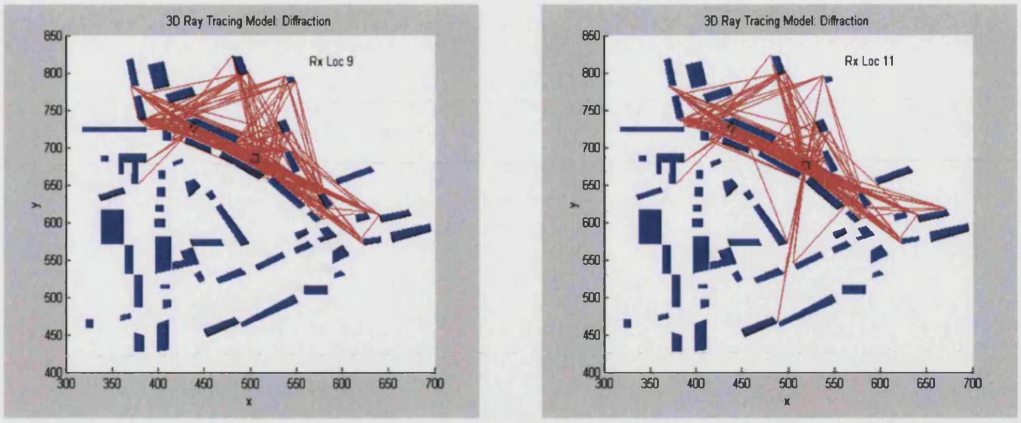

(a) (b)

Figure 6.10: *Simulated diffracted valid ray-paths (Sim02), (a) Rx Location 9 at Albert Park Road, (LoS) scenario, (b) Rx Location 11 at Albert Park Road, (LoS) scenario.*

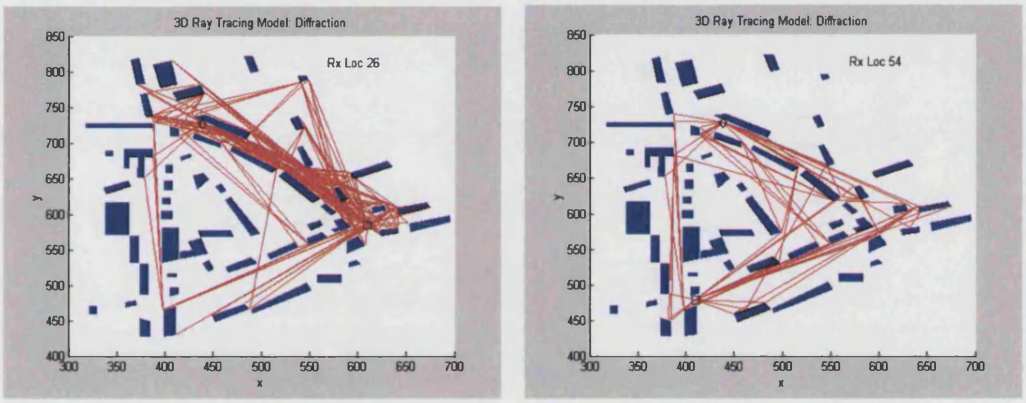

(a) (b)

Figure 6.11: *Simulated diffracted valid ray-paths (Sim02), (a) Rx Location 26 at the intersection of Albert Park and Queens Road, (NLoS) scenario, (b) Rx Location 54 at Queens Road, (NLoS) scenario.*

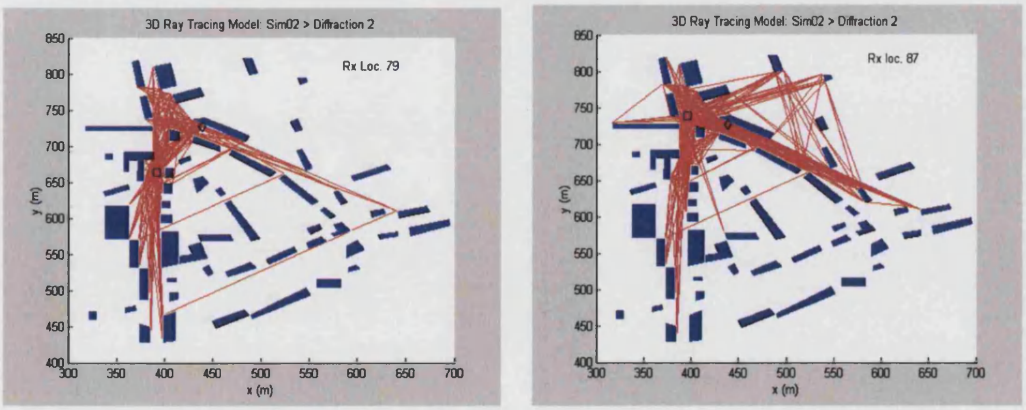

(a) (b)

Figure 6.12: *Simulated diffracted valid ray-paths (Sim02), (a) Rx Location 79 at New Town Road, (NLoS) scenario, (b) Rx Location 87 at intersection of New Town and Albert Park Road, (NLoS) scenario.*

6.3.3 Simulated power delay profiles

A total of 1,012 simulated CIR and PDPs were obtained for all 11 simulation types. Examples are shown in Figure 6.13 - 6.16.

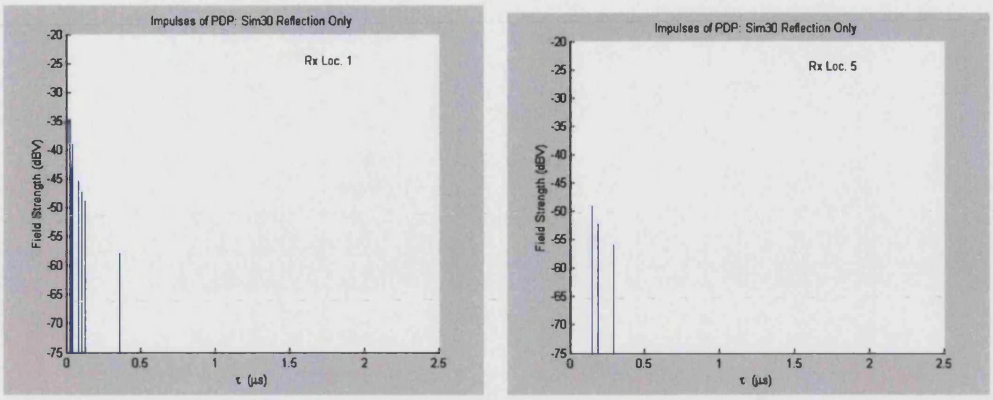

(a) (b)

Figure 6.13: *Discrete PDPs (Sim30)*
(a) Rx at location 1 (Albert Park Road), (b) Rx at location 5 (Albert Park Road).

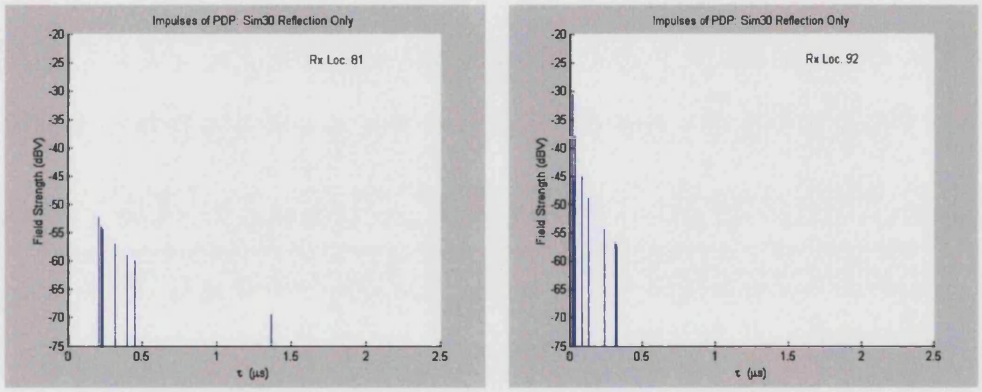

(a) (b)

Figure 6.14: *Discrete PDPs of (Sim30)(a) Rx at location 81 (New Town Road), (b) Rx at location 92 (Albert Park Road).*

Figures 6.15 - 6.16 show simulated PDPs for Sim02.

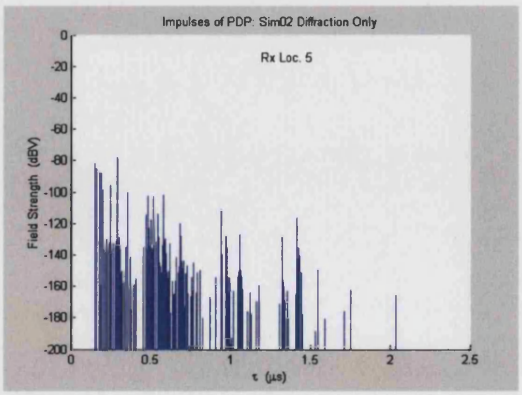

Figure 6.15: *Simulated PDP (Sim02): Rx location 5 (Albert Park Road).*

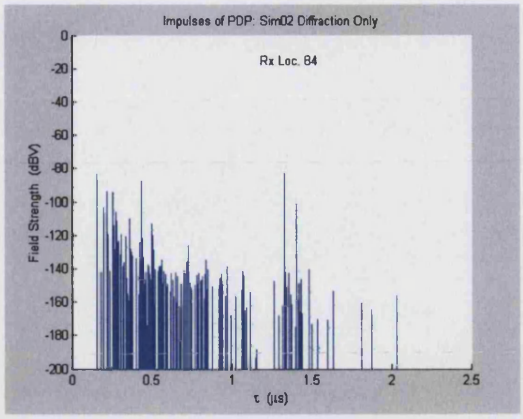

Figure 6.16: *Simulated PDP (Sim02) Rx location 84 (New Town Road).*

6.3.4 Simulated channel parameters

Received power, transmission loss, average delay spread and RMS delay spread have been calculated for each CIR along the route.

6.3.4.1 Power

The total received power at each point along the measurement route was obtained for reflection orders up to three, diffraction orders up to two and all combinations of reflection and diffraction orders. Figures 6.17 - 6.19 shows the simulated received power and the corresponding cdfs. Figure 6.20 shows all combined simulated received power of reflection and diffraction for Sim10, Sim20, Sim30, Sim11, Sim21, Sim31, Sim12, Sim22, Sim 32.

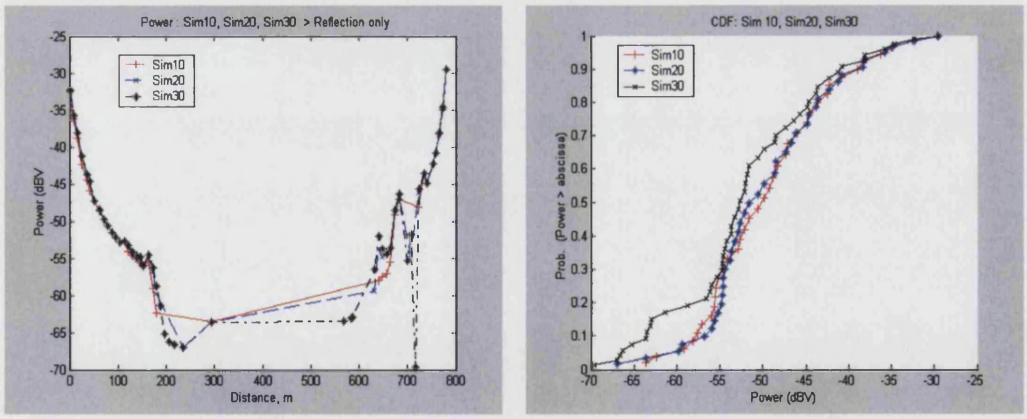

(a) (b)

Figure 6.17: *Simulated received power for Sim10, Sim20 and Sim30: (a) As a function of distance travelled (b) corresponding cdfs.*

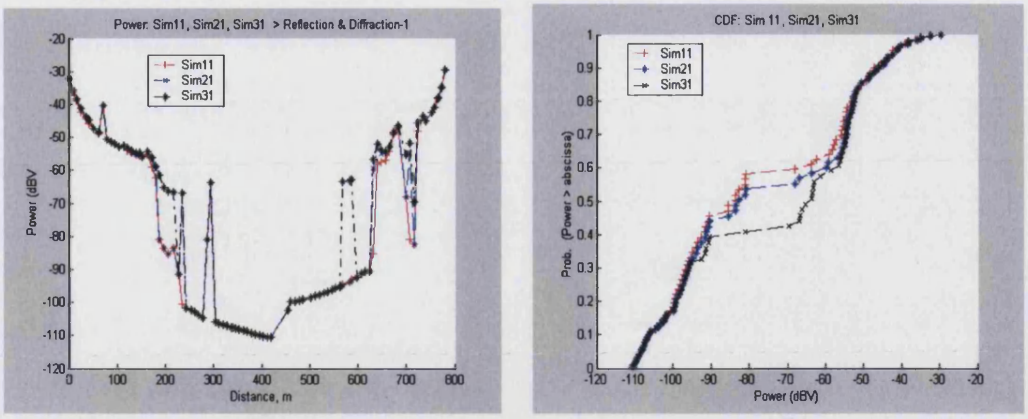

(a) (b)

Figure 6.18: *Simulated received power for Sim11, Sim21 and Sim31: (a) As a function of distance travelled (b) corresponding cdfs.*

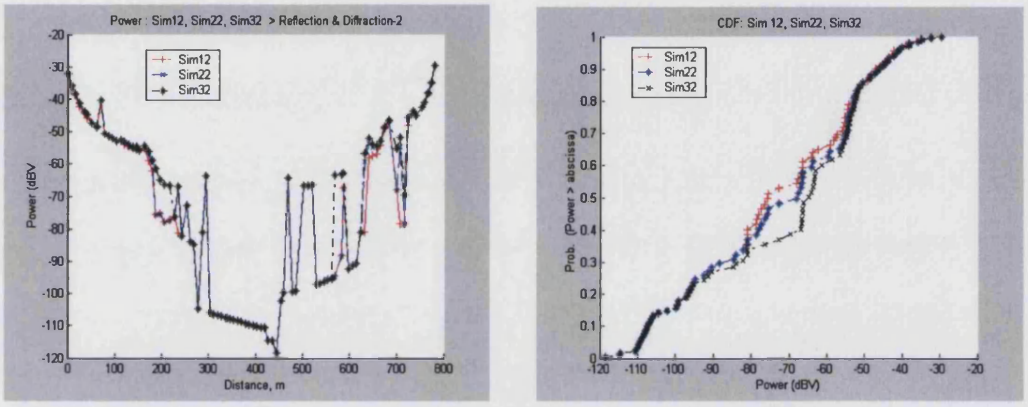

(a) (b)

Figure 6.19: *Simulated received power for* Sim12, Sim22 and Sim32: *(a) As a function of distance travelled (b) corresponding cdfs.*

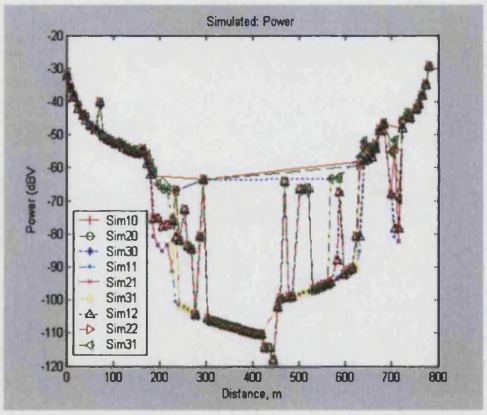

Figure 6.20: *Simulated received power for Sim10, Sim20, Sim30, Sim11, Sim21, Sim31, Sim12, Sim22, Sim32, as a function of distance travelled.*

In Figure 6.17(a), the curves from 0 to 218 m (Albert Park Road) represent LoS conditions, the curves from 227 m to 470 m (Queen's Road) are of, which

represent a deeply shadowed (NLoS) region, the curves from 478 m to 758 m (New Town Road) also represent a shadowed region, and the curves from 765 m to 780 m (Albert Park Road) which completes the measurement route represent a LoS area. It is apparent from Figure 6.20 that power decreases as the Tx –Rx separation distance increases. We have also observed that as the number of reflection or diffraction interactions increases the power decreases. This is expected since, as the number of interactions increases, contributions in the signal due to long delayed ray-paths (i.e. distant buildings) increases (e.g. Figure 6.8 – 6.9). The difference in received power between reflection only and combined reflection and diffraction is small which suggests that reflections signal dominate in terms of gross power levels.

6.3.4.2 Transmission loss

Figure 6.21 – 6.24 shows the transmission loss curves corresponding to the received power of Figure 6.17 – 6.20.

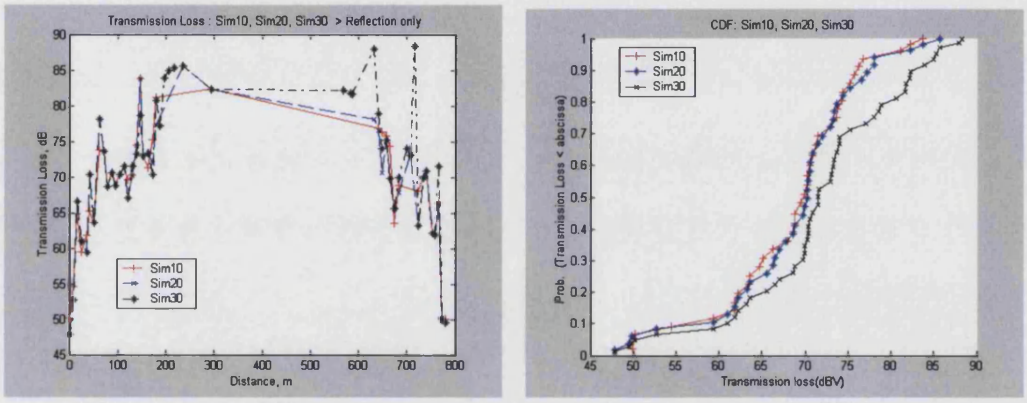

(a) (b)

Figure 6.21: *Simulated transmission loss for Sim10, Sim20 and Sim30: (a) As a function of distance travelled (b) corresponding cdfs.*

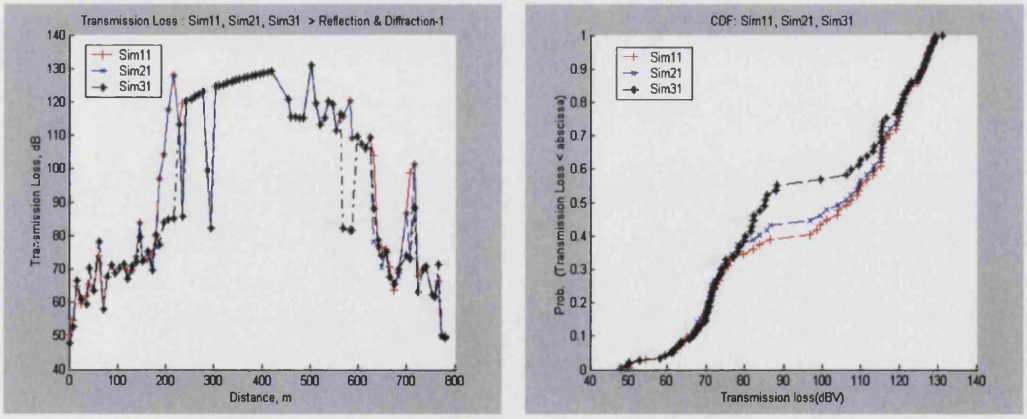

(a) (b)

Figure 6.22: *Simulated transmission loss for Sim11, Sim21 and Sim31: (a) as a function of distance travelled (b) corresponding cdfs.*

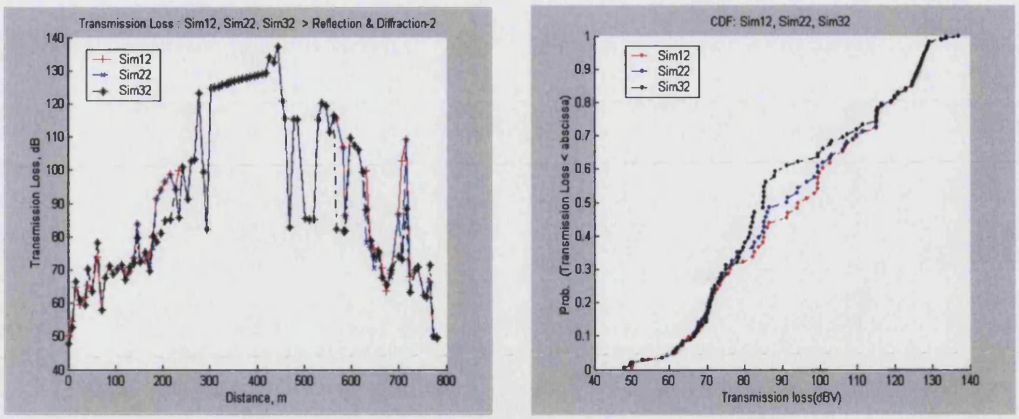

(a) (b)

Figure 6.23: *Simulated transmission loss for Sim12, Sim22 and Sim32: (a) as a function of distance travelled (b) corresponding cdfs.*

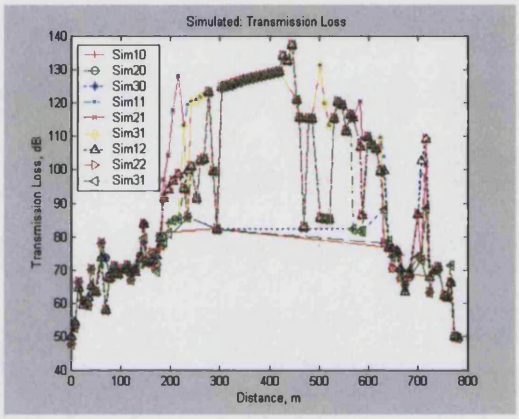

Figure 6.24: *Simulated transmission loss for Sim10, Sim20, Sim30, Sim11, Sim21, Sim31, Sim12, Sim22 and Sim32, as a function of distance travelled.*

6.3.4.3 RMS delay spread

RMS delay spread (RMS-DS) was obtained as a function of displacement around the measurement route for reflection orders up to three, diffraction orders up to two and all combinations of reflection and diffraction orders. Figures 6.25 - 6.27 shows the simulated RMS-DS. Figure 6.28 shows the all combined simulated RMS-DS of reflection and diffraction for Sim10, Sim20, Sim30, Sim11, Sim21, Sim31, Sim12, Sim22, Sim 32.

Comparisons between the simulated the RMS-DS data shows large, rapid and spatial variation. This is not unreasonable since paths of disparate length may be born and die over relatively small spatial scales.

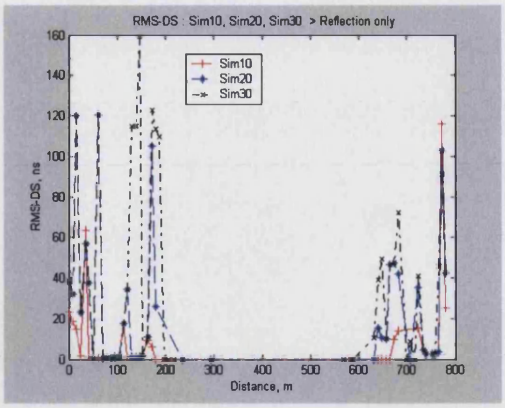

Figure 6.25: *Simulated RMS-DS for Sim10, Sim20 and Sim30, as a function of travel distance around measurement route.*

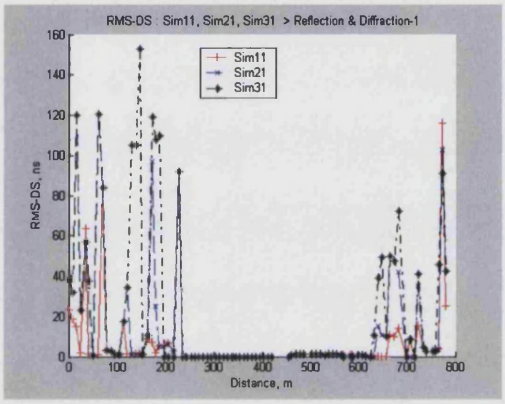

Figure 6.26: *Simulated RMS-DS for Sim11, Sim21 and Sim31, as a function of travel distance around measurement route.*

It is apparent from Figure 6.28 that RMS-DS increases with increasing interaction orders. We have also observed that as the number of interactions increases RMS-DS may increase or decrease. This is expected since, as the number of interactions increases, contributions in the signal due to short and long delayed ray-paths decreases and increases, respectively. It is also apparent from Figure 6.28 that there is no significant difference in the values of the RMS-DS observed between the reflection only predictions and reflections plus diffraction. This, again, suggests that reflected signals dominate. Large peaks in delay at particular points around the measurement route are due to reflections from distant buildings (e.g. Figure 6.8 – 6.9).

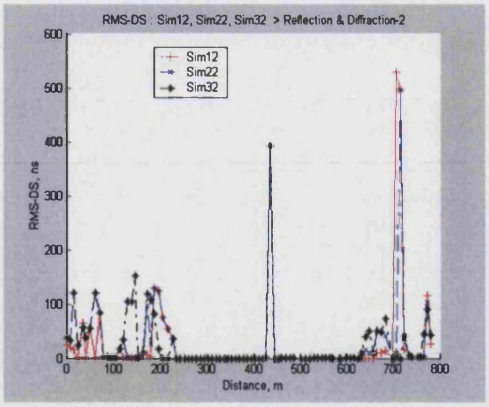

Figure 6.27: *Simulated RMS-DS for Sim12, Sim22 and Sim32, as a function of travel distance around measurement route.*

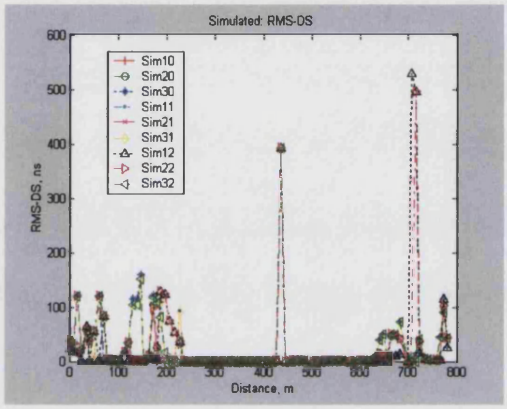

Figure 6.28*: Simulated RMS-DS for Sim10, Sim20, Sim30, Sim11, Sim21, Sim31, Sim12, Sim22 and Sim32, as a function of travel distance around measurement route.*

6.3.5 Comments

The following paragraphs summarise each simulated result.

A gradual decrease in power and a gradual increase in transmission loss is observed with an increase in the Tx – Rx separation distance. As described earlier, as the number of reflection or diffraction interactions increases the power decreases. This is expected since, as the number of interactions increases, contributions in the signal due to long delayed ray-paths (i.e. distant buildings) increases (e.g. Figure 6.8 – 6.9).

We observed that RMS-DS increases with increasing interaction orders. We have also observed that as the number of interactions increases, RMS-DS may increase or decrease. This is expected since, as the number of interactions increases, contributions in the signal due to short and long delayed ray-paths decreases and increases, respectively. Large peaks in RMS-DS at particular points around the measurement route are due to reflections or diffraction from distant buildings.

It is also observed that there is no significant difference in the values of the RMS-DS observed between the reflection only predictions and reflections plus diffraction. This, again, suggests that reflected signals dominate.

There is strong evidence that a single reflection model is inadequate in terms of RMS-DS prediction. Three order of reflection interaction is adequate to predict the channel characteristic as reflection dominates in terms of gross signal variations. We have also observed that diffraction is significant in the deep shadowed regions but not elsewhere, and two order of diffraction interaction is adequate to predict the channel characteristics in the shadowed regions.

6.4 Comparison between the predicted and measured results

Predicted and measured received power and delay spread are compared below.

6.4.1 Comparison between predicted and measured received power

Figure 6.29 compares the measured received power to that predicted using a reflection order of three but with no diffraction contributions and Figure 6.30 makes the same comparison with diffraction contributions (up to order two) added.

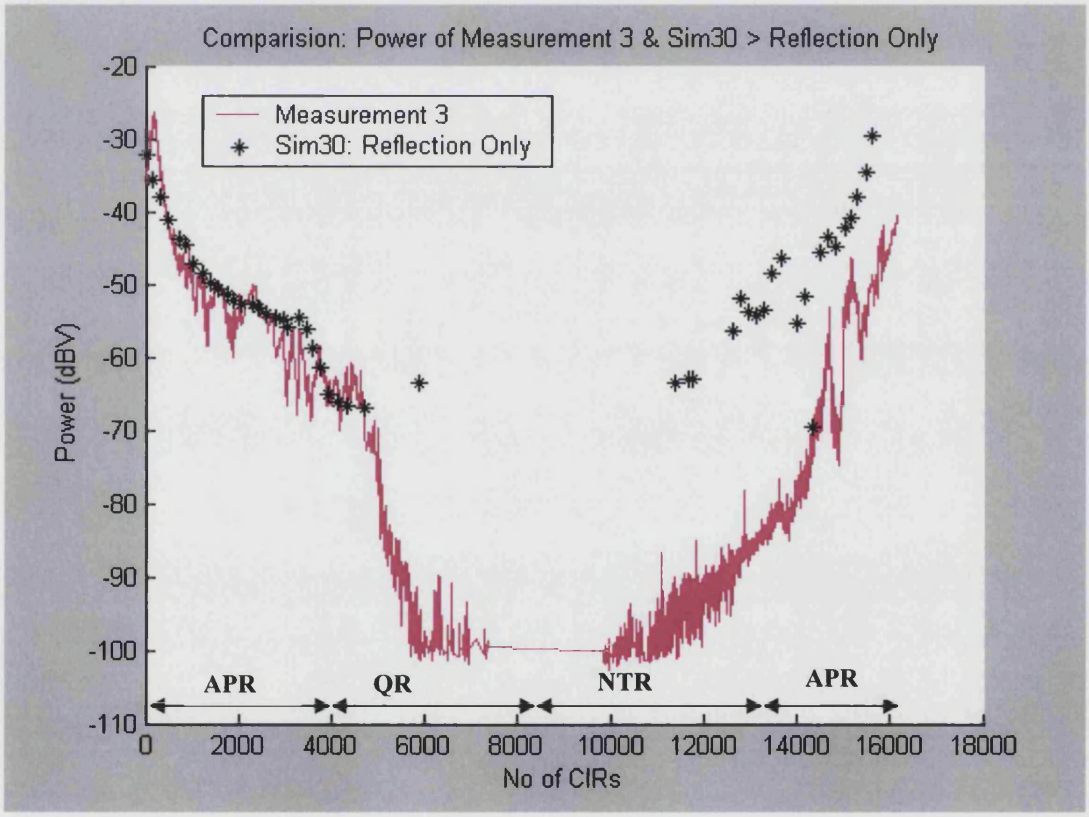

Figure 6.29: *A comparison of predicted (Sim30) and measured total received power.*

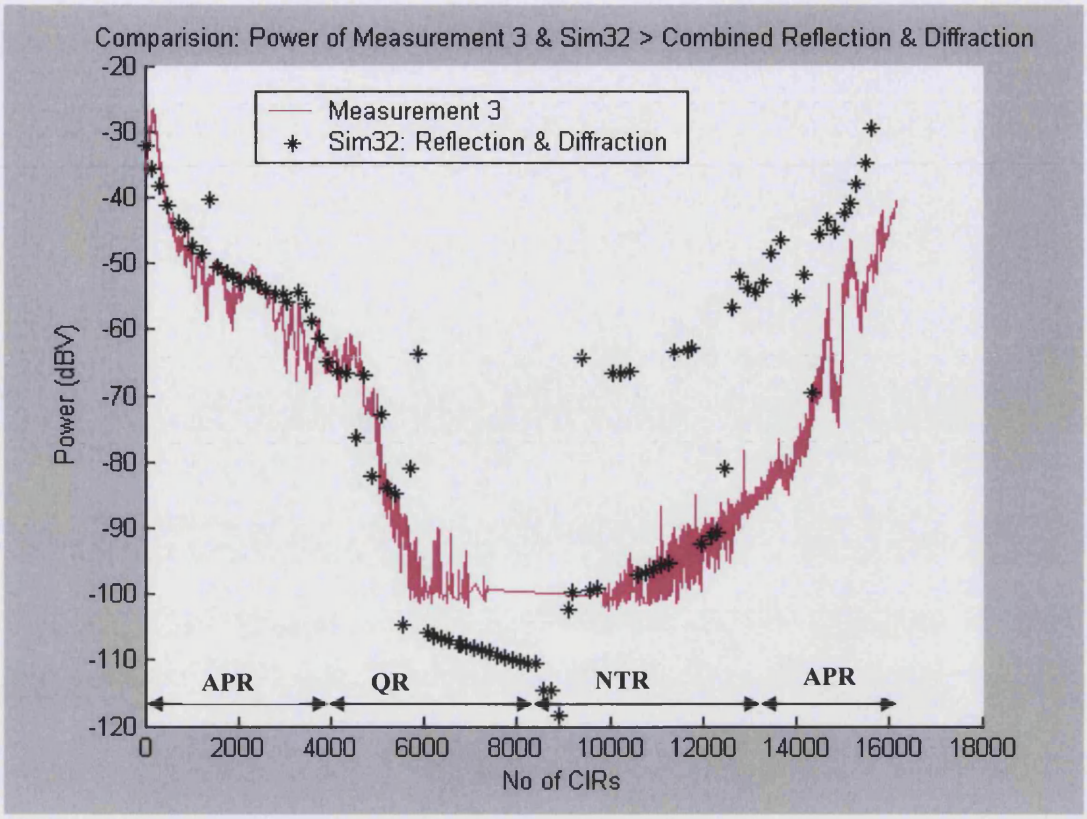

Figure 6.30: *A comparison of predicted (Sim32) and measured total received power.*

The similarity of Figures 6.29 and 6.30 strongly suggest that reflected paths dominate diffracted paths.

The only significant difference between Figures 6.29 and 6.30 is the prediction in Figure 6.30 of low level signals is the region 600 m to 1200 m. These low level signals are clearly due to diffraction. These figures taken together give good confidence in the ray tracing software. They also suggest strongly that, at least from a signal level coverage point of view, reflections dominate in all but strongly shadowed regions.

6.4.2 Comparison between predicted and measured delay spread

Figure 6.31 compares measured and predicted RMS delay spread. The prediction is based on reflections only up to order 3 (i.e. Sim30).

Figure 6.32 compares the delay spread measurements with a prediction based on reflections up to order 3 and diffractions up to order 2 (i.e. Sim32).

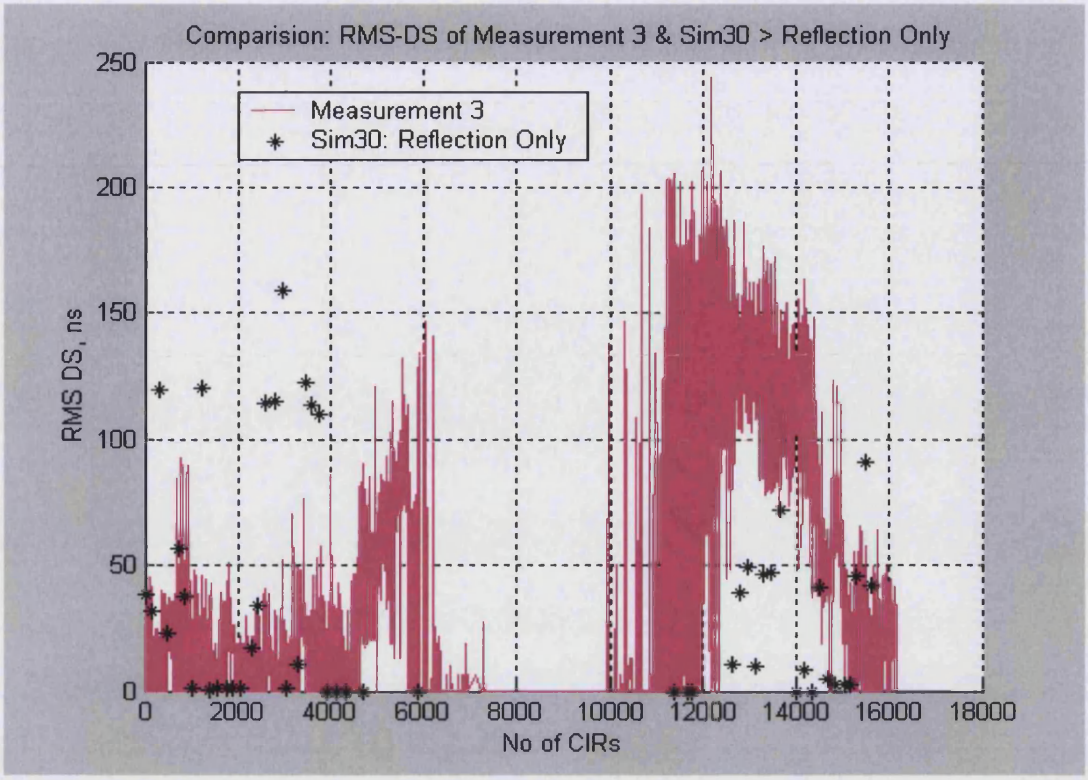

Figure 6.31: A *comparison of predicted (Sim30) and measured RMS delay spread.*

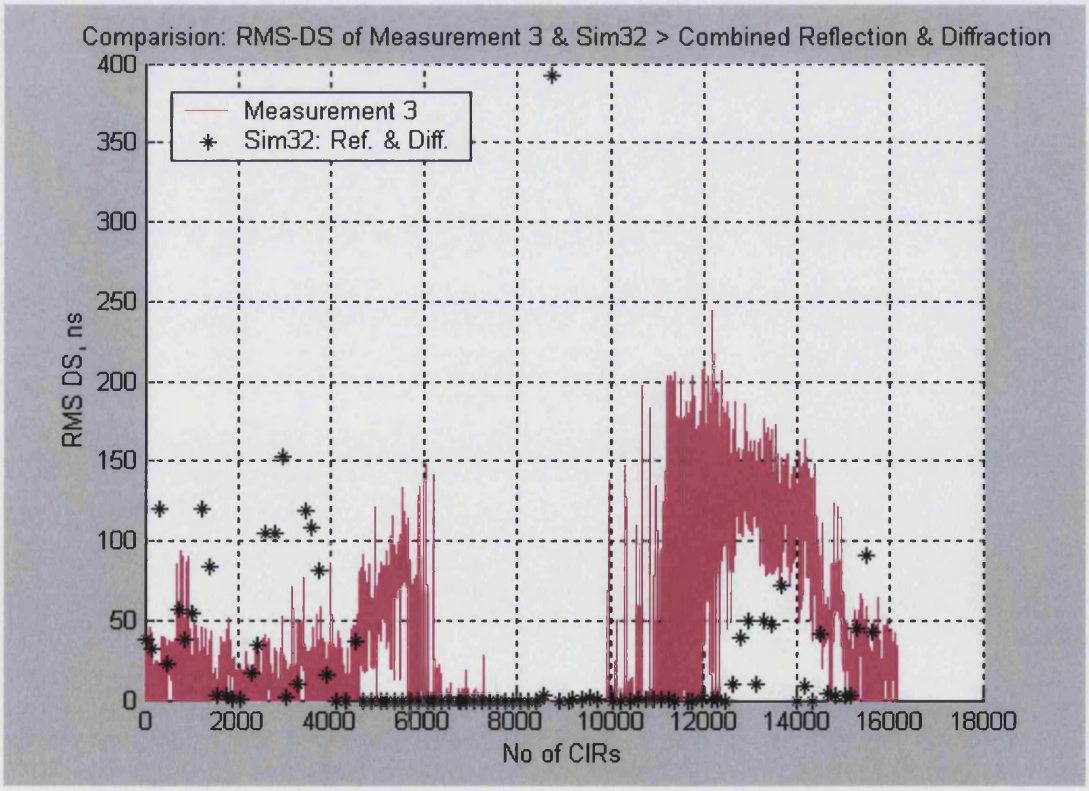

Figure 6.32: A *comparison of predicted (Sim32) and measured RMS delay spread.*

In both figures it is clear that the ray-tracer is not capable of precisely reproducing the measured RMS delay spread at a particular point in space. The values are, generally, of the correct order, however. Table 6.3 summarises the comparison numerically.

Table 6.3: *Comparison of predicted and measured received power and RMS delay spread.*

	Received power (dBV)			RMS delay spread (ns)	
	Minimum	**Maximum**	**Mean**	**Maximum**	**Mean**
Prediction (reflection only)	-69.7	-29.5	-41.8	159.3	35.6
(Prediction (reflection plus diffraction)	-118.4	-29.5	-41.7	152.6	37.6
Measurement	-102.7	-26.5	-45.6	243.7	48.9

There is a paradox in the minimum received power values reported in Table 6.3 in that the minimum received power appears to decrease with the addition of diffracted components. Whilst this is not theoretically impossible (the diffracted components could add destructively to the field at all points where the total field is sampled) it is certainly improbable (we would expect the fields to add with random phase and thus the reflected and diffracted powers to sum). The resolution of the paradox is simply that the prediction using only reflections leads to zero field strength in many (shadowed) locations. These shadowed regions are illuminated by diffracted (and generally weak) fields when the diffraction mechanism is added. The minimum values reported are the minimum non-zero values and so the low values of diffracted field actually represent an increase on zero field values.

6.5 Conclusion

This chapter described the simulated results and comparisons between predicted and measured channel characteristics.

The 3D MRT-1 model accounts for the multiple reflections and multiple diffraction interactions with maximum numbers of 3-reflection-interactions and 2-diffraction-interactions for each ray-path. The model was configured to produce the multipath channel parameters, such as CIR, PDPs, transmission loss, received power, AV-DS and RMS-DS. In order to validate the 3D MRT-1 model, comparison between the simulated and measured PDPs, received power and RMS-DS were made at 2.38 GHz in microcellular residential suburban area of Malvern, UK.

The statistics of the simulated ray-paths showed that the number of interactions has a strong influence on the variability of the simulated channel characteristics, the accuracy and computational efficiency of the ray-tracing models.

We have observed that short and long delayed ray-paths have significant influence on the simulated channel characteristics.

Comparisons between predicted and measured channel characteristics have been made. We observed that the reflection interactions have strong influence on the channel characteristics.

The contribution of diffraction to total received power is small in all but deeply shadowed regions. The contribution to delay spread, however, may be more significant.

In terms of the dependency of the accuracy on the number of reflection intersections showed that consideration of 3-order reflection in 3D modelling is very important and leads to best accuracy in terms of the simulated channel characteristics. We have also observed that diffraction is significant in the deep shadowed regions but not elsewhere, and 2-order of diffraction interaction is adequate to predict the channel characteristics in the shadowed regions.

The similarity between predicted and measured results gives confidence in the utility of the 3D MRT-1 model.

Chapter 7: Conclusions and Further Work

7.1 Conclusions

The work reported in this thesis is concerned with measurement, modelling and characterisation of wideband mobile radio channels in suburban microcellular environments.

Chapter 1 began with a brief review of the evolution of mobile cellular and PCN systems. It went on to addresses several issues and limitations of the radio communication systems. The centrality of the dispersive time-variant multipath mobile radio channel and its characterisation to the planning, design and implementation of future microcellular systems was justified.

In Chapter 2 the different approaches to modelling and characterisation of the radio channels were outlined. Fundamental concepts and quantities, central to virtually all approaches and important in the context of benchmarking and comparisons, were described and defined.

Chapter 3 presented a comprehensive literature review of existing work. The relative merits of deterministic and empirical modelling were discussed and the use of deterministic approaches, in the form of ray-tracing, justified. The GO basis of ray-tracing was described and the role of UTD to model diffraction pointed out.

Luebber's enhanced UTD diffraction coefficient for a non-perfectly conducting wedge, recommended by ITU-R was used.

The advantages of the method of images over ray-shooting in terms of the exactness of the solution it provides (within the approximations inherent in GO) was explained and its immunity to spatial aliasing underlined.

The problem of limited computational resources to the application of ray-tracing technique was referred to and the exponential increase in resources required with increasing environment size/complexity stated. Efficient ray-path search methods were identified as the critical component in a practical ray-tracing tool. Visibility criteria were suggested as a way of implementing such efficient algorithms. A number of visibility approaches were reviewed and their principal disadvantages discussed. The dependence of deterministic propagation model on the accuracy and resolution of terrain and building databases was stated and explained.

A new wideband, three dimensional, ray-tracing propagation prediction model '3D MRT-1' was presented in Chapter 4. Several novel techniques have been incorporated to realise an efficient ray-tracing algorithm.

3D MRT-1 uses the method of images to trace reflected rays up to order three and the principle of least time to find diffracted rays up to order two. It allows buildings of arbitrary shape (consistent with being synthesised from plane

polygons) and arbitrary electrical properties (conductivity and permittivity), arbitrary frequency, arbitrary antennas (radiation pattern and polarisation) and arbitrary antenna locations and orientations.

The amplitude, phase, polarisation, angle-of-arrival (AoA), angle-of-departure (AoD) and optical path length of each ray traced is recorded and the channel impulse response and power delay profile are constructed. The most important system parameters, received power and RMS delay spread, are then calculated.

Wideband measurements at 2.38 GHz in a microcellular, suburban, environment were reported in Chapter 5. Data in the form of the time-varying complex channel impulse responses (CIRs) were recorded and discrete multipath components extracted. The first-order statistics of these components, including exceedance curves of path number, received power and RMS-DS were calculated and presented.

Chapter 6 compared simulated results using the prediction tool 3D MRT-1 with the measurements reported in Chapter 5. There is close agreement between predicted and measured received power and reasonable agreement between predicted and measured RMS-DS giving good confidence in the 3D MRT-1 tool.

An examination of the effect of varying the number of reflection and diffraction interactions suggests that for path loss purposes diffraction can be neglected in all but strongly shadowed regions. There is evidence that for practical engineering purposes predictions based on three reflections and two diffractions are adequate.

7.2 Further work

The following limitations of 3D MRT-1 could be usefully addressed.

1. The current environment database is created manually. Additional software is required to convert commercial digital databases into the required format
2. Although the building and terrain database in 3D MRT-1 allows for surfaces with non-zero roughness, diffuse scattering is currently neglected
3. Transmission into the interior of buildings is currently neglected.
4. Calculation of computation time of image method with and without visibility matrices can be made
5. Improvements in the algorithmic efficiency of 3D MRT-1 can still be made

Furthermore, the newly developed 3D MRT-1 model can be configured to study the following areas of research:

1. To study radio channel characteristics in different microcellular environment with different frequency bands, antenna and building heights
2. To investigate the transmission loss through buildings. Inclusion of this can improve more accurate prediction of the channel parameters
3. To study the influence of different antenna heights on RMS-DS

4. To study the influence of different diffraction coefficients (classical UTD) and different electrical properties of building walls on the radio channel characterises
5. To study the influences of diffracted ray-paths over pitch rooftops (i.e. the rooftops with different shapes). Such diffracted ray-paths are important for more accurate prediction
6. To investigate the radio channel characteristics in different indoor, multiple indoor, building floors, indoor-to-outdoor, outdoor-to-indoor environments. The models applicability to these environments is important due to increased popularity and demand for the WLANs and WPAN. With such a capability, the 3D MRT-1 will then be greatly enhanced as a powerful tool for the planning, design, implementation and analysis of the future mobile radio systems
7. To investigate the radio channel characteristics due to multiple-input-multiple-output (MIMO) system
8. To investigate the radio channel characteristics due to mobile-to-mobile radio communication
9. To study terrain effects
10. To study vegetation effect
11. To study scattering effect by various scatterers
12. To implement parallel processing techniques

Appendix 1

Characteristics of finite length dipole antenna

We assumed finite length dipole antennas with vertical polarisation. The characteristics of the antenna are defined as follows:

A.1 Radiation pattern of the antenna

The radiation pattern of the antenna (i.e. field strength gain), E_θ is given by [404]:

$$E_\theta \cong j\eta \frac{I_o e^{-jkr}}{2\pi r}\left[\frac{\cos\left(\frac{kl}{2}\cos\theta\right)-\cos\left(\frac{kl}{2}\right)}{\sin\theta}\right] \qquad \text{(A.1)}$$

where

η: for a free-space medium ($\eta \cong 120\pi$)

I_o: is a constant

r: is a distance

k: is wave number ($k=\frac{2\pi}{\lambda}$)

l: is the length of the antenna ($l=\frac{\lambda}{2}$)

In Eq. (A.1), we assume

$$j\eta \frac{I_o e^{-jkr}}{2\pi r} = 1 \qquad \text{(A.2)}$$

Therefore, we get the radiation pattern (i.e. field strength gain), E_θ, of the antenna as:

$$E'\theta = \left[\frac{\cos\left(\frac{kl}{2}\cos\theta\right)-\cos\left(\frac{kl}{2}\right)}{\sin\theta}\right] \qquad \text{(A.3)}$$

A.2 The radiation resistance

The radiation resistance or load impendence, (Z_L) can be calculated as:

$$Z_L = \frac{2P_{rad}}{|I_o|^2} = \frac{\eta}{2\pi}\{C + \ln(kl) - C_i(kl) + \frac{1}{2}\sin(kl)\times[S_i(2kl) - 2S_i(kl)] + \frac{1}{2}\cos(kl)\times\left[C + \ln\left(\frac{kl}{2}\right) + C_i(2kl) - 2C_i(kl)\right]\} \quad \text{(A.4)}$$

where $C = 0.5772$ (Euler's constant), k is the wave number, l is the length of the antenna, $C_i(x)$ and $S_i(x)$ are the cosine and sine integrals given by:

$$C_i(x) = \int_{\infty}^{x} \frac{\cos y}{y} dy \quad \text{(A.5)}$$

$$C_i(x) = \int_{0}^{x} \frac{\sin y}{y} dy \quad \text{(A.6)}$$

A.3 The maximum gain of the antenna

The maximum gain ($G_{\max}$) of the antenna can be defined as:

$$G_{\max} = D_{\max} = D_o = \frac{2F(\theta)|_{\max}}{Q} \quad \text{(A.7)}$$

where $D_{\max} = D_o$ is the maximum directivity, $F(\theta)$ is the radiation intensity given as:

$$F(\theta) = \left[\frac{\cos\left(\frac{kl}{2}\cos\theta\right) - \cos\left(\frac{kl}{2}\right)}{\sin\theta}\right]^2 \quad \text{(A.8)}$$

The maximum radiation intensity $F(\theta,\phi)|_{\max}$ is unity. Therefore:

$$F(\theta,\phi)|_{\max} = 1 \quad \text{(A.9)}$$

and Q is calculated as:

$$Q = \{C + \ln(kl) - C_i(kl) + \frac{1}{2}\sin(kl)\times[S_i(2kl) - 2S_i(kl)] + \frac{1}{2}\cos(kl)\times\left[C + \ln\left(\frac{kl}{2}\right) + C_i(2kl) - 2C_i(kl)\right]\} \quad \text{(A.10)}$$

Therefore, by substituting Eq. (A.9) into Eq. (A.7), we get:

$$G_{max} = \frac{2}{Q} \tag{A.11}$$

References

[1] Casal C.R., Schoute F., and Prasad R., "A Novel Concept for Fourth Generation Mobile Multimedia Communication," *Vehicular Technology Conference, VTC'99*, vol. 1 pp. 381-385, 19-22 September, 1999.

[2] Rappaport T.S., "Wireless Communications Principles and Practice," *Prentice Hall PTR*, 1996.

[3] Zeng M. et al., "Recent Advances in Cellular Wireless Communications," *IEEE Communication Magazine*, pp. 128-138, September, 1999.

[4] Lee B.S., "Propagation Modelling of the Radio Channel Characteristics for Indoor and Outdoor Systems," *PhD Thesis, University of Bristol, UK*, 2002.

[5] *http://www.fcc.gov*, 2006.

[6] MacDonald V.H., "The Cellular Concept," *The Bell Systems technical Journal*, vol. 58, no.1 pp. 15-43, January, 1979.

[7] Boucher N., "Cellular Radio Handbook," *Quantum Publishing*, 1991.

[8] Calhoun G., "Digital Cellular Radio," *Artech House*, 1988.

[9] *www.tagish.co.uk/ethosub/lit6/f51a.htm*, 2005.

[10] ""Vision for the Evolution from GSM to UMTS", GSM MoU Association 1998, TG.13," *www.gsmworl.com/3g/index.html*, 1998.

[11] Yarwood A. et al., "European Radiopaging," *British Telecom Tech. Journal*, vol. 8 pp. 67-68, 1990.

[12] Santamaría A. and López-Hernández F.J., "Wireless LAN Standards and Applications," *Artech House, London*, 2001.

[13] Rappaport T.S., "Wireless Personal Communications Trends and Challenges," *IEEE Antennas and Propagation Magazine*, vol. 33, No. 5 pp. 19-29, October, 1991.

[14] MacNamee R.J.G., Vadgama S.K., and Gibson R.W., "Universal Mobile Telecommunication System - A Concept-," *IERE Fourth International Conference on Land Mobile Radio, University of Warwick, Coventry, Publication No.78, 15-17 December*, 1987.

[15] Tachikawa K., "A Perspective on the Evolution of Mobile Communications," *IEEE Communication Magazine*, pp. 66-73, October, 2003.

[16] Rapeli J., "UMTS: Targets, System Concept, and Standardization in a Global Framework," *IEEE Personal Communications*, pp. 20-28, 1995.

[17] Damosso E. and de Brito G., "COST 231 Achievements as a Support to the Development of UMTS: A Look into the Future," *IEEE Communications Magazine*, pp. 90-96, 1996.

[18] Brand A.E. and Aghvami A.H., "Multidimensional PRMA with Prioritized Bayesian Broadcast - A MAC Strategy for Multiservice Traffic over UMTS," *IEEE Transactions on Vehicular Technology*, vol. 47, no. 4 pp. 1148-1164, November, 1998.

[19] Efthymiou N. et al., "Performance of Intersegment Handover Protocols in an Integrated Space/Terrestrial-UMTS Environment," *IEEE Transactions on Vehicular Technology*, vol. 47, no. 4 pp. 1179-1181, November, 1998.

[20] Holma H. and Toskala A., "WCDMA for UMTS," *John Wiley & Sons, Ltd.*, 2004.

[21] Samukic A., "UMTS Universal Mobile Telecommunications System: Development of Standards for the Third Generation," *IEEE Transactions on Vehicular Technology*, vol. 47, no. 4 pp. 1099-1104, November, 1998.

[22] Dixit S. and Antoniou Z., "Resource Management and Quality of Service in Third-Generation Wireless Networks," *IEEE Communication Magazine*, pp. 125-133, February, 2001.

[23] EL-Sallabi H.M., "Modelling and Characterization of Urban Radio Channels for Mobile Communications," *PhD Thesis, Helsinki University of Technology, Department of Electrical and Communications Engineering, Finland*, 2003.

[24] Walke B., "UMTS: The Fundamental," *John Wiley & Sons, Ltd.*, 2003.

[25] Tanenbaum A.S., "Computer Networks," *Prentice Hall, PTR, New Jersey, 4th Ed.*, 2003.
[26] Xia H.H. et al., "Urban and Suburban Microcellular Propagation," *IEEE 1992*, pp. 5-9, 1992.
[27] Tenerelli P.A., "Diffraction by Building Corners at 28 GHz: Measurements and Modelling," *MS Thesis, Virginia Polytechnic Institute*, 1998.
[28] Fairhurt G., "Metropolitan Area Networks (MANs)," *http://www.erg.abdn.ac.uk /users /gorry/eg3561/intro-pages/man.html*, 2001.
[29] "Metropolitan Area Networks," *http://en.wikipedia.org/wiki/Metropolitan_area_network*, 2006.
[30] "Metropolitan Area Networks: Challenges and Wireless Solutions," *http://www.proxim.com /solutions/man/*, 2005.
[31] Prögler M. et al., "Air Interface Access Schemes for Broadband Mobile Systems," *IEEE Communication Magazine*, vol. 37, no. 9 pp. 106-115, September, 1999.
[32] Correia L.M. and Prasad R., "An Overview of Wireless Broadband Communications," *IEEE Communications Magazine*, pp. 28-33, January, 1997.
[33] Cox D.C., "Wireless Personal Communications: What Is It?" *IEEE Personal Communications*, pp. 20-35, 1995.
[34] Pahlavan K. and Levesque A.H., "Wireless Information Networks," *Wiley & Sons, New York*, 1995.
[35] *http://www.mwrf.com/Articles/ArticleID/5423/5423.html*, 2006.
[36] *http://grouper.ieee.org/groups/802/11/*, 2006.
[37] *http://en.wikipedia.org/wiki/ISM_band*, 2006.
[38] IEEE 802.11, http://en.wikipedia.org/wiki/IEEE_802.11
[39] "About Wireless Networking," http://compnetworking.about.com/cs/ wireless 80211/a/aa 80211 standard.htm, 2006.
[40] *http://www.comnets.rwthaachen.de/report96/node211.html*, 2005.
[41] Umeda N. et al., "Overview of the Fourth-generation Mobile Communication System," *NTT Technical Review, Japan*, vol. 2, no. 9 pp. 12-17, September, 2004.
[42] Mähönen P. and Polyzos G.C., "European R&D on Fourth - Generation Mobile and Wireless IP Networks," *http://www.comsoc.org/pci/Public/2001/Dec/current.html*, pp. 1-3, 2001.
[43] Kivinen J., "Development of Wideband Radio Channel Measurement and Modeling techniques for Future Radio Systems," *PhD Thesis, Department of Electrical and Communications Engineering, Helsinki University of Technology, Finland*, 2001.
[44] Correia L., "An Overview of Wireless Broadband Communications," *IEEE Communications Magazine*, vol. 35, no. 1 pp. 28-33, January, 1997.
[45] Rustako A.J. et al., "Measurements of Microcellular Propagation Loss at 6 GHz and 2 GHz over Non-Line-of-Sight Paths in the City of Boston," *IEEE 1995*, pp. 758-763, 1995.
[46] Molkdar D., "Channel Characteristics, Planning and Deployment of Picocellular Systems at UHF: An Overview," *Electronics and Communication Engineering Journal*, pp. 167-179, August, 2000.
[47] Parsons J.D., "Mobile Radio Propagation Channel," *John Wiley & Sons, Ltd*, 2000.
[48] Steele R. and Prabhu V.K., "Mobile Radio Cell Structures for High User Density and Large Data rates," *IEE Proceedings Part F*, vol. 132, no. 5 pp. 396-404, 1985.
[49] Heddergott R. and Leuthold P.E., "An Extension of Stochastic Radio Channel Modelling Considering Propagation Environments With Clustered Multipath Components," *IEEE Transactions on Antennas and Propagation*, vol. 51, no. 8 pp. 1729-1739, August, 2003.
[50] Bajwa A.S., "Wideband Characterisation of UHF Mobile Radio Propagation in Urban and Suburban Areas," *PhD Thesis, Department of Electronic and Electrical Engineering, University of Birmingham, UK*, 1979.
[51] Steels R., "Mobile Radio Communications," *New York IEEE Press*, 1994.
[52] COST 231 Final Report, "Digital Mobile Radio: COST 231 View on the Evolution towards 3rd Generation Systems," *Commission of the European Communities and COST Telecommunications*, 1999.
[53] Barclay L., "Propagation of Radio Waves, 2nd Edition," *The Institution of Electrical Engineers, London, UK*, 2003.
[54] Bertoni H.L., "Radio Propagation for Modern Wireless Systems," *Prentice Hall, New Jersey*, 2000.

[55] Jakes W.C., "Microwave Mobile Communications," *New York: Wiley*, pp. 50, 1974.
[56] Lee W.C.-Y., "Mobile Communications Design Fundamentals," *Sams & Co., Indianapolis*, 1993.
[57] Lee W.C.Y., "Mobile Communications Design Fundamental," *John Wiley & Sons, Inc*, 1993.
[58] Lee W.C.Y., "Mobile Cellular Telecommunications Systems," *McGraw-Hill, New York*, 1989.
[59] Lee W.C.-Y., "Mobile Communications Engineering," *McGraw-Hill, New York*, 1982.
[60] Lavergnat J. and Sylvain M., "Radio Wave Propagation Principles and Techniques," *John Wiley & Sons, Inc*, 1997.
[61] Macario R.C.V., "Cellular Radio Principles and Design," *Macmillan Press Ltd, London*, 1993.
[62] Macario R.C.V., "Personal & Mobile Radio Systems," *Peter Pergrinus Ltd, London, UK*, 1991.
[63] Parsons J.D. and Gardiner J.G., "Mobile Communication Systems," *Blackie, London*, 1989.
[64] Pätzold M., "Mobile Fading Channels," *John Wiley & Sons, Ltd*, 2002.
[65] Proakis J.G., "Digital Communications, 2nd ed.," *McGraw Hill, New York*, 1989.
[66] Saunders S.R., "Antennas and Propagation for Wireless Communication Systems," *John Willey & Sons, Ltd, New York*, 1999.
[67] Vaughan R. and Andersen J.B., "Channels, Propagation and Antennas for Mobile Communications," *The Institution of Electrical Engineers, London, UK*, 2003.
[68] Walke B.H., "Mobile Radio Networks Networking and Protocols," *John Wiley & Sons, Inc*, 1999.
[69] Tarng J.H., Chang W.R., and Hsu B.J., "Three-Dimensional Modeling of 900-MHz and 2.44-GHz Radio Propagation in Corridors," *IEEE Transactions on Vehicular Technology*, vol. 46, no. 2 pp. 519-527, May, 1997.
[70] Tarng J.H., Liu W.S., Huang Y.F., and Huang J.M., "A Novel and Efficient Hybrid Model of Radio Multipath-Fading Channels in Indoor Environments," *IEEE Transactions on Antennas and Propagation*, vol. 51, no. 3 pp. 585-594, March, 2003.
[71] Löfsved E., "Investigation of Two Wideband UHF Radio Channel Models," *Defence Research Establishment, Sweden*, 1999.
[72] Bello P.A., "Characterization of Randomly Time-Variant Linear Channels," *IEEE Transactions on Communication Systems*, pp. 360-393, December, 1963.
[73] Salous S.et al., "Digital techniques for mobile radio chirp sounders," *IEE Proceedings Communications*, vol. 145 pp. 191-196, 1998.
[74] Salous S. et al., "IF digital generation of FMCW waveforms for wideband channel characterisation," *IEE Proceedings 1 on Communications*, Speech and Vision, vol. 139 pp. 281-288, 1992.
[75] Bailey R.J. and Summers G.R., "Radio Channel Characterisation for the Digital European Cordless Telecommunications System," *British Telecom Tech Journal*, vol. 8, No. 1 1990.
[76] Cullen P.J., Fannin P.C., and Molina A., "Wide-Band Measurement and Analysis Techniques for the Mobile Radio Channel," *IEEE Transactions on Vehicular Technology*, vol. 42, no. 4 pp. 589-603, November, 1993.
[77] Cox D.C., "910 MHz Urban Mobile Radio Propagation: Multipath Characteristics in New York City," *IEEE Transactions on Communications*, vol. COM-21, no. 11 pp. 1188-1194, November, 1973.
[78] Fannin P.C. and Molina A., "Accuracy and Dynamic Range Improvement of Band Pass Impulse Response Measurements Using Pseudorandom Noise," *Electronics Letters*, vol. 27, no. 19 pp. 1755-1756, 12 September, 1991.
[79] Nielson D.L., "Microwave Propagation Measurement for Mobile Digital Radio Application," *IEEE Transactions on Vehicular Technology*, vol. VT-27, No. 3 pp. 117-132, August, 1978.
[80] Turin G.L., Clapp F.D., Johnston T.L., Fine S.B., and Lavry D., "A Statistical Model of Urban Multipath Propagation," *IEEE Transactions on Vehicular Technology*, vol. VT-21, no. 1 pp. 1-9, February, 1972.

[81] Bultitute R.J. and Bedal K., "Propagation Characteristics on Microcellular Urban Mobile Radio Channels at 910 MHz," *IEEE Journal on Selected Areas in Communications*, vol. 7, no. 1 pp. 31-39, January, 1989.

[82] Cook G. and Zaknich A., "Chirp Sounding the Shallow Water Acoustic Channel," *IEEE International Conference on Acoustic, Speech and Signal Processing, WA, USA*, 1998.

[83] Cox D.C., "Multipath Delay Spread and Path Loss Correlation for 910 MHz Urban Mobile Radio Propagation," *IEEE Transactions on Vehicular Technology Conference*, vol. VT-26 pp. -November, 1972.

[84] Cox D.C. and Leck R.P., "Correlation Bandwidth and Delay Spread Multipath Propagation Statistics for 910-MHz Urban Mobile Radio Channels," *IEEE Transactions on Communications*, vol. COM-23, No. 11 pp. 1271-1280, November, 1975.

[85] Gürdenli E. and Huish P.W., "Propagation Measurements and Modelling for Digital Cellular Radio Systems," *British Telecommunications Technology Journal*, vol. 8, no. 1 pp. 44-56, January, 1990.

[86] Haese S., Moullec C., Coston P., and Sayegrih K., "Wideband Measurements of the Outdoor Propagation Channel Using a New Time Domain Channel Sounder, "*IEEE 50th Vehicular Technology Conference, VTC'99*, pp. 2248-2252, 1999.

[87] Huish P.W. and Gurdenli E., "Radio Channel Measurement and Predictions for Future Mobile Radio Systems," *British Telecom Tech. Journal*, vol. 6, no. 1 pp. 43-53, 1988.

[88] Jones S.M.R., Browne J.A., Robinson A., and Glover I.A., "Wideband Measurements Across the Indoor-Outdoor Interface at 2.5 GHz," *International Conference on Antennas and Propagation, Davos, Switzerland*, March, 2000.

[89] Jorgensen J. et al., "Application of Channel Sounding to CDMA PCS Design at 1900 MHz," *IEEE*, pp. 1937-1941, 1997.

[90] Levy A.J. et al., "An Improved Channel Sounding Technique applied for Wideband Mobile 900 MHz Propagation Measurement," *40th IEEE Conference on Vehicular Technology*, pp. 513-519, 6-9 May, 1990.

[91] Nche C. et al., "Channel Sounder for PCN Network," *IEE Colloquium Digest No.1993/233*, 1993.

[92] Olivier P. and Tiffon J., "Fast fading Characterisation in Urban Mobile Radio Propagation at 855 MHz in Paris," *Electronic Letters*, vol. 21, No. 19 pp. 830-832, 1985.

[93] Rækken R.H., Langaas H., Løvnes G., and Paulsen S.E., "Wideband Impulse Response Measurements at 900 MHz and 1.7 GHz," *IEEE Global Telecommunications Conference Globecom'91*, pp. 1303-1307, 1991.

[94] Rappaport T.S. and McGillem C.D., "UHF Fading in Factories," *IEEE Journal on Selected Areas in Communications*, vol. 7, no. 1 pp. 40-48, January, 1989.

[95] Rees J.V., "Measurements of the wideband Radio Channel Characteristics for Rural, Residential, and Suburban," *IEEE Transactions on Vehicular Technology*, vol. VT-36, no. 1 pp. 2-6, February, 1987.

[96] Rees J.V., "Measurements of Impulse Response of a Wideband Radio Channel at 910 MHz from a Moving Vehicle," *Electronics Letters*, vol. 22, no. 5 pp. 246-247, 27 February, 1986.

[97] Sass P.F, "Propagation Measurements for UHF Spread Spectrum Mobile Communications," *IEEE Transactions on Vehicular Technology*, vol. VT-32, No. 2 pp. 168-176, May, 1983.

[98] Kivinen J., Zhao X., and Vainikainen P., "Wideband Indoor Radio Channel Measurements with Direction of Arrival Estimations in the 5 GHz Band," *IEE Proceeding, VTC'99*, pp. 2308-2312, 1999.

[99] Zhao X., "Multipath Propagation Characterization for Terrestrial Mobile and Fixed Microwave Communications," *PhD Thesis, Helsinki University of Technology, Department of Electrical and Communications Engineering, Finland*, 2002.

[100] Athanasiadou G., "Development, Investigation and Evaluation of Novel Indoor and Outdoor Ray Tracing Propagation Models," *PhD Thesis, Faculty of Engineering, Department of Electrical Engineering, University of Bristol, UK*, 1997.

[101] Anderson H.R., "Development and Application of Site-Specific Microcell Communications Channel Modelling Using Ray-Tracing," *PhD Thesis, Faculty of Engineering, Department of Electrical Engineering, University of Bristol, UK*, 1994.

[102] Fitton M.P., Nix A.R., and Beach M.A., "Evaluation of Metrics for Characterising the Dispersion of the Mobile Channel," *IEEE 46th Vehicular Technology Conference, VTC'96*, vol. 3 pp. 1418-1422, April 28 - May 1, Atlanta, USA, 1996.

[103] Hammoudeh A., Scammell D.A., and Sánchez M.G., "Measurements and Analysis of the Indoor Wideband Millimetre Wave Wireless Radio Channel and Frequency Diversity Characterization," *IEEE Transactions on Antennas and Propagation*, vol. 51, no. 10 pp. 2974-2986, October, 2003.

[104] Fleury B.H., "An Uncertainty Relation for WSS Processes and its Application to WSSUS Systems," *IEEE Transaction on Communications*, vol. 44, no 12 pp. 1632-1634, 1996.

[105] Gans M.J., "A Power-Spectral Theory of Propagation in the Mobile Radio Environment," *IEEE Transactions on Vehicular Technology*, vol. 21, no. 1 pp. 27-38, 1972.

[106] Lauer A. et al., "FDTD Simulations for Indoor Propagation," *IEEE 44th Vehicular Technology Conference, VTC'94*, pp. 883-886, 1994.

[107] Lee J.W.H. and Lai A.K.Y., "FDTD Analysis of Indoor Radio Propagation," *IEEE Transactions on Antennas and Propagation*, vol. 3 pp. 1664-1667, 1998.

[108] Lu Y.E., "Site Precise Radio Wave Propagation Simulations by Time Domain Finite Difference Methods," *IEEE 43rd Vehicular Technology Conference, VTC'93*, pp. 875-878, 1993.

[109] Schuster J.W. and Luebbers R.J., "Using FDTD to evaluate ray-tracing models for propagation prediction in urban microcells," *IEEE Antennas and Propagation Society International Symposium*, vol. 3 pp. 1676-1679, 21-26 June, 1998.

[110] Wang Y., Safavi-Naeini S., and Chaudhuri S.K., "A Hybrid Technique Based on Combining Ray Tracing and FDTD Methods for Site-Specific Modelling of Indoor Radio Wave Propagation," *IEEE Transactions on Antennas and Propagation*, vol. 48, no. 5 pp. 743-754, May, 2000.

[111] Ying W. et al., "A Hybrid Technique based on Combining Ray tracing and FDTD Methods for Site-Specific Modelling of Indoor Radio wave Propagation," *IEEE Transactions on Antennas and Propagation*, vol. VT-48, no. 5 pp. 743-754, May, 2000.

[112] Iskander M.F. and Yun Z., "Propagation Prediction Models for Wireless Communication Systems," *IEEE Transactions on Microwave Theory and Techniques*, vol. 50, no. 3 pp. 662-673, March, 2002.

[113] Iskander M.F. and Yun Z., "Propagation Prediction Models for Wireless Communication Systems," *IEEE transactions on Microwave Theory Technology*, vol. 50, pp. 662-673, March, 2002.

[114] Iskander M.F., "Channel Characterisation and Propagation Models for Wireless Communication Systems," *WTEC Panel Report on Wireless Technologies and Information Networks*, July, 2000.

[115] Sarkar T.K. et al., "A Survey of Various Propagation Models for Mobile Communication," *IEEE Antennas and Propagation Magazine*, vol. 45, No. 3 pp. 51-82, June, 2003.

[116] Aryanfar F. and Sarabandi K., "A Millimetre-Wave Scaled Measurement System for Wireless Channel Characterisation," *IEEE Transactions on Microwave Theory and Techniques*, vol. 52, no. 6 pp. 1663-1670, June, 2004.

[117] Agelet F.A., Formella A., Rábanos J.M.H., Vicente I D., and Fontá F.P., "Efficient Ray-Tracing Acceleration Techniques for Radio Propagation Modelling," *IEEE Transactions on Vehicular Technology*, vol. 49, no. 6 pp. 2089-2104, November, 2000.

[118] Aryanfar F. and Safavi-Maeini S., "Electromagnetic Modelling of Radio wave Propagation in Micro- and Pico-cellular Environments," *IEEE Antennas and Propagation for Wireless Communications Conference.*, vol. 43 pp. 25-28, November, 1998.

[119] Walfisch J. and Bertoni H.L., "A Theoretical Model of UHF Propagation in Urban Environments," *IEEE Transactions on Antennas and Propagation*, vol. 36, no. 12 pp. 1788-1796, December, 1988.

[120] Rizk K., "Propagation in Microcellular and Small Cell Urban Environment," *PhD Thesis, Swiss Federal Institute of Technology of Lausanne*, 1997.

[121] Allsebrook K. and Parsons J.D., "Mobile Radio Propagation in British Cities at Frequencies in the VHF and UHF Bands," *IEEE* Transactions *on Vehicular Technology*, VT-26, 313-323, 1977.

[122] Berg J.E., "A Macrocell Model based on the Parabolic Differential Equations," *Proceedings Virginia Tech.4th Symposium on Wireless Personal Communications*, pp. 9.1-9.10, 1994.

[123] Durgin G.D. and Rappaport T.S., "Theory of Multipath Shape Factors for Small-Scale Fading Wireless Channels," *IEEE Transactions on Antenna and Propagation*, vol. 48, no. 5 pp. 682-693, May, 2000.

[124] Hviid J.T. et al., "Terraibased Propagation Model for Rural Areas -An Integral Equation Approach," *IEEE Transactions on Antennas and Propagation*, vol. 43, no. 1 pp. 41-46, 1995.

[125] Ibrahim M.F. et al., "Signal Strength Prediction in Built-up Areas, Part 1: Median Signal Strength," *IEE Proceedings*, vol. 130, Pt. F, no. 5 pp. 377-384, August, 1983.

[126] Parsons J.D. et al., "Signal Strength Prediction in Built-up Areas, Part 2: Signal Variability," *IEE Proceedings*, vol. 130, Pt. F, No. 5 pp. 385-391, August, 1983.

[127] Reudink D.O. and Wazowicz M.F., "Some propagation Experiments Relating Foliage Loss and Diffraction Loss at X-Band and UHF Frequencies," *IEEE Transactions on Communications*, vol. COM-21, no. 11 pp. 1198-1206, November, 1973.

[128] Stocker K.E. et al., "An Application of Neural Networks to Prediction of Terrestrial Wave Propagation for Mobile Radio," *IEE Proceedings Part H*, vol. 140, no. 4 pp. 315-320, 1993.

[129] Young W.R., "Comparison of Mobile Radio Transmission at 150, 450, 900 and 3700 MC.," *Bell System Technical Journal*, vol. 31 pp. 1068-1085, 1952.

[130] Okumara Y. et al., "Field Strength Variability in VHF and UHF Land Mobile Service," *Rev. Elect. Commun. Lab.*, vol. 16, no. 9-10 pp. 825-873, September, 1968.

[131] Hata M., "Empirical Formula for Propagation Loss in Land Mobile Radio Service," *IEEE Transactions on Vehicular Technology*, vol. VT-29 pp. 317-325, 1980.

[132] Ibrahim M.F. and Parsons J.D., "Signal Strength Prediction in Built-up Areas, Part 1: Median Signal Strength," *IEE Proceedings Part F*, vol. 130, no. 5 pp. 377-384, 1983.

[133] Ikegami F. et al., "Theoretical Prediction of Mean Field Strength for Urban Mobile Radio," *IEEE Transactions on Antennas and Propagation*, vol. 39 pp. 299-302, March, 1991.

[134] Bertoni H.L. and Walfish J., "A Diffraction based Theoretical Model for Predicting UHF Path Loss," *IEEE transactions on Vehicular Technology*, vol. 37 pp. 1788-1796, 1988.

[135] Xia H.H., Bertoni H.L., and Maciel L.R., "Microcellular Propagation Characteristics for Personal Communications in Urban and Suburban Environments," *IEEE Transactions on Vehicular Technology*, vol. 43, no. 3 pp. 743-752, Augusts, 1994.

[136] Xia H.H., Kim S.C., and Bertoni H.L., "Microcellular Propagation measurements in Dallas City," *IEEE 43rd Vehicular Technology Conference, VTC'93*, pp. 593-597, 1993.

[137] Xia H.H. et al., "Urban and Suburban Microcellular Propagation," *IEEE Conference on Universal Personal Communications, ICUPC'92*, pp. 5-9, 1992.

[138] Xia H.H., Grindstaff L., and Bertoni H.L., "Microcell Propagation Measurements at Three Different Antenna Heights," IEEE *International Symposium on Antennas and Propagation*, pp. 1372-1375, 1992.

[139] Xia H.H., Bertoni H.L., Maciel L.R., and Lindsay-Stewart A., "Radio Propagation Measurements and Modelling for Line-of-Sight Microcellular Systems," *IEEE 42nd Vehicular Technology Conference, VTC'92*, pp. 349-354, 1992.

[140] Zadeh L.A., "Frequency Analysis of Variable networks," *Proceedings IRE*, vol. 38 pp. 291-299, March, 1950.

[141] Kailath T., "Sampling Models for Linear Time-variant Filters," *M.I.T. Research Lab. of Electronics, Cambridge, Mass.*, vol. Report No. 352 1959.

[142] Aulin T., "A Modified Model for the Fading Signal at a Mobile Radio Channel," *IEEE Transactions on Vehicular Technology*, vol. VT-28, No. 3 pp. 182-203, August, 1979.

[143] Clarke R.H., "A Statistical Theory of Mobile Radio Reception," *Bell Systems Technical Journal*, vol. 47, no. 6 pp. 957-1000, 1968.

[144] Gans M.J., "A Power-Spectral Theory of Propagation in the Mobile Radio Environment," *IEEE Transactions on Vehicular Technology*, vol. VT-21, No. 1 pp. 27-38, February, 1972.

[145] Gilbert E.N., "Energy Reception for Mobile Radio," *Bell Systems Technical Journal*, vol. 44 pp. 1779-1803, 1965.

[146] Jakes W.C. Jr. and Reudink D.O., "Comparison of Mobile Radio Transmission at UHF and X band," *IEEE Transactions on Vehicular Technology*, vol. VT-16 pp. 10-14, October, 1967.

[147] Felden M. Jr. and Jakes W.C. et al., "The Contributors," *IEEE Transactions on Microwave Theory and Techniques*, vol. 14 1966.

[148] Jakes W.C. Jr., "A Comparison of Specific Space Diversity Techniques for Reduction of Fast Fading in UHF Mobile Radio Systems," *IEEE Transactions on Vehicular Technology*, vol. VT-20, no. 4 pp. 81-92, November, 1971.

[149] Lee W.C.Y., "Effects on Correlation between Two Mobile Radio Base-Station Antennas," *IEEE Transactions on Vehicular Technology*, vol. VT-22, no. 4 pp. 13 0-140, November, 1973.

[150] Ossanna J.F., "A Model for Mobile Radio Fading due to Building Reflections: Theoretical and Experimental Fading Waveform Power Spectra," *Bell Systems Technical Journal*, vol. 43, no. 6 pp. 2935-2971, November, 1964.

[151] Nielson D.L., "Microwave Propagation Measurement for Mobile Digital Radio Application," *IEEE Transactions on Vehicular Technology*, vol. VT-27, no. 3 pp. 117-132, August, 1978.

[152] Suzuki H., "A Statistical Model for Urban radio Propagation," *IEEE Transactions on Communications*, vol. COM-25, no. 7 pp. 673-679, July, 1977.

[153] Cox D.C., "Delay Doppler Characteristics of Multipath Propagation at 910 MHz in a Suburban Mobile Radio Environment," *IEEE Transactions on Antennas and Propagation*, vol. AP--20, no. 5 pp. 625-635, September, 1972.

[154] Cox D.C. and Leck R.P., "Distributions of Multipath Delay Spread and Average Excess Delay for 910-MHz Urban Mobile Radio Paths," *IEEE Transactions on Antennas and Propagation*, vol. AP-23, no. 2 pp. 206-213, March, 1975.

[155] Huschka T., "Ray-Tracing Model for Indoor Environments and their Computational Complexity," *IEEE 5th International symposium on Personal, Indoor and Mobile Radio Communications, PIMRC'94*, pp. 486-490, 1994.

[156] Bajwa A.S. and Parsons J.D., "Small-area Characterisation of UHF Urban and Suburban Mobile Radio Propagation," *IEE Proceeding*, vol. 129, Part F, no. 2 pp. 102-109, April, 1982.

[157] Parsons J.D. and Bajwa A.S., "Wideband Characterisation of Fading Mobile Radio Channels," *IEE Proceeding*, vol. 129, Part F. no. 2 pp. 96-101, April, 1982.

[158] Demery D.A., "Wideband Characterisation of UHF Mobile Radio Channels in Urban Areas," *PhD Thesis, Department of Electrical Engineering and Electronics, University of Liverpool, UK*, 1989.

[159] Bahai A.R.S. and Sarraf M., "A Frequency Offset Estimation Technique for Wireless Channels," *IEEE 1st Workshop on Signal Processing*, pp. 397- 400, April, 1997.

[160] Beneat J., Pahlavan K., and Krishnamurthy P., "Radio Channel Characterization for Geolocation at 1 GHz, 500 MHz, 500 MHz and 60 MHz in SUO/SAS," *IEEE Military Communications Conference Proceedings*, vol. 2, Piscataway, NJ, USA pp. 1060-1063, 1999.

[161] Benvenuto N., "Distortion Analysis on Measuring the Impulse Response of a System Using a Cross correlation Method," *AT&T Bell Laboratories Technical Journal*, vol. 63, no. 10 pp. 2171-2193, December, 1984.

[162] Coulson A.J. and Kakarala R., "Excess Delay Estimation from Time-Varying Mobile Radio Channe Impulse Response Measurements," *IEEE Communications Letters*, vol. 3, no. 8 pp. 239-241, August, 1999.

[163] Devasirvatham D.M.J., "Multipath Time delay Spread in the Digital Portable radio Environment," *IEEE Communication Magazine*, vol. 25, no. 6 pp. 13-21, June, 1987.

[164] Ganesh R. and Pahlavan K., "On the Modelling of Fading Multipath Indoor Radio Channels," *IEEE Global Telecommunications Conference, Globecom'89* vol. 3, pp. 1346-1350, November, 1989.

[165] Gurunathan S. and Feher K., "Multipath Simulation Models for Mobile Radio Channels," *IEEE 42nd Vehicular Technology Conference, VTC'92*, vol. 1 pp. 131-134, Denver, CO, USA, 10-13 May, 1992.

[166] Han Youngyearl, "On the Minimization of Overhead in Channel Impulse Response Measurement," *IEEE Transactions on Vehicular Technology*, vol. 47, no. 2 pp. 631-636, May, 1998.

[167] Hatzinakos D. and Nikias C.L., "Estimation of Multipath Channel Response in Frequency Selective Channels," *IEEE Journal on Selected Areas in Communications*, vol. 7, no. 1 pp. 12-19, January, 1989.

[168] Marques P., Fernandes J., and Neves J., "Complex Impulse Response Modeling for Wideband Channels," *IEEE 48th Vehicular Technology Conference, VTC'98*, pp. 702-706, May, 1998.

[169] Melancon P. and Bel J.L., "A Characterization of the Frequency Selective Fading of the Mobile Radio Channel," *IEEE Transactions on Vehicular Technology*, vol. VT-35, No. 4 pp. 153-161, November, 1986.

[170] Mohr W. and Becher R., "Mobile Communications beyond third Generation," *IEEE 52nd Vehicular Technology Conference, VTC'2000,* vol. 2, pp. 654 – 661, September 2000.

[171] Molina A. and Fannin P.C., "Application of Mismatched Filter Theory on BandPass Impulse Response Measurements," *Electronics Letters*, vol. 29, no. 2 pp. 162-163, 21 January, 1993.

[172] Patenaude F., Lodge J., and Choinard J.Y., "Eigen Analysis of Wideband-Band Fading Channel Impulse Responses," *IEEE Transactions on Vehicular Technology*, vol. 48, no. 2 pp. 593-605, March, 1999.

[173] Salous S. and Bertel L., "Analysis of Wideband Fading on UHF Mobile Radio Channels," *International Conference on Antennas and Propagation, ICAP'2000,* pp. 124-127, Switzerland, April, 2000.

[174] Skog K. et al., "Wideband Outdoor Radio Channel Measurements at 5.3 GHz," *International Conference on Antennas and Propagation, ICAP'2000*, pp. 2 -7, Switzerland, April, 2000.

[175] Wales S.W., "Channel Modelling and Equalisation Techniques for Broadband Mobile Communications at 60 GHz," *IEE Colloquium on Methods of Combating Multipaths*, pp. 7/1-7/8, January 1996.

[176] Wepman J.A., Hoffman J.R., and Loew L.H., "Impulse Response Measurements in the 1850-1990 MHz Band in Large Outdoor Cells," *http://www.its.bldrdoc.gov/pub/imp94 /cimpab.htm*, pp. 1-48, May, 1997.

[177] Wittmann M., Marti J., and Kurner T., "Impact of the Power Delay Profile Shape on the Bit Error Rate in Mobile Radio Systems," *IEEE Transactions on Vehicular Technology*, vol. 46, pp. 329-339, May, 1997.

[178] Patwari N., Durgin G.D., Rappaport T.S., and Boyle R.J., "Peer-to-Peer Low Antenna Outdoor Radio Wave Propagation at 1.8 GHz," *IEEE 49th Vehicular Technology Conference*, vol. 1 pp. 371-375, 16-20 May, 1999.

[179] Bohdanowicz A., Janssen G.J.M., and Pietrzyk S., "Wideband Indoor and Outdoor Multipath Channel Measurements at 17 GHz," *IEEE 50th Vehicular Technology Conference*, vol. 4 pp. 1998-2003, 19-22 Sept., 1999.

[180] Domazetovic A., Greenstein L.J., Mandayam N.B., and Seskar I., "A New Modelling Approach for Wireless Channels with Predictable Path Geometrics," *IEEE 56th Vehicular Technology Conference, VTC-2002*, vol. 1 pp. 454-458, 24-28 Sept., 2002.

[181] Feurstein M.J. et al., "Path Loss, Delay Spread, and Outage Models as function of Antenna Heights for Microcellular System Design," *IEEE Transactions on Vehicular Technology*, vol. 43 pp. 487-498, August, 1994.

[182] Rustako, Jr. A. J., Amitay N., Owens G.J., and Roman R.S., "Radio Propagation at Microwave Frequencies for Line-of-Sight Microcellular Mobile and Personal Communications," *IEEE Transactions on Vehicular Technology*, vol. 40, no. 1 pp. 203-210, February, 1991.

[183] Rautiainen T., Wölfle G., and Hoppe R., "Verifying Path Loss and Delay Spread Predictions of a 3D Ray Tracing Propagation Model in Urban Environment," *IEEE 56th Vehicular Technology Conference, VTC'2002*, pp. 2470-2474, September 2002.

[184] Son H.W. and Myung N.H., "A Deterministic ray Tube Method for Microcellular Wave Propagation Prediction Model," *IEEE Transactions on Antennas and Propagation*, vol. 47, no. 8 pp. 1344-1350, August, 1999.

[185] Schaubach K.R., Davis IV N.J., and Rappaport T.S., "A Ray Tracing Method for Predicting Path Loss and Delay Spread in Microcellular Environments," *IEEE Proceeding Vehicular Technology Conference, Denver*, pp. 932-935, May, 1992.

[186] Kim S.C., Guarino, Jr. B. J., Willis III T.M., Erceg V., Fortune S.J., Valenzuela R.A., Thomas L.W., Ling J., and Moore J.D., "Radio Propagation Measurements and Prediction Using Three-Dimensional Ray Tracing in Urban Environments at 908 MHz and 1.9 GHz," *IEEE Transactions on Vehicular Technology*, vol. 48, no. 3 pp. 931-946, May, 1999.

[187] Liang G. and Bertoni H.L., "A New approach to 3-D Ray Tracing for Propagation Prediction in Cities," *IEEE Transactions on Antennas and Propagation*, vol. 46, no. 6 pp. 853-863, June, 1998.

[188] Liang G. and Bertoni H.L., "A New Approach to 3D Ray Tracing for Site Specific Propagation Modelling," *IEEE 47th Vehicular Technology Conference, VTC'97, Phoenix USA*, pp. 1113-1117, May, 1997.

[189] Piazzi L. and Bertoni H.L., "Achievable Accuracy of Site-Specific path-Loss Predictions in Residential Environments," *IEEE Transactions on Vehicular Technology*, vol. 48, no. 3 pp. 922-930, May, 1999.

[190] Piazzi L. and Bertoni H.L., "Effect of Terrain on Path Loss in Urban Environments for Wireless applications," *IEEE Transactions on Antennas and Propagation*, vol. 46, no. 8 pp. 1138-1147, August, 1998.

[191] Piazzi L. and Bertoni H.L., "A Path Loss Formulation for Wireless Applications Considering Terrain for Urban Environments," *IEEE 48th Vehicular Technology Conference, VTC'98*, vol. 1, pp. 159-163, 1998.

[192] Piazzi L., Liang G., Bertoni H.L., and Kim S.C., "Comparison of Measurement based and Site Specific Ray based Microcellular Path Loss predictions," *IEEE 5th International Conference on Universal Personal Communications*, vol. 2, pp. 656-660, 1996.

[193] Seidel S.Y. and Rappaport T.S., "Site-Specific Propagation Prediction for Wireless In-Building Personal Communication System Design," *IEEE Transactions on Vehicular Technology*, vol. 43, no. 4 pp. 879-891, November, 1994.

[194] Seidel S.Y., Schaubach K.R., Tran T.T., and Rappaport T.S., "Research in Site-specific Propagation Modelling for PCS System Design," *Proceedings Vehicular Technology Conference, Secaucus, NJ, USA*, pp. 261-264/F, 1993.

[195] Seidel S.Y. et al., "Path Loss, Scattering, and Multipath Delay Statistics in Four European Cities for Digital Cellular and Microcellular Radiotelephone," *IEEE Transactions on Vehicular Technology*, vol. 40, no. 4 pp. 721-730, November, 1991.

[196] de Jong Y.L.C. and Herben M.H.A.J., "Prediction of Local Mean Power using 2-D Ray-tracing-based Propagation Models," *IEEE transactions on Vehicular Technology*, vol. 50 pp. 325-331, January, 2001.

[197] Dietert J.E et al., "Statistical Channel Modelling based on Ray-Tracing Simulations," *COST 259, TD (00)004: http://www.it.pt/cost259/*, 2000.

[198] Dietert J.E et al., "Stochastic Channel Model for Outdoor Applications based on Ray-Tracing Simulations," *COST 259, TD(00)005: http://www.it.pt/cost259/*, 2000.

[199] Torres R.P., Loredo S., Valle L., and Domingo M., "An Accurate and Efficient Method based on Ray-Tracing for the Prediction of Local Flat-Fading statistics in Picocell Radio Channels," *IEEE Journal on Selected Areas in Communications*, vol. 19, no. 2 pp. 170-178, February, 2001.

[200] Sheethalnath P.T., "Novel Site-Specific Technique for Predicting Radio Wave Propagation," *PhD Thesis, Department of Electrical and Computer Engineering, Virginia Tech., USA*, 2001.

[201] Balanis C.A., "Advanced Engineering Electromagnetics," *John Wiley & Sons, Inc, New York*, 1989.

[202] Bon M. and Wolf E., "Principles of Optics: Electromagnetic Theory of Propagation Interference and Diffraction of Light," *Cambridge University Press*, 1980.

[203] Croswell W.F., "From Wave Theory to Ray Optics," *IEEE Antennas and Propagation Magazine*, vol. 36, no. 4 pp. 35-42, August, 1994.

[204] Griffiths J., "Radio Wave Propagation and Antennas," *Prentice-Hall International Englewood Cliffs, NJ*, 1987.

[205] Bullington K., "Radio Communication at Frequencies above 30 Mc," *Proc. IRE, 35(10)*, pp. 1122-1136, 1947.

[206] Deygout J., "Multiple Knife-edge Diffraction of Microwaves," *IEEE Transactions on Antenna and Propagation*, vol. 4 pp. 480-489, 1966.

[207] Epstein J. and Peterson D.W., "An Experimental Study of Wave Propagation at 850 Mc," *Proc. IRE, 41(5)*, pp. 595-611, 1953.

[208] Giovaneli C.L., "An Analysis of Simplified Solutions for Multiple Knife-edge Diffraction," *IEEE Transactions of Antenna and Propagation*, vol. 32 pp. 297-301, 1984.

[209] Furutzu K., "On the Theory of Radio wave Propagation over Inhomogeneous Earth," *J. Res. NBS, 67D*, pp. 39-62, 1963.

[210] Millington G. et al., "Double Knife-edge Diffraction in Field Strength Prediction," *IEEE Monograph 507*, pp. 419-429, 1963.

[211] Vogler L.E., "The Attenuation of Electromagnetic Waves by Multiple Knife-edge Diffraction," *NTIA Report*, 1981.

[212] ITU Recommendation Committee, "Propagation by Diffraction," *ITU-R P.526-8*, pp. 1-22, 2003.

[213] Arablouei R. and Ghorbani A., "An Improved Model based on UTD for Multiple Diffractions by Buildings," *Day on Diffraction' 2002*, pp. 24-35, 2002.

[214] Saunders S.R. and Bonar F.R., "Explicit Multiple Building Diffraction Attenuation Function for Mobile Radio Wave Propagation," *Electronic Letters*, vol. 27, no. 14 pp. 1276-1277, July, 1991.

[215] Neve M.J. and Rowe G.B., "Assessment of GTD for Mobile Radio Propagation Predictions," *Electronic Letters*, vol. 29, no. 7 pp. 618-620, April, 1993.

[216] Zhang W., "Fast Two-Dimensional Diffraction Modelling for Site-Specific Propagation Prediction in Urban Microcellular Environments," *IEEE Transactions on Vehicular Technology*, vol. 49, no. 2 pp. 428-436, March, 2000.

[217] Constantinou C.C. and Mughal M.J., "On the Modelling of Reflected Energy from Building Faces in Microcellular Environment Mobile Radio Planning Tools," *IEEE Transactions on Antennas and Propagation*, vol. 53 pp. 2623-2630, 2005.

[218] Luebbers R.J., "Finite Conductivity Uniform GTD versus Knife Edge Diffraction in Prediction of Propagation Path Loss," *IEEE Transactions on Antennas and Propagation*, vol. AP-32, no. 1 pp. 70-76, January, 1984.

[219] Anantha V. and Taflove A., "Calculation of Diffraction Coefficients of Three Dimensional Infinite Conducting Wedges Using FDTD," *IEEE Transactions on Antennas and Propagation*, vol. 46, No. 11 pp. 1755-1758, November, 1998.

[220] Burnside W.D. and Burgener K.W., "High frequency Scattering by a Thin Lossless Dielectric Slab," *IEEE Transactions on Antennas and Propagation*, vol. AP-31, no. 1 pp. 104-110, January, 1983.

[221] Cui S. and Fang D., "Analysis of the Diffraction Coefficients of Corrugated Surfaces with the Use of the Numerical GTD Method," *Microwave and Optical Technology Letters*, vol. 15, no. 5 pp. 297-303, August, 1997.

[222] Jakobsen K.R., "An Alternative Diffraction Coefficient for the Wedge," *IEEE Transactions on Antennas and Propagation*, vol. AP-32, no. 2 pp. 175-177, February, 1984.

[223] Haslett C.J., "The Diffraction of Microwaves by Buildings - A Model for System Planners," *IEE Colloquium on Diffraction Propagation Modelling Techniques Embracing Surface Feature Data*, pp. 1-6, 1990.

[224] Manara G., Nepa P., kouyoumjian R.G., and Taute J.E., "The Diffraction of an Inhomogeneous Plane Wave by an Impedance Wedge in a Lossy Medium," *IEEE Transactions on Antennas and Propagation*, vol. 46, no. 11 pp. 1753-1755, November, 1998.

[225] Osipov A. et al., "High-frequency approximations for electromagnetic field near a face of an impedance wedge," *IEEE Transactions on Antennas and Propagation*, vol. 50 pp. 930-940, 2002.

[226] Croswell W.F., "Diffraction: The First Recorded Observation," *IEEE Antennas and Propagation Society Magazine*, vol. 32, no. 2 pp. 27-30, April, 1990.

[227] Tsingos N. et al., "Modelling Acoustics in Virtual Environments Using the Uniform Theory of Diffraction," *ACM Computer Graphics, Ann. Conf. Series (Proc. Siggraph 01)*, pp. 545-552, 2001.

[228] Hansen R.C., "Geometrical Theory of Diffraction," *IEEE Press New York*, 1981.

[229] Chamberlin K.A. and Luebbers R.J., "An Evaluation of Longley-Rice and GTD Propagation Models," *IEEE Transactions on Antennas and Propagation*, vol. AP-30, no. 6 pp. 1093-1098, November, 1982.

[230] Kouyoumjian R.G. and Pathak P.H., "A Uniform Geometric Theory of Diffraction for an Edge in a Perfectly Conducting Surface," *Proceedings of the IEEE*, vol. 62, no. 11 pp. 1448-1461, November, 1974.

[231] Luebbers R.J., "Propagation Prediction for Hilly Terrain Using GTD Wedge Diffraction," *IEEE Transactions on Antennas and Propagation*, vol. AP-32, no. 9 pp. 951-955, September, 1984.

[232] Keller J.B., "Geometric Theory of Diffraction," *Journal on Optical Society of America*, vol. 52 pp. 116-130, February, 1962.

[233] Kouyoumjian R.G. and Pathak P.H., "An analysis of the radiation from apertures in curved surfaces by the geometrical theory of diffraction," *IEEE Proceedings*, vol. 62, no. 11 pp. 1438-1447, November, 1974.

[234] Holm P.D., "A New Heuristic UTD Diffraction Coefficient for Non-perfectly Conducting Wedges," *IEEE Transactions on Antennas and Propagation*, vol. 48, no. 8 pp. 1211-1219, August, 2000.

[235] Holm P.D., "UTD-Diffraction Coefficients for Higher Order Wedge Diffracted Fields," *IEEE Transactions on Antennas and Propagation*, vol. 44, no. 6 pp. 879-888, June, 1996.

[236] McNamara D.A., Pistorius C.W.I., and Malherbe J.A.G., "Introduction to the Uniform Geometrical Theory of Diffraction," *Norwood, MA: Artech House*, 1990.

[237] Ji Z. et al., "Efficient Ray-Tracing Methods for Propagation Prediction for Indoor Wireless Communications," *IEEE Antennas and Propagation Magazine*, vol. 43, no. 2 pp. 41-49, April, 2001.

[238] Tarng J.H., Chang W.R., and Hsu B.J., "Three-Dimensional Modelling of 900-MHz and 2.44-GHz Radio Propagation in Corridors," *IEEE Transactions on Vehicular Technology*, vol. 46, no. 2 pp. 519-527, May, 1997.

[239] Lee B.S., Tan C.M., Foo S.E., Nix A.R., and McGeehan J.P., "Site Specific Prediction and Measurement of Indoor Power Delay and Power Azimuth Spectra at 5 GHz," *IEEE 54th Vehicular Technology Conference, VTC 2001*, vol. 2 pp. 733-737, 2001.

[240] Kouyoumjian R.G. and Pathak P.H., "High Frequency Diffraction, Focus on Ray Methods," *IEEE International Symposium* on Antennas and Propagation, vol. 3, pp. -1638, July 2000.

[241] Bernardi P., Cicchetti R., Gennarelli C., Pelosi G., and Riccio G., "A UAPO solution for the field diffracted by building corners in wireless radio environments," *Antennas and Wireless Propagation Letters*, vol. 1 pp. 169-172, 2002.

[242] Büyükdura O.M., Goad S.D., and Kouyoumjian R.G., "A Spherical Wave representation of the Dyadic Green's Function for a Wedge," *IEEE Transactions on Antennas and Propagation*, vol. 44, no. 1 pp. 12-22, January, 1996.

[243] Christiansen P.L., "Comparison between Edge Diffraction Processes," *IEEE Proceedings*, vol. 62 pp. 1462-1468, November, 1974.

[244] Hill K.C. and Pathak P.H., "A UTD Solution for the EM Diffraction by a Corner in a Plane Angular Sector," IEEE *International Symposium on Antennas and Propagation, AP-S. Digest*, vol. 1, pp. 2-5, July 1991.

[245] Hwang Y., Zhang Y.P., and Kouyoumjian R.G., "Ray-Optical Prediction of Radio-Wave propagation Characteristics in Tunnel Environments - Part1: Theory," *IEEE Transactions on Antennas and Propagation*, vol. 46, no. 9 pp. 1328-1336, September, 1998.

[246] Manara G., "A UTD Description of Surface and Space Wave Excitation at the Edge of an Impendence Wedge," *IEEE International Symposium on Antennas and Propagation*, vol. 1, pp. 14-17, June 1991.

[247] Norris A.N. and Osipov A.V., "Far-field Analysis of the Malyuzhinets Solution for Plane and Surface Wave Diffraction by an Impedance Wedge," *Wave Motion, 30*, pp. 69-89, 1999.

[248] Remley K.A., Weisshaar A., and Anderson H.R., "Improved Diffraction Coefficients for Lossy Dielectric Wedges," *Electronics Letters*, vol. 35, no. 21 pp. 1826-1827, 14th October, 1999.

[249] Rizk K. et al., "Lamppost and Panel scattering compared to building reflection and diffraction," *COST 259 TD (97)*, pp. 158-167, May, 1996.

[250] Rojas R.G. and Pathak P.H., "Diffraction of EM wave by a Dielectric/Ferrite half-Plane and Related Configurations," *IEEE Transactions on Antennas and Propagation*, vol. 37, no. 6 pp. 751-763, June, 1989.

[251] Rojas R.G., "Scattering by an inhomogeneous dielectric/ferrite cylinder of arbitrary cross-section shape-oblique incidence case," *IEEE Transactions on Antennas and Propagation*, vol. 36 pp. 238-246, 1998.

[252] Rojas R.G., "Electromagnetic Diffraction of an Obliquely Incident Plane Wave Field by a Wedge with Impedance Faces," *IEEE Transactions on Antennas and Propagation*, vol. 36, no. 7 pp. 956-970, July, 1988.

[253] Tiberio R., Pelosi G., Manara G., and Pathak P.H., "High-Frequency Scattering from a Wedge with Impedance faces Illuminated by a Line Source, Part I: Diffraction," *IEEE Transactions on Antennas and Propagation*, vol. 37, no. 2 pp. 212-217, February, 1989.

[254] Tiberio R., Pelosi G., Manara G., and Pathak P.H., "A UTD Diffraction Coefficient for a Wedge with Impedance faces Illuminated by a Line Source," *IEEE International Symposium on Antennas and Propagation*, vol. 25, pp. 1078-1081, June 1987.

[255] Tiberio R., Pelosi G., and Manara G., "A Uniform GTD Formulation for the Diffraction by a Wedge with Impedance Faces," *IEEE Transactions on Antennas and Propagation*, vol. AP-33, no.8 pp. 867-873, August, 1985.

[256] Tiberio R. and Pelosi G., "High-Frequency Scattering from the Edges of Impedance Discontinuities on a Flat Plane," *IEEE Transactions on Antennas and Propagation*, vol. AP-31, no. 4 pp. 590-596, July, 1983.

[257] Wang H. and Rappaport T.S., "A Parametric Formulation of the UTD Diffraction Coefficients or a Dielectric Wedge," *IEEE International Symposium on Antennas and Propagation*, vol. 1, pp. 962 – 965, June 2004.

[258] Wang Y., Safavi-Naeini S., and Chaudhuri S.K., "Comparative Study of Lossy Dielectric Wedge Diffraction for Radio Wave Propagation Modelling using UTD and FDTD," *IEEE International Symposium on Antennas and Propagation*, vol. 4, pp. 2826 – 2829, July 1999.

[259] Volakis J.L., "A Uniform Geometrical Theory of Diffraction for an Imperfectly Conducting Half - Plane," *IEEE Transactions on Antennas and Propagation*, vol. AP-34, no. 2 pp. 172-180, February, 1986.

[260] Leubbers R.J, "Finite Conductivity Uniform GTD Versus Knife Edge Diffraction in Prediction of Propagation Path Loss," *IEEE Transactions on Antennas and Propagation*, vol. AP-32, no. 1 pp. 70-76, January, 1984.

[261] Aidi M. and Lavergnat J., "Comparison of Luebbers' and Maliuzhinets' Wedge Diffraction Coefficients in Urban Channel Modelling," *Progress In Electromagnetics Research, PIER 33*, pp. 1-28, 2001.

[262] Mokhtari H. and Lazariddis P., "Comparative Study of Lateral Profile Knife-Edge Diffraction and Ray Tracing Technique Using GTD in Urban Environment," *IEEE Transactions on Vehicular Technology*, vol. 48, no. 1 pp. 255-261, January, 1999.

[263] Bertoncini F., Kouyoumjian R.G., Manara G., and Nepa P., "High-Frequency Scattering by Objects Buried in Lossy Media," *IEEE Transactions on Antennas and Propagation*, vol. 49, no. 12 pp. 1649-1656, December, 2001.

[264] Technical Committee, "Time domain models of edge diffraction," *http://www.tele.ntnu.no /users/svensson/ED.html*, 2003.

[265] Anderson H.R., "Building Corner Diffraction Measurements and Prediction Using UTD," *IEEE Transactions on Antennas and Propagation*, vol. 46, no. 2 pp. 292-293, February, 1998.

[266] Anderson H.R. and McGeehan J.P., "Direct Calculation of Coherence bandwidth in Urban Microcells using a Ray-tracing Propagation Model," *IEEE 5th International Symposium on Personal, Indoor and Mobile Radio Communications, PIMRC'94*, vol. 1, pp. 20-24, September 1994.

[267] Anderson H.R., "A Ray-Tracing Propagation Model for Digital Broadcast Systems in Urban Areas," *IEEE Transactions on Broadcasting*, vol. 39, no.3 pp. 309-317, September, 1993.

[268] Erceg V., Rustako A.J., and Roman R.S., "Diffraction around corners and its effects on the microcell coverage area in urban and suburban environments at 900 MHz, 2 GHz, and 6 GHz," *IEEE Transactions on Vehicular Technology*, pp. 43-762, 1994.

[269] Luebbers R.J., "Comparison of Lossy Wedge Diffraction Coefficients with Application to Mixed Path Propagation Loss Prediction," *IEEE Transactions on Antennas and Propagation*, vol. 36, no. 7 pp. 1031-1035, July, 1988.

[270] Luebbers R.J., "A Heuristic UTD Slope Diffraction Coefficient for Rough Lossy Wedges," *IEEE Transactions on Antennas and Propagation*, vol. 37, no. 2 pp. 206-211, February, 1989.

[271] Richhter J., Al-Nuaimi M.O., and Ivissimtzis, "Optimisation of Radio Coverage in Urban Microcells using a UTD based Ray-Tracing Model," *IEE Proceedings on Microwave Antennas Propagation*, vol. 151, no. 3 pp. 187-192, June, 2004.

[272] Tan S.Y. and Tan H.S., "A Microcellular Communications Propagation Model based on the Uniform Theory of Diffraction and Multiple Image Theory," *IEEE Transactions on Antennas and Propagation*, vol. 44, no. 10 pp. 1317-1326, October, 1996.

[273] Technical Committee, "Real-Time Geometrical Theory of Diffraction," *http://www-sop.inria.fr/reves/personnel/Nicolas.Tsingos/reseach/GTD.html*, 2004.

[274] Technical Committee, "SuperNEC: UTD Technical Reference Manual, Version 2.3," *http://www.poynting.co.za/software/manuals/snutdtrm.htm*, 2003.

[275] Kawai T., "Sound Diffraction by a many sided barrier or pillar," *Journal of Sound and Vibration*, vol. 79, No. 2 pp. 229-242, 1981.

[276] Tan S.Y., Ang T.W., and Tan H.S., "Measurement Validation of Ray-Tracing Propagation Model on Double-Diffracted Paths," *IEEE Transactions on Antennas and Propagation*, vol. 50, no. 3 pp. 411-413, March, 2002.

[277] Kara A., Bertoni H.L., and Yazgan E., "Limit and Application Range of the Slope-Diffraction Method for Wireless Communications," *IEEE Transactions on Antennas and Propagation*, vol. 51, no. 9 pp. 2512-2514, September, 2003.

[278] Hassan-Ali M. and Pahlavan K, "A New Statistical Model fro Site-Specific Indoor Radio Propagation Prediction Based on Geometric Optics and Geometric Probability," *IEEE Transactions on Wireless Communications*, vol. 1, no. 1 pp. 112-124, January, 2002.

[279] Rossi J.P. and Gabillet Y., "A Mixed Ray Launching / Tracing Method for Full 3-D UHF Propagation Modelling and Comparison with Wide-Band Measurements," *IEEE Transactions on Antennas and Propagation*, vol. 50, no. 4 pp. 517-523, April, 2002.

[280] Lee B.S., Tan C.M., Foo S.E., Nix A.R., and McGeehan J.P., "Site Specific Prediction and Measurement of Indoor Power Delay and Power Azimuth Spectra at 5 GHz," *IEEE 54th Vehicular Technology Conference, VTC 2001*, vol. 2 pp. 733-737, 2001.

[281] Durgin G., Patwari N., and Rappaport T.S., "An Advanced 3D Ray Launching Method for Wireless Propagation Prediction," *IEEE 47 th Vehicular Technology Conference*, vol. 2 pp. 785-789, 1997.

[282] Tarng J.H., Chang W.R., and Hsu B.J., "Three-Dimensional Modelling of 900-MHz and 2.44-GHz Radio Propagation in Corridors," *IEEE Transactions on Vehicular Technology*, vol. 46, no. 2 pp. 519-527, May, 1997.

[283] Chen S.H. and Jeng S.K., "An SBR/Image Approach for Radio Wave Propagation in Indoor Environments with Metallic Furniture," *IEEE Transactions on Antennas and Propagation*, vol. 45, no. 1 pp. 98-106, January, 1997.

[284] Suzuki H. and Mohan A.S., "Ray Tube Tracing Method for Predicting Indoor Channel Characteristic Map," *Electronic Letters*, vol. 33, no. 17 pp. 1495-1496, 1997.

[285] Yun Z., Zhang Z., and Iskander M.F., "A Ray-Tracing Method Based on the Triangular Grid Approach and Application to Propagation Prediction in Urban Environments," *IEEE Transactions on Antennas and Propagation*, vol. 50, no. 5 pp. 750-758, May, 2002.

[286] Yun Z., Iskander M.F., and Zhang Z., "Development of a New Shooting-and-Bouncing Ray (SBR) Tracing Method that avoids Ray Double Counting," *IEEE International Symposium on Antennas and Propagation*, vol. 1 pp. 464-467, July, 2001.

[287] Yun Z. et al., "Fast Ray Tracing Procedure using Space Division with Uniform Rectangular Grid," *Electronic Letters*, vol. 36, No. 10 pp. 895-897, May, 2000.

[288] Athanasiadou G.E., Nix A.R., and McGeehan J.P., "A Microcellular Ray-Tracing Propagation Model and Evaluation of its Narrow-Band and Wide-Band Prediction," *IEEE Journal on Selected Areas in Communications*, vol. 18, no. 3 pp. 322-335, March, 2000.

[289] Lawton M.C., "Prediction Modelling of Radio Channel Characteristics for Small Cell Systems," *Ph.D. Thesis, Department of Electrical Engineering, University of Bristol*, 1994.

[290] Dersch U. and Zollinger E., "Propagation Mechanisms in Microcell and Indoor Environments," *IEEE Transactions on Vehicular Technology*, vol. 43, no.4 pp. 1058-1066, November, 1994.

[291] Rizk K., Wagen J.F., and Gardiol F., "Two-Dimensional Ray-Tracing Modelling for Propagation Prediction in Microcellular Environments," *IEEE Transactions on Vehicular Technology*, vol. 46, no. 2 pp. 508-518, May, 1997.

[292] Rossi J, P. and Levy A., "A Ray Model for Decimetric Radio wave Propagation in an Urban Area," *Radio Science*, vol. 27, no. 6 pp. 971-979, November - December, 1992.

[293] Tan S.Y. and Tan H.S., "UTD Propagation Model in an Urban Street Scene for Microcellular Communications," *IEEE Transactions on Electromagnetic Compatibility*, vol. 35, no. 4 pp. 423-428, November, 1993.

[294] Tan S.Y. and Tan H.S., "Propagation Model for Microcellular Communication Applied to Path Loss Measurements in Ottawa City Streets," *IEEE transactions on Vehicular Technology*, vol. 44 pp. 313-317, 1995.

[295] Huschka T., "Ray-Tracing Model for Indoor Environments and their Computational Complexity," *IEEE 5th International Symposium on Personal, Indoor and Mobile Radio Communications, PIMRC'94*, vol. 2, pp. 486-490, September 1994.

[296] Erricolo D. and Uslenghi P.L.E., "Propagation Path Loss - A Comparison between Ray-Tracing Approach and Empirical Models," *IEEE Transactions on Antennas and Propagation*, vol. 50, no. 5 pp. 766-768, May, 2002.

[297] Erricolo D. et al., "Two-Dimensional Simulator for propagation in Urban Environments," *IEEE Transactions on Vehicular Technology*, vol. 50, no. 4 pp. 1158-1168, July, 2001.

[298] Bertoni H.L. et al., "UHF propagation prediction for wireless personal communications," *IEEE Proceedings*, vol. 82, no. 9 pp. 1333-1359, September, 1994.

[299] Chen Z., Bertoni H.L., and Delis A., "Progressive and Approximate Techniques in Ray-Tracing-Based Radio Wave Propagation Prediction Models," *IEEE Transactions on Antennas and Propagation*, vol. 52, no. 1 pp. 240-251, January, 2004.

[300] Coco S., Laundani A., and Mazzurco L., "A Novel 2-D Ray Tracing Procedure for the Localization on EM Field Sources in Urban Environment," *IEEE Transactions on Magnetics*, vol. 40, no. 2 pp. 1132-1135, March, 2004.

[301] Eibert T.F. and Kuhlmann P., "Notes on Semi empirical Terrestrial Wave Propagation Modelling for Macrocellular Environments - Comparisons With Measurements," *IEEE Transactions on Antennas and Propagation*, vol. 51, no. 9 pp. 2252-2259, September, 2003.

[302] Honcharenko W. and Bertoni H.L., "Prediction of Wideband RF Propagation Characteristics in Buildings Using 2D Ray Tracing," *IEEE 45th Vehicular Technology Conference*, vol. 1, pp. 429-433, July 1995.

[303] Rizk K., Wagen J.F., and Gardiol F., "Influence of Database Accuracy on Two Dimensional Ray tracing Based Predictions in Urban Microcells," *IEEE Transactions on Vehicular Technology*, vol. 49, no. 2 pp. 631-642, March, 2000.

[304] Rizk et al., "Ray-Tracing based Path Loss Prediction in two Microcellular Environments," *IEEE 5th International Symposium on Personal, Indoor and Mobile Radio Communications, PIMRC'94*, pp. 384-388, September 1994.

[305] Zhang W. and Moayeri N., "Closed-Form Expressions for the Prediction of Microcellular Mobile Radio Propagation in Urban Environments," *IEEE Transactions on Antennas and Propagation*, vol. 51, no. pp. 952-956, May, 2003.

[306] Zhang W. et al., "A Practical Aspects of Over-rooftop Multiple Building forward Diffraction from a Low Source," *IEEE Transactions on Electromagnetic Compatibility.*, vol. 41 pp. 115-119, May, 1999.

[307] Zhang W., "A Wide-band propagation Model based on UTD for Cellular Mobile Radio Communications," *IEEE Transactions on Antennas and Propagation*, vol. 45 pp. 1669-1678, November, 1997.

[308] Jan S.C. and Jeng S.K., "A Novel Propagation Modelling for Microcellular Communications in Urban Environments," *IEEE Transactions on Vehicular Technology*, vol. 46, no. 4 pp. 1021-1026, November, 1997.

[309] Technical Committee, "Radiowave Propagation Modelling for Sat Com Services at Ku-Band and Above," *Final Report, COST Action 255, European Space Agency*, 2002.

[310] Aryanfar F. and Sarabandi K., "3-D Wave Propagation Simulation in Complex Indoor Structures," *IEEE International Symposium on Antennas and Propagation*, vol. 2, pp. 1635-1638, June 2004.

[311] O' Brien W.M. et al., "An Efficient Implementation of a Three-Dimensional Micocell Propagation Tool for Indoor and Outdoor Urban Environments," *IEEE Transactions on Vehicular Technology*, vol. 49 pp. 622-630, March, 2000.

[312] Cátedra M.F. et al, "Efficient Ray-Tracing Techniques for Three Dimensional Analyses of Propagation in Mobile Communications: Application to Picocell and Microcell Scenarios," *IEEE Antennas and Propagation Magazine, Note See Ian's Magazine*, vol. 40, no. 2 pp. 15-28, April, 1998.

[313] Cheon C. and Bertoni H.L., "Fading of Wide Band Signals Associated with Displacement of the Mobile in Urban Environments," *IEEE 55th Vehicular Technology Conference, VTC'2002*, vol. 1, pp. 1-5, May 2002.

[314] Cheon C., Liang G., and Bertoni H.L., "Simulating Radio Channel Statistics for Different Building Environments," *IEEE Journal on Selected Areas in Communications*, vol. 19, no. 11 pp. 2191-2200, November, 2001.

[315] Döttling M., Jahn A., Didascalou D., and Wiesbeck W., "Two-and Three-Dimensional Ray Tracing Applied to the Land Mobile Satellite (LMS) Propagation Channels," *IEEE Antennas and Propagation Magazine*, vol. 43, no. 6 pp. 27-37, December, 2001.

[316] Durgin G. et al., "Improved 3D Ray Launching Method for Wireless propagation Prediction," *Electronic Letters*, vol. 33, No. 16 pp. 1412-1413, July, 1997.

[317] Erceg V. et al., "Comparisons of a Computer-based Propagation Prediction Tool with Experimental Data Collected in Urban Microcellular Environments," *IEEE Journal on Selected Areas in Communications*, vol. 15 pp. 677-684, May, 1997.

[318] Fuschini F., Degli-Esposti V., and Falciasecca G., "A Statistical Model for Over Rooftop Propagation," *IEEE Transactions on Antennas and Propagation*, vol. 52, no. 1 pp. 230-239, January, 2004.

[319] Fuschini F. and Degli-Esposti V., "A Statistical Field Prediction Model for Urban Environment," *IEEE International Symposium on Antennas and Propagation*, vol. 1, pp. 236-239, June 2002.

[320] Kürner T. and Meier A., "Prediction of outdoor and outdoor-indoor-to-indoor coverage in urban areas at 1.8 GHz," *IEEE Journal on Selected Areas in Communications*, vol. 20, no. 3 pp. 496-506, April, 2002.

[321] Montiel E., Aguado A.S., and Sillion F., "A Radiance Model for Predicting Radio Wave Propagation in Irregular Dense Urban Areas," *IEEE Transactions on Antennas and Propagation*, vol. 51, no. 11 pp. 3097-3108, November, 2003.

[322] Papadakis N., Kanatas A.G., and Constantinou P., "Microcellular Propagation Measurements and Simulation at 1.8 GHz in Urban Radio Environment," *IEEE Transactions on Vehicular Technology*, vol. 47, no. 3 pp. 1012-1026, August, 1998.

[323] Rizk K., Valenzuela R.A., Fortune S.J., Chizhik D., and Gardiol F., "Lateral, Full-3D and Vertical Plane Propagation in Microcells and Small Cells," *IEEE 48th Vehicular Technology Conference, VTC*, vol. 2 pp. 998-1003, 18-21 May, 1998.

[324] Rossi J.P, "A Ray Launching Method for Radio-Mobile Propagation in Urban Area," *Proceedings of Antenna and Propagation Society Symposium, London, ON, Canada*, pp. 1540-1543, 24-28 June, 1991.

[325] Tameh E.K., "The Development and Evaluation of a Deterministic Mixed cell Propagation Model based on Radar cross-section Theory," *PhD Thesis, Faculty of Engineering, Department of Electrical Engineering, University of Bristol, UK*, 1999.

[326] Huschka T., "Ray-Tracing Model for Indoor Environments and their Computational Complexity," *IEEE 5th International Symposium on Personal, Indoor and Mobile Radio Communications, PIMRC'94*, pp. 486-490, September 1994.

[327] Kanatas A.G. and Constantinou P., "A Propagation Prediction Tool for Urban Mobile Radio Systems," *IEEE Transactions on Vehicular Technology*, vol. 49, no. 4 pp. 1348-1355, July, 2000.

[328] Kurner T. et al., "Concepts and Results for 3D Digital Terrain-Based Wave Propagation Models: An Overview," *IEEE Journal on Selected Areas in Communications*, vol. 11 pp. 1002-1012, September, 1993.

[329] Clearly J.G. and Wyvill G., "Analysis of an Algorithm for fast Tay Tracing using Uniform Space Subdivision," *The Visual Computer*, vol. 4 pp. 65-83, 1998.

[330] Fortune S.F. et al., "WISE Design of Indoor Wireless Systems: Practical Computation and Optimization," *IEEE Computational Science and Engineering Magazine*, vol. 2, no. 58, pp. 68, 1995.

[331] Zhang Z. et al., "Ray Tracing Method for Propagation Models in Wireless Communication Systems," *Electronic Letters*, vol. 36, no. 5 pp. 464-465, 2000.

[332] Agelet F. et al., "Fast Ray Tracing for Microcellular and Indoor Environments," *IEEE Transactions on Magnetics*, vol. MAG-33 pp. 1484-1487, 1997.

[333] Chen J.S. and Hall S.B., "Efficient Indoor and Outdoor EM Wave propagation in a Compact Terrain Database (CTBD) Representation of the Urban Canyon Environment," *IEEE 56th Vehicular Technology Conference*, vol. 2, pp. 802-806, September 2002.

[334] Dobkin D.P., "Computational Geometry and Computer Graphics," *IEEE Proceedings*, vol. 80, no. 9 pp. 1400-1411, 1992.

[335] Hoppe R., Wertz P., Wölfle G., and Landstorfer F.M., "Measurement of building penetration loss and propagation models for radio transmission into buildings," *IEEE 50th Vehicular Technology Conference, VTC'1999*, vol. 4 pp. 2298-2302, 1999.

[336] Wölfle G., Gschwendtner B.E., and Landstorfer F.M., "Intelligent Ray Tracing - A New Approach for Field Strength Prediction in Microcells," *IEEE 56th Vehicular Technology Conference*, vol. 2, pp. 790-794, 1997.

[337] Ghali S. and Stewart A.J., "Incremental Update of the Visibility Map as Seen by a Moving Viewpoint in Two Dimensions," *Proc. of Euro graphics Workshop on Computer Animation and Simulation*, pp. 1-11, 1996.

[338] Ghali S. and Stewart A.J., "Maintenance of the set if Segments Visible from a Moving Viewpoint in two Dimensions," *Proc.12th Annual ACM Symposium on Computational Geometry*, pp. V3-V4, 1996.

[339] Aguado A.F. et al., "UTD Electromagnetic Simulation for Microcell and Indoor Environments based on 2 1/2 Ray Tracing," *Proc.of PIERS: Progress in Electromagnetics Esearch Symposium*, pp. 599, 1996.

[340] Sánchez M.G. et al., "Exhaustive Ray Tracing Algorithm for Microcellular Propagation Prediction Models," *IEE Electronic Letters*, vol. 32 pp. 624-625, 1996.

[341] Agelet F.A. et al., "Efficient ray-tracing acceleration techniques for radio propagation modelling," *IEEE Transactions on Vehicular Technology Conference*, vol. 49 pp. 2089-2104, November, 2000.

[342] Athanasiadou G.E. et al., "A Novel 3-D Indoor Ray-Tracing Propagation Model: The Path Generator and Evaluation of Narrow-band and Wide-band Predictions," *IEEE Transactions on Vehicular Technology*, vol. 49 pp. 1152-1168, July, 2000.

[343] Lawton M.C. and McGeehan J.P., "The Application of a Deterministic Ray Launching Algorithm for the Prediction of Radio Channel Characteristics in Small-Cell Environments," *IEEE Transactions on Vehicular Technology*, vol. 43, no. 4 pp. 955-969, November, 1994.

[344] Athanasiadou G.E. and Nix A.R., "Investigation into the Sensitivity of the Power Predictions of a Microcellular Ray Tracing Propagation Model," *IEEE Transactions on Vehicular Technology*, vol. 49, no. 4 pp. 1140-1151, July, 2000.

[345] Rossi J.P. and Levy A.J., "A Ray Model for Decimetric Radio Wave Propagation in Urban Area," *Radio Science*, vol. 27 pp. 971-979, 1992.

[346] Lee D.J.Y. and Lee W.C.Y., "Propagation Prediction in and Through Buildings," *IEEE Transactions on Vehicular Technology*, vol. 49, no. 5 pp. 1529-1533, September, 2000.

[347] Rizk K., Wagen J.F., Khomri S., and Gardiol F., "Influence of Database Accuracy on Ray-Tracing-Based-Prediction in Urban Microcells," *IEEE 45th Vehicular Technology Conference, VTC'1995, Chicago, USA*, pp. 252-256, July, 1995.

[348] Lampard G. and Vu-Dinh, "The Effect of Terrain on Radio Propagation in Urban Microcells," *IEEE Transactions on Vehicular Technology*, vol. 42, no. 3 pp. 314-317, August, 1993.

[349] Lee W.C.Y. and Lee D.J.Y., "Microcell Prediction in Dense Urban Area," *IEEE Transactions on Vehicular Technology*, vol. 47, no. 1 pp. 246-253, February, 1998.

[350] Valenzuela R.A., "Ray Tracing Prediction of Indoor Radio Propagation," *IEEE 5th International Symposium on Personal, Indoor and Mobile Radio Communications, PIMRC'94*, vol. 1 pp. 140-144, September 1994.

[351] Klaassen M.G.J. and Mawira A., "A Deterministic Model for the Planning of Microcellular Mobile Radio Communication Systems," *IEEE 5th International Symposium on Personal, Indoor and Mobile Radio Communications, PIMRC'94*, pp. 389-395, September 1994.

[352] Cichon D.J. and Wiesbeck W., "Indoor and Outdoor Propagation Modeling in Pico Cells," *IEEE 5th International Symposium on Personal, Indoor and Mobile Radio Communications, PIMRC'94E*, pp. 491-495, September 1994.

[353] Cichon D.J. and Wiesbeck W., "Ray Optical Wave Propagation Modelling in Urban Micro Cells," *IEEE 5th International Symposium on Personal, Indoor and Mobile Radio Communications, PIMRC'94*, pp. 407-410, September 1994.

[354] El-Sallabi H.M. and Vainikkainen P., "Radio Wave Propagation in Perpendicular Streets of Urban Street Grid for Microcellular Communications. Part 1: Channel Modelling," *Progress In Electromagnetics Research, PIER 40*, pp. 229-254, 2003.

[355] El-Sallabi H.M., Liang G., Bertoni H.L., and Vainikkainen P., "Influence of Diffraction Coefficient on Ray Prediction of Power and Delay Spread in Urban Microcells," *IEEE 55th Vehicular Technology Conference, VTC'2002*, vol. 1, pp. 16-20, May 2002.

[356] El-Sallabi H.M., Liang G., Bertoni H.L., Rekanos I.T., and Vainikkainen P., "Influence of Diffraction Coefficient and Corner Shape on Ray Prediction of Power and delay Spread in Urban Microcells," *IEEE Transactions on Antennas and Propagation*, vol. 50, no. 5 pp. 703-712, May, 2002.

[357] EL-Sallabi H.M. and Vainikainen P., "Modelling and Simulation of Wideband Radio Channel Characterization for an Urban Line-of-Sight Microcell," *IEEE 50th Vehicular Technology Conference, VTC'1999*, vol. 4, pp. 2383 - 2387, September 1999.

[358] EL-Sallabi H.M. et al., "Full 360° Azimuth Angle Wideband Propagation Modelling for an Urban Line-of-Sight Microcellular Environment," *IEEE International Communication Conference (ICC'99), Vancouver, Canada*, pp. 1608-1612, June, 1999.

[359] Lawton M.C. and McGeehan J.P., "The Application of GTD and Ray-Launching Techniques to Channel Modelling for Cordless Radio Systems," *IEEE Proceedings Vehicular Technology Conference, Denver*, pp. 125-130, May, 1992.

[360] Mackown J.W. and Hamilton, Jr. R. L., "Ray Tracing as Design Tool for Radio Networks," *IEEE Network Magazine*, pp. 27-30, November, 1991.

[361] Lee B.S., Nix A.R., and McGeehan J.P., "Indoor Space-Time propagation Modelling using a Ray Launching Technique," *IEE 11th International Conference on Antennas and Propagation, Conference Publication No.480*, pp. 279-283, 17-20 April, 2001.

[362] Athanasiadou G.E., Nix A.R., and McGeehan J.P., "A Ray Tracing Algorithm for Microcellular Wideband Propagation Modelling," *IEEE 45th Vehicular Technology Conference, VTC'1995*, vol. 1, pp. 261 -265, July 1995.

[363] Lee B.S., Nix A.R., and MacGheehan J.P., "A spatio-temporal ray launching propagation model for UMTS pico and microcellular environments," *IEEE 53rd Vehicular Technology Conference*, vol. 1 pp. 367-371, 6-9 May, 2001.

[364] Tan S.Y. and Chua C.L., "Investigation of Propagation Mechanisms in a Typical Cellular Communication System," *IEEE Microwave Conference, Asia- Pacific*, pp. 253-256, 3-6 December, 2000.

[365] Tan S.Y. and Tan H.S., "A Microcellular Communications Propagation Model based on the Uniform Theory of Diffraction and Multiple Image Theory," *IEEE Transactions on Antennas and Propagation*, vol. 44, no. 10 pp. 1317-1326, October, 1996.

[366] Durgin G.D. et al., "Wideband Measurements of Angles and Delay Dispersion for Outdoor and Indoor Peer-to-Peer Radio Channels at 1920 MHz," *IEEE Transactions on Antennas and Propagation*, vol. 51, no. 5 pp. 936-944, May, 2003.

[367] Whitteker J.H., "Measurements of Path Loss at 910 MHz for Proposed Microcell Urban Mobile Systems," *IEEE Transactions on Vehicular Technology*, vol. 37, no. 3 pp. 125-129, August, 1988.

[368] Blaunstein N., Giladi R., and Levin M., "Characteristics' Prediction in Urban and Suburban Environments," *IEEE Transactions on Vehicular Technology*, vol. 47, no. 1 pp. 225-234, February, 1998.

[369] Rustako, Jr. A. J., Amitay N., Owens G.J., and Roman R.S., "Radio Propagation at Microwave Frequencies for Line-of-Sight Microcellular Mobile and Personal Communications," *IEEE Transactions on Vehicular Technology*, vol. 40, no. 1 pp. 203-210, February, 1991.

[370] Xia H.H., Bertoni H.L., and Maciel L.R., "Radio Propagation Characteristics for line-of-sight Microcellular and Personal Communications," *IEEE Antenna and Propagation Magazine*, vol. 41 pp. October, 1993.

[371] Taga T., Furuno T., and Suwa K., "Channel Modelling for 2-GHz-Band Urban Line-of-Sight Street Microcells," *IEEE Transactions on Vehicular Technology*, vol. 48, no. 1 pp. 262-272, January, 1999.

[372] Wang S.S. and Reed J.D., "Analysis of Parameter Sensitivity in Ray-Tracing Propagation Environment," *IEEE Proceedings 47th Vehicular technology Conference, VTC'1997, Phoenix, USA*, pp. 805-809, May, 1997.

[373] Biseglia B., "Symbolic Code Approach to GTD Ray Tracing," *IEEE Transactions on Antennas and Propagation*, vol. AP-37, no. 10 pp. 1492-1495, October, 1988.

[374] Braun W.R. and Dersch U., "A Physical Mobile Radio Channel Model," *IEEE Transactions on Vehicular Technology*, vol. 40, no. 2 pp. 472-482, May, 1991.

[375] Chuang J.C-I, "The Effects of Time Delay Spread on Portable Radio Communications Channels with Digital Modulation," *IEEE Journal on Selected Areas in Communications*, vol. SAC-5, no. 5 pp. 879-889, June, 1987.

[376] Dersch U. and Rüegg R.J., "Simulations of the Time and frequency Selective Outdoor Mobile Radio Channel," *IEEE Transactions on Vehicular Technology*, vol. 42, no. 3 pp. 338-344, August, 1993.

[377] Dersch U., "Physical Modelling of Macro, Micro and In-house Cell Mobile Radio Channels," *IEEE 3rd International Symposium on Personal, Indoor and Mobile Radio Communications, PIMRC'92*, pp. 64-68, October 1992.

[378] Hammoudeh A.M. et al., "Experimental Analysis of Propagation at 62 GHz in Suburban Mobile Radio Microcells," *IEEE Transactions on Vehicular Technology*, vol. 48, No. 2 pp. 576-588, March, 1999.

[379] Kürner T., Cichon D.J., and Wiesbeck W., "Evaluation and Verification of the VHF/UHF Propagation Channel Based on a 3-D-Wave Propagation Model," *IEEE Transactions on Antennas and Propagation*, vol. 44, no. 3 pp. 393-404, March, 1996.

[380] Laspougeas P. et al., "Radio Propagation in Urban Small Cells Environment at 2 GHz: Experimental Spatio-Temporal Characterisation and Spatial Wideband Channel Model," *IEEE 52nd Vehicular Technology Conference, VTC'2000*, vol. 2, pp. 885-892, September 2000.

[381] Marques P., Fernandes J., and Neves J., "Complex Impulse Response Modelling for Wideband Channels," *IEEE 48th Vehicular Technology Conference, VTC'1998*, vol. 2, pp. 702-706, May 1998.

[382] Russell T.A., "Use of a Building database in Prediction of Three-Dimensional Diffraction," *IEEE 42nd Vehicular Technology Conference, VTC'1992*, vol. 2, pp. 943-946, May 1992.

[383] Vaughan R.G. and Scott N.L., "Super-Resolution of Pulsed Multipath Channels for Delay Spread Characterization," *IEEE Transactions on Communications*, vol. 47, no. 3 pp. 343-347, March, 1999.

[384] Xu H., Rappaport T.S., Boyle R.J., and Schaffner J.H., "38 GHz Wideband Point-to-Point Radio Wave Propagation Study for a Campus Environment," *IEEE 49th Vehicular Technology Conference, VTC'1999*, vol. 2, pp. 1575 - 1579, May 1999.

[385] Xu H., Rappaport T.S., Boyle R.J., and Schaffner J.H., "Measurements and Models for 38-GHz Point-to-Multipoint Radio wave Propagation," *IEEE Journal on Selected Areas in Communications*, vol. 18, no. 3 pp. 310-321, March, 2000.

[386] Lauer A. et al., "Multi-mode FDTD Simulations for Indoor Propagation including Antenna Properties," *IEEE 45th Vehicular technology Conference*, vol. 1, pp. 454 - 458, July 1995.

[387] Simpson J.J. and Taflove A., "Three-Dimensional FDTD Modelling of Impulsive ELF Propagation About the Earth-Sphere," *IEEE Transactions on Antennas and Propagation*, vol. 52, no. 2 pp. 443-451, February, 2004.

[388] De Backer B. et al., "The Study of Wave-Propagation through a Windowed Wall at 1.8 GHz," *IEEE 46th Vehicular Technology Conference*, VTC'1996, vol. 1 pp. 165-169, 1996.

[389] Yang C. and Wu B., "Simulations and Measurement for Indoor Wave propagation through Periodic Structures," *IEEE International Symposium on Antennas and Propagation Digest, 1*, pp. 384-387, 1999.

[390] Yang C. et al., "A Ray-Tracing Method for Modelling Indoor Wave Propagation and Prediction," *IEEE Transactions on Antennas and Propagation*, vol. VT-46, no. 6 pp. 907-919, June, 1998.

[391] Wang Y., Safavi-Naeini S., and Chaudhuri S.K., "A Hybrid Technique Based on Combining Ray Tracing and FDTD Methods for Site-Specific Modelling of Indoor Radio Wave Propagation," *IEEE Transactions on Antennas and Propagation*, vol. 48, no. 5 pp. 743-754, May, 2000.

[392] Sandor Z. et al., "3D Ray launching and Moment Method for Indoor Propagation Purposes," *The 8th IEEE International Symposium on Personal, Indoor and Mobile Radio Communications, PIMRC'97*, vol. 1 pp. 130-134, 1997.

[393] Chaves J. et al." Comparison of Propagation Models for Small Urban Cells in GSM 900 and 1800," *http://scholar.google.com*, 2000.

[394] Smithson A.G. and Glover I.A., "Prediction of attenuation and delay-spread for systems with outdoor base-stations and indoor users," *European Conference on Wireless Technology (ECWT 06), 36th European Microwave Conference, Manchester, UK*, 2006.

[395] Smithson A.G. and Glover I.A., "A viable 3D ray tracing technique for cellular planning," *International Conference on Telecommunication and Computer Networks, (IADAT-TCN 2005), Portsmouth, UK*, 2005.

[396] Smithson A.G. and Glover I.A., "A new model for radio propagation prediction of wideband systems spanning the indoor/outdoor interface," *International Association for the Development of Advances in Technology, 2nd International Conf. on Telecommunication and Computer Networks, (IADAT-tcn 2005), Portsmouth, UK*, 2005.

[397] Smithson A.G. and Glover I.A., "Inference of propagation channel impulse response from channel sounding measurement using interpolation and simulated annealing," *UK National URSI Meeting, University of Bath, UK*, 2004.

[398] Smithson A.G. and Glover I.A., "High performance digital radio channel sounder for use at 2 and 5 GHz," *Proc.12th IEE International Conference on Antennas and Propagation, Exeter, ICAP'2003, UK*, 2003.

[399] Unar M.H., Glover I.A., Heaton J., Williams C., and Cannon P.S., "Wide-Band Mobile Radio Channel Characterisation in UHF Band for Residential Suburban Areas," *12th International Conference on Antennas and Propagation, ICAP'2003, University of Exeter, UK*, 2003.

[400] Unar M.H., Glover I.A., and Cannon P.S., "3-D Ray-Tracing Propagation Model for the Microcellular Environment in the UHF Band," *PREP 2005 Conference, Lancaster University, UK.*, 2005.

[401] Unar M.H., Glover I.A., and Vaccaro G., "Propagation Modelling for the Microcellular Environment in the UHF Band," *UK National URSI Symposium, University of Bath, UK*, 2004.

[402] "MEDAV RUSK WLLL Documents," *http://www.medav.de, Medav, Gmbh, Germany*, 1995.

[403] Sousa E.S. et al., "Delay Spread Measurements for the Digital cellular Channel in Toronto," *IEEE Transactions on Vehicular Technology*, vol. 43 pp. 837-847, November, 1994.

[404] Balanis C.A., "Antenna Theory Analysis and Design," *John Wiley & Sons, Inc*, 1982.

[405] Janssen G. J. et al., "Wideband Indoor Channel Measurements and BER Analysis of Frequency Selective Multipath Channels at 2.4, 4.75, and 11.5 GHz," *IEEE Transactions on Communications*, vol. 44, no. 10, pp. 1272-1288, October, 1996.